Making Decentralized Desalination More Affordable Using Improved Process Design, Control, and Energy Recovery

by

Sahil R. Shah

Submitted to the Department of Mechanical Engineering
in partial fulfillment of the requirements for the degree of

Doctor of Philosophy in Mechanical Engineering

at the

MASSACHUSETTS INSTITUTE OF TECHNOLOGY

September 2021

Author .....
Department of Mechanical Engineering
August 20, 2021

Certified by .....
Amos G. Winter, V
Associate Professor of Mechanical Engineering
Thesis Supervisor

Accepted by .....
Nicolas Hadjiconstantinou
Chairman, Department Committee on Graduate Theses

Making Decentralized Desalination More Affordable Using Improved Process Design, Control, and Energy Recovery

by

Sahil R. Shah

Submitted to the Department of Mechanical Engineering
on August 20, 2021, in partial fulfillment of the
requirements for the degree of
Doctor of Philosophy in Mechanical Engineering

Abstract

In countries such as India, where continuous access to treated piped-water is uncommon, many have resorted to desalinating brackish groundwater to meet their drinking needs. This form of decentralized treatment is performed at the community-scale, as is common in rural areas, and within individual homes, using point-of-use (POU) purifiers. This thesis develops methods to lower the costs and improve the efficiencies of two technologies for these applications: electrodialysis (ED) and reverse osmosis (RO).

Batch ED desalination, which relies on recirculating water to reach a desired product concentration, is often conducted at constant voltage. This operation scheme causes the membrane area to be underutilized because the ratio of applied current to limiting current is initially low during the batch cycle. By applying a time-varying voltage to the ED stack, we raised this ratio and increased production rate by up to 37% using the same membrane area. In parallel, we derived an analytical prediction of the batch time and validated it under varying feed and product concentrations, and flow velocities. The experiments and model together suggest that the proposed control scheme will improve production rate most significantly when desalinating through large concentration changes at low flow velocities. This work will assist engineers and operators seeking to size, evaluate, and maximize the production performance of new and existing batch ED systems.

Decreasing the energy requirements of community-scale RO, by recovering hydraulic power from the brine stream, will make off-grid deployments more affordable. However, existing energy recovery devices (ERDs) are prohibitively expensive. We investigated the feasibility of leveraging ubiquitous gear and sliding vane positive-displacement mechanisms within a fixed-recovery architecture to provide a low-cost ERD solution. By modeling the coupled behavior of the pump, ERD, and RO train, we showed that production performance is sensitive to volumetric efficiency. Based on this finding, vanes were selected over gears for prototyping. The prototype enabled a 17% decrease in measured power consumption, and through characterizing friction, we determined that these savings could be doubled by balancing pressure loads on the

vane mechanism's rotor. This work lays the groundwork for realizing an affordable ERD for community-scale RO treatment.

Finally, today's POU RO purifiers only recover 20-30% of the input feed as drinking water and consume significant energy. By testing and analyzing a POU RO system, it was identified that recirculating the brine within a semi-batch configuration could help address these limitations. We engineered such a system using off-the-shelf parts, and in initial testing, showed that it could achieve recoveries of up to 75% without affecting production rate and quality. With further testing and refinement, this semi-batch system could make POU water desalination more efficient.

Thesis Supervisor: Amos G. Winter, V
Title: Associate Professor of Mechanical Engineering

Acknowledgments

First and foremost, I must thank my family for their boundless love and support throughout this journey. Above all, I am forever indebted to my parents, who have made enormous sacrifices so I could pursue a graduate degree at MIT.

Thank you Amos for granting me the freedom to explore the problems that interested me most, while also pushing me to explore them comprehensively. Your mentorship over the past six years has played a strong role in shaping my capabilities as a researcher and engineer.

Professors Lienhard and Karnik, I am sincerely grateful for your guidance on several aspects central to my PhD experience: this research, the entrepreneurial activities, and on career decisions. You have both served as important role-models during my time at MIT as you clearly exemplify what it means to be an academic.

I am also grateful for the market insight and feedback that my research collaborators have provided through the years. In particular, I thank S.K. Sankar, Suresh Reddy, Dr. Raman Venkatesh, and Dr. Sathish Kumar, at Eureka Forbes, and Mark Shu, Samuel Long, Poul Hansen, Stig Andersen, and Georg Enevoldsen, at Danfoss. Your guidance helped to ensure that the research was grounded in practice.

To the GEAR Lab members of past and present, including all the UROPs that have worked with me, thank you for all the exchanges. They were most thoughtful, creative, and fun. I feel blessed to have worked with colleagues who are so brilliant and inspiring.

Thank you to all my caring friends from Cambridge, Houston, and Edmonton. You have brought brightness, laughter, and adventure, to this journey. Victor, I will forever cherish the numerous hours we spent together on fun side projects, furiously competitive squash games, and exhilarating windsurfing sessions. Emily, thank you for being by my side through both the happiest and most challenging times over the past six years. You have taught me to be more patient and thoughtful, and I look forward to all our adventures to come.

To the many teachers and mentors that have shaped my thinking and the staff

that have helped me navigate MIT, including Saana, Una, Leslie, Cakky, and Janice, thank you all for the effort invested in my education.

Finally, I wish to express my deepest gratitute to the several institutions that have financially supported me and funded this work: Eureka Forbes Ltd, the Tata Center for Technology and Design at MIT, Tata Projects Ltd, the Natural Sciences and Engineering Research Council of Canada (NSERC), the Abdul Latif Jameel Water and Food Systems Lab at MIT (J-WAFS), and the Julia Burke Foundation. Without their support, I would not have been so privileged to conduct this research.

Contents

THIS PAGE INTENTIONALLY LEFT BLANK

List of Figures

List of Tables

Chapter 1

Introduction

This thesis develops methods to lower the cost and energy consumption of electrodialysis (ED) and reverse osmosis (RO) desalination for community-scale and point-of-use water treatment. These solutions are explored within the socioeconomic context of India, where decentralized treatment is widely used as a means to produce drinking water.

1.1 Centralized Water Systems

Over the past decade, there has been an increase in the population of Indians with access to a piped-water supply from a centralized water treatment facility (Fig. 1-1). Unfortunately, this development has lagged population growth, and the presence of such a supply does not guarantee that sufficient water is available, nor that it is of drinkable quality.

In urban areas, the piped-water supply is often intermittent and contaminated. In a comprehensive assessment of water utilities performed by the Ministry of Urban Development in 2013 [2], urban homes received five hours of water supply on average across the country and only 83% of the tested samples met drinking water standards (Table 1.1). More recently in 2019, the Bureau of Indian Standards collected and tested water samples from 21 cities for drinking quality. Of those cities, Mumbai was found to be the only city where all water samples met drinking standards [3].

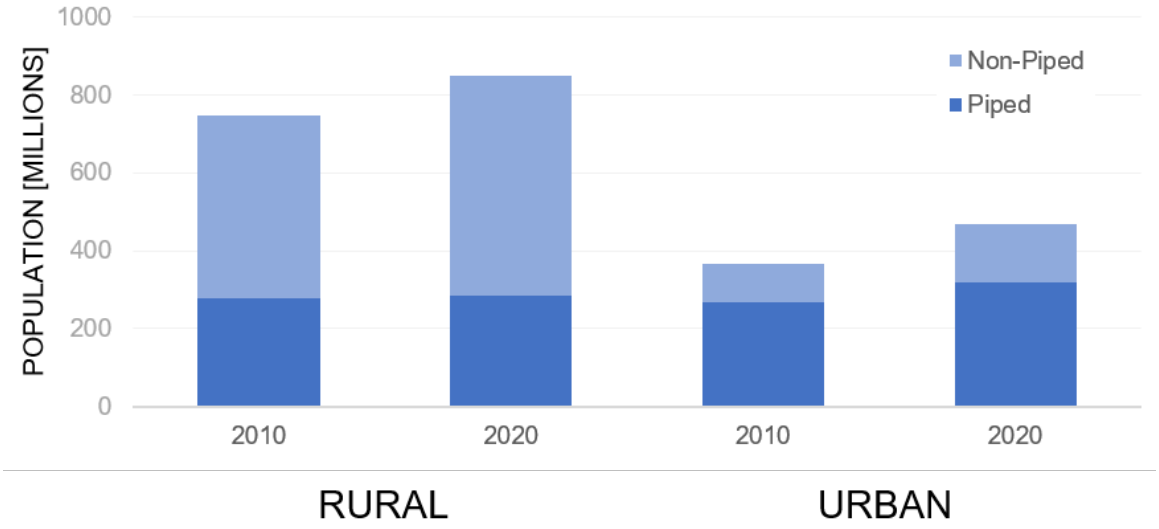

Figure 1-1: **Progress toward providing piped water supply in rural and urban India**. Breakdown of rural and urban populations in India with piped and non-piped access to an *improved source* of drinking water. An improved source, as defined by the Joint Monitoring Programme for Water and Sanitation, is one that has the potential to deliver safe water by nature of its design and construction [1]. These sources include piped water, boreholes, tubewells, protected dug wells, protected springs, rainwater, and packaged water.

.

The public is aware of these quality issues and do not consider their municipal water safe for drinking [4]. Complicating matters further, water tariffs collected by the utilities only fund approximately 50% of the water treatment costs, excluding capital equipment recovery. Hence, the existing centralized urban water systems are also financially unsustainable.

In rural regions, where 65% of the population currently resides, piped-water coverage significantly lags national goals. In 2012, the government introduced the National Rural Drinking Water Programme to improve rural water access [5]. After investing $11 billion USD, the percentage of villages with adequate water supply (defined as 55 L/capita-day) had increased from 39% to only 44% over a five-year period through 2017. Over the same duration, the government had aimed to increase the percentage of rural households with individual piped connections to 50%. However, only 18% of the households were equipped with such a supply. Given this slow progress, it seems unlikely the government will meet their objective to connect 80% of rural homes with

Table 1.1: **Average national performance of water utilities.** Targets were set in 2009 and performance was measured in 2013 [2].

Service-level Benchmark	Target	Performance
Coverage Connections with Direct Service	100	55
Per Capita Supply [LPCD]	135	100
Metering of Water Connections [%]	100	16
Non-Revenue Water [%]	20	25
Continuity of Supply [hrs]	24	5
Quality and Treatment [%]	100	83
Redressal of Customer Complaints within 24 hrs [%]	80	93
Cost Recovery [%]	100	50
Efficiency in Collection Charges [%]	90	58

individual piped-water supplies by 2022.

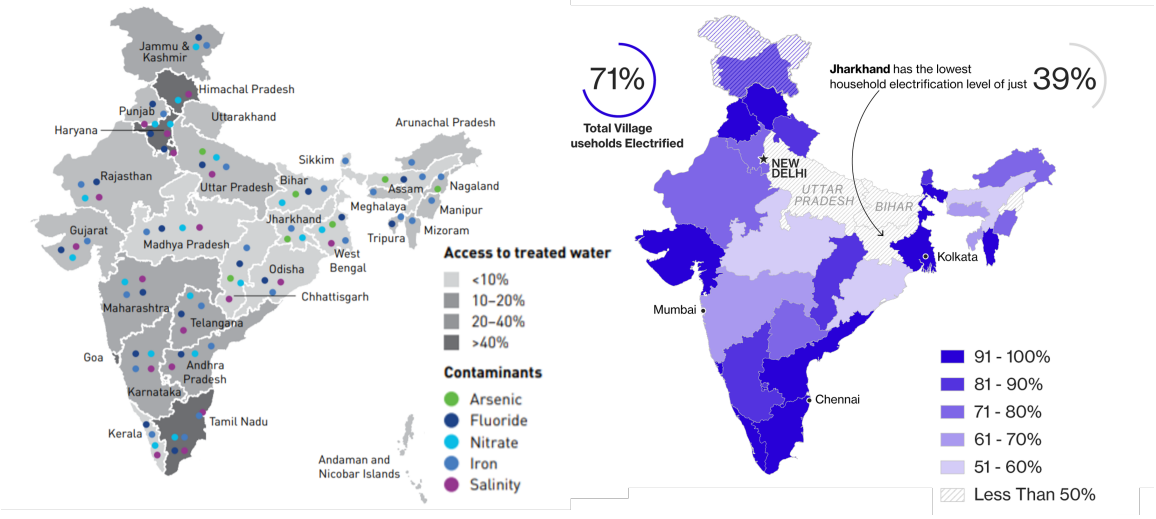

Figure 1-2: **Households that lack access to treated water tend to be in regions that also have low electrification.** The map on the left indicates the percentage of households in each state with access to treated water [6]. On the right is the percentage of village households with access to electricity [7]

.

The deficient water supply in urban areas and the low piped coverage in rural areas has driven a high reliance on groundwater. In a 2007 survey conducted by Shaban and Sharma, 67% of the 2,734 households in seven cities were considered to be water deficient [8]. To cope, 7% relied solely on groundwater, and 38% used it to supplement their piped supply. Across the whole country, the World Bank estimates that 85% of drinking water is supplied by groundwater [9]. However, much of the groundwater

underlying India is also unsafe for drinking without treatment. It is contaminated with nitrates, iron, arsenic, and fluoride (Fig. 1-2). Groundwater that underlies 60% of India is also brackish, with total dissolved solids (TDS) of up to 3000 mg/L, exceeding the 500 mg/L threshold recommended by the Bureau of Indian Standards for drinking purposes [10]. The need to treat both this brackish groundwater and piped-water prior to consumption has led to the widespread adoption of decentralized community-scale water treatment systems and point-of-use purification products. The following sections describe these solutions and highlight their limitations.

1.2 Community Water Purification Plants

Community Water Purification Plants (CWPPs) or Community Safe Water Solutions (CSWS), in capacities ranging from 500 to 2000 L/h, have been installed across India to provide drinking water to those living beyond piped supply [6, 11, 12]. These plants typically use brackish water reverse osmosis (BWRO) (Fig. 1-3).

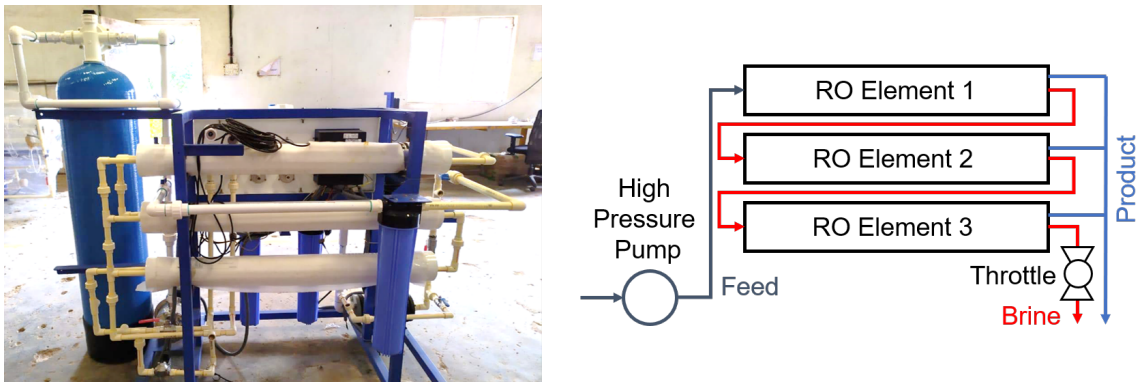

Figure 1-3: **Community-scale BWRO systems use a small number of RO elements to produce drinking water from brackish groundwater.** The photograph (left) shows a 0.5 m3/h system manufactured by Tata Project Ltd. The schematic (right) highlights the RO process in such a system. Feed water passes through three RO elements in series, each recovering a fraction as product water. The throttle enables the feed stream to be pressurized, but dissipates all hydraulic power remaining in the brine stream.

1.2.1 BWRO - The Tool of Choice

In RO, a mechanical pressure is applied to overcome the osmotic pressure of a feed, causing water to flow across a semi-permeable membrane. RO is the favored technology for this application for several reasons:

1. RO systems are easy to operate. Local operators are trained to operate them in rural communities.

2. They are effective against all the major contaminants found in Indian groundwater. For SWEs, it is therefore more cost-effective and logistically easier to procure and deploy standardized BWRO solutions everywhere than to build expertise over several technologies and select among them on a case-by-case basis.

3. Parts and replacement membranes are easily available. This availability of components helps to ensure that the systems can be maintained.

4. Customers are accustomed to the taste of low salinity bottled water that is often produced by RO desalination. The aesthetic quality of water, which includes its taste, plays an important role in customers' perceptions of water quality [13].

Despite these benefits, they have two major limitations: low recovery ratio and high specific energy consumption. Unlike large BWRO plants where extensive pretreatment and trains of several membrane elements are used to achieve recoveries of 70-90% [14–16], these smaller units typically recover only 50% of the input feed as drinking water [11, 12]. Dissipation of brine pressure, particularly when such large fractions of the input feed are expelled as brine, results in high specific energy consumption (SEC). At 50% recovery, for example, approximately half the hydraulic power from the pump is dissipated at the brine throttle. Furthermore, these losses are compounded by the poor efficiency of small pumps and motors.

The high energy requirements of the BWRO process has hindered adoption by communities that do not have access to the grid, even though regions that lack electrical infrastructure generally overlap with those lacking access to treated water. When

photovoltaic (PV) systems are needed to generate power for BWRO desalination in off-grid applications, the high SEC of the process translates to large power system capital costs [17]. A 2018 study found that commercially available 1-10 m^3/h BWRO systems powered by the grid cost $4,000-8,000, while their PV-powered counterparts cost $20,000-80,000 [11]. Safe Water Network, an operator of these community-scale BWRO systems, also reports that the capital cost of their standard 1 m^3/h systems rises from $7,000 -$10,000 when grid-powered to ∼$24,000 when PV-powered [17]. Decreasing this capital cost premium, by making the process more energy-efficient, will therefore increase affordability to target users in off-grid communities across India and other developing countries [17–19]. This thesis investigates one method to decrease the energy consumption of community-scale BWRO systems: adding an energy recovery device (ERD) to recover hydraulic power from the brine stream.

1.2.2 ED - A Viable Alternative

Electrodialysis (ED) has been previously proposed as an alternative technology for community-scale brackish water desalination. In ED, an electric field is applied across a series of flow channels that are separated by alternating cation (CEM) and anion (AEM) exchange membranes (Fig. 1-4). The selective transport of cations and anions through these membranes results in one set of channels being desalinated and the alternating set being concentrated. Several studies have shown this process to be more energy-efficient than RO when desalinating feeds of less than 5000 mg/L concentration [12, 20–22] to product concentrations of approximately 300-500 mg/L, which are suitable for drinking. Another advantage is that the degree of salt-removal can be adjusted in ED to tune the product concentration. The same adjustment is not feasible in RO, as it is a water-removal technology. Instead, small feed volumes are typically re-added to the RO permeate if a higher product concentration is desired.

To test whether ED is an economically viable solution for community-scale desalination, the Global Engineering and Research (GEAR) Lab collaborated with Tata Project Ltd. to pilot a batch ED system (Fig. 1-5) and evaluate its performance against a BWRO system on groundwater in Medchal, India (Table 1.2). The team

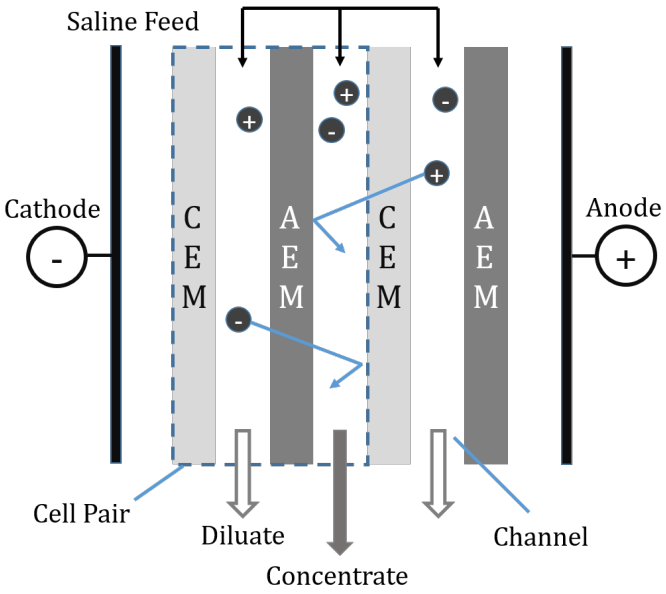

Figure 1-4: **Schematic of an electrodialysis (ED) stack.** In ED, a voltage potential is applied across a series of alternating cation (CEM) and anion (AEM) exchange membranes to transport ions from the diluate channels to the concentrate channels.

calculated the equipment costs for both systems and measured the energy that they consumed. When the feed was desalinated to 200 mg/L TDS, a concentration that is considered suitable for drinking purposes, the ED process had a 31% lower energy consumption than the RO process. For a 100 mg/L TDS output, the energy consumption was still 5% lower than for the RO process. The ED pilot was also capable of producing twice as much drinkable water from the feed than the RO process. Although ED was more energy- and water-efficient, the equipment costs were almost 5x greater than for RO. To be commercially competitive with RO, these costs must be decreased. This thesis investigates a method to control the ED process such that less membrane area is needed to achieve a target production rate. By decreasing membrane usage, we aim to make ED systems more affordable.

Figure 1-5: **Batch ED pilot deployed in Medchal, India.** The GEAR Lab collaborated with Tata Projects Ltd. to pilot a 500 L/h ED groundwater desalination system and evaluate its performance against a RO system.

1.3 Point-of-Use Treatment

As discussed in Section 1.1, intermittent and inadequate piped-water supply has driven a high reliance on brackish groundwater in Indian cities. Point-of-use (POU) reverse osmosis (RO) purifiers offer a means for households to treat this saline supply for drinking purposes. Even when piped-water is available, it can still be unfit for consumption due to other contamination [3]. The need to purify this water has further contributed to the widespread use of POU RO devices even though desalina-

Table 1.2: **Cost and energy consumption comparison of community-scale ED and RO systems.** This data was compiled during a GEAR Lab pilot study in Medchal, India

Parameter	**ED**		**RO**
Production Rate	500 L/h		
Feed TDS	800 mg/L		
Capital Cost	\$9,800		\$1,650
Recovery Ratio	80%		40%
Product TDS	200 mg/L	100 mg/L	100 mg/L
SEC	2.7 kWh/m^3	3.7 kWh/m^3	3.9 kWh/m^3

tion may not be required. In 2016, Ghosh et al. found that 77%, 44%, and 27% of surveyed high, middle, and low income households in Delhi used POU RO systems [4]. Therefore, they have become a common appliance in urban homes.

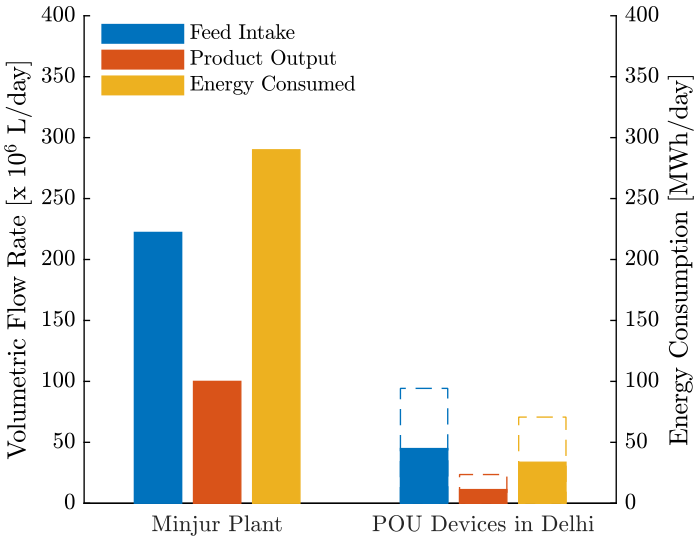

Figure 1-6: **Comparing point-of-use (POU) desalination to centralized desalination at a large-scale plant.** Energy and water consumption are compared for all POU RO devices in Delhi versus one of India's largest seawater desalination plants, Minjur. The POU devices produce an equivalent of 11% of Minjur's capacity but consume 12% as much energy (*solid*). Their collective energy consumption is projected to double by 2023 due to increased adoption (*dashed*).

Significant advances have been made to decrease the energy consumption of RO at a municipal scale [23], but they have not translated to POU systems. The consequence of this disparity is demonstrated in Figure 1-6, where we compare the energetic cost of distributed POU desalination to a centralized solution. Here, we estimate that POU RO devices in Delhi alone collectively produce 11% as much potable water as one of India's two largest municipal seawater desalination plants (Minjur) but consume 12% as much energy. These estimates are derived in Appendix A. This ratio may seem reasonable at first glance, but POU devices primarily treat groundwater with TDS content that is 20-30 times lower than that of the seawater. Therefore, it would be fair to expect a lower total energy consumption from the POU devices.

Operating at recovery ratios of 32% or less [24], today's POU RO systems also withdraw significantly more water per unit volume of produced water than treatment

plants. While the Minjur plant desalinates seawater at a 45% recovery [25], brackish water RO plants can recover 70-90% from lower-salinity feeds [14–16]. Thus it may also be possible for POU RO systems to process groundwater more effectively, as this resource is becoming increasingly scarce in urban India [26].

Adoption of POU RO purifiers is on the rise due to growth in India's middle-class income, and poor water quality in many parts of the country. Frost and Sullivan recently forecast sales to grow at 16% from 2018 to 2023 [27]. Without technological upgrades, environmental impact can be expected to grow in a similar manner. Projecting from estimates in Figure 1-6, POU devices in Delhi will consume one-fourth the energy of Minjur by 2023. The same market research also suggests that there is a lack of product differentiation among competing units. Beyond the addition of more pre- and post-filtration stages, the core architecture of RO modules has remained largely unchanged since their introduction to the Indian market in 1999. Therefore, there is both an environmental impetus and an economic incentive to innovate in this space.

1.3.1 The National Green Tribunal

The National Green Tribunal is a specialized body established by the National Green Tribunal Act of 2010 that manages cases related to environmental protection and conservation of India's natural resources. To promote more efficient use of scarce water resource, the NGT has recommended that the government regulate manufacturers of POU RO products to meet several requirements [28], of which the most important include:

- POU RO should only be recommended and sold in places where the input water TDS exceeds 500 mg/L.
- Where RO use is permitted, the products should satisfy a minimum recovery ratio of 60%. Eventually, the NGT aims to raise this minimum to 75%.
- Products must provide the capability to collect brine so that it can be used for other household purposes such as washing and gardening.

- Treated water should have a minum 150 mg/L TDS concentration.

Given that POU RO systems currently only recover 20-30% of the feed [24], raising the recovery to 60% is the most technically challenging requirement among the above. In this thesis, we engineer a POU RO system that may be capable of satisfying this recovery requirement while also being more energy-efficient than existing products.

1.4 Outline of the Thesis

Decentralized desalination systems provide an effective solution to produce drinking water in regions where public infrastructure is either absent or incapable of reliably delivering treated water. However, as discussed in Sections 1.2 through 1.3, each approach has its key limitations: high capital cost for ED, high energy consumption for community-scale RO, and low water recovery for POU RO. This thesis investigates solutions to address these limitations using a combination of modeling, prototyping, and testing, as is outlined below.

- **Chapter 2: Feed-Forward Voltage-Control of Batch Electrodialysis Desalination**

  A method of controlling batch ED processes that maximizes salt flux is proposed and experimentally demonstrated. By controlling the voltage applied to the stack such that the applied current density tracks the limiting current density, it is shown that the desalination rate can be significantly improved with minimal changes to the hardware.

- **Chapter 3: Modeling the Recovery and Specific Energy Consumption of Single-Stage Reverse Osmosis Systems**

  A simple model for estimating the recovery and specific energy consumption of single-stage RO systems is derived and validated against experimental data compiled from literature. The same model is used in the following chapter when simulating the coupled behavior of the pump, energy recovery device, and RO train.

- **Chapter 4: Using Gear and Vane Mechanisms as Energy Recovery Devices in Small-Scale Reverse Osmosis Applications**

  A fixed-recovery architecture that couples two rotary positive displacement (PD) stages, a pump and energy recovery device, is proposed and modeled. The production rate and specific energy consumption of such a device is compared for two candidate PD mechanisms: gears and sliding vanes.

- **Chapter 5: Experimental Evaluation of a Fixed-Recovery Coupled Vane Pump-ERD Prototype**

  A prototype fixed-recovery system is assembled using purchased vane pumps and experimentally evaluated. From analyzing the friction sources, methods to improve the vane ERD are additionally identified.

- **Chapter 6: Evaluating the Production and Energetic Performance of Point-of-Use Reverse Osmosis Devices**

  Experiments, paired with an exergy analysis, are used to explain the low recovery ratio and high specific energy consumption (SEC) of point-of-use reverse osmosis (RO) devices. This analysis was used to identify methods for improving their performance.

- **Chapter 7: Engineering a Semi-Batch Reverse Osmosis System for Point-of-Use Applications**

  A preliminary evaluation of a semi-batch RO prototype engineered using off-the-shelf parts indicates that it may be a viable high-recovery solution for point-of-use desalination. A description of this prototype is provided, along with suggestions on how to improve it.

Bibliography

[1] WHO/UNICEF Joint Monitoring Programme. Prograss on Household Drinking Water, Sanitation and Hygiene. Technical report, 2021.

[2] Meera Mehta and Dinesh Mehta. Water and Sanitation Service Levels in Cities of India (2011-12 and 2012-13). Technical report, CEPT University, 2014.

[3] Bureau of Indian Standards. Report of Testing of Piped Drinking Water Samples from 20 Capital Cities and Delhi. 2019.

[4] Ruchira Ghosh, Arun Kansal, and Sakshi Aghi. Implications of end-user behaviour in response to deficiencies in water supply for electricity consumption – A case study of Delhi. *Journal of Hydrology*, 536(March 2015):400–408, 2016.

[5] Comptroller and Auditor General of India. Report No.15 of 2018 - Performance Audit on National Rural Drinking Water Programme. Technical report, Ministry of Drinking Water and Sanitation, 2018.

[6] Safe Water Network. Community Safe Water Solutions: India Sector Review - 2014. Technical Report August, 2014.

[7] Rajesh Kumar Singh and Saket Sundria. Living in the Dark: 240 million Indians have no electricity, jan 2017.

[8] Abdul Shaban and R.N. Sharma. Water Consumption Patterns in Domestic Households in Major Cities Water Required for Different Activities. *Economic and Political Weekly*, (1993):2190–2197, 2007.

[9] The World Bank. Deep Wells and Prudence : Towards Pragmatic Action for Addressing Groundwater Overexploitation in India. Technical report, The International Bank for Reconstruction and Development/The World Bank, Washington, DC, 2010.

[10] Bureau of Indian Standards. IS 10500 - Drinking Water Specification, 2012.

[11] Kathryn S Boden and Chinmayee V Subban. A Road Map for Small Scale Desalination. (May), 2018.

[12] Natasha C. Wright and Amos G. Winter. Justification for community-scale photovoltaic-powered electrodialysis desalination systems for inland rural villages in India. *Desalination*, 352:82–91, 2014.

[13] PATH. User Testing of Household Water Treatment and Storage Products in Andhra Pradesh, India. (March), 2011.

[14] M.A. Alghoul, P. Poovanaesvaran, K. Sopian, and M.Y. Sulaiman. Review of brackish water reverse osmosis (BWRO) system designs. *Renewable and Sustainable Energy Reviews*, 13(9):2661 – 2667, 2009.

[15] W. Arras, N. Ghaffour, and A. Hamou. Performance evaluation of BWRO desalination plant - a case study. *Desalination*, 235(1):170 – 178, 2009.

[16] M.A. Al-Obaidi, A.A. Alsarayreh, A.M. Al-Hroub, S. Alsadaie, and I.M. Mujtaba. Performance analysis of a medium-sized industrial reverse osmosis brackish water desalination plant. *Desalination*, 443:272 – 284, 2018.

[17] Safe Water Network. India Sector Review - Small Water Enterprises to Mitigate the Drinking Water Challenge. (October), 2018.

[18] Michael Papapetrou, Marcel Wieghaus, and Charlotte Biercamp. Roadmap for the development of desalination powered by renewable energy. Technical report.

[19] Manoj Chandra Garg and Himanshu Joshi. A Review on PV-RO Process: Solution to Drinking Water Scarcity due to High Salinity in Non-Electrified Rural Areas. *Separation Science and Technology (Philadelphia)*, 50(8):1270–1283, 2015.

[20] H. Strathmann. Electrodialysis, a mature technology with a multitude of new applications. *Desalination*, 264(3):268–288, 2010.

[21] Ronan K Mcgovern, Syed M Zubair, and John H. Lienhard. The benefits of hybridising electrodialysis with reverse osmosis. *Journal of Membrane Science*, 469:326–335, 2014.

[22] Sohum K. Patel, P. Maarten Biesheuvel, and Menachem Elimelech. Energy Consumption of Brackish Water Desalination: Identifying the Sweet Spots for Electrodialysis and Reverse Osmosis. *ACS ES&T Engineering*, 1(5):851–864, 2021.

[23] Menachem Elimelech and William A. Phillip. The future of seawater desalination: Energy, technology, and the environment. *Science*, 333(6043):712–717, 2011.

[24] Comprehensive Initiative on Technology Evaluation. Household Water Filter Evaluation, Project Evaluation Report. Technical report, Massachusetts Institute of Technology, 2015.

[25] Chennai Metropolitan Water Supply and Sewerage Board. Republic of India Preparatory Survey on Chennai Seawater Desalination Plant Project, Final Report. pages 3–44, 2017.

[26] Tom Gleeson, Yoshihide Wada, Marc F P Bierkens, and Ludovicus P H van Beek. Water balance of global aquifers revealed by groundwater footprint. *Nature*, 488(7410):197–200, 2012.

[27] Frost & Sullivan. Indian Water Purifiers Market, FY2018. Technical report, 2018.

[28] National Green Tribunal. Friends through its General Secretary vs. Ministry of Water Resources, Original Application No. 134/2015, 2019.

Chapter 2

Feed-Forward Voltage-Control of Batch Electrodialysis Desalination

A version of this chapter was published in the Journal of Desalination in 2019, under the title "Using feed-forward voltage-control to increase the ion removal rate during batch electrodialysis desalination of brackish water." Sandra L. Walter helped perform the experiments for this work.

2.1 Introduction

In recent years, the need for energy-efficient and high-recovery solutions for brackish water desalination has revived an interest in Electrodialysis (ED) technology [1–4]. An ED stack relies on the use of an electric field, across alternating cation (CEM) and anion exchange membranes (AEM) arranged in repeating cell-pairs, to draw ions from a desalinated diluate solution to a concentrated solution (Fig. 2-1). In industrial processes, a feed solution is continuously desalinated to a desired product concentration, within a single pass through one or more discrete ED stages (Fig. 2-2a). Where space is a constraining factor, the diluate is recirculated through a single ED stack several times to achieve the desired product concentration in a batch process (Fig. 2-2b) [5–8].

Several authors have investigated the cost-minimizing design of both continuous

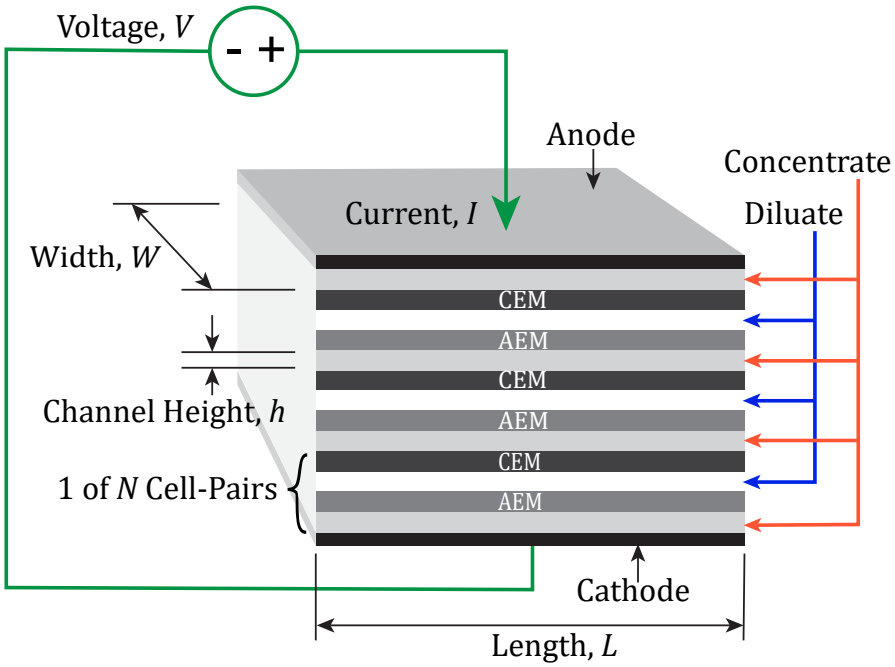

Figure 2-1: In ED, an electric field is applied across alternating cation (CEM) and anion (AEM) exchange membranes to transport ions from the diluate channels to the concentrate channels. Diluate and concentrate outflows are omitted here for visual clarity.

and batch processes [9–16], where the capital cost is primarily a function of the required membrane area. In these studies, the required membrane area is decreased by raising the current density i. This term represents the per unit-area flux of ions through an individual membrane. In continuous systems, this current density is maximized throughout the process length by applying different voltages V and numbers of cell-pairs N to the individual ED stages [12, 17, 18] (Fig. 2-2a). However, with batch desalination, most studies do not take the analogous approach of adjusting the stack voltage in a time-variant manner. Instead, the batch is often processed at a constant voltage [19–24]. Min and Kim performed constant-voltage desalination experiments and demonstrated that increasing voltage provided diminishing improvements in the salt removal rate [23]. Tanaka used simulation to identify the voltages and feed concentrations at which a constant-voltage batch ED process provides a lower energy consumption than reverse osmosis (RO) [20]. Nayar *et al.* [24] and Bian *et al.* [25] designed batch desalination systems for household and community-scale applications,

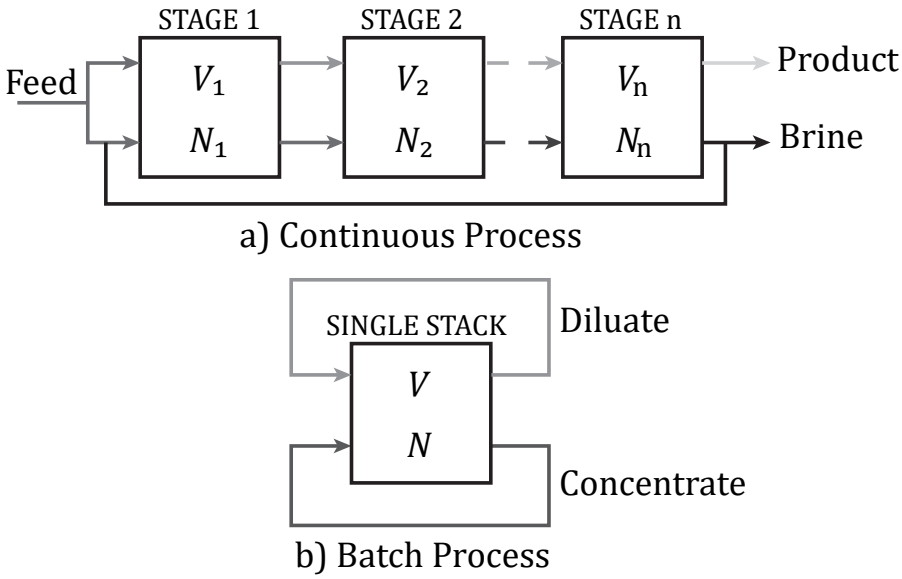

Figure 2-2: (a) A saline feed is desalinated within a single pass through multiple ED stages in a *continuous process*, each with a different voltage V and number of cell-pairs N. (b) In a *batch process*, diluate is recirculated through a single ED stack until it is desalinated to a desired product concentration.

respectively, but also limited their parameter-space to consider only constant-voltage operation.

Previous studies that have examined controlling the batch desalination process in a time-varying manner mostly focus on energy consumption. Parulekar mathematically demonstrated that a time-varying voltage or current can yield a lower energetic cost than a constant-voltage process, when considering both pumping and desalination, but did not explore potential membrane area savings [26]. Leitz recommended controlling the batch process to maintain a constant ratio of current to diluate concentration, but did not justify his suggestion in detail, nor discuss the expected effect on batch time [27]. Rohman and Aziz investigated the optimal current density and flow rate, as a function of time, for several performance metrics related to a hydrochloric acid recovery process [13]. However, they did not implement a concentration-dependent limiting current density constraint in their simulations, which becomes important when desalinating to low concentrations. Chehayeb and Lienhard compared operation at constant voltage, constant current, and constant entropy generation, on batch ED electrical power consumption [28]. They showed that

operating at constant current was always energetically preferable to constant voltage. However, they also concluded that this operating condition was not cost-effective for brackish water desalination due to the high ratio of ED equipment costs relative to energy costs. In this work, we instead examine controlling the process to minimize the size of the equipment needed for a given batch process and in doing so, show that the same operating scheme could also be energy-saving when pumping energy is also considered. Additionally, to our knowledge, the existing literature does not provide descriptions of batch ED controllers or experimental demonstrations of time-variant voltage-control.

Building upon this previous work, we sought to provide a comprehensive description, analysis, and experimental demonstration of time-variant voltage-control for batch ED desalination of brackish water. Specifically, we

1. detailed the concept and potential advantages of active voltage-control;

2. designed a bench-scale, feed-forward controller and experimentally implemented different voltage trajectories;

3. evaluated the decrease in batch duration, membrane usage, and energy consumption that can be safely achieved; and

4. derived a model to predict batch completion times, and validated it against voltage-controlled and constant-voltage tests.

While the use of time-variant voltage or current control is uncommon in ED, we acknowledge that it has been previously applied in other electrochemical processes [29–32]. Most notably, Panizza *et al.* varied the stepwise current over time to increase the mineralization rate of organic pollutants on boron-doped diamond anodes in an electrolysis process, and lower energy consumption [33]. We therefore employ a similar approach in this work, adapting it to enhance batch ED.

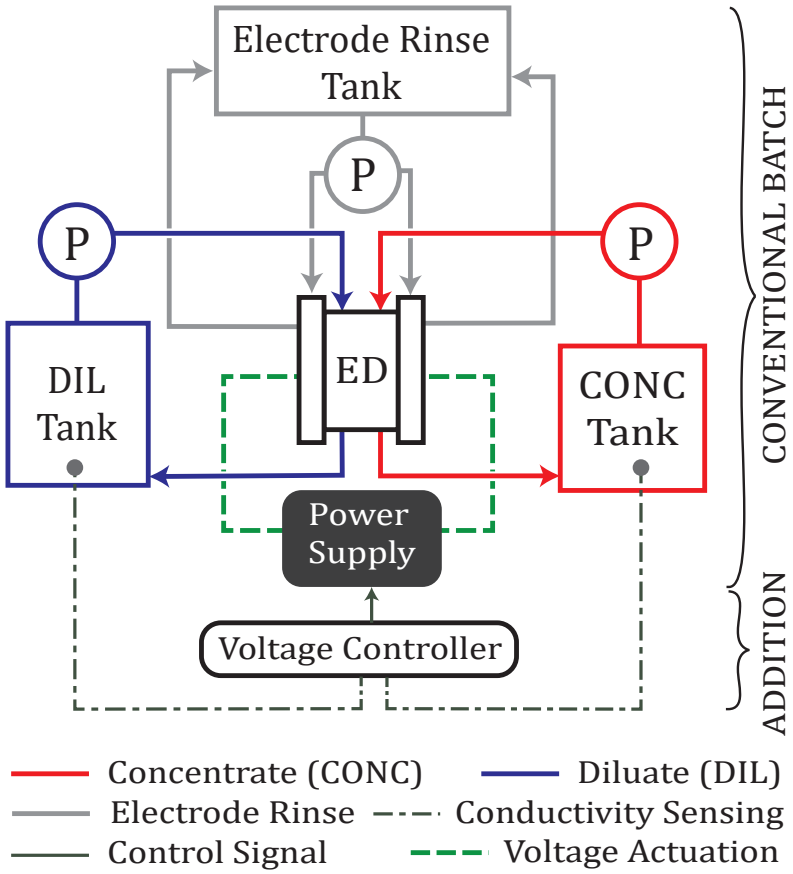

Figure 2-3: Schematic of a conventional batch process. The addition of a controller allows voltage-controlled operation, based on conductivity measurements. “P" and “ED" represent the pump and ED stack, respectively.

2.2 The Concept

In batch ED desalination, an initial feedwater volume is separated at the desired recovery ratio into two circuits, one for the diluate and the other for the concentrate (Fig. 2-3). During desalination, the solutions are recirculated through the stack and a voltage is applied until the desired product concentration is obtained in the diluate tank. Both in simulation and practice, the voltage and recirculation flow rates are conventionally held constant during this process, as previously discussed. An additional third circuit may also be required to rinse the electrodes, but does not affect the following discussion.

The limiting current density is the concentration-dependent maximum salt removal rate that can be achieved before ions are depleted at the membrane surfaces.

To avoid splitting water, affecting the product pH, and increasing the resistance to ion-transport, the ED stack is conventionally operated below this limiting current density. Assuming a short flow path and neglecting spatial concentration variations within the stack [28], the limiting current density i_{lim} [A/m^2] is plotted against the diluate concentration C_d^b, which only varies in time from the start to the end of one batch cycle (Fig. 2-4). When a constant voltage (CV) is applied, the corresponding current density trajectory is as shown for a sample scenario where a 2000 mg/L feed is desalinated to 100 mg/L. For this example, we require the instantaneous current density i [A/m^2] to be maintained below 90% of i_{lim}. This constraint only becomes active at the end of the constant-voltage batch process, when the diluate concentration has decreased to the desired product concentration C_{prod}. However, this point sets the maximum voltage that can be applied. Additionally, since the voltage is fixed, this point determines the current density trajectory for the full batch cycle. For earlier times in the cycle, the current density is much lower than limiting current density, causing the membranes to be under-utilized. The 'untapped capacity' represents the additional current that can be transmitted initially during the batch cycle, but remains unused with constant-voltage operation. This scenario is synonymous with continuous desalination using a series of ED stacks, but all at the same voltage which is determined by the limiting current density at the product concentration of the last stack.

Active voltage-control (VC) based on diluate conductivity measurements provides additional degrees of freedom to track (with an appropriate safety-margin) the limiting current density throughout the batch process (Fig. 2-4) and subsequently achieve higher ion-transfer rates. As a result, it can substantially increase the production rate of a system, or lower capital cost by decreasing the membrane-area required to satisfy a target production rate. When investigating the optimal design and operation of ED for brackish water desalination, Chehayeb et al. also showed that this strategy of operating close to the limiting current density was cost-optimal at the present ratio of ED equipment costs to energy costs [34]. In Appendix B, I explore an analogous solution for continuous ED, where instead I optimize the geometry of the flow paths

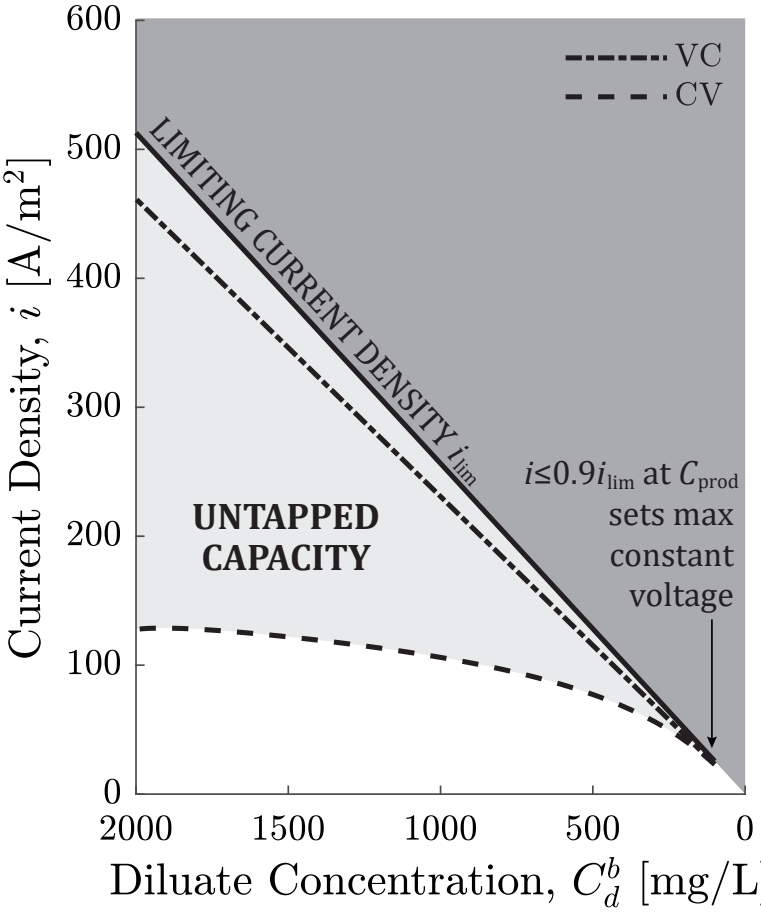

Figure 2-4: Simulated current trajectories indicating the additional "untapped" desalination capacity captured with a voltage-controlled (VC) batch process over a constant-voltage (CV) batch. The bulk diluate concentration C_d^b is shown as decreasing in time along the x-axis, and the instantaneous current density i does not exceed 90% of the limiting current density $i_{\lim}$ for both cases.

to operate at a fixed fraction of the limiting current density throughout the process.

Measuring the diluate and concentrate conductivities is standard practice, and allows an operator to track the progress of a batch desalination process. The same data can be used to estimate the voltage for a desired current density (fully described in Sec. 2.4.2), thereby requiring no additional sensors for basic feed-forward control. The only addition required to implement voltage-control in this manner is a controller to administer an appropriate voltage to the ED stack based on conductivity measurements (Fig. 2-3).

2.3 Models

To maximize the current density i using feed-forward voltage-control, subject to $i < i_{\text{lim}}$, models for the limiting and applied current densities are required. The models applied below have been previously proposed and validated [19, 35–37]. We additionally only consider the simple case of desalinating a sodium chloride solution in this study, which was found previously to provide reasonable estimates of the batch durations for real groundwater [36]. Lastly, although all concentrations are reported in more intuitive units of mg/L in this article, the following equations require concentrations expressed in units of mol/m^3.

2.3.1 Limiting Current Density

Assuming perfectly permselective ion-exchange membranes, the limiting current density is given as a function of the bulk diluate concentration C_d^b [mol/m^3] according to the modified Peers equation [38],

$$i_{\text{lim}} = \frac{C_d^b z F k}{1 - t^{+/-}}. \tag{2.1}$$

The charge number of either ion is $z = 1$ for sodium chloride, F is the Faraday constant (96485 C/mol), and $t^{+/-}$ is taken to be the minimum between the dimensionless anion and cation transport numbers in the bulk solution. The transport number represents the fraction of the total current carried by each ionic species.

Other theoretical and empirical expressions have been previously applied to model the limiting current density for solutions containing two [10, 39], or more [40], ionic species. They can be used in place of Equation 2.1. For these models, the limiting current density varies linearly with diluate concentration; therefore, the underlying parametric relationships derived in this work are not expected to change.

The boundary layer mass transfer coefficient k [m/s] is generally expressed in

terms of the non-dimensional Sherwood number Sh,

$$Sh = \frac{k d_h}{D_{aq}}, \tag{2.2}$$

where D_{aq} [m^2/s] is the diffusion coefficient of the ions in the aqueous solution, and d_h [m] is the hydraulic diameter.

The Sherwood Number, which characterizes the mass-transfer, is correlated to the flow behavior and material properties of the diluate solution using an expression of the form

$$Sh = aRe^b Sc^c, \tag{2.3}$$

where the Reynolds Re and Schmidt Sc numbers are respectively defined as

$$Re = \frac{u_{ch} d_h}{\nu}, \text{ and} \tag{2.4}$$

$$Sc = \frac{\nu}{D_{aq}}, \tag{2.5}$$

with respect to the kinematic viscosity ν [m^2/s].

In this study, we use the coefficients $a = 0.29$, $b = 0.50$, and $c = 0.33$ based on the work of Pawlowski *et al.* [41]. These coefficients were previously [36] found to provide a good match with the limiting current density measurements on the same ED stack used in the following experiments (Section 2.4.1). This correlation relies on the following definitions of the hydraulic diameter d_h and linear flow velocity u_{ch} [m/s]:

$$d_h = \frac{4\epsilon}{2/h + (1-\epsilon)(8/h)} \text{ and} \tag{2.6}$$

$$u_{ch} = \frac{Q}{\epsilon W h N}, \tag{2.7}$$

where h [m] is the thickness of the channel, W [m] is the width of the channel, Q [m^3/s] is the volumetric flow rate of diluate through the ED stack, N is the number of cell-pairs, and ϵ is the void fraction of the spacer occupying the channel.

Note that the diffusivity, transport numbers, and viscosity vary with sodium chlo-

ride concentration, but this dependence (Table 2.1) has a negligible effect on the limiting current density estimation for brackish water concentrations (<∼3000 mg/L). Therefore, they are treated as constants in this study. It follows then that once the flow rate through the ED stack is set, the limiting current density only varies linearly with the time-varying diluate concentration.

Table 2.1: Transport properties and sensitivities to concentration and temperature

Variable	**Value**	**Variation**	**Ref**
Transport Numbers	$t^+ = 0.39$, $t^- = 0.61$	<3% over 15-45 °C and 0-5000 mg/L	[42]
Diffusion Coefficient, D_{aq}	1.6 x 10^{-9} m^2/s	<8% over 0-5800 mg/L at 25 °C	[43]
Kinematic Viscosity, ν	1 x 10^{-6} m^2/s	<12% over 0-3000 mg/L at 20-25 °C	[44]

2.3.2 Applied Current Density

The objective of the proposed feed-forward voltage-control method is to maintain a desired instantaneous current density ratio r_i, defined as

$$r_i = \frac{i}{i_{\text{lim}}}. \tag{2.8}$$

The voltage V [V] required to produce the desired current density i is

$$V = E_{\text{el}} + N[E_{\text{mem}} + i(R_d + R_c + R_{\text{mem}})], \tag{2.9}$$

where E_{el} is the potential drop of approximately 1.4 V due to redox reactions at the electrodes, E_{mem} [V] is the membrane potential, and R_{mem} [Ohm-m^2] is the sum of the anion (AEM) and cation (CEM) exchange membrane resistances, respectively. An empirical model of R_{mem} for the experimental stack is described in 2.3.3. The resistances of the diluate and concentrate channels, respectively R_d and R_c [Ohm-m^2], are related to the concentrations of the respective bulk flows, C_d^b and C_c^b, by

$$R_{d/c} = \frac{h}{\Lambda_C C_{d/c}^b}, \tag{2.10}$$

where the equivalent conductance Λ_C [S-m^2/mol] is a function of concentration and

temperature (Fig. 2-5), and can be calculated using the Onsager/Falkenhagen equation with coefficients for NaCl [45]. During operation, conductivities ($\Lambda_C C^b$) are directly measured and used to compute the diluate and concentrate concentrations.

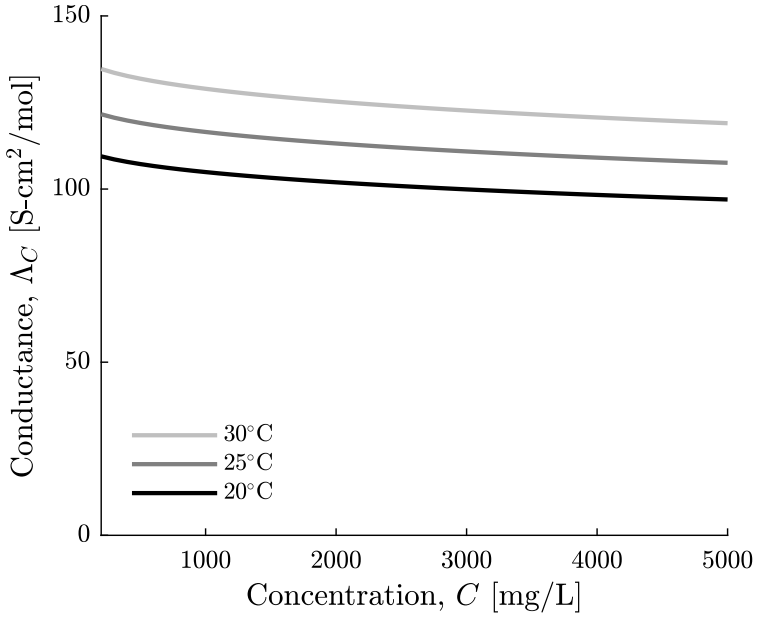

Figure 2-5: Equivalent conductance of NaCl solution at varying temperatures, calculated as a function of concentration using the Onsager/Falkenhagen equation with empirical coefficients [45].

Under justified simplifications of equal diluate and concentrate channel flow rates and heights, perfectly permselective membranes, equal cation and anion transport numbers, and activity coefficients of 1, it is shown in Section 2.3.4 that

$$E_{\text{mem}} = \frac{2RT}{F} \ln\left(\frac{\frac{C_c^b}{C_d^b} + r_i}{1 - r_i}\right), \tag{2.11}$$

where R is the gas constant (8.314 J/mol-K) and T [K] is temperature.

Note that once an ED system's architecture (h, ϵ, N, R_{mem}) and its operation (Q) are specified, Equations 2.9-2.11 can be used to compute the voltage V required to operate the stack at a desired current density ratio r_i based on diluate and concentrate conductivity measurements alone. This feature facilitated a straightforward implementation of the model in the experimental feed-forward voltage controller.

In the absence of a concentrate conductivity sensor, the concentrate concentration can be estimated using the mass-balance

$$C_{\text{feed}} = C_d^b r + C_c^b (1 - r), \tag{2.12}$$

where r is the recovery ratio, and the feed concentration is C_{feed}.

Finally, we relate the measured current I [A] to the current density by considering the area that is available for ion-transport,

$$I = i\eta LW, \tag{2.13}$$

where η represents the the open-area fraction of the spacer that occupies the flow channels, and L and W [m] are the channel lengths and widths, respectively (Fig. 2-1).

2.3.3 Empirical Membrane Resistance Model

Constant-voltage experiments spanning the same concentration ranges and flow rates as those in Table 2.4 were conducted. Membrane resistances were calculated from the applied voltage and measured current, by assuming that the other terms in Equation 2.9 were accurately predicted.

Then, using the equation-form recommended by [46], the empirical model of the total (CEM + AEM) membrane resistance was

$$R_{\text{mem}} = \text{A}_0 + \frac{\text{A}_1}{\text{A}_2} \frac{\exp(-\text{A}_2 C_d^b) - \exp(-\text{A}_2 C_c^b)}{C_c^b - C_d^b}, \tag{2.14}$$

where A_0, A_1, and A_2 were experimentally-determined coefficients: 0.0046 Ohm-m^2, 0.2131 Ohm-m^5/mol, and 0.1906 m^3/mol; and C_d^b and C_c^b were the bulk diluate and concentrate concentrations, respectively. Comparison of the model-fit and experimental membrane resistances, which were evaluated as described above, is provided in Figure 2-6.

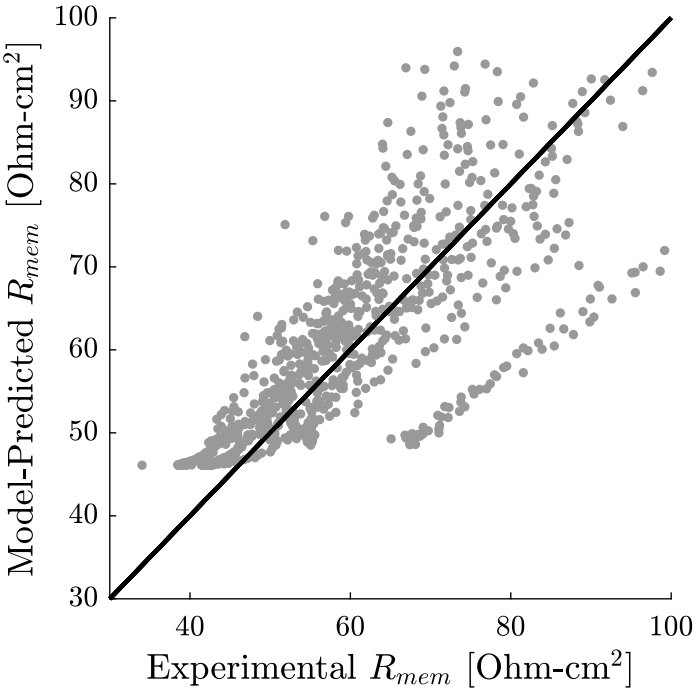

Figure 2-6: Model-predicted vs. experimentally derived membrane resistances. The solid line represents a 1:1 relationship.

2.3.4 Derivation of a Simplified Membrane Potential Term

A simplified expression for the membrane potential was sought to reduce the real-time computation onboard the voltage-controller. The full expressions for the individual AEM and CEM potentials, taken from previous work [19, 36] are

$$E^{AEM} = \frac{(2t^{AEM} - 1)RT}{F} \log\left(\frac{\gamma_c C_c^{AEM}}{\gamma_d C_d^{AEM}}\right) \text{ and} \tag{2.15}$$

$$E^{CEM} = \frac{(2t^{CEM} - 1)RT}{F} \log\left(\frac{\gamma_c C_c^{CEM}}{\gamma_d C_d^{CEM}}\right), \tag{2.16}$$

where γ is the activity coefficient of the solution and t^{AEM} and t^{CEM} are the apparent transport numbers of the counterions (the anions in the AEM and cations in the CEM, respectively). The wall concentrations C_d^{AEM}, C_d^{CEM}, C_c^{AEM}, and C_c^{CEM} are obtained from balancing the diffusion of ions from the bulk flow to the membrane with migration across it. The individual expressions are

$$C_d^{AEM} = C_d^b - \frac{i(t^{AEM} - t^-)}{zFk}, \tag{2.17}$$

$$C_d^{CEM} = C_d^b - \frac{i(t^{CEM} - t^+)}{zFk}, \tag{2.18}$$

$$C_c^{AEM} = C_c^b + \frac{i(t^{AEM} - t^-)}{zFk}, \text{ and} \tag{2.19}$$

$$C_c^{CEM} = C_c^b + \frac{i(t^{CEM} - t^+)}{zFk}, \tag{2.20}$$

where C_c^b and C_d^b represent the bulk concentrate and diluate concentration, respectively.

To simplify these terms, we employ the following approximations in this work:

1. Membranes are assumed to be perfectly permselective, so that both t^{AEM} and t^{CEM} equal 1. McGovern *et al.* measured them to be 0.96 ± 0.04 for concentrations below 10 000 mg/L [47]; hence, this is an easily justified simplification.

2. The activity coefficients γ_d and γ_c are set to 1. In reality, they are temperature and concentration dependent, but our previous work [36] found that setting them to 1 affects the membrane potential prediction by less than 10% for the concentration ranges investigated in this paper. Furthermore, since the diluate channels offer the dominant impedance in brackish water desalination, the error introduced by this approximation has an even smaller effect on the voltage calculation (Eqn. 2.9).

3. For the purposes of estimating the membrane potential, the transport numbers of the cation and anion are both approximated as being equal to the minimum of the actual transport numbers: $t^+/- = \min(t^+, t^-)$. This simplification is made so that together with approximation 1, the wall concentrations can be expressed as functions of the limiting current density by substituting Equation 2.1 and getting

$$\frac{C_d^{MEM}}{C_d^b} = 1 - \frac{i}{i_{\text{lim}}}, \text{ and} \tag{2.21}$$

$$\frac{C_c^{MEM}}{C_d^b} = \frac{C_c^b}{C_d^b} + \frac{i}{i_{\text{lim}}}. \tag{2.22}$$

Note that within each channel, the wall concentrations at both membranes are equal under this approximation. Equations 2.21 and 2.22 further assume that the mass transfer coefficient k is equal in both the diluate and concentrate channels. This is a reasonable assumption if the channels and flow rates are identical, which is true for conventional ED processes.

Incorporating the above approximations into Equations 2.15 and 2.16, and summing the two gives the simplified total membrane potential

$$E_{\text{mem}} = \frac{2RT}{F} \ln\left(\frac{\frac{C_c^b}{C_d^b} + r_i}{1 - r_i}\right), \tag{2.23}$$

where r_i is defined as the ratio i/i_{lim}.

2.3.5 Batch Completion Time

To derive an analytical prediction for the batch completion time, we neglected the secondary mass-transfer modes of osmosis, back-diffusion, and electroosmosis, and considered only migration. The rate change of concentration in the diluate tank, with volume V_{dil} [m^3], is related to the migration of ions in the ED stack by

$$V_{\text{dil}} \frac{dC_d^b}{dt} = -\frac{i\eta LWN}{zF}. \tag{2.24}$$

Incorporating Equations 2.1 and 2.8 for the limiting current density and current ratio gives

$$\frac{dC_d^b}{dt} = -\frac{r_i \eta LWNkC_d^b}{V_{\text{dil}}(1 - t^{+/-})}. \tag{2.25}$$

The dilute tank concentration only varies in time during a batch desalination process. Therefore, it is theoretically possible to express any arbitrary function of r_i in time. We can then separate variables and integrate since

$$\int_{C_{\text{feed}}}^{C_{\text{prod}}} \frac{dC_d^b}{C_d^b} = \int_0^{t_b} -\frac{r_i \eta LWNk}{V_{\text{dil}}(1-t^{+/-})} dt. \tag{2.26}$$

Therefore,

$$\ln\left(\frac{C_{\text{feed}}}{C_{\text{prod}}}\right) = \frac{\eta LWNk}{V_{\text{dil}}(1-t^{+/-})} \int_0^{t_b} r_i dt. \tag{2.27}$$

Introducing a time-averaged current density ratio $\overline{r_i}$ defined as

$$\overline{r_i} = \frac{1}{t_b} \int_0^{t_b} r_i dt, \tag{2.28}$$

and substituting this definition into Equation 2.27 gives our final expression for the batch completion time t_b [s] to desalinate from a given feed concentration C_{feed} to a desired product concentration C_{prod},

$$t_b = \frac{V_{\text{dil}}(1-t^{+/-})}{\overline{r_i} \eta LWNk} \ln\left(\frac{C_{\text{feed}}}{C_{\text{prod}}}\right). \tag{2.29}$$

Note that this prediction is expected to be a lower bound on the actual duration since back-diffusion of ions from the concentrate to diluate channels was neglected. Beyond this simplification, we expect this model to be valid for any trajectory of r_i in time, provided that $0 < r_i < 1$.

2.4 Experiments

2.4.1 Experimental Setup

The experimental setup mirrored the schematic in Figure 2-3, and was comprised of a PCA GmbH 64-002 ED stack with the construction outlined in Table 2.2. Geometric parameters were provided by the manufacturer, membrane resistances were determined through system characterization (Sec. 2.3.3), and the void fraction and

spacer open-area fraction were measured in a previous study [36].

Table 2.2: Test stack parameters

Properties	**Values**
Number of Cell Pairs, N	14
Flow Path Width, W	8 cm
Flow Path Length, L	8 cm
Channel Height, h	0.35 mm
Void Fraction, ϵ	0.60 ± 0.04
Open-Area Fraction, η	0.62 ± 0.04
Cation Exchange Membranes	PC-SK
Anion Exchange Membranes	PC-SA

Two KNF Flodos NF300 KPDC diaphragm pumps were used to recirculate the diluate and concentrate through their respective circuits and into separate magnetically-stirred 1 L glass beakers. Flow rates were measured and controlled using two King Instrument 7430 Series glass tube flowmeters with valves (± 6%). To rinse the electrodes, a 0.2 mol/L sodium sulfate solution was circulated at 2.40 ± 0.05 L/min from a separate beaker using a third KNF Flodos NF300 diaphragm pump. All three pumps were powered at a voltage of 23.8 V (± 1%) by a single Mastech HY3003D power supply, which was also used to measure current draw (± 2%).

The conductivities of the diluate and concentrate tanks were measured (± 2%) using Conductivity Instruments CDCE-90 inline conductivity probes, interfacing with CDCN-91 conductivity controllers, with cell constants of K = 1/cm and K = 10/cm, respectively. Conductivity measurements were collected using a National Instruments NI9203 data acquisition module and processed in National Instruments LabVIEW 2018 to calculate, in real-time, the actuation voltage for the voltage-controlled experiments. The computed voltage was then applied (± 0.1%) across the stack using an Agilent Technologies N8760A DC power supply, which also measured current draw (± 0.1%). Diluate and concentrate pH (± 0.01) were recorded at the start and end of each test using a VWR International SympHony H10P handheld meter with a gel-filled pH electrode (89231-608), calibrated using reference solutions of pH 4.00, and 7.00.

Feed-water was prepared by adding sodium-chloride to distilled water with a mea-

sured initial conductivity of <10 uS/cm. Before each test, the diluate and concentrate circuits were repeatedly drained and flushed with distilled water from a common beaker until the conductivity of the water in the channels dropped below 30 uS/cm. The feed water was then separated into two volumes and circulated through the system; 1050 ± 10 mL diluate, and 450 mL ± 10 mL concentrate, providing a recovery of 70 ± 1% for all tests.

2.4.2 Controller Description

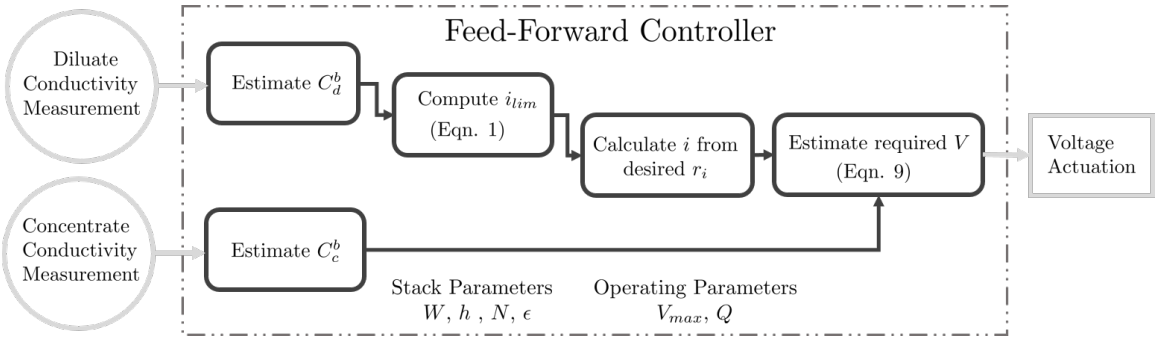

Figure 2-7: Flow diagram indicating sensing, controller logic, and actuation for feed-forward voltage-controlled batch. Stack geometry and operating parameters are pre-programmed onto the controller.

To design the feed-forward controller highlighted in Figure 2-3, which was implemented in National Instruments LabVIEW 2018, we assumed the following simplifications to the system behavior:

1. The dynamics of the concentration boundary layer were neglected, because it was expected to respond at a characteristic mass-diffusion time scale τ_{diff} that is approximately 840 times shorter (Table 2.3) than the time scale associated with concentration change in the diluate tank τ_{desal}. Using the ED stack properties in Table 2.2 and sample operating conditions in Table 2.3,

$$\tau_{diff} = \frac{l_{BL}^2}{D_{aq}} = \frac{d_h^2}{Sh^2 D_{aq}} \tag{2.30}$$

since $l_{BL} = \frac{d_h}{Sh}$ is the relevant length-scale, and

$$\tau_{desal} = \frac{V_{\text{dil}}(C_{\text{feed}} - C_{\text{prod}})zF}{i\eta WLN}. \tag{2.31}$$

2. Spatial concentration variations across the length of the channels within the ED stack were neglected because the residence time of the solution τ_{res} was approximately 180 times smaller than τ_{desal} (Table 2.3), where

$$\tau_{res} = \frac{L}{u_{ch}}. \tag{2.32}$$

Alternatively, the maximum change in concentration obtained with a single pass of diluate,

$$\Delta C = \tau_{res}\frac{i\eta}{zF\epsilon h}, \tag{2.33}$$

was <28% of the stack inlet concentration C_d^b (for I <1 A), which in turn is assumed equal to the tank concentration at all times.

Table 2.3: Sample operating conditions, corresponding time scales, and estimated concentration change for the experimental ED stack

Variables	**Values**
Flow Rate, Q	54 L/h
Resultant Linear Flow Velocity, u_{ch}	0.06 m/s
Diluate Tank Volume, V_{dil}	1.05 L
Feed Concentration, C_{feed}	2000 mg/L
Product Concentration, C_{prod}	200 mg/L
Current Density, i	250 A/m^2
Current, I	1 A
Diffusion Time Scale, τ_{diff}	0.3 s
Desalination Time Scale, τ_{desal}	226 s
Residence Time, τ_{res}	1.3 s
Concentration Change, ΔC	557 mg/L
Fractional Change, $\Delta C/C_{\text{feed}}$	28%

Given the two key assumptions above, the simple controller implemented in this study used conductivity measurements, from the diluate and concentrate tanks, to calculate the stack voltage that would produce a desired current density (Fig. 2-7). The input voltage V control signal was not adjusted based on measurements of the

system output, the current I. This subtle distinction explains why the proposed method is classified as a *feed-forward*, and not a *feedback*, control strategy.

The characteristic time scales provided in Table 2.3 were also used to identify appropriate frequencies for conductivity measurement and voltage actuation. Diluate conductivity was measured at a frequency of 1 Hz, which is greater than the estimated characteristic frequency of change: $1/\tau_{desal} = 0.004$ Hz. We frequently updated the voltage input in response to the changing diluate concentration. However, the corresponding frequency of voltage actuation did not exceed the rate at which the concentration boundary layer redeveloped, nor the rate at which diluate traveled through the system. Hence,

$$\frac{1}{\tau_{diff}} > \frac{1}{\tau_{res}} > \frac{1}{\tau_{act}} > \frac{1}{\tau_{desal}}, \tag{2.34}$$

where $1/\tau_{act} = 0.1$ Hz. Note that this method of voltage control differs from pulsed-field ED, whereby voltage is actuated at a frequency matching $1/\tau_{diff}$ to perturb the concentration boundary layer within the channels [48, 49].

2.4.3 Tests

A summary of the tests conducted in this study is provided in Table 2.4. Tests 1-5 were baseline conventional constant-voltage batch processes. For the voltage-controlled tests, 6-8, 9-11, and 12-14 systematically investigated the effects of varying the maximum voltage, the current density ratio, and the recirculation flow rates, respectively. The flow rates of 72, 54, and 36 L/h, correspond to linear flow velocities of 8.5, 6.4, and 4.3 cm/s in the channels. Lastly, the limiting current density was intentionally exceeded for Test 15 to examine the effect on pH.

Table 2.4: Summary of test parameters

No.	**Operation**	**Feed Conc.** $C_{\mathbf{feed}}$ **(mg/L)**	**Product Conc.** $C_{\mathbf{prod}}$ **(mg/L)**	**Applied (CV) or Max (VC) Voltage** V **(V)**	**Max (CV) or Target (VC) Current Density Ratio** r_i	**Flow Rate** Q **[L/h]**
1	CV	1500	500	16.7	0.7	54
2	CV	3000	400	12.3	0.6	54
3	CV	2000	300	14.5	0.6	72
4	CV	2000	300	11.6	0.6	54
5	CV	2000	300	10.7	0.6	36
6	VC	1500	500	20.0	0.7	54
7	VC	1500	500	23.0	0.7	54
8	VC	1500	500	26.0	0.7	54
9	VC	3000	400	-	0.4	54
10	VC	3000	400	-	0.6	54
11	VC	3000	400	-	0.8	54
12	VC	2000	300	-	0.6	72
13	VC	2000	300	-	0.6	54
14	VC	2000	300	-	0.6	36
15	CV	3000	400	60	>1	54

Notes:

- 'CV' refers to constant-voltage, and 'VC' refers to voltage-controlled.
- Applied Voltage for constant-voltage experiments is determined by the limiting current density at C_{prod} and r_i.
- Maximum voltage was not constrained for tests 9-14.

2.5 Results and Discussion

2.5.1 Current-Tracking Accuracy

The feed-forward controller was capable of providing the desired current with acceptable performance. The measured current was approximately within -15 to +20% of the current predicted by the model, at the voltages applied through Tests 1-14 (Fig. 2-8). A comparison for Test 15 is not included because the model is invalid at over-limiting currents.

The current-tracking accuracy of the proposed feed-forward controller can be improved by considering the effect of flow rate on stack resistance. The apparent increase in measured current with flow rate (Fig. 2-8) indicated that the resistance of the ED stack decreases with increasing linear flow velocity. This observation is consistent with the work of Długołecki *et al.* [50] and Galama *et al.* [51], who used electrochemical impedance spectroscopy (EIS) to demonstrate that this flow-dependent resistance is associated with the diffusion boundary layers at fluid-membrane interfaces. By adjusting the membrane resistance model to accommodate this phenomenon, the current-draw may be more accurately predicted over a broad range of flow rates. Another possible explanation is that a low flow rate increases the residence time of the solution, producing a large concentration change between the stack inlet and outlet, which consequently increases resistance. For ED stacks consisting of flow paths that are several times longer than those in our experimental bench-scale system, the model recommended in this work may introduce additional errors by neglecting the spatial concentration variations within the stack. Feedback control could also improve current tracking. Here, current measurements would be used to regulate the voltage input to the ED stack.

2.5.2 pH Changes

An acidic shift in the diluate pH is encountered when water-splitting occurs [52, 53]. When the stack was intentionally operated above the limiting current density for

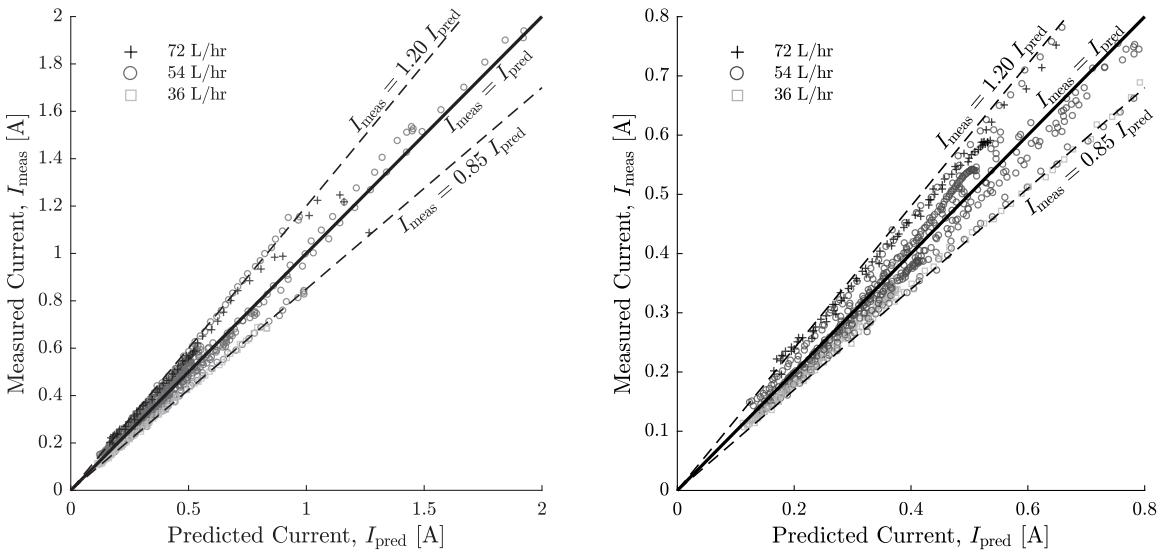

Figure 2-8: Measured current I_{meas} was within approximately -15 to +20% of the predicted current I_{pred} at the voltages applied during tests 1-14. Comparison over the full range of measured currents is shown on the *left*, and over the lower (<0.8 A) range on the *right* for visual clarity.

Test 15, the pH decreased from 6.01 ± 0.02 to 4.65 ± 0.01 (pH data provided as supplementary material). To identify other tests where the limiting current density may have been exceeded, the ratio of the final to initial pH was plotted (Fig. 2-9).

During all voltage-controlled tests but 11, the pH increased by a similar or greater factor than the corresponding constant-voltage benchmark tests. The pH decrease in Test 11 (pH ratio <1) signified that voltage-control at the aggressive target current ratio of 0.8 caused the limiting current density to be exceeded. In this work, the limiting current density was calculated using the measured diluate tank (or stack inlet) concentration C_d^b. Combining Equations 2.1, 2.8, and 2.33, the fractional concentration change across the stack is approximately

$$\frac{\Delta C}{C_b^d} = \frac{r_i k \eta L}{(1 - t^{+/-}) \epsilon h u_{ch}}. \tag{2.35}$$

Evaluated at a target current ratio of $r_i = 0.8$, and using the geometric and experimental parameters listed in Tables 2.2 and 2.4, the concentration decreased by 38% across the stack in Test 11. Consequently, the local limiting current density was proportionally 38% lower at the outlet than at the inlet of the experimental ED stack

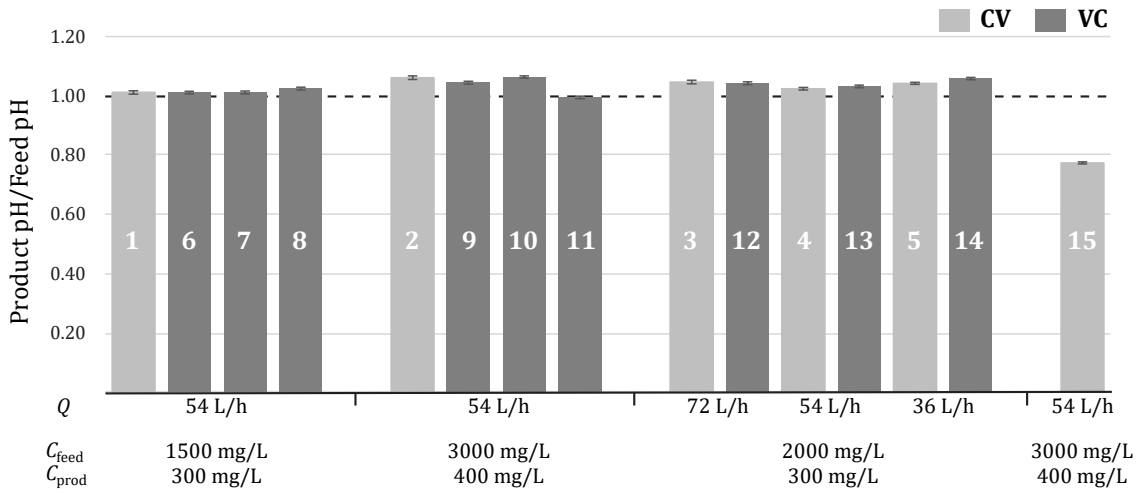

Figure 2-9: Ratio of the product pH to feed pH is plotted for both constant-voltage (CV) and voltage-controlled (VC) tests. Tests are identified by the number on each bar, and are first grouped by concentration change, followed by flow rate. Test 15 represents the case where the limiting current density was deliberately exceeded.

(Eqn. 2.1). It follows that we did not provide an appropriate safety-margin against water-splitting for Test 11, because the voltage evaluated for $r_i = 0.8$ at the inlet concentration caused $r_i > 1$ locally at the outlet. Equation 2.35 further indicates that longer flow paths will increase the concentration change, thereby decreasing the current ratio that can be safely achieved.

2.5.3 The Effect of Varying Current Ratio

The total area under the i_{lim} vs C_b^d curve represents a system's available desalination capacity from a feed to a product concentration (Fig. 2-4). At higher current density ratios, feed-forward voltage-control captures a larger fraction of this capacity than constant-voltage operation (Fig. 2-10a). As a direct result, our tests showed that as the target current density ratio was increased from tests 9 through 11, the batch completion time decreased (Fig. 2-10b).

Measured batch completion times t_b (Table 2.5) agreed with predictions (Eqn. 2.29) at the experimental time-averaged current density ratios $\overline{r_i}$. These ratios were computed by dividing the measured current density by the calculated limiting current density (Eqn. 2.1), and averaging over time. A small but systematic under-prediction

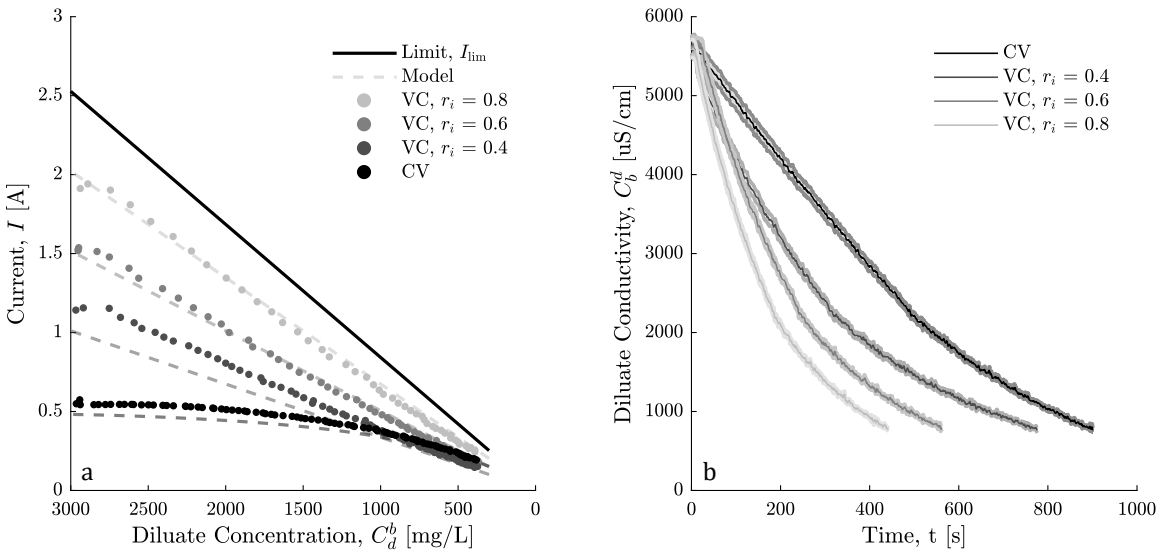

Figure 2-10: Current is plotted against diluate concentration for voltage-controlled (VC) and constant-voltage (CV) desalination (*left*). Error-bars are smaller than the markers. Diluate conductivity is plotted against time, indicating that as the target current ratio r_i was increased, the time to desalinate 1.05 ± 0.01 L from 1500 mg/L to 500 mg/L decreased (*right*). The shaded region represents measurement uncertainty.

Table 2.5: Summary of batch completion times at varying target current ratios

Test	**Operation**	**Target r_i**	**Time-Averaged Meas $\overline{r_i}$**	**Pred t_b at $\overline{r_i}$ [s]**	**Meas t_b [s]**
2	CV	-	0.39 ± 0.01	760 ± 95	888 ± 13
9	VC	0.4	0.45 ± 0.02	660 ± 80	752 ± 9
10	VC	0.6	0.57 ± 0.02	520 ± 65	556 ± 6
11	VC	0.8	0.74 ± 0.03	400 ± 50	430 ± 7

of batch completion time was observed, because back-diffusion of ions from the concentrate to the diluate channels was neglected in the analytical prediction (Sec. 2.3.5).

At the same 54 L/h flow rate and concentration change of 3000 to 400 mg/L, the constant-voltage process achieved an actual time-averaged current density ratio $\overline{r_i}$ of 0.39 ± 0.01; therefore, the reduction in the batch time of 15 ± 1% observed for Test 9 is explained by the controller exceeding the target r_i of 0.40 during the experiment (Table 2.5). It is important to note however that while the constant-voltage operation provided a similar *average* current density ratio, the *instantaneous* ratio was lower than 0.40 at the start but approached 0.60 by the end of the batch process. In this specific case then, voltage-controlled desalination at a constant 0.40 current density ratio would provide the same batch completion time as constant-voltage desalination,

while decreasing the risk of water splitting.

Increasing the target r_i from 0.4 to 0.6 provided a more substantial decrease in the batch completion time than an equivalent increase from 0.6 to 0.8 (Fig. 2-10 and Table 2.5). This observation signifies that the batch completion time decreases at a diminishing rate with increasing current density ratio because from our predictive model (Eqn. 2.29),

$$t_b \propto \frac{1}{\overline{r_i}}. \tag{2.36}$$

This result agrees with the work of Min and Kim who also experimentally observed diminishing improvements in the salt removal rate as voltage was increased in their batch desalination trials of groundwater samples [23]. A 61% decrease in the time to achieve 80% chloride ion removal was observed when the applied voltage was raised from 10 to 20 V, but the additional decrease was only 31% when the voltage was again raised by 10 V. Similarly, by raising the applied voltage from 40 to 60 V, Ortiz *et al.* experimentally measured a 17.9% reduction in the batch processing time of a 2000 mg/L NaCl solution to 500 mg/L [19]. A further increase of 20 V only decreased the processing time by an additional 11.8%. Note that in both cases, increasing the applied voltage raised the time-averaged current ratio.

From the same predictive model, if the production rate V_{dil}/t_b is held constant, then the total required membrane area scales as

$$NLW \propto \frac{1}{\overline{r_i}}. \tag{2.37}$$

Hence, reductions in the batch completion time can be alternatively interpreted as membrane-area savings. Therefore, the capital cost of an ED system can be decreased by raising the average current density ratio $\overline{r_i}$ using feed-forward voltage-control.

Having verified the predictive batch completion time model (Eqn. 2.29) at different r_i, we used it to develop scaling arguments for the pumping and desalination energy consumption. The solutions were circulated at a constant flow rate; hence, the energy consumed by pumping E_p was expected to scale proportionally with batch

duration t_b at a constant pumping power, giving

$$\mathrm{E}_p \propto \frac{1}{\overline{r_i}}. \tag{2.38}$$

Extending the circuit analogy for ED (Eqn. 2.9), the power consumed by ion-transport P_d scales with current squared from Ohm's Law, entailing that

$$P_d \propto \overline{r_i}^2 \tag{2.39}$$

for a constant membrane area. Multiplying this equation with the scaling relationship for batch duration t_b (Eqn. 2.36) gives

$$\mathrm{E}_d \propto \overline{r_i}, \tag{2.40}$$

where E_d is the desalination energy consumption.

Experimental measurements of the desalination and pumping energy consumption matched the proposed scaling arguments (Fig. 2-11). The desalination energy is reported as the numerical integration of the measured ED power in time through the batch cycle, whereas pumping energy is the power-draw of the pumps multiplied by the batch completion time. As shown, voltage-controlled operation decreased the total (E_d + E_p) specific energy consumption E_s (Fig. 2-11) because pumping consumed more energy than desalination for this system. From the scaling trend-lines, the minimum energy consumption is expected at a high average current density ratio of $\overline{r_i} = 0.75$. A higher pump efficiency, wider flow channels, and higher-resistance ion-exchange membranes are all expected to shift this optimal point to lower values of $\overline{r_i}$.

2.5.4 The Effect of Varying Linear Flow Velocity

The measured and predicted batch completion times were plotted against linear flow velocity (Fig. 2-12). The model curves were derived using Equation 2.5, and the experimental data are labeled with the measured time-averaged current density ratios.

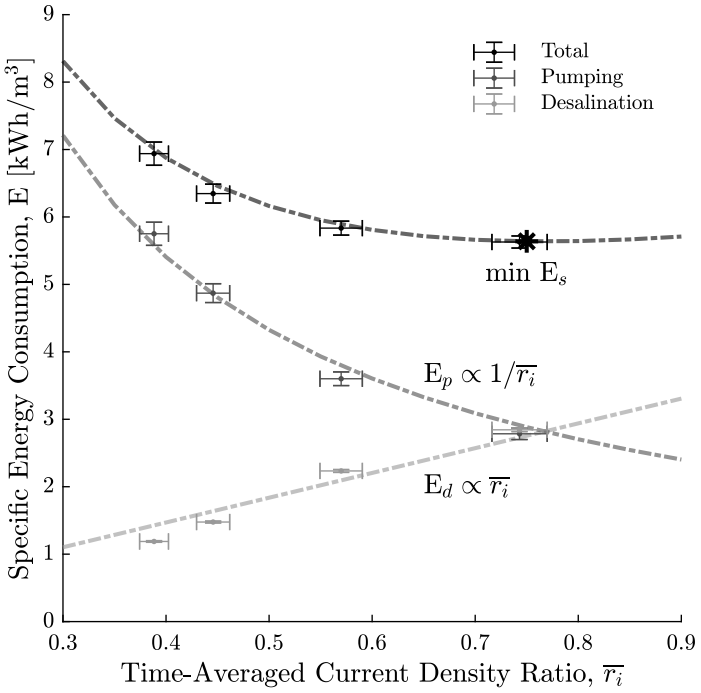

Figure 2-11: Increasing the time-averaged current density ratio $\overline{r_i}$ using feed-forward voltage-control decreased total specific energy consumption E_s, by reducing pumping energy consumption E_p. For all cases, the system desalinated 1.05 $\pm$ 0.01 L from 3000 mg/L to 400 mg/L, with diluate and concentrate solutions recirculating at 54 L/h.

Our observations include:

1. The measured batch completion times agree with the model, but are slightly under-predicted. As previously discussed, this small discrepancy is likely explained by back-diffusion of ions from the concentrate to the diluate channels, which lengthens the desalination process.

2. The relative reduction in batch completion time between constant-voltage and voltage-controlled operation (t_b^{VC}/t_b^{CV}) was equal to the inverse fraction of the time-averaged current density ratios ($\overline{r_i}^{CV}/\overline{r_i}^{VC}$), within experimental error at all three flow rates (Table 2.6). This result further validates the predictive batch time model (Eqn. 2.29).

3. Irrespective of operation mode (voltage-controlled or constant-voltage), it follows from the item above that increasing $\overline{r_i}$ from one fixed value to another will

yield the same *fractional* change in the batch completion time at all flow rates.

4. Any fixed increase in the current density ratio produces a greater *absolute* reduction in batch completion time at lower flow velocities, compared to higher flow velocities. Graphically represented, the difference in t_b at $\overline{r_i}$ = 0.2 vs. $\overline{r_i}$ = 1 decreases as flow velocity increases (Fig. 2-12). Therefore, feed-forward voltage-control yields the greatest production and/or cost benefits, relative to constant-voltage operation, at low flow velocities.

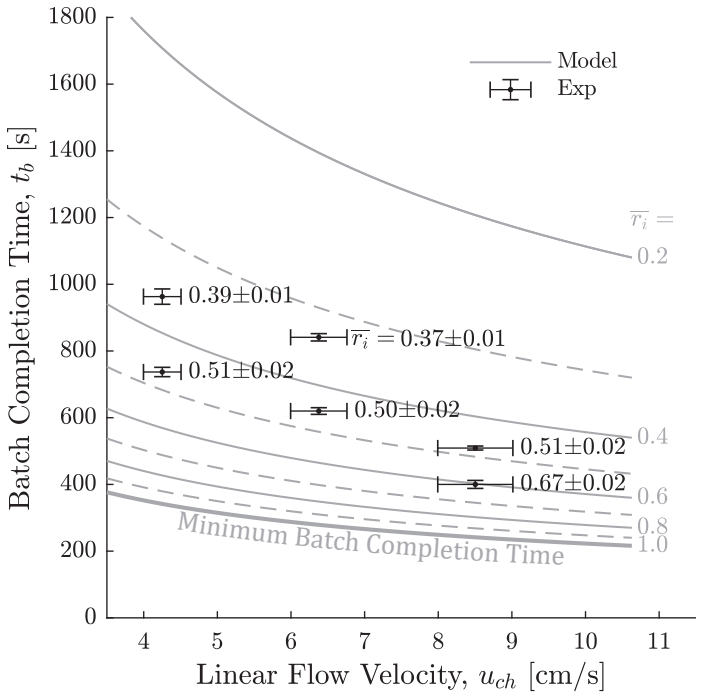

Figure 2-12: The measured batch times t_b at varying linear flow velocities and average current density ratios $\overline{r_i}$ agree with model predictions. In all cases, the system desalinated 1.05 ± 0.01 L from 2000 mg/L to 300 mg/L.

5. Shown again here is that increasing $\overline{r_i}$ will provide diminishing returns on production rate (or capital cost), whereby the batch completion time t_b (or total membrane area NLW) converges to a velocity dependent theoretical minimum at $\overline{r_i} = 1$.

In addition, Figure 2-12 forms a useful tool for designing and analyzing the performance of ED systems. After plotting the measured performance of an existing

Table 2.6: Fractional reduction of batch completion times at varying linear flow velocities

Velocity, u_{ch} [cm/s]	$\overline{r_i}^{CV}/\overline{r_i}^{VC}$	t_b^{VC}/t_b^{CV}
8.5 ± 0.5	0.77 ± 0.04	0.79 ± 0.03
6.4 ± 0.4	0.74 ± 0.04	0.74 ± 0.02
4.3 ± 0.3	0.76 ± 0.04	0.77 ± 0.02

batch process, it provides a graphical means for determining the maximum possible production rate, and the improvements that can be attained using voltage-control and higher flow velocities.

2.5.5 The Effect of Varying Maximum Voltage

Thus far, we have analyzed the performance of feed-forward voltage-control at varying target current density ratios, with no limitations on stack voltage. Now we assess the behavior at a fixed target current density ratio of $r_i = 0.6$, but impose varying maximum stack voltages (Fig. 2-13).

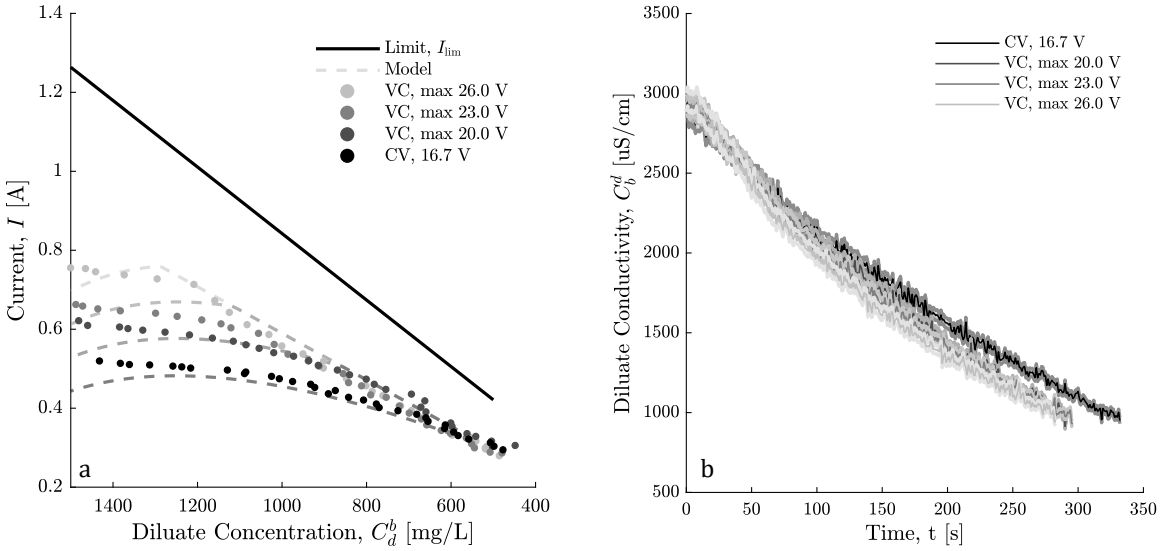

Figure 2-13: By raising the maximum voltage allowable for feed-forward voltage-control (VC), a higher initial current was obtained than with constant-voltage desalination (CV) (*left*). Error-bars are smaller than the markers. Diluate conductivity is plotted against time, indicating that the VC tests desalinated 1.05 ± 0.01 L from 1500 mg/L to 500 mg/L within a similar duration, but all quicker than the CV trial (*right*). The shaded region represents measurement uncertainty.

Table 2.7: Summary of batch completion times at varying maximum voltages

Test	**Max** V	**Operation**	**Time-Averaged Meas** $\overline{r_i}$	**Pred** t_b **at** $\overline{r_i}$ **[s]**	**Meas** t_b **[s]**
1	16.7	CV	0.57 ± 0.02	283 ± 44	336 ± 19
6	20.0	VC	0.63 ± 0.02	256 ± 39	283 ± 6
7	23.0	VC	0.62 ± 0.02	260 ± 40	277 ± 6
8	26.0	VC	0.65 ± 0.02	248 ± 38	276 ± 6

Again, the batch completion times for trials 1 and 6-8 matched theoretical predictions within experimental error (Table 2.7), providing further validation that Equation 2.29 is valid for any function of r_i in time. However, in contrast to previous cases, voltage-control did not substantially decrease the batch completion time when compared to constant-voltage operation. In addition, there was no measurable difference in batch completion time as the maximum voltage was varied from 20.0 to 26.0 V. By comparing these results with the other trials conducted at 54 L/h, this behavior was attributed to three factors:

1. From Equation 2.29, the batch completion time scales as

$$t_b \propto \ln\left(\frac{C_{\text{feed}}}{C_{\text{prod}}}\right). \tag{2.41}$$

   As a result, any change in the average current ratio $\overline{r_i}$ will yield a higher reduction in the batch time when desalinating through larger concentration changes. This relationship is graphically represented is Figure 2-14, and shown to agree with all trials conducted at 54 L/h.

2. A high average current ratio can be obtained with standard constant-voltage operation when the concentration difference between the feed and product is small, because the 'untapped capacity' in Figure 2-4 is narrow. For example, we observed a time-averaged current ratio of 0.57 ± 0.02 when desalinating from 1500 to 500 mg/L in Test 1, whereas this ratio is lower for Tests 2 (3000 to 400 mg/L) and 4 (2000 to 300 mg/L): 0.39 ± 0.01 and 0.37 ± 0.01, respectively. Conversely, when desalinating through large concentration differences, the average current ratio achieved at a constant-voltage is low. Here, small $\overline{r_i}$

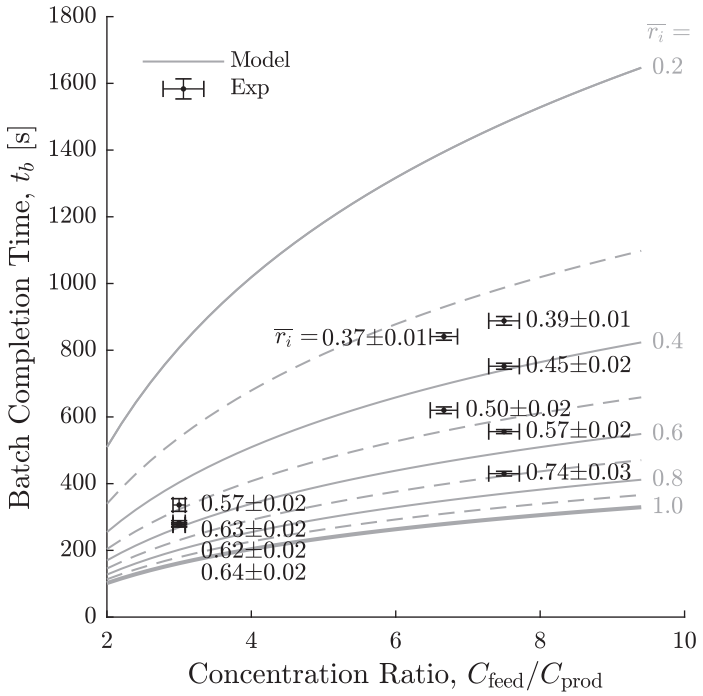

Figure 2-14: The measured batch times t_b at varying feed-to-product concentration ratios, and average current density ratios $\overline{r_i}$, agree with model predictions for all trials conducted at a 54 L/h flow rate. As this concentration ratio increases, a larger reduction in batch completion time t_b can be obtained using voltage-control.

changes using feed-forward voltage-control can improve production performance significantly.

3. When plotting current against diluate concentration (Fig. 2-13a), we observed that increasing the maximum voltage results in significant differences in the current-draw at concentrations exceeding 1000 mg/L. However, the change in diluate concentration from 1500 (2942 uS/cm) to 1000 mg/L (1993 uS/cm) occurs within only ∼100 s of the full ∼300 s batch duration (Fig. 2-13a). At concentrations below 1000 mg/L, current differences between the voltage-controlled trials become negligible. Averaging over time then, the overall differences in $\overline{r_i}$ are diminished.

Together, items 1-3 indicate that the highest utility is derived from time-variant voltage-control when producing low-salinity water from highly concentrated feeds.

2.6 Conclusions

Batch desalination using a single ED stack is implemented when space constraints prohibit continuous desalination using a cascade of ED stages. However, batch desalination is often performed at a constant voltage, causing the membranes to be under-utilized initially during the cycle when higher currents could be sustained. Time-variant, feed-forward voltage-control was investigated as a method to utilize this unused membrane capacity, and increase production rate or decrease the required membrane area relative to conventional constant-voltage operation. Without affecting pH change, a maximum reduction in batch completion time of 37% $\pm$ 2% was experimentally obtained while desalinating from 3000 to 400 mg/L at a linear flow velocity of 6.4 cm/s.

We analytically predicted the batch completion times, and demonstrated close agreement with experimental measurements for varying brackish feeds (1500, 2000, and 3000 mg/L), products (200, 300, and 500 mg/L), linear flow velocities (4.3, 6.4, and 8.5 cm/s), and for both constant-voltage and voltage-controlled desalination. This model indicates that the batch completion time is inversely proportional to the time-averaged ratio of applied to limiting current density. Therefore, voltage-control increased the production rate by achieving higher ratios than is possible with constant-voltage desalination. The largest productivity gains are derived at low flow velocities and high feed-to-product concentration ratios. If pumping consumes more energy than ion-transport, voltage-control was shown to also decrease the total specific energy consumption.

Finally, we designed and experimentally evaluated a feed-forward voltage-controller that can be fitted to a conventional batch ED system without additional sensors. Using diluate and concentrate conductivity measurements, and a simple model of the ED process, the controller tracked the desired current to within -15 to +20%. This performance can be improved by addressing flow velocity effects on diffusion boundary layer resistance, resolving spatial concentration variations across long flow paths, and implementing feedback.

It is our aim that this work will provide designers and operators with both graphical (Fig 2-12) and simple analytical tools (Eqn. 2.29) to design and assess batch ED processes, as well as a method to maximize their systems' production performance. For cost-critical applications such as groundwater desalination in rural communities, we have additionally demonstrated that feed-forward voltage-control is one manner by which drinking water may be more affordably produced.

Bibliography

[1] Natasha C. Wright and Amos G. Winter V. Justification for community-scale photovoltaic-powered electrodialysis desalination systems for inland rural villages in India. *Desalination*, 352:82–91, 2014.

[2] H. Strathmann. Electrodialysis, a mature technology with a multitude of new applications. *Desalination*, 264(3):268–288, 2010.

[3] REvivED Water Consortium. *Low energy solutions for drinking water production by a Revival of Electrodialysis systems*, 2016.

[4] A. Campione, L. Gurreri, M. Ciofalo, G. Micale, A. Tamburini, and A. Cipollina. Electrodialysis for water desalination: A critical assessment of recent developments on process fundamentals, models and applications. *Desalination*, 434(October 2017):121–160, 2018.

[5] J.J. Schoeman, A. Steyn, and M. Makgae. Evaluation of electrodialysis for the treatment of an industrial solid waste leachate. *Desalination*, 186(1):273 – 289, 2005.

[6] A. Elmidaoui, L. Chay, M. Tahaikt, M.A. Menkouchi Sahli, M. Taky, F. Tiyal, A. Khalidi, and My R. Alaoui Hafidi. Demineralisation for beet sugar solutions using an electrodialysis pilot plant to reduce melassigenic ions. *Desalination*, 189(1):209 – 214, 2006. Selected paper from the 10th Aachen Membrane Colloquium.

[7] J. M. Ortiz, E. Expósito, F. Gallud, V. García-García, V. Montiel, and V. a. Aldaz. Desalination of underground brackish waters using an electrodialysis system powered directly by photovoltaic energy. *Solar Energy Materials and Solar Cells*, 92(12):1677–1688, 2008.

[8] Y. Oren, E. Korngold, N. Daltrophe, R. Messalem, Y. Volkman, L. Aronov, M. Weismann, N. Bouriakov, P. Glueckstern, and J. Gilron. Pilot studies on high recovery bwro-edr for near zero liquid discharge approach. *Desalination*, 261(3):321 – 330, 2010. Special Issue in memory of Sidney Loeb (1917-2008).

[9] Robert C. Harries, David Elyanow, Dale N. Heshka, and Kelly L. Fischer. Desalination of brackish groundwater for a prairie community using electrodialysis reversal. *Desalination*, 84(1-3):109–121, 1991.

[10] Hong Joo Lee, F. Sarfert, H. Strathmann, and Seung Hyeon Moon. Designing of an electrodialysis desalination plant. *Desalination*, 142(3):267–286, 2002.

[11] Marian Turek. Optimization of electrodialytic desalination in diluted solutions. *Desalination*, 153(1-3):383–387, 2003.

[12] Panagiotis Tsiakis and Lazaros G. Papageorgiou. Optimal design of an electrodialysis brackish water desalination plant. *Desalination*, 173(2):173–186, 2005.

[13] F. S. Rohman and N. Aziz. Optimization of batch electrodialysis for hydrochloric acid recovery using orthogonal collocation method. *Desalination*, 275(1-3):37–49, 2011.

[14] Ronan K. McGovern, Syed M. Zubair, and John H. Lienhard. Design and Optimization of Hybrid ED-RO Systems for the Treatment of Highly Saline Brines. In *International Desalination Association World Congress*, Tianjin, China, 2013.

[15] Karim M. Chehayeb, Daniel M. Farhat, Kishor G. Nayar, and John H. Lienhard. Optimal design and operation of electrodialysis for brackish-water desalination and for high-salinity brine concentration. *Desalination*, 420(June):167–182, 2017.

[16] Sahil R. Shah, Natasha C. Wright, Patrick A. Nepsky, and Amos G. Winter. Cost-optimal design of a batch electrodialysis system for domestic desalination of brackish groundwater. *Desalination*, 443:198–211, oct 2018.

[17] Karim M. Chehayeb, Kishor G. Nayar, and John H. Lienhard. On the merits of using multi-stage and counterflow electrodialysis for reduced energy consumption. *Desalination*, 439(December 2017):1–16, 2018.

[18] Bilal Ahmed Qureshi and Syed M. Zubair. Design of electrodialysis desalination plants by considering dimensionless groups and variable equivalent conductivity. *Desalination*, 430(October 2017):197–207, 2018.

[19] J. M. Ortiz, J. A. Sotoca, E. Expósito, F. Gallud, V. García-García, V. Montiel, and A. Aldaz. Brackish water desalination by electrodialysis: Batch recirculation operation modeling. *Journal of Membrane Science*, 252(1-2):65–75, 2005.

[20] Yoshinobu Tanaka. A computer simulation of batch ion exchange membrane electrodialysis for desalination of saline water. *Desalination*, 249(3):1039–1047, 2009.

[21] J. Uche, F. Círez, A. A. Bayod, and A. Martínez. On-grid and off-grid batch-ED (electrodialysis) process: Simulation and experimental tests. *Energy*, 57:44–54, 2013.

[22] Laura J. Banasiak, Thomas W. Kruttschnitt, and Andrea I. Schäfer. Desalination using electrodialysis as a function of voltage and salt concentration. *Desalination*, 205(1-3):38–46, 2007.

[23] Ji-Hee Min and Han-Seung Kim. Effect of operating conditions on the treatment of brackish groundwater by electrodialysis. *Desalination and Water Treatment*, 51:5132–5137, 2013.

[24] Kishor G Nayar, P Sundararaman, J D Schacherl, C L O'Connor, Michael L Heath, Mario O Gabriel, Sahil R Shah, Natasha C. Wright, and Amos G. Winter V. Feasibility Study of an Electrodialysis System for In-Home Water Desalination in Urban India. *Development Engineering*, 2:38–46, 2016.

[25] D. W. Bian, S. M. Watson, N. C. Wright, S. R. Shah, T. Buonassisi, D. Ramanujan, I. M. Peters, and A. G. Winter V. Optimization and Design of a Low-Cost, Village-Scale, Photovoltaic-Powered, Electrodialysis Reversal Desalination System for Rural India. *Desalination*, Under Review, 2018.

[26] Satish J. Parulekar. Optimal current and voltage trajectories for minimum energy consumption in batch electrodialysis. *Journal of Membrane Science*, 148(1):91–103, 1998.

[27] Frank B. Leitz. Chapter 2.7 Measurements and control in electrodialysis. *Desalination*, 59(C):381–401, 1986.

[28] Karim M. Chehayeb and John H. Lienhard. On the electrical operation of batch electrodialysis for reduced energy consumption. *Environmental Science: Water Research and Technology*, 5(6):1172–1182, 2019.

[29] L. Orlovskaja, N. Periene, M. Kurtinaitiene, and S. Surviliene. Ni–sic composite plated under a modulated current. *Surface and Coatings Technology*, 111(2):234 – 239, 1999.

[30] C Müller, M Sarret, and T Andreu. Znmn alloys obtained using pulse, reverse and superimposed current modulations. *Electrochimica Acta*, 48(17):2397 – 2404, 2003.

[31] Alejandra Chávez-Valdez and Aldo R. Boccaccini. Innovations in electrophoretic deposition: Alternating current and pulsed direct current methods. *Electrochimica Acta*, 65:70 – 89, 2012.

[32] Bo Lu, Yanfei Zhao, Yicheng Song, and Junqian Zhang. Stress-limited fast charging methods with time-varying current in lithium-ion batteries. *Electrochimica Acta*, 288:144 – 152, 2018.

[33] M. Panizza, Agnieszka Kapalka, and Ch Comninellis. Oxidation of organic pollutants on BDD anodes using modulated current electrolysis. *Electrochimica Acta*, 53(5):2289–2295, 2008.

[34] Karim M. Chehayeb, Daniel M. Farhat, Kishor G. Nayar, and John H. Lienhard. Optimal design and operation of electrodialysis for brackish-water desalination and for high-salinity brine concentration. *Desalination*, 420(June):167–182, 2017.

[35] M. S. Isaacson and Ain A. Sonin. Sherwood Number and Friction Factor Correlations for Electrodialysis Systems, with Application to Process Optimization. *Industrial & Engineering Chemistry Process Design and Development*, 15:313–321, 1976.

[36] N.C. Wright, S.R. Shah, S.E. Amrose, and A.G. Winter V. A robust model of brackish water electrodialysis desalination with experimental comparison at different size scales. *Desalination*, 443, 2018.

[37] Sylwin Pawlowski, João G. Crespo, and Svetlozar Velizarov. Pressure drop in reverse electrodialysis: Experimental and modeling studies for stacks with variable number of cell pairs. *Journal of Membrane Science*, 462:96–111, 2014.

[38] A. M. Peers. General Discussions. *Discussions of the Faraday Society*, 21:124, 1956.

[39] Akira Nakayama, Yoshihiko Sano, Xiaohui Bai, and Kenji Tado. A boundary layer analysis for determination of the limiting current density in an electrodialysis desalination. *Desalination*, 404:41–49, 2017.

[40] Vitor Geraldes and Maria Diná Afonso. Limiting current density in the electrodialysis of multi-ionic solutions. *Journal of Membrane Science*, 360(1):499 – 508, 2010.

[41] Sylwin Pawlowski, Philippe Sistat, João G. Crespo, and Svetlozar Velizarov. Mass transfer in reverse electrodialysis: Flow entrance effects and diffusion boundary layer thickness. *Journal of Membrane Science*, 471:72–83, 2014.

[42] R.W. Allgood and A.R. Gordon. The Variation of the Transference Numbers of Sodium Chloride in Aqueous Solution with Temperature. *Journal of Chemical Physics*, 10:124–126, 1942.

[43] R.H. Stokes. The Diffusion Coefficients of Eight Uni-univalent Electrolytes in Aqueous Solution at 25 °C. *Journal of the American Chemical Society*, 72(5):2243–2247, 1950.

[44] H. Ozbek, J.A. Fair, and S.L. Phillips. Viscosity Of Aqueous Sodium Chloride Solutions From 0 - 150C. Technical report, Lawrence Berkley Laboratory, University of California, Berkeley, California, 1977.

[45] G. Kortüm. *Treatise on Electrochemistry*. Elsevier Publishing Company, 1965.

[46] J. Veerman, M. Saakes, S. J. Metz, and G. J. Harmsen. Reverse electrodialysis: Performance of a stack with 50 cells on the mixing of sea and river water. *Journal of Membrane Science*, 327(1-2):136–144, 2009.

[47] Ronan K. McGovern, Adam M. Weiner, Lige Sun, Chester G. Chambers, Syed M. Zubair, and John H. Lienhard. On the cost of electrodialysis for the desalination of high salinity feeds. *Applied Energy*, 136:649–661, December 2014.

[48] P. Sistat, P. Huguet, B. Ruiz, G. Pourcelly, S.A. Mareev, and V.V. Nikonenko. Effect of pulsed electric field on electrodialysis of a NaCl solution in sub-limiting current regime. *Electrochimica Acta*, 164:267–280, may 2015.

[49] Nicolás Cifuentes-Araya, Gérald Pourcelly, and Laurent Bazinet. Impact of pulsed electric field on electrodialysis process performance and membrane fouling during consecutive demineralization of a model salt solution containing a high magnesium/calcium ratio. *Journal of Colloid and Interface Science*, 361(1):79–89, 2011.

[50] Piotr Długołecki, Piotr Ogonowski, Sybrand J. Metz, Michel Saakes, Kitty Nijmeijer, and Matthias Wessling. On the resistances of membrane, diffusion boundary layer and double layer in ion exchange membrane transport. *Journal of Membrane Science*, 349(1-2):369–379, 2010.

[51] A. H. Galama, D. A. Vermaas, J. Veerman, M. Saakes, H. H.M. Rijnaarts, J. W. Post, and K. Nijmeijer. Membrane resistance: The effect of salinity gradients over a cation exchange membrane. *Journal of Membrane Science*, 467:279–291, 2014.

[52] Victor V. Nikonenko, Anna V. Kovalenko, Mahamet K. Urtenov, Natalia D. Pismenskaya, Jongyoon Han, Philippe Sistat, and Gérald Pourcelly. Desalination at overlimiting currents: State-of-the-art and perspectives. *Desalination*, 342:85 – 106, 2014. Special Issue: Electromembrane Processes for Desalination.

[53] M.A. Andreeva, V.V. Gil, N.D. Pismenskaya, L. Dammak, N.A. Kononenko, C. Larchet, D. Grande, and V.V. Nikonenko. Mitigation of membrane scaling in electrodialysis by electroconvection enhancement, ph adjustment and pulsed electric field application. *Journal of Membrane Science*, 549:129 – 140, 2018.

Chapter 3

Modeling the Recovery and Specific Energy Consumption of Single-Stage Reverse Osmosis Systems

3.1 Introduction

The decrease in reverse osmosis (RO) specific energy consumption over the last 40-50 years has resulted in its widespread application to brackish water and seawater desalination [1, 2]. In the next four years alone, the installed capacity is anticipated to expand from approximately 45 to 65 million m^3/day to help satisfy the growing worldwide demand for freshwater [3]. To design and evaluate the RO processes that will enable this growth, designers and engineers require access to simple but reliable modeling tools.

The literature offers a variety of RO modeling methods. One approach is to fit polynomial functions or neural networks with collected data to enable future predictions of performance [4–6]. This is a suitable approach when considering one specific process, but requires re-calibration when translated to others. A more common treatment involves one-dimensional water and salt mass balances along the RO process [7–12], and their evolution in time [13, 14]. Two-dimensional [15–17] and quasi-two-

dimensional models [18, 19] expand upon this approach to capture both longitudinal and lateral variations in concentration and flow quantities. These analytical methods are more general than the fitted models previously discussed, but sometimes require either numerical integration or a system of several equations to be solved simultaneously. They can therefore be cumbersome to apply in initial process sizing and analysis.

This chapter derives among the simplest one-dimensional analytical models to evaluate the recovery and energy consumption of single-stage RO processes. Equivalent models have been previously proposed and applied [20–23], but often with limited or no supporting validation. Here, we aim to validate those models against experimental brackish water and seawater RO data from one spiral-wound element through to a full plant. We demonstrate that models of this type are accurate and useful, and additionally provide an 'uncertainty estimator' to help assess when more precise modeling is necessary to capture the effects of pressure drop through the feed channels.

Section 3.2 first outlines the proposed model. The model is simplified by neglecting frictional pressure drop in the feed channel. We then provide an analytical uncertainty function to bound the impact of this pressure drop on the predicted recovery ratio and specific energy consumption (Sec. 3.3). This treatment is notably different from previous approaches that either neglect the pressure drop altogether, or precisely calculate it by spatially discretizing the RO process. Finally, Section 3.4 explores the similarities with models previously proposed, offers a demonstrative example of the model's application to brackish water (BWRO) and seawater RO (SWRO) simulations, and compares model predictions against experimental measurements compiled from literature.

3.2 Model Derivation

The conceptual framework underlying this model (Fig. 3-1) is borrowed from previous studies [1, 20, 21, 24–27]. The local permeate flux J_w in an RO process is proportional

to the difference between the applied applied P_f and retentate osmotic pressure π. Integrated over the process, this permeate flux gradually raises the recovery ratio. There is a accompanying increase in osmotic pressure since the retentate becomes more concentrated. Therefore, the process achieves a maximum recovery once the osmotic pressure outgrows the applied pressure.

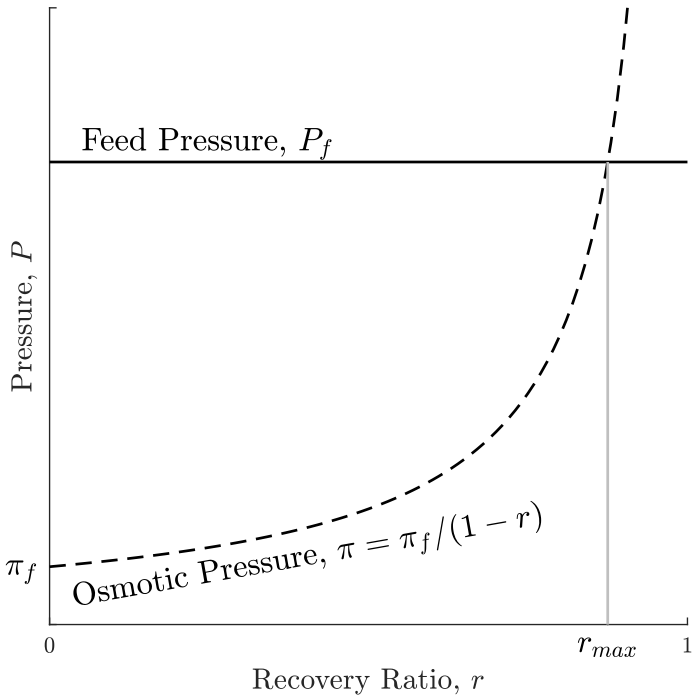

Figure 3-1: This graphical representation of a single-stage RO process assumes negligible pressure drop in the feed channel. The retentate osmotic pressure π starts at the feed osmotic pressure π_f and increases as a function of the instantaneous recovery ratio r. r_{max} represents the maximum attainable recovery, which occurs at the the intersection of the feed pressure P_f and retentate osmotic pressure

Applying the assumptions listed in Section 3.2.1 to this framework, we derived equations for the maximum recovery ratio r_{max}, the actual recovery ratio r, and the specific energy consumption SEC. The full derivation is provided below, but Equations 3.1, 3.11, and 3.18 constitute the final result.

3.2.1 Assumptions

1. Osmotic pressure varies linearly with concentration, based on van't Hoff theory.

2. There is perfect salt rejection, so the permeate is pure water at atmospheric pressure.

3. The density of water ρ is assumed to be constant.

4. Frictional pressure drop in the feed channel is neglected in the main model, but we estimate the uncertainty in the modeled performance arising from this simplification (Sec. 3.3).

5. Concentration polarization is neglected in the main model derivation and evaluation in favor of simplicity. However, Appendix 3.2.3 details an alternate form of the recovery ratio equation (Eqn. 3.11) that accounts for concentration polarization.

3.2.2 Maximum Recovery Ratio

The model presented in this paper relies on the understanding that the maximum recovery ratio r_{max} for a single RO stage occurs where the feed pressure P_f intersects the osmotic pressure π curve in Figure 3-1. Therefore,

$$r_{max} = 1 - \frac{\pi_f}{P_f}, \text{ where } r_{max} < 1. \tag{3.1}$$

3.2.3 Recovery Ratio

The actual recovery ratio r is evaluated by applying salt and water mass balances along the length of the RO process.

Salt Mass Balance

Assuming a constant water density, the salt mass balance is

$$C_f Q_f = C_p Q_p + C_b Q_b, \tag{3.2}$$

where C_f, C_p, and C_b are the respective feed, permeate, and retentate concentrations and Q_f, Q_p, and Q_b are the corresponding volumetric flow rates. Neglecting salt transport across the membrane so that $C_p \approx 0$ simplifies the above expression to

$$C_b = C_f \frac{Q_f}{Q_b} = C_f \left(\frac{1}{1-r} \right), \tag{3.3}$$

where r is the recovery ratio. If the osmotic pressure π is assumed to vary linearly with concentration, then

$$\pi = \pi_f \left(\frac{1}{1-r} \right), \tag{3.4}$$

where π_f is the osmotic pressure of the feed. Referring to Figure 3-1, the maximum recovery ratio r_{max} occurs where the feed pressure intersects the osmotic pressure curve, so

$$\frac{P_f}{\pi_f} = \left(\frac{1}{1-r_{max}} \right) \text{ or} \tag{3.5}$$

$$r_{max} = 1 - \frac{\pi_f}{P_f} < 1. \tag{3.6}$$

Water Mass Balance

The local rate of water production at an infinitesimal section of the membrane is

$$dQ_p = A_m (P_f - \pi) dS, \tag{3.7}$$

where A_m is the membrane water permeability coefficient, and S is the membrane area. Note that we do not model concentration polarization in this simple model, but a concentration polarization coefficient can be multiplied to the osmotic pressure π to account for this effect (see Appendix 3.2.3 for more details on this treatment). Dividing by the feed flow rate Q_f and substituting Equations 3.4 and 3.5 gives

$$d\left(\frac{Q_p}{Q_f} \right) = \frac{A_m}{Q_f} \pi_f \left(\frac{1}{1-r_{max}} - \frac{1}{1-r} \right) dS \tag{3.8}$$

$$dr = \frac{A_m \pi_f}{Q_f} \left(\frac{r_{max} - r}{(1-r_{max})(1-r)} \right) dS. \tag{3.9}$$

Grouping terms allows integration, such that

$$\int_0^{r<r_{max}} \frac{1-r}{r_{max}-r} dr = \int_0^S \frac{A_m \pi_f}{Q_f(1-r_{max})} dS. \tag{3.10}$$

The final result is

$$r(1-r_{max}) - (1-r_{max})^2 \ln\left(1 - \frac{r}{r_{max}}\right) = \frac{A_m \pi_f S}{Q_f}. \tag{3.11}$$

The result above relates the recovery ratio and required feed pressure (via r_{max}) on the left, to the process parameters (Q_f and π_f) and system properties (S and A_m) on the right. As the actual recovery r approaches the maximum recovery ratio r_{max}, the membrane area requirement S tends to infinity (Eqn. 3.11). Therefore r_{max} more precisely represents the maximum theoretical recovery ratio given infinite membrane area. This relationship is visualized in Figure 3-2.

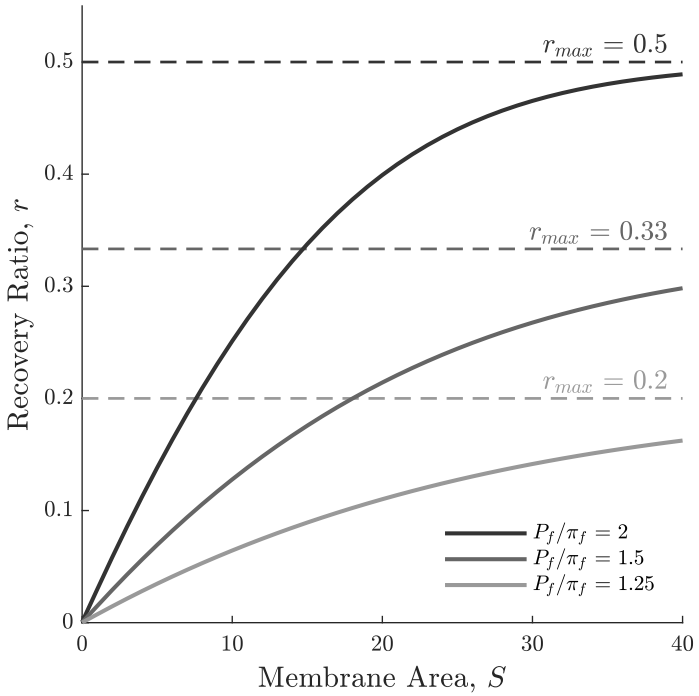

Figure 3-2: Recovery ratio r is plotted for increasing membrane area S at different pressure ratios (Eqn. 3.11). The feed flow rate, feed osmotic pressure, and membrane permeability are 1000 L/h, 30 bar, and 1 L/m^2-h-bar, respectively. As membrane area increases, the recovery ratio approaches the maximum recovery ratio r_{max} (Eqn.3.1).

Designers are often more concerned with achieving a target permeate flow rate

Q_p. In this case, substituting $Q_p = rQ_f$ gives an alternate form of Equation 3.11, where

$$1 - r_{max} - \frac{(1 - r_{max})^2}{r} \ln\left(1 - \frac{r}{r_{max}}\right) = \frac{A_m \pi_f S}{Q_p}. \tag{3.12}$$

Note that the right hand side can also be expressed in terms of the average permeate flux $\bar{J}_w$, where

$$\bar{J}_w = \frac{Q_p}{S}. \tag{3.13}$$

With this substitution, one can analyze RO performance without assigning a physical scale to the process. We provide an example of such an analysis in Section 3.4.2.

Accounting for Concentration Polarization

We do not account for concentration polarization in the derivation above. A simple adjustment to account for it begins with adding a concentration polarization factor β in Equation 3.7 to get

$$dQ_p = A_m(P_f - \beta\pi)dS, \tag{3.14}$$

as previously shown by Fraidenraich et al. [23]. This concentration polarization factor can be calculated using

$$\beta = \exp\left(\frac{\bar{J}_w}{\bar{k}_m}\right) \tag{3.15}$$

from film theory [28], where J_w is the permeate flux and k_m is boundary-layer mass-transfer coefficient. For typical feed flow velocities of 10-25 cm/s and 15-30 L/m^2-h permeate flux, β varies between 1.03 - 1.1. Treating this factor as a constant gives a similar solution to Equation 3.11. The only difference being that r_{max} is replaced with r'_{max}, where

$$r'_{max} = \beta r_{max} + 1 - \beta. \tag{3.16}$$

3.2.4 Specific Energy Consumption

The specific energy consumption SEC of the RO membrane train is

$$SEC = \frac{P_f Q_f}{Q_p} = \frac{P_f}{r}. \tag{3.17}$$

Substituting Equation 3.1 gives the simple final result that

$$SEC = \frac{\pi_f}{r(1 - r_{max})}. \tag{3.18}$$

The same result is obtained by first rearranging Equation 3.12 to get

$$1 - \frac{(1 - r_{max})}{r} \ln\left(1 - \frac{r}{r_{max}}\right) = \frac{A_m \pi_f S}{Q_p(1 - r_{max})}. \tag{3.19}$$

Then, substituting Equation 3.1 so

$$1 - \frac{(1 - r_{max})}{r} \ln\left(1 - \frac{r}{r_{max}}\right) = \frac{A_m P_f S}{Q_p}, \tag{3.20}$$

and finally dividing by Equation 3.11 to get

$$\frac{1 - \frac{(1-r_{max})}{r} \ln\left(1 - \frac{r}{r_{max}}\right)}{r(1 - r_{max}) - (1 - r_{max})^2 \ln\left(1 - \frac{r}{r_{max}}\right)} = \frac{\frac{A_m P_f S}{Q_p}}{\frac{A_m \pi_f S}{Q_f}} \tag{3.21}$$

$$\frac{\pi_f}{r(1 - r_{max})} = \frac{P_f Q_f}{Q_p}. \tag{3.22}$$

This result implies that Equations 3.1, 3.11, and 3.18 are consistent.

Equation 3.18 does not account for energy recovery and component efficiencies. They can only be considered once the full process is defined (Fig. 3-3). For example, for a standard BWRO process without energy recovery, the corresponding expression is

$$SEC_{STD} = \frac{1}{\eta_P} \frac{\pi_f}{r(1 - r_{max})}. \tag{3.23}$$

where η_P is the pump efficiency. SWRO processes typically implement energy recovery. In this case, the expression is

$$SEC_{ERD} = \frac{\pi_f}{(1 - r_{max})} \left(\frac{1}{\eta_P} + \frac{1}{\eta_{BP}} \left(\frac{1 - r}{r}\right) (1 - \eta_{ERD})\right), \tag{3.24}$$

where η_{ERD} is the energy recovery device (ERD) efficiency and η_{BP} is the booster pump efficiency.

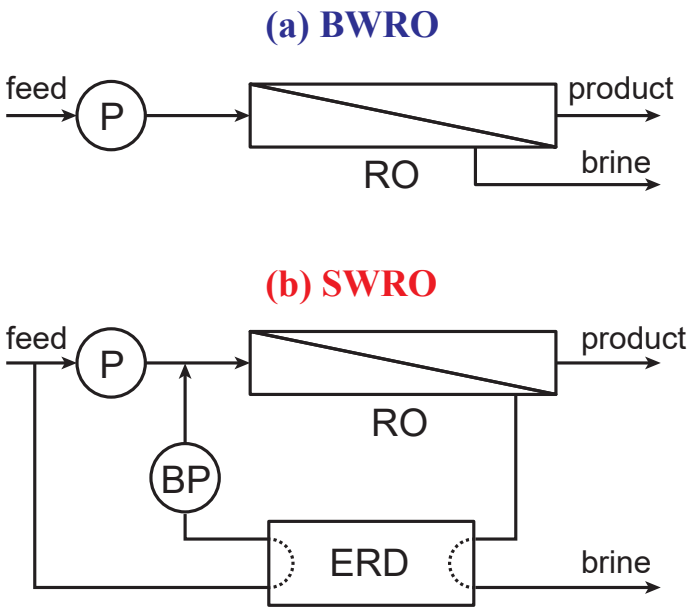

Figure 3-3: Typical single-stage configurations for brackish water (BWRO) and seawater reverse osmosis (SWRO). 'P' and 'BP' are the pump and booster pump, respectively. Given lower operating pressures and higher recoveries, energy recovery devices (ERDs) are not typical in BWRO.

3.3 Uncertainty from Neglecting Pressure Drop

The model described above assumes that the applied pressure is constant and equal to the feed pressure. In reality, friction in the feed channel gradually decreases the applied pressure. Neglecting this pressure drop thereby introduces uncertainty in the modeled recovery ratio and specific energy consumption. This uncertainty is quantified in this section to help decide when more detailed modeling is required.

3.3.1 Recovery Ratio Uncertainty

The recovery ratio is a function of the feed pressure P_f given a fixed feed flow rate, membrane area, and feed osmotic pressure. The uncertainty in recovery ratio predictions δ_r from neglecting frictional pressure drop in the feed channel ΔP_f is approximately

$$\delta_r = \frac{dr}{dP_f}(-\Delta P_f) = \left(\frac{dr}{dr_{max}}\right)\left(\frac{dr_{max}}{dP_f}\right)(-\Delta P_f)\,, \tag{3.25}$$

where r_{max} is the maximum recovery ratio. Differentiating Equation 3.11, gives the first term

$$\begin{aligned}\frac{dr}{dr_{max}} &= \frac{(r_{max}-r)}{(1-r)(1-r_{max})}\left[r - 2(1-r_{max})\ln\left(1-\frac{r}{r_{max}}\right) + \frac{r(1-r_{max})^2}{r_{max}(r_{max}-r)}\right] \\ &= F(r, r_{max}).\end{aligned} \tag{3.26}$$

Similarly, differentiating Equation 3.1 gives the second term

$$\frac{dr_{max}}{dP_f} = \frac{(1-r_{max})}{P_f}. \tag{3.27}$$

Next, we evaluate an expression for the frictional pressure drop ΔP_f and combine terms to provide a final expression for δ_r.

Pressure Drop

Pressure drop in channel is modeled by equations of the form

$$dP_f = \frac{1}{2} f \frac{\rho u_r^2}{d_h} dx, \tag{3.28}$$

where u_r is the retentate flow velocity, f is the friction factor, ρ is the density of the solution, and d_h is the hydraulic diameter. Note that the retentate flow velocity and volumetric flow-rate are related through

$$u_r = \frac{Q_r}{n_l \epsilon W h} \tag{3.29}$$

where n_l is the number of leaves in a spiral-wound element, W is the active width of the membrane in each leaf, h is the channel height, and ϵ is the spacer void fraction. The retentate flow quantities can also be expressed in terms of the respective feed quantities u_f and Q_f through

$$u_r = u_f(1-r), \text{ and} \tag{3.30}$$

$$Q_r = Q_f(1-r). \tag{3.31}$$

Furthermore, the membrane area S is related to the distance along the feed spacer via

$$dS = 2n_l W dx. \tag{3.32}$$

The factor of 2 accounts for permeate production occurring at both walls of the feed channel.

Next, we perform a series of substitutions to Equation 3.28, beginning with Equations 3.29 through 3.32 so that

$$dP_f = \frac{1}{4d_h n_l W} f\rho u_f^2 (1-r)^2 dS. \tag{3.33}$$

Then, we substitute Equation 3.4 for dS, which gives

$$dP_f = \frac{1}{4d_h n_l W} f\rho u_f^2 (1-r)^2 \frac{dQ_p}{A_m(P-\pi)}, \tag{3.34}$$

where A_m is the membrane water permeability and π is the retentate osmotic pressure. The retentate pressure P, which drives permeate flux, decreases with pressure drop. This higher order effect is neglected for the purposes of deriving an uncertainty estimate. Instead, the retentate pressure is held at the feed pressure P_f. Relating the feed and osmotic pressures to the recovery ratio (Eqns. 3.5 and 3.4, respectively) then gives

$$dP_f = \frac{f\rho u_f^2 Q_f}{4d_h n_l W A_m P_f} \frac{(1-r)^3}{(r_{max}-r)} dr \tag{3.35}$$

since $dQ_p = Q_f dr$. Integrating both sides, and substituting u_f for Q_f (Eqn. 3.29) gives the final expression for the pressure drop,

$$\Delta P_f = \frac{\epsilon h}{4d_h} \frac{f\rho u_f^3}{A_m P_f} \int_0^{r<r_{max}} \frac{(1-r)^3}{r_{max}-r} dr. \tag{3.36}$$

The expression above assumes a constant friction factor. This is a good approximation for our purposes since Schock and Miquel experimentally measured it to be 0.7-1.5 for different feed spacers over a broad range of Reynolds Numbers (100- 1000) [29].

Substitution and Result

Substituting Equations 3.26, 3.27, and 3.36 in the initial expression (Eqn. 3.25) gives the final result that

$$\delta_r = -\underbrace{\frac{\epsilon h}{4d_h}\frac{f\rho u_f^3}{A_m P_f^2}}_{K} F(r, r_{max})G(r, r_{max}) \tag{3.37}$$

when considering designs with fixed feed flow rates. The negative coefficient indicates pressure drop causes the recovery to decrease. When deriving this expression, it was assumed that the applied pressure across the full channel was reduced by the total pressure drop (Eqn. 3.37). In practice, the pressure at the entry is higher than at the exit. Therefore, this expression is conservative. The function F was defined previously (Eqn. 3.26) and G is the solution to the integral in Equation 3.36:

$$\begin{aligned} G(r, r_{max}) = (1-r_{max})^2 r + \frac{1}{2}(1-r_{max})\left[1-(1-r)^2\right] + \frac{1}{3}\left[1-(1-r)^3\right] \\ -(1-r_{max})^3 \ln\left(1-\frac{r}{r_{max}}\right). \end{aligned} \tag{3.38}$$

If the design is instead constrained to provide a fixed product flow rate (or flux), then function F is replaced by a different function E to capture a different sensitivity of recovery ratio to pressure ratio (Eqn. 3.12 vs. 3.11). Substituting the derivative of Equation 3.12 for Equation 3.26 then gives that

$$\begin{aligned} E(r, r_{max}) = \frac{r(r_{max}-r)}{(1-r_{max})\left[r+(r_{max}-r)\ln\left(1-\frac{r}{r_{max}}\right)\right]} \\ \left[r - 2(1-r_{max})\ln\left(1-\frac{r}{r_{max}}\right) + \frac{r(1-r_{max})^2}{r_{max}(r_{max}-r)}\right]. \end{aligned} \tag{3.39}$$

The non-dimensional constant K defines the magnitude of the uncertainty, and depends on process and design parameters. The explicit analytical functions E, F and G resolve to values between 0.1-35 for combinations satisfying $0.1 < r < r_{max} < 0.95$.

The definitions of the feed flow velocity u_f and hydraulic diameter d_h depend on

the friction factor f correlation being applied. In this work, we use

$$f = 6.23Re^{-0.3}, \tag{3.40}$$

which was shown to accurately model a variety of feed spacers at Reynolds numbers Re ranging from 100 to 1000 [29]. For this correlation,

$$d_h = \frac{2\epsilon h}{5 - 4\epsilon}, \text{ and} \tag{3.41}$$

$$u_f = \frac{Q_f}{\epsilon W h}, \tag{3.42}$$

where W, h, and ϵ are the width, height, and porosity of the feed spacer, respectively. The friction factor is evaluated at the feed flow velocity when estimating uncertainty.

3.3.2 Specific Energy Consumption

The process configuration affects how frictional pressure drop impacts specific energy consumption. For a single-stage process without energy recovery (Eqn. 3.23), the pressure drop lowers recovery ratio. The corresponding increase in energy consumption δ_{SEC}^{STD} is

$$\delta_{SEC}^{STD} = -SEC_{STD}\frac{\delta_r}{r}. \tag{3.43}$$

With energy recovery (Eqn. 3.24), the feed channel pressure drop decreases both recovery ratio and the recaptured brine pressure. Considering both effects, the uncertainty in model predictions δ_{SEC}^{ERD} is

$$\delta_{SEC}^{ERD} = -P_f\frac{(1 - \eta_{ERD})}{\eta_{BP}r^2}\delta_r + \frac{(1 - r)}{r}\frac{\eta_{ERD}}{\eta_{BP}}\Delta P_f. \tag{3.44}$$

From Equation 3.36, the feed channel pressure drop ΔP_f is approximated by

$$\frac{\Delta P_f}{P_f} = KG(r, r_{max}), \tag{3.45}$$

where K and G are respectively the same constant and function as defined for the recovery uncertainty (3.37).

3.4 Interpretation, Application, and Validation

We first show that although interpreted differently, the model derived here is equivalent to work from other authors (Sec. 3.4.1). This is a useful exercise because the different authors offer unique insight on the same equations. Next, the model is used to predict the energy consumption and recovery ratio for representative single-stage BWRO and SWRO processes (Sec. 3.4.2). These sample simulations are meant to demonstrate the model's utility in analyzing processes. Finally, model predictions are compared against experimental data to evaluate accuracy (Sec. 3.4.3).

3.4.1 Equivalence with Other Models

Song and Tay derived an analytical model for a long crossflow RO membrane channel [20]. An important parameter in their model is the characteristic pressure Δp^* defined as

$$\Delta p^* = \frac{u_0 h R_m}{L}, \tag{3.46}$$

where u_0 is the void channel feed flow velocity at the inlet, h is the channel height, R_m is the membrane resistance or the inverse of the membrane permeability A_m, and L is the length of the channel. The right hand side of of our recovery ratio model (Eqn. 3.11) can be expressed in terms of Δp^*, since

$$\frac{\pi_f A_m \frac{S}{W}}{\frac{Q_f}{W}} = \frac{\pi_f L}{R_m u_0 h} = \frac{\pi_f}{\Delta p^*}. \tag{3.47}$$

The two models are equivalent with this substitution.

Song and Tay also showed that the process approaches the *thermodynamic restriction* at high ratios of feed pressure to characteristic pressure. Then, the recovery ratio is bound by $(1 - \pi_f / P_f)$. This result is also consistent with the present work,

since r_{max} in our model equals the same quantity by definition.

Zhu et al. gave the following expression for the average net driving pressure $\overline{NDP}$ for a crossflow RO system [21]:

$$\begin{aligned}\overline{NDP} &= \frac{P_f}{1+\frac{\pi_f}{P_f}\frac{1}{r}\ln\left(\frac{1-\pi_f/P_f}{1-r-\pi_f/P_f}\right)}, \text{ or} \\ &= \frac{P_f}{1-\frac{(1-r_{max})}{r}\ln\left(1-\frac{r}{r_{max}}\right)}\end{aligned} \tag{3.48}$$

Substituting $\overline{NDP}$ into the right hand side of Equation 3.12 gives the same result since

$$\overline{NDP} = \frac{Q_p}{A_m S}. \tag{3.49}$$

Hence, the two models are again equivalent.

Qiu and Davies derived the theoretical minimum energy consumption to be

$$SEC^{min}_{STD,th} = \frac{\pi_f}{r(1-r)} \text{ and} \tag{3.50}$$

$$SEC^{min}_{ERD,th} = \frac{\pi_f}{1-r} \tag{3.51}$$

for single-stage RO processes with and without energy recovery, respectively [24]. These expressions match Equations 3.24 and 3.23 when $r = r_{max}$ and all component efficiencies are unity. This condition implies that the applied pressure is exactly that which is necessary to achieve a desired recovery ratio using infinite membrane area; no excess pressure is applied. It also follows that the SEC expressions from this work generalize the results from Qiu and Davies to provide the minimum energy consumption when operating at a finite flux, where $r \neq r_{max}$. These expressions are

$$SEC^{min}_{STD} = \frac{\pi_f}{r(1-r_{max})} \text{ and} \tag{3.52}$$

$$SEC^{min}_{ERD} = \frac{\pi_f}{1-r_{max}} \tag{3.53}$$

for processes with and without energy recovery, respectively.

3.4.2 Sample BWRO and SWRO Simulations

The model was used to predict the recovery ratio and energy consumption (Fig. 3-4) of the single-stage BWRO and SWRO configurations introduced in Figure 3-3. Parameters for this case-study were chosen to reflect conventional design and operation (Table 3.1) [27, 30, 31]. The theoretical energy consumption at the limit of zero flux (Eqns. 3.50 and 3.51) is also plotted for each configuration. Key observations include:

Table 3.1: BWRO and SWRO Simulation Parameters

Parameter	**BWRO**	**SWRO**
Feed Osmotic Pressure, π_f [bar]	3	30
Membrane Water Permeability, A_m [L/m^2-h-bar]	5	1
Average Flux, $\bar{J}_w$ [L/m^2-h]	25	15
Feed Channel Height, h [mm]	0.77	0.77
Feed Channel Porosity, ϵ	0.9	0.9
Feed Channel Velocity, u_f [m/s]	0.15	0.15
Feed Pump Efficiency, η_P	0.8	0.8
Booster Pump Efficiency, η_{BP}	-	0.8
ERD Efficiency, η_{ERD}	-	0.9

1. The x-intercepts in Figure 3-4A are the minimum pressure ratios required to generate the prescribed permeate flux at the given A_m values. Lowering A_m or raising the average flux requirement shifts the intercept to higher pressure ratios (or r_{max} values).

2. Recovery ratio is initially limited by membrane permeability. A higher permeability raises recovery ratio in this region. Recovery eventually becomes pressure-limited; hence r approaches r_{max} (thermodynamic restriction).

3. Shaded regions indicate that neglecting frictional pressure drop has a negligible impact when modeling the performance of single-stage SWRO at typical 30-50% recoveries [2]. Here, the SEC and recovery is predicted with a maximum uncertainty of 2% and 4%, respectively. This result matches the assessment by Zhu et al. who estimated the relative error due to frictional pressure drop to lie in the range of 10^{-5}-10^{-2} for $r = 0.3 - 0.95$ [21].

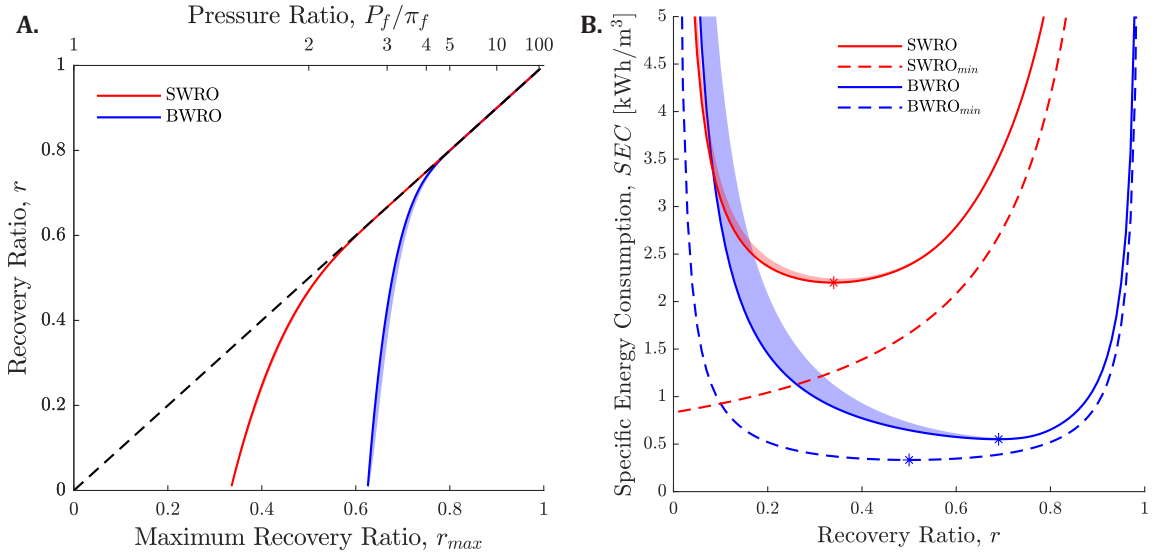

Figure 3-4: Predicted recovery ratio r (**A**) and specific energy consumption SEC (**B**) for single-stage BWRO without energy recovery, and SWRO with energy recovery, at fixed average permeate flux (Eqns. 3.12 and 3.18). Simulated parameters are summarized in Table 3.1. Dashed lines represent the thermodynamic limit whereby $r = r_{max}$ on (**A**), and on (**B**) the theoretical energy consumption at zero permeate flux (Eqns. 3.50 and 3.51). The solid lines represent the predicted recovery and SEC, $*$ symbols indicate SEC minima, and the shaded regions represent the uncertainty in the model predictions from neglecting pressure drop in the feed channel (Eqns. 3.37 and 3.43).

4. Neglecting pressure drop introduces more uncertainty when modeling BWRO recovery and energy consumption because lower pressures are involved. Recall that the uncertainty magnitude K (Eqn. 3.37) scales as

$$K \propto 1/P_f^2, \tag{3.54}$$

and as with the case simulated, feed pressures are generally lower in BWRO processes.

5. When recovery ratio is raised at a fixed average permeate flux, the brine flow rate decreases. The corresponding decrease in the frictional pressure drop (relative to feed pressure) is reflected in the shape of the shaded uncertainty regions. Hence, the model is generally expected to be more accurate at higher recoveries.

6. The minimum theoretical SEC without energy recovery occurs at a recovery

ratio of 0.5. This result was previously shown by Qiu and Davies [24]. At a finite flux, the optimum operating point shifts to higher recoveries. The optimum recovery ratio is 0.69 for the simulated BWRO process.

7. Unlike the theoretical value, the actual SWRO energy consumption increases at low recoveries due to ERD inefficiency. Permeate flux is fixed for these simulations. Therefore, SEC increases at low recoveries because power loss at the non-ideal ERD grows from increased brine flow.

8. Following from Item 7, we see that a recovery ratio of 34% minimizes SWRO energy consumption with the specified flux and component efficiencies while the theoretical minimum occurs at zero recovery.

3.4.3 Experimental Validation

Model predictions were compared against experimental data compiled from literature (Table 3.2). These data represent a broad range of system sizes and operating parameters spanning both brackish and seawater RO.

Table 3.2: Summary of Compiled Experimental Data

Source	**Type**	**Feed Pressure** [bar]	**Feed Flow** [L/h]	**Membrane Area** [m^2]	**Recovery** [%]
Shah and Winter [32]	BW	0.7-5.6	56-104	0.49	2-25
Avlonitis et al. [33], Li [19]	SW	60-80	615-655	2	8-14
Fraidenraich et al. [8]	BW	6.8-11.0	425-630	7.5	16-32
Li and Noh [34]	BW	12.6	310,000 - 355,000	7284, 3642[a]	79-91
Song and Tay [20]	BW	2-17	330-500	10.8	6-98
Geraldes et al. [35]	SW	57-59	70,200-82,400	1680	30-32
Mohamed et al. [36]	SW	37	847	5.6	12

a - Membrane areas for first and second trains, respectively. Brine from the first train was processed by the second train without re-pressurization.

Recovery ratio and SEC predictions (Eqns. 3.11 and 3.18) agree with experimental measurements with a mean relative error of 7% (Figs. 3-5 and 3-6). Therefore, the model is reasonably accurate for a broad range of RO applications despite its simplicity.

The comparison also confirms that the model generally over-predicts recovery ratio and under-predicts SEC by neglecting frictional pressure drop. The associated

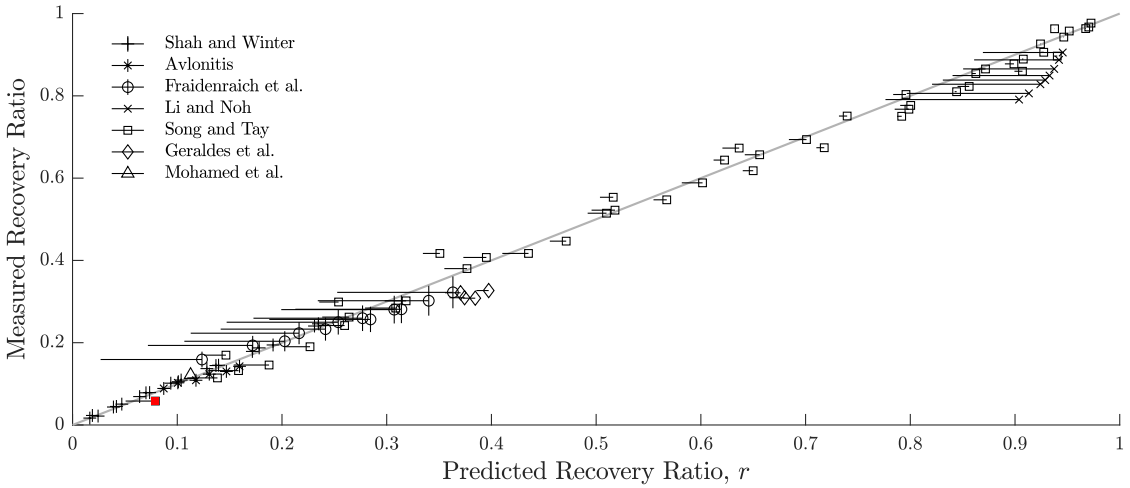

Figure 3-5: Recovery ratio predictions from Equation 3.11 were compared against experimental measurements compiled from literature. Horizontal error bars represent estimated prediction uncertainty from neglecting feed channel pressure drop while vertical error bars represent measurement uncertainty as reported in the sources. The red data point has the highest relative error of 36% between measured and predicted values.

uncertainty in the modeled performance was computed (Eqns. 3.37 and 3.43) and plotted as horizontal error bars on Figures 3-5 and 3-6. Note that even though some measurements significantly deviate from nominal model predictions, the error falls within the uncertainty in most cases. The recovery ratio data point with the highest relative error of 36% is one case where this agreement is observed (Fig. 3-5, highlighted in red). This agreement indicates that the frictional pressure drop in the feed channel likely explains the discrepancy between the nominal predictions and the measurements. For predictions that closely match measurements, the proposed method generally provides a smaller window of uncertainty. Thus, the proposed uncertainty metric is a good indicator of the extent to which the model can be trusted.

BWRO processes with high feed flow velocities have the highest modeling uncertainty. Recall that the uncertainty magnitude K (Eqn. 3.37) scales as

$$K \propto u_f^3 / P_f^2. \tag{3.55}$$

Feed flow velocities ranged between 15-22 cm/s in the BWRO process investigated

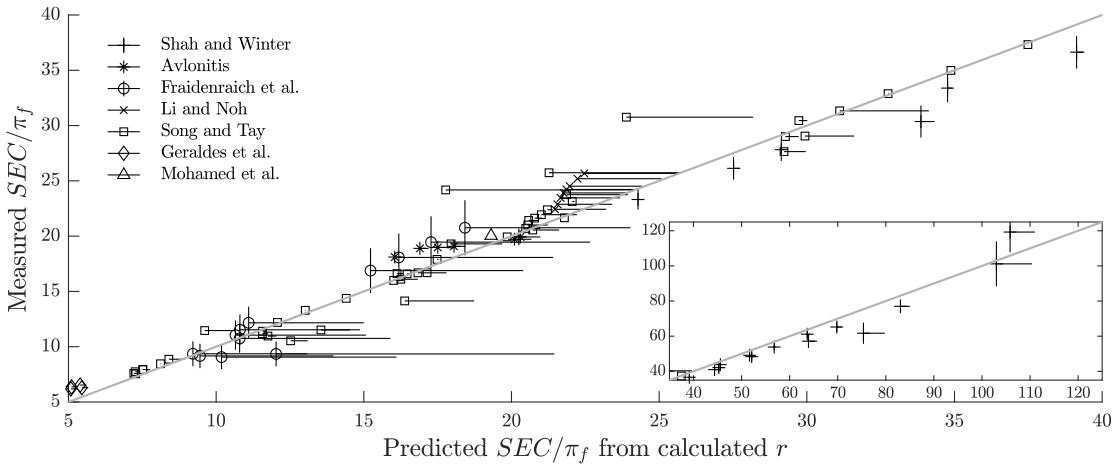

Figure 3-6: Specific energy consumption predictions from the model are compared against experimental measurements compiled from literature. Comparison is drawn for the SEC of the RO membrane train only (Eqn. 3.17); component efficiencies and energy recovery are not considered. Horizontal error bars represent prediction uncertainty from neglecting feed channel pressure drop (Eqn. 3.43) while vertical error bars represent measurement uncertainty

by Fraidenraich et al. [8], In the plant optimized by Li and Noh, the velocities were 26-30 cm/s [19]. To predict performance more precisely under these conditions, we recommend alternative approaches that more precisely capture the effect of pressure drop on the spatial variation in net driving pressure [7–14].

3.5 Conclusions

This work derived a simple set of equations to model the recovery ratio and energy consumption of single-stage RO processes. Despite the simplicity, model predictions matched experimental measurements for both BWRO and SWRO processes with a mean relative error of 7%.

Neglecting frictional pressure drop in the feed channel introduces uncertainty in the predicted performance. This uncertainty was analytically quantified and shown to be negligible when modeling conventional single-stage SWRO, but significant for BWRO with high feed flow velocities (>15 cm/s). Consequently, modeling the latter may require a more detailed approach.

While only single-stage RO processes were considered here, we have laid the groundwork for others to expand the method to more complex process configurations.

Bibliography

[1] Menachem Elimelech and William A. Phillip. The future of seawater desalination: Energy, technology, and the environment. *Science*, 333(6043):712–717, 2011.

[2] Jungbin Kim, Kiho Park, Dae Ryook Yang, and Seungkwan Hong. A comprehensive review of energy consumption of seawater reverse osmosis desalination plants. *Applied Energy*, 254(July):113652, 2019.

[3] Rory Weaver and Yumeng Yang. Desalination & Reuse Market Update January 2020. Technical report, GWI DesalData, 2020.

[4] Vanessa Haluch, Everton F. Zanoelo, and Christian J.L. Hermes. Experimental evaluation and semi-empirical modeling of a small-capacity reverse osmosis desalination unit. *Chemical Engineering Research and Design*, 122:243 – 253, 2017.

[5] Jasir Jawad, Alaa H. Hawari, and Syed Zaidi. Modeling of forward osmosis process using artificial neural networks (ANN) to predict the permeate flux. *Desalination*, 484:114427, 2020.

[6] Dan Libotean, Jaume Giralt, Francesc Giralt, Robert Rallo, Tom Wolfe, and Yoram Cohen. Neural network approach for modeling the performance of reverse osmosis membrane desalting. *Journal of Membrane Science*, 326(2):408 – 419, 2009.

[7] Shoji Kimura and S. Sourirajan. Analysis of data in reverse osmosis with porous cellulose acetate membranes used. *AIChE Journal*, 13(3):497–503, 1967.

[8] Naum Fraidenraich, Olga de Castro Vilela, Milton dos Santos Viana, and Jeffrey M. Gordon. Improved analytic modeling and experimental validation for brackish-water reverse-osmosis desalination. *Desalination*, 380:60–65, 2016.

[9] Abdul Sattar Kahdim, Saleh Ismail, and Alaa' Abdulrazaq Jassim. Modeling of reverse osmosis systems. *Desalination*, 158(1):323 – 329, 2003. Desalination and the Environment: Fresh Water for All.

[10] Wenwen Zhou, Lianfa Song, and Tay Kwee Guan. A numerical study on concentration polarization and system performance of spiral wound RO membrane modules. *Journal of Membrane Science*, 271(1):38 – 46, 2006.

[11] S. Sundaramoorthy, G. Srinivasan, and D.V.R. Murthy. An analytical model for spiral wound reverse osmosis membrane modules: Part I — Model development and parameter estimation. *Desalination*, 280(1):403 – 411, 2011.

[12] J.M. Gozálvez, J. Lora, J.A. Mendoza, and M. Sancho. Modelling of a low-pressure reverse osmosis system with concentrate recirculation to obtain high recovery levels. *Desalination*, 144(1):341 – 345, 2002.

[13] K. Jamal, M.A. Khan, and M. Kamil. Mathematical modeling of reverse osmosis systems. *Desalination*, 160(1):29 – 42, 2004.

[14] Evangelos Dimitriou, Panagiotis Boutikos, Essam Sh. Mohamed, Slawomir Koziel, and George Papadakis. Theoretical performance prediction of a reverse osmosis desalination membrane element under variable operating conditions. *Desalination*, 419:70 – 78, 2017.

[15] Junhyung Park and Kwang Soon Lee. A two-dimensional model for the spiral wound reverse osmosis membrane module. *Desalination*, 416:157 – 165, 2017.

[16] Mohammad Kahrizi, Jiuyang Lin, Guozhao Ji, Lingxue Kong, Chengwen Song, Ludovic F. Dumée, Soleyman Sahebi, and Shuaifei Zhao. Relating forward water and reverse salt fluxes to membrane porosity and tortuosity in forward osmosis: CFD modelling. *Separation and Purification Technology*, 241:116727, 2020.

[17] Boram Gu, Xiao Yun Xu, and Claire S. Adjiman. A predictive model for spiral wound reverse osmosis membrane modules: The effect of winding geometry and accurate geometric details. *Computers & Chemical Engineering*, 96:248 – 265, 2017.

[18] S. Avlonitis, W.T. Hanbury, and M.Ben Boudinar. Spiral wound modules performance. an analytical solution, part i. *Desalination*, 81(1):191 – 208, 1991. Proceedings of the Twelfth International Symposium on Desalination and Water Re-use.

[19] Mingheng Li. Predictive modeling of a commercial spiral wound seawater reverse osmosis module. *Chemical Engineering Research and Design*, 148:440–450, 2019.

[20] Lianfa Song and Kwee Guan Tay. Performance prediction of a long crossflow reverse osmosis membrane channel. *Journal of Membrane Science*, 281(1-2):163–169, 2006.

[21] Aihua Zhu, Panagiotis D. Christofides, and Yoram Cohen. Effect of thermodynamic restriction on energy cost Optimization of RO membrane water desalination. *Industrial and Engineering Chemistry Research*, 48(13):6010–6021, 2009.

[22] Shihong Lin and Menachem Elimelech. Kinetics and energetics trade-off in reverse osmosis desalination with different configurations. *Desalination*, 401:42–52, 2017.

[23] Naum Fraidenraich, Olga C. Vilela, Gilmário A. Lima, and Jeffrey M. Gordon. Reverse osmosis desalination: Modeling and experiment. *Applied Physics Letters*, 94(12):10–13, 2009.

[24] Tianyu Qiu and Philip A. Davies. Comparison of configurations for high-recovery inland desalination systems. *Water*, 4(3):690–706, 2012.

[25] Shihong Lin and Menachem Elimelech. Staged reverse osmosis operation: Configurations, energy efficiency, and application potential. *Desalination*, 366:9–14, 2015.

[26] David M. Warsinger, Emily W. Tow, Kishor G. Nayar, Laith A. Maswadeh, and John H. Lienhard. Energy efficiency of batch and semi-batch (CCRO) reverse osmosis desalination. *Water Research*, 106:272–282, 2016.

[27] Quantum J. Wei, Carson I. Tucker, Priscilla J. Wu, Ali M. Trueworthy, Emily W. Tow, and John H. Lienhard. Impact of salt retention on true batch reverse osmosis energy consumption: Experiments and model validation. *Desalination*, 479(October 2019):114177, 2020.

[28] Suhan Kim and Eric M.V. Hoek. Modeling concentration polarization in reverse osmosis processes. *Desalination*, 186(1):111 – 128, 2005.

[29] G. Schock and A. Miquel. Mass transfer and pressure loss in spiral wound modules. *Desalination*, 64(C):339–352, 1987.

[30] DOW Water & Process Solutions. FILMTEC BW30-4040 Product Specifications.

[31] DOW Water & Process Solutions. Water & Process Solutions, FILMTEC ™ Reverse Osmosis Membranes: Technical Manual. *Dow Chemical Company*, pages 82–83, 2011.

[32] Sahil R. Shah and Amos G Winter V. Evaluating the Production and Exergetic Performance of Point-of-Use Reverse Osmosis Devices for Brackish Water Desalination. *Desalination*, Submitted, 2020.

[33] S Avlonitis, W T Hanbury, and M Ben Boudinar. Spiral Wound Modules Performance, An Analytical Solution: Part II. *Desalination*, 89:227–246, 1993.

[34] Mingheng Li and Brian Noh. Validation of model-based optimization of brackish water reverse osmosis (BWRO) plant operation. *Desalination*, 304:20–24, 2012.

[35] Vitor Geraldes, Nuno Escórcio Pereira, and Maria Norberta de Pinho. Simulation and optimization of medium-sized seawater reverse osmosis processes with spiral-wound modules. *Industrial and Engineering Chemistry Research*, 44(6):1897–1905, 2005.

[36] Essam Sh Mohamed, G. Papadakis, E. Mathioulakis, and V. Belessiotis. The effect of hydraulic energy recovery in a small sea water reverse osmosis desalination system; experimental and economical evaluation. *Desalination*, 184(1-3):241–246, 2005.

Chapter 4

Using Gear and Vane mechanisms as Energy Recovery Devices in Small-Scale Reverse Osmosis Applications

4.1 Introduction

This study investigates the feasibility of a low-cost energy recovery device (ERDs) for small-scale reverse-osmosis (RO) applications. By recapturing brine pressure, ERDs can decrease the specific energy consumption (SEC) of all RO processes. However, most ERDs today (Fig. 4-1) are designed for large-scale seawater desalination plants where the high pressures (40-55 bar) and flow rates (>100 m^3/h) can amplify small SEC reductions into large energy cost savings. At this scale, initial ERD costs are on the order of $100-1000 per m^3/h and are easily superceded by the energy cost savings that they enable [1–3].

ERDs can also lower the SEC of smaller RO processes but the total power recoverable from the brine stream drops with decreasing pressures and flow rates, providing a lower opportunity for cost savings. Consequently, fewer ERD products have been

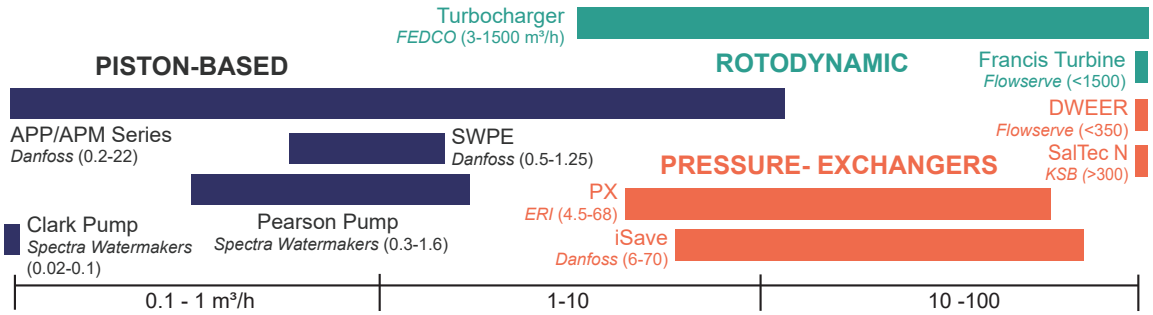

Figure 4-1: **Examples of commercially-available ERDs at varying capacities.** Color-coding by mechanism type shows that pistons are prevalent at approximately < 1 m^3/h capacities, while rotodynamic devices and work-exchangers are generally designed for >10 m^3/h.

developed for small RO applications with <5 m^3/h permeate production capacity (Fig. 4-1) and they only tend to be cost-effective when energy is either scarce or expensive. For example, the Clark Pump is a piston-based ERD designed for sea-water desalination aboard sailboats and costs on the order of $10,000 per m^3/h [2]. Clark Pumps have also been suggested for use in off-grid installations where decreasing the power consumption can lead to significant savings on photovoltaic generation costs [4]. Decreasing the cost of small-scale energy recovery could expand usage to on-grid and lower-pressure brackish water desalination applications, thus making it more efficient to produce drinking water using small-scale RO treatment [5–7].

Gear and sliding vane pumps are ubiquitous, inexpensive ($\sim$\$100 per m^3/h), and available in a variety of sizes. They can be adapted as hydraulic motors to recover power from the brine stream and to convert it into mechanical power to assist with pumping feed. However, the feasibility of energy recovery using gears has not been previously explored and only one study evaluates small-scale vane ERDs. In this study, Lu et al. [8] tested a 1.5-2 m^3/h prototype that provided a 20% energy savings at a maximum 41 bar test pressure. However, their system's recovery dropped from an expected 55% to a measured 15-20% due to the leakage of water from the high pressure side to the low pressure side of the device. The geometry of the device nor sources of these losses was explained so it remains unclear whether performance can be improved. There are additionally two studies that modeled a 1200 m^3/h vane ERD

[9, 10]. Since efficiency tends to improve with device size, the predicted performance is likely to differ from the performance at the smaller <5 m^3/h capacities of present interest. Therefore, this study assesses the technical feasibility and challenges of gear- and vane-based ERDs while crucially accounting for how efficiency degrades as these mechanisms are scaled down. In doing so, we also aim to provide insight on whether it is possible to improve upon the measured performance reported by Lu et al.

To assess feasibility, we propose a fixed-recovery pump-ERD architecture that can adopt either gears or sliding vanes and evaluate its performance for typical BWRO and SWRO operation. To do this, we first model the proposed device coupled to an RO membrane train and simulate the impact of pump and ERD inefficiencies on desalination production rate, recovery, and energy consumption. Results are then used to identify the better-performing mechanism between gears and vanes and predict the SEC reduction against conventional operation without energy recovery.

4.2 Proposed Fixed-Recovery Pump-ERD Concept

This work explores a fixed-recovery concept involving two rotary positive displacement stages (pump and ERD) coupled on a single shaft that is directly driven by an electric motor (Fig. 4-2). A positive displacement mechanism displaces a fixed volume of fluid per rotation of the shaft from the input port to the output port. This volume, which is set by the device's geometry, is defined as its displacement d. In the proposed configuration, the pump is specified to have a displacement d^I. Then, for a shaft speed ω, the ideal feed flow rate Q_f^{id} is

$$Q_f^{id} = \frac{\omega d^I}{2\pi}. \tag{4.1}$$

The ERD has a smaller displacement of $d^{II} < d^I$. Therefore, for the same shaft speed, the ideal brine flow rate Q_b^{id} that is discharged by the ERD is

$$Q_b^{id} = \frac{\omega d^{II}}{2\pi}. \tag{4.2}$$

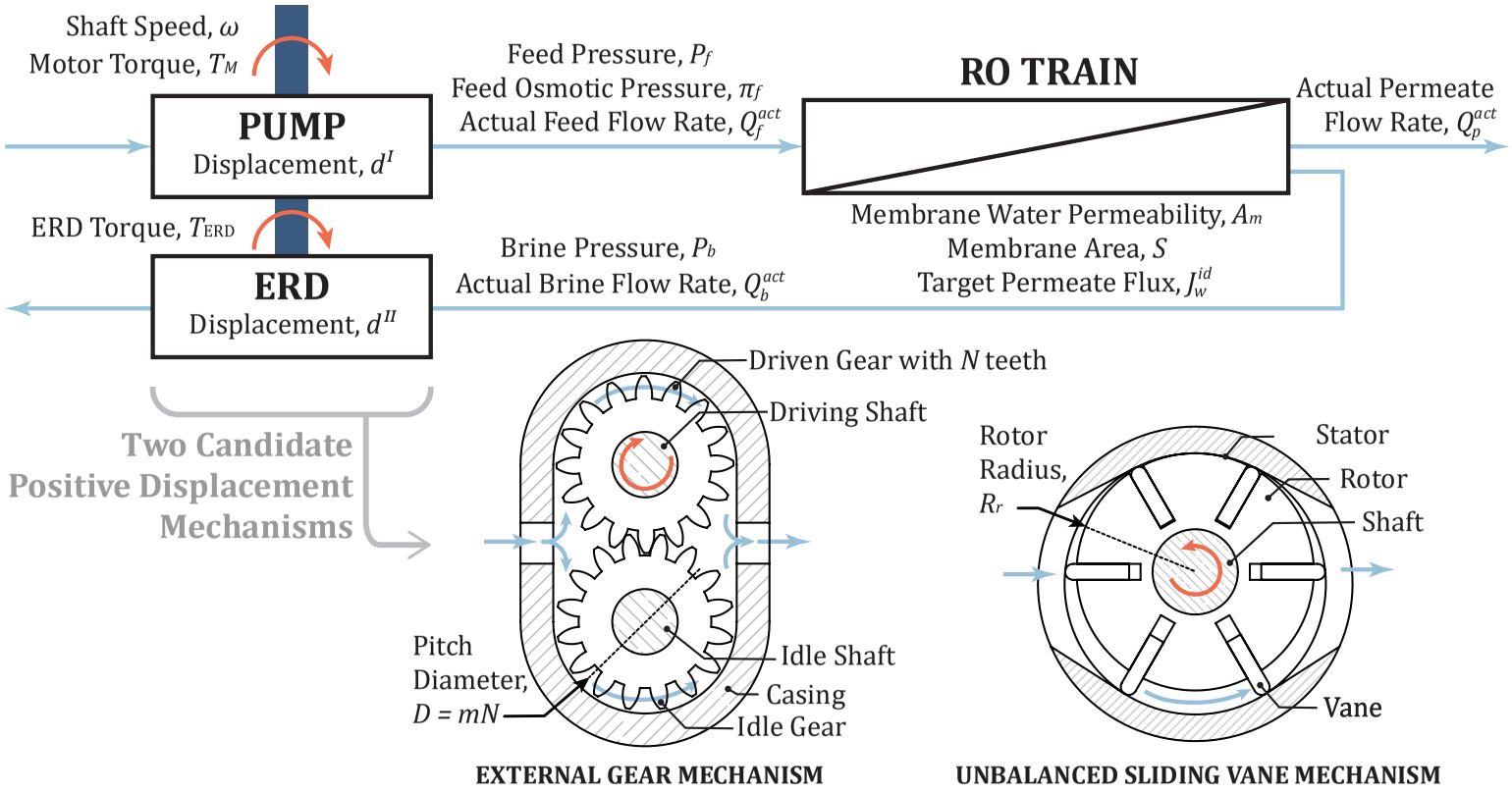

Figure 4-2: **A fixed recovery architecture that uses two rotary positive displacement stages.** The two positive stages are coupled on the same shaft that is driven by an electric motor (not shown here). The pump stage pressurizes incoming feed and the ERD stage recaptures pressure from outgoing brine. The displacement ratio d^{II}/d^I dictates the ideal recovery ratio, which is the ratio of permeate flow rate to feed flow rate. Two candidate positive displacement mechanisms are assessed in this study: gears and sliding vanes. Parameters defined here are referenced in the subsystem models (Table 4.1).

By applying a mass-balance on the RO train, the ideal permeate flow rate Q_p^{id} must then be

$$Q_p^{id} = \frac{\omega(d^I - d^{II})}{2\pi}. \tag{4.3}$$

Taking the ratio of the permeate flow rate to the feed flow rate, the ideal recovery ratio r^{id} is

$$r = 1 - \frac{d^{II}}{d^I}. \tag{4.4}$$

Therefore, the geometries of the pump and ERD stages fix the ideal recovery ratio of the system.

An ideal power balance on the fixed-recovery system gives

$$T_m^{id}\omega = P_f Q_f^{id} - P_b Q_b^{id}, \tag{4.5}$$

where T_m^{id} is the ideal torque output of the motor, P_f is the feed pressure, and P_b is the brine pressure. Assuming negligible brine pressure drop through the RO element so that $P_f = P_b$, Eqn. 4.5 simplifies to

$$T_m^{id}\omega = P_f Q_p^{id}. \tag{4.6}$$

The above equation implies that the motor only provides the necessary power to generate the permeate flow rate; the remainder of the hydraulic power output from the pump is recaptured by the ERD.

The proposed device could provide several advantages for small-scale RO applications. First, the system is rotary and operates continuously to decrease complexity. In contrast, the Clark Pump is a linear piston-based fixed-recovery mechanism that requires a complex secondary hydraulic circuit to periodically reverse the piston's direction of travel [11, 12]. Second, the proposed device can be directly coupled to an electric motor, thereby eliminating the need for an additional feed or booster pump. Finally, the geometries of the positive displacement stages dictates the system's production rate and recovery ratio, thus minimizing the need for manual tuning. To verify technical feasibility, we first use a detailed model to explain the performance

of fixed-recovery architectures in general. Then, we evaluate the performance for two specific choices for the positive displacement mechanism: gears and sliding vanes (Fig. 4-2).

4.3 Detailed Model of Fixed-Recovery Systems

For an ideal fixed-recovery system, the previous section showed that the flow rate, recovery, and energy savings are strictly a function of geometry. However, there are two types of parasitic losses that will cause the actual performance to diverge from these ideal expectations. Volumetric loss, or slip, is the leakage that detracts from the flow that the positive displacement device is geometrically designed to deliver. This leakage is driven by the pressure difference across the device. Slip decreases the pump's supply so that the actual feed flow rate is less than the ideal rate ($Q_f^{act} < Q_f^{id}$), but raises the ERD's discharge so that the actual brine flow rate is greater than the ideal rate ($Q_b^{act} > Q_b^{id}$). Separately, mechanical losses such as friction affect the conversion between mechanical and hydraulic power. These losses raise the input torque needed by the pump and decrease the output torque produced by the ERD.

A hierarchical model was applied to simulate these losses and assess their impact on the productivity and energy consumption of the desalination process (Fig. 4-3). The upper tier of this model evaluates the operating point of the system due to the coupled behaviour of the three sub-systems (pump, ERD, and RO train), while the intermediate tier models their individual behavior. These subsystem models (Table 4.1) apply to all positive-displacement mechanisms arranged in the same fixed-recovery configuration. Finally, the lowest tier accounts for how the operating parameters and the specific mechanism type, geometry, and size affect subsystem performance. At this layer, additional models for the displacement per shaft revolution d, slip flow rate Q_s, and friction torque T_f are required. As these are specific to mechanism type, gears and vanes are treated separately in Sections 4.4 and 4.5, respectively. The following subsections detail the other modules comprising this approach.

Table 4.1: **Summary of equations used to model the pump, ERD, and RO train subsystems**

	Descriptions	**Equations**
Pump (Stage I)	Energy balance: Input mechanical power from the motor and ERD is converted to the actual output hydraulic power and losses to slip and friction.	$(T_M + T_{ERD})\omega = P_f Q_f^{act} + P_f Q_s^I + T_{fr}^I \omega$
	Ideal flow rate equals the product of displacement and rotational speed.	$Q_f^{id} = \omega d^I/(2\pi)$
	Mass balance: Actual flow rate is less than the ideal flow rate by the slip flow rate.	$Q_f^{act} = Q_f^{id} - Q_s^I$
	Volumetric efficiency is the ratio of actual flow rate to ideal flow rate.	$\eta_v^I = Q_f^{act}/Q_f^{id}$
	Mechanical efficiency is the ratio of useful torque to total input torque.	$\eta_m^I = (T_M + T_{ERD} - T_{fr}^I)/(T_M + T_{ERD})$
ERD (Stage II)	Energy balance: Output ERD power is converted from actual input hydraulic power minus losses to slip and friction.	$T_{ERD}\omega = P_b Q_b^{act} - P_b Q_s^{II} - T_{fr}^{II}\omega$
	Ideal flow rate is the product of displacement and rotational speed.	$Q_b^{id} = \omega d^{II}/(2\pi)$
	Mass balance: Actual flow rate exceeds the ideal flow rate by the slip flow rate.	$Q_b^{act} = Q_b^{id} + Q_s^{II}$
	Volumetric efficiency is the ratio of ideal flow rate to actual flow rate.	$\eta_v^{II} = Q_b^{id}/Q_b^{act}$
	Mechanical efficiency is the ratio of output torque to total useful torque.	$\eta_m^{II} = T_{ERD}/(T_{ERD} + T_{fr}^{II})$
RO Train	Membrane area is specified to provide the target flux at ideal permeate flow rate.	$S = Q_p^{id}/J_w^{id}$
	Maximum recovery occurs when feed pressure converges with brine osmotic pressure	$P_f = \pi_b = \pi_f/(1 - r_{max})$
	Constitutive RO equation relating actual recovery to membrane properties and operating parameters	$r^{act}(1 - r_{max}) - (1 - r_{max})^2 \ln\left(1 - r^{act}/r_{max}\right) = A_m \pi_f S/Q_f^{act}$
	Permeate flow rate is the product of recovery and feed flow rate	$Q_p^{act} = r^{act} Q_f^{act}$
	Mass balance: Brine flow rate is the difference between feed and permeate flow rates	$Q_b^{act} = Q_f^{act} - Q_p^{act}$
	Negligible feed channel pressure drop is assumed	$P_b = P_f$

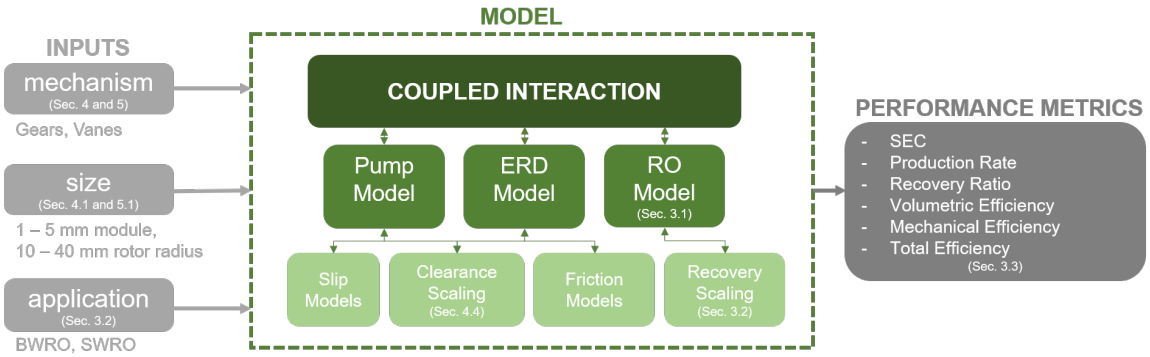

Figure 4-3: **Flowchart highlighting the overall process by which the fixed recovery system was modeled and evaluated.** Additional details regarding specific modules are provided in the bracketed sections.

4.3.1 Reverse Osmosis (RO) Model

The single-stage RO model, which was previously derived in Chapter 3 by integrating the permeate flux through the length of the RO train, and validated against experimental data compiled from literature, relates recovery ratio to feed pressure given solution and membrane properties. This model notably assumes zero pressure drop in the feed channel and does not account for concentration polarization. These simplifications are deemed acceptable since the present focus is to assess pump and ERD performance.

As the pump and ERD increase in capacity, so should the membrane area. Therefore, for each combination of pump and ERD that was simulated, the corresponding RO membrane area S was specified such that the ideal permeate flow Q_p^{id} from that pump-ERD combination (Eqn. 4.3) would provide a target flux J_w^{id}. Therefore, the membrane area S changes to match the size of the process being simulated.

4.3.2 Application

The fixed-recovery device's performance was evaluated under typical brackish water (BWRO) and seawater reverse osmosis (SWRO) conditions. The two applications were differentiated as summarized in Table 4.2. Note that recovery ratio was specified to increase with BWRO permeate capacity as per the trend observed in compiled data

Table 4.2: **Simulated process parameters and membrane properties for BWRO and SWRO applications**

Parameter	BWRO	SWRO
Feed Osmotic Pressure, π_f [bar]	3	30
Membrane Water Permeability, A_m [L/m^2-h-bar] [13, 14]	5	1
Target Permeate Flux, J_w^{id} [L/m^2-h] [15]	25	15
Ideal Recovery Ratio, r^{id}	0.17 log $\left(Q_p^{id}/Q_0\right)$; $Q_0 = 0.0028$ m^3/h (Fig.4-4)	0.40

(Fig. 4-4). This trend occurs because an increase in RO process capacity is achieved by increasing the number of RO membrane elements. Each of these elements is designed to recovery a maximum of 12-19% of its individual incoming feed flow [15]. Therefore, adding more membranes in series enables higher overall recoveries. This relationship is important to consider because as recovery increases, the fraction of the total input hydraulic power carried by the brine stream decreases. However, similar recovery versus production rate data for small-scale SWRO are sparse; therefore, a fixed target recovery of 40% was assumed for that case. As will be seen later (Sec. 4.7.3), this assumption does not change the outcomes on SWRO feasibility.

4.3.3 Performance Metrics

Performance was evaluated using efficiencies, productivity losses, and specific energy consumption. These are defined as follows.

Efficiencies

Volumetric and mechanical efficiencies characterize the relative magnitude of the two parasitic losses discussed previously. Volumetric efficiency η_v is a measure of the slip flow as a ratio of the ideal flow while mechanical efficiency η_m is a measure of frictional losses relative to the ideal input (pump) or output (ERD) power.

The mechanical and volumetric efficiencies for the pump stage are defined in Table

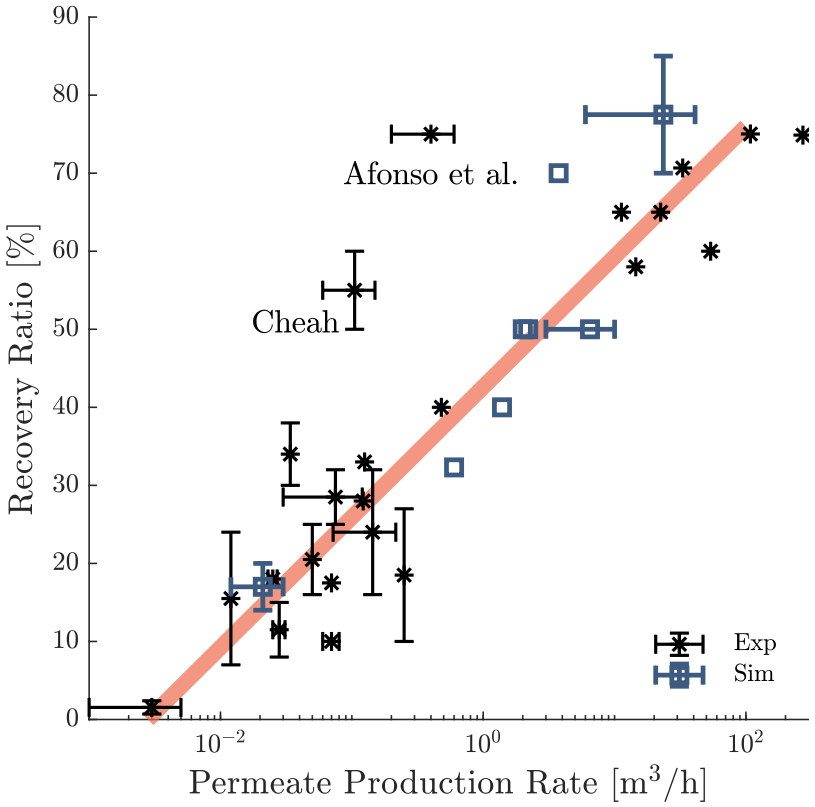

Figure 4-4: **Larger BWRO systems enable higher recoveries.** Plotted data are measured [16–35] and simulated [36–42] recovery ratios from continuous BWRO systems of varying capacities. The fitted red line indicates a logarithmic increase in recovery with increasing permeate production capacity. The systems built by Cheah [22] and Afonso et al. [32] are outliers. The former suffered from calcium-sulfate scaling while the latter was an experimental system operated below the manufacturer's feed flow requirements due to pump limitations. Hence, both fall outside the recommended operation for long-term reliability.

4.1. Substituting them into the energy balance gives

$$\eta_m^I \eta_v^I (T_M + T_{ERD})\omega = P_f Q_f^{act}, \tag{4.7}$$

which captures the non-ideal conversion of input mechanical power to output hydraulic power. Following the same process for the ERD stage gives

$$T_{ERD}\omega = \eta_m^{II} \eta_v^{II} P_b Q_b^{act}, \tag{4.8}$$

because the input hydraulic power is only partially converted to output mechanical

power. Note that both efficiencies affect power losses, therefore the total efficiency for either stage is

$$\eta = \eta_m \eta_v. \tag{4.9}$$

Productivity Losses

As discussed previously, slip will decrease the feed flow rate while increasing the brine flow rate. These losses will impact desalination productivity by causing the permeate production rate and recovery to both decrease. Therefore, while the ideal recovery r^{id} is determined by the displacement ratio or ideal flow rates (Eqn. 4.4, the system's actual recovery ratio based on actual flow rates is

$$r^{act} = 1 - \frac{Q_b^{act}}{Q_f^{act}}. \tag{4.10}$$

Substituting the volumetric efficiency definitions from Table 4.1 relates the two recovery definitions, giving

$$r^{act} = 1 - \frac{1}{\eta_v^I \eta_v^{II}} \frac{Q_b^{id}}{Q_f^{id}} = 1 - \frac{(1 - r^{id})}{\eta_v}, \tag{4.11}$$

where $\eta_v = \eta_v^I \eta_v^{II}$ is the device's overall volumetric efficiency.

Specific Energy Consumption

The specific energy consumption SEC is evaluated at the actual permeate flow rate Q_p^{act}. Therefore,

$$SEC^{act} = \frac{T_M \omega}{Q_p^{act}}. \tag{4.12}$$

This energy consumption is compared to three benchmarks. The first is the the minimum specific energy SEC^{min} to produce the same permeate flow rate at the same recovery, where

$$SEC^{min} = P_f. \tag{4.13}$$

This lower-bound represents the minimum SEC achievable with ideal pumping and energy recovery. The second benchmark is

$$SEC^{pmin} = \frac{P_f}{r^{act}}, \tag{4.14}$$

which is the minimum SEC with ideal pumping, but without energy recovery. Finally, we can compare against the SEC with non-ideal pumping,

$$SEC^{p} = \frac{P_f}{\eta_p r^{act}}, \tag{4.15}$$

where η_p is the pump's total efficiency. Equations 4.12-4.15 do not account for the motor efficiency. Losses at the motor will further raise energy consumption.

4.4 Gear Mechanism Geometry and Models

To simulate the performance of a gear mechanism within the proposed fixed-recovery architecture, we first specify a representative geometry. Then, for that geometry, we model the displacement, slip flow, and friction torque.

4.4.1 Geometry

The assumed gear mechanism geometry (Fig. 4-5) is parametrically defined (Table 4.3) with respect to the gear module m, a measure of the gear tooth size that prescribes the mechanism's physical scale. A larger gear module represents a larger device. Specifying the geometry in this manner facilitates rescaling the design for varying permeate capacities. The ideal recovery ratio for a pump-ERD combination is then dictated by the width W^{II} of the ERD stage relative to the width of the pump stage W^{I} while the rest of the geometry is kept equal.

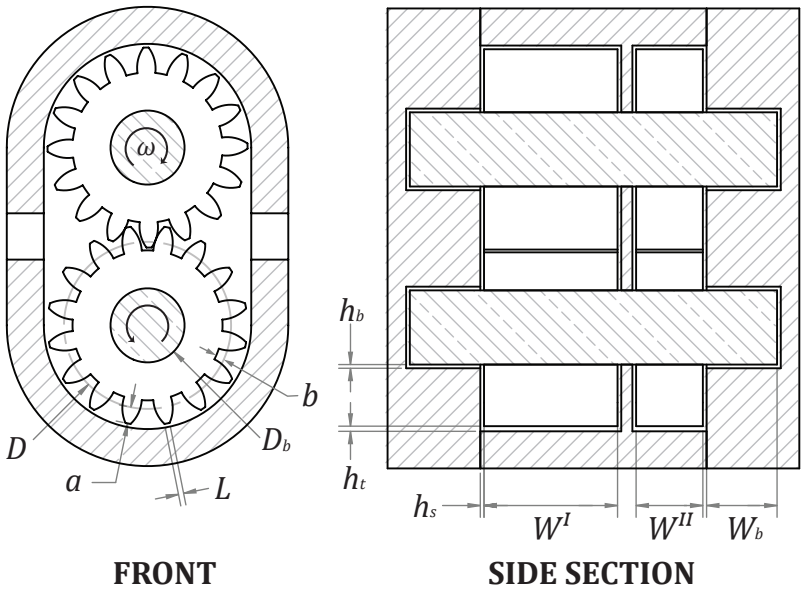

Figure 4-5: **Gear mechanism geometry and clearances.** Marked variables are defined in Table 4.3

4.4.2 Displacement

Recall that the displacement d is the volume of fluid transported from the inlet to the outlet of each positive displacement stage per rotation of the shaft under zero pressure differential. For gears, the total displacement has two contributions,

$$d = d_g + d_t. \tag{4.16}$$

The geometric displacement d_g is the volume displaced within the gaps between the gear teeth, given by

$$d_g = 2\pi m^2 W \left(N + 1 - \frac{\pi^2 \cos^2(\alpha)}{12} \right) [44]. \tag{4.17}$$

The Couette displacement d_t, where

$$d_t = W R_a h_t, \tag{4.18}$$

is the volume dragged by the gear teeth through the radial clearance h_t with the housing through the action of viscosity.

Table 4.3: **Parametric geometry of the simulated gear mechanism.** The same geometry applies to both pump and ERD stages unless specified.

Parameter	**Value**
Number of Teeth, N	14
Gear Pitch Diameter, D	mN
Pump Stage Gear Width, W^I	$12m$
ERD Stage Gear Width, W^{II}	$W^I(1-r^{id})$
Pressure Angle, α	20^o
Gear Addendum, a	m
Gear Dedendum, b	$1.25m$
Gear Tooth Width, W_t	$\pi D/(2N)$
Addendum Radius, R_a	$D/2+a$
Gear Tip Length, L	$m(\pi-4\sin(\alpha))/2$
Bearing Diameter Ratio, β	0.4
Bearing Diameter, D_b	βD
Bearing Width, W_b	D_b
Nominal Efficiency, η_0	0.9
Bearing Clearance, h_b	$0.0015D_b$ [43]
Tip Clearance, h_t	see Sec. 4.4.4
Side Clearance, h_s	see Sec. 4.4.4

4.4.3 Slip Flow

The pressure difference ΔP across each stage drives a total slip flow Q_s approximated by

$$\begin{aligned} Q_s = 2\left(C_d\sqrt{\frac{4\Delta P}{\rho N}}Wh_t\right) + 8\left(\frac{1}{24\mu}\Delta P(1-\beta)h_s^3\right) \\ + 2\left(\frac{1}{6\mu}\frac{\Delta P}{\pi D_b/2}W_b h_b^3\right) + 4\left(\frac{1}{12\mu}\frac{\Delta P}{W_t N/2}(a+b)h_s^3\right), \end{aligned} \tag{4.19}$$

where μ and ρ are the viscosity and density of water and all geometry parameters (N, W, W_b, D_b, β, a, b, h_s, h_t, and h_b) are defined in Table 4.3. The terms in Eqn. 4.19 represent the slip past the tips of the gear teeth, across the gear faces, across the sides of the gear teeth, and through the hydrodynamic bearing, respectively. These paths are depicted later on Fig. 4-12C. Slip through the backlash between the two meshing gears is neglected for being small with respect to the other contributions [45]. The slip past the gear teeth tips was treated as an orifice flow with a discharge

coefficient of $C_d = 0.6$ while the other contributions were derived from lubrication theory. The Reynolds numbers evaluated for these flows justify this treatment for the BWRO pressures, but the flow across the teeth sides transitions to being turbulent at SWRO pressures.

4.4.4 Clearance Scaling

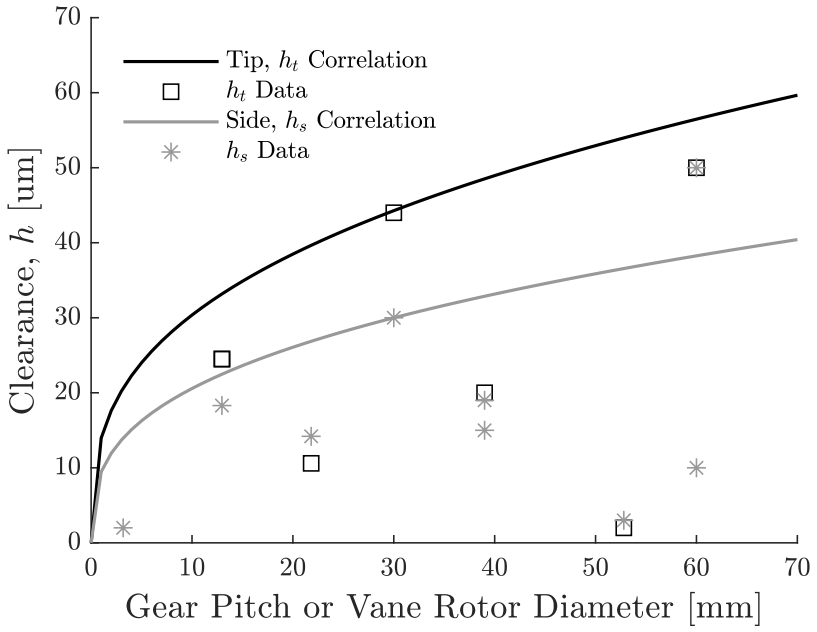

Figure 4-6: **Side and tip clearances change non-linearly with the size of the mechanism.** Curves represent the assumed conservative correlation (Eqn. 4.20) to the gear pitch diameter or vane rotor diameter, while points represent sparse clearance data from experimental and analytical studies of gear [45–54] and vane pumps [8, 55–57].

In addition to the bearing clearance h_b defined in Table 4.3, slip flows are also sensitive to the side h_s and tip h_t clearances (Eqn. 4.19). Poor data availability prevents accurate characterization of these clearances and how they vary with device size. Therefore, the approach taken was to fit a conservative upper-bound estimate to available data (Fig. 4-6). The fitting function used for side and tip clearances was

$$h = 10^{0.2(ITG-1)} \left(0.45 D^{1/3} + 0.001 D\right). \tag{4.20}$$

It was adopted from the International Tolerance Grades (ITG) standard which is an established reference for tolerances achievable by various manufacturing processes, for a given dimension D. ITG grades of 7.6 and 8.5 were used to bound the available side and tip clearance data using the gear pitch diameter and vane rotor diameter as reference dimensions. These fitted coefficients relate to processes that are commonly used to manufacture gear and vane pumps (turning, boring, and reaming processes), thereby justifying this approach.

These scaling correlations suggest that clearances do not scale linearly with mechanism size. As will be shown in Sec. 4.7, the consequence is that larger devices are more efficient, a trend consistent with real systems.

4.4.5 Friction Torque

Viscous drag from the four slip sources identified in Sec. 4.4.3 respectively contribute to a friction torque T_{fr} in each stage that is

$$\begin{aligned} T_{fr} = {} & 2\left(\frac{\mu\omega R_a^2 WLN}{2h_t}\right) + 4\left(\frac{\pi\mu\omega D^4(1-\beta)^4}{32h_s}\right) \\ & + 2\left(\frac{\mu_b \Delta P D W D_b}{2}\right) + 4\left(\frac{\mu\omega R^2 W_t(a+b)N}{h_s}\right) \\ & + (1-\eta_0)\, T_0. \end{aligned} \tag{4.21}$$

The first two terms were derived by integrating the viscous shear stresses acting on the gear teeth and along the gear faces. The third term is the bearing friction due to the pressure difference across the gears. We elaborate further on this term in Sec. 4.5.5. The last term represents other losses, for example due to shaft misalignment, friction against seals, and sliding gear teeth contact. These losses detract from the nominal torque output of the ERD and increase the torque required at the pump, so

$$T_0 = \begin{cases} T_{ERD} \text{ for the ERD, and} \\ T_M + T_{ERD} \text{ for the pump.} \end{cases} \tag{4.22}$$

4.4.6 Gear Model Validation

The models above were validated by comparing resulting efficiencies against empirical correlations fitted by Michael et al. [58] (Fig. 4-7). The geometry (Table 4.3) and clearances (Fig. 4-6) assumed for this comparison are the same as used in the feasibility analysis. The correlations fit volumetric and mechanical efficiency measurements performed using oil on sixteen gear pumps from different manufacturers whose displacements ranged from 31.8 - 56.5 cm^3. Modeled displacements that match this displacement range (open circles) are differentiated from those that do not (points) because efficiency is size-dependent. Smaller pumps tend to be less efficient.

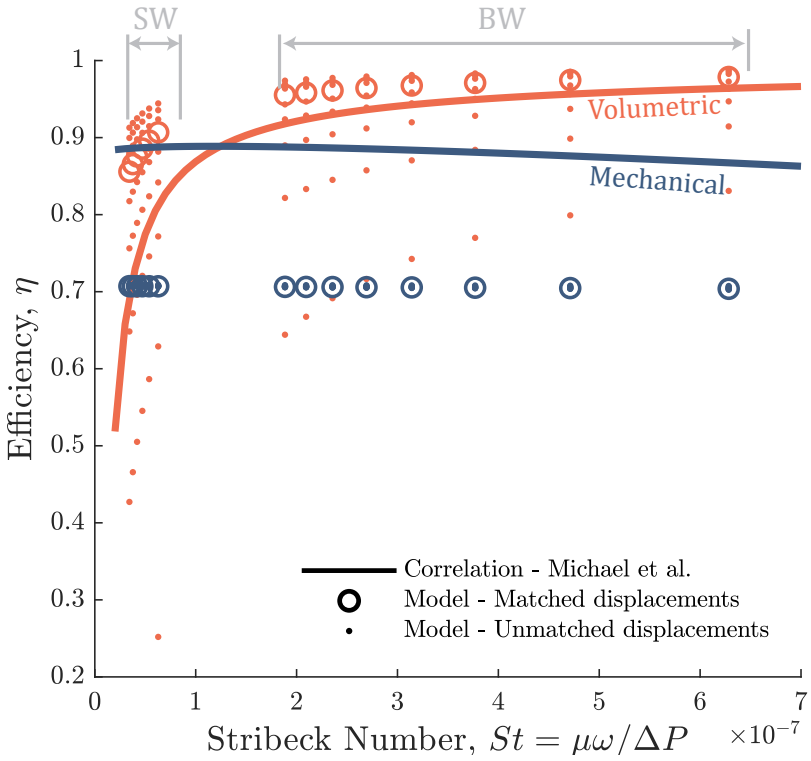

Figure 4-7: **Model predictions of gear mechanism efficiencies were compared to experimentally-derived correlations from Michael et al.** [58]. Modeled conditions span 1 - 5 mm gear modules, pressure differences of 3-10 bar for BWRO and 30-55 bar for SWRO, and a fixed 1800 RPM rotational speed. Modeled mechanisms matching the 31.8 - 56.5 cm^3 displacement range tested by Michael et al. are represented as open circles; others are represented as points.

When displacements are matched, the simulated volumetric efficiency exceeds the empirical correlation. For the BWRO regime, the error is within the scatter observed

in the source data (not reproduced in Fig. 4-7). The error is greater in the SWRO regime likely because some slip flow rates increase as they transition from being laminar to turbulent. In contrast, simulated mechanical efficiencies are lower than suggested by the experimental correlation at all pressures. We model increased friction at the bearings due to the poor lubrication properties of water versus oil; therefore, a lower mechanical efficiency is expected. Overall, this comparison indicates that the model estimates realistic pump efficiencies for BWRO operation, but optimistic efficiencies for SWRO. The same conclusions apply for the ERD stage since identical models for slip flow and friction torque are used for both stages.

4.5 Vane Mechanism Geometry and Models

This section details the geometry and models that were used to simulate the performance of the sliding vane mechanism. The approach detailed here borrows from the methods applied by Al-Hawaj [59] and Ye et al [10] in their analyses of sliding vane ERDs. The key differences are that we parametrize the geometry to investigate the impact of size, and the assumed clearances are informed by manufacturing considerations (Sec. 4.4.4).

4.5.1 Geometry and Material Properties

The assumed vane mechanism geometry (Fig. 4-8) is defined in Table 4.4 with respect to the rotor radius R_r. The same table also summarizes the material properties used to evaluate sliding friction between moving parts. Here, the vanes and stator are assumed to be manufactured from graphite while the rotor and shaft are assumed to be steel components. The same combination is often used in small water vane pumps.

4.5.2 Kinematic Relationships

Kinematic relationships are drawn to evaluate the displacement and vane dynamics. From the cosine law, the distance R from the rotor center to the stator-vane contact

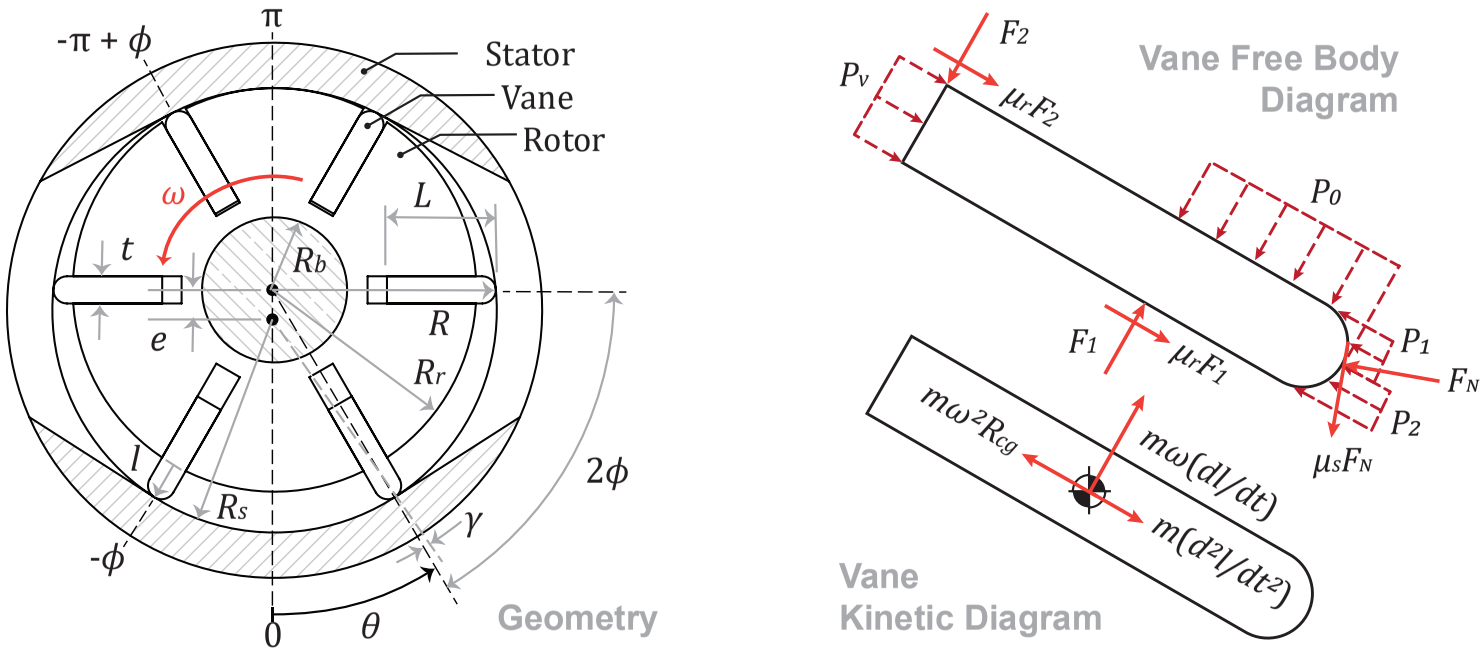

Figure 4-8: **Sliding vane mechanism geometry and dynamics.** Key parameters defining the rotor, stator, and vane are geometry shown on the left and quantified in Table 4.4. Vane forces and accelerations are shown on the right. Dashed arrows represent pressures, while solid arrows represent forces.

Table 4.4: **Vane mechanism geometry and frictional properties.** The same geometry and friction coefficients are used in both pump and ERD stages unless otherwise specified.

Parameter	**Value**
Number of Vanes, N	6
Pump Stage Rotor Width, W^I	R_r
ERD Stage Rotor Width, W^{II}	$R_r^I(1-r^{id})$
Vane Length, L	$0.6R_r$
Vane Thickness, t	$0.15R_r$
Eccentricity, e	$0.75t$
Stator Radius, R_s	$R_r + e$
Vane Density, ρ	2200 kg/m^3
Rotor-Vane Friction Coefficient, μ_r	0.15
Stator-Vane Friction Coefficient, μ_s	0.15
Bearing-Shaft Friction Coefficient, μ_b	0.05
Shaft-to-Rotor Radius Ratio, β	0.4
Bearing Radius, R_b	βR_r
Bearing Width, W_b	$2R_b$
Nominal Efficiency, η_0	0.9
Bearing Clearance, h_b	$0.0015D_b$ [43]
Side Clearance, h_s	see Sec. 4.4.4

point varies as

$$R^2 = R_s^2 - e^2 + 2eR\cos\theta, \tag{4.23}$$

where e, R_s, and θ are the eccentricity, stator radius, and angular vane position, respectively (Fig. 4-8). Then, the vane extension l past the rotor radius R_r is

$$l = R - R_r. \tag{4.24}$$

Table 4.5: **Pressures acting on the vane through one rotation within the stator.** P_h is the high pressure at the pump outlet and ERD inlet. P_l is the low pressure at the pump inlet and ERD outlet.

For θ from:	$-\pi+\phi$	$-\phi$	ϕ	$\pi-\phi$
to:	$-\phi$	ϕ	$\pi-\phi$	$-\pi+\phi$
Actuation Pressure, P_v	P_h	P_l	P_h	P_h
Face Pressure, P_l	P_h	P_l	P_l	$-P_l$
Tip-Leading Pressure, P_1	P_l	P_h	P_h	P_l
Tip-Trailing Pressure, P_2	P_l	P_l	P_h	P_h

Likewise, the distance from the rotor center to the vane center of gravity is approximately

$$R_{cg} = R - \frac{L}{2}, \tag{4.25}$$

where L is the vane length. Applying the cosine law also gives that the stator-vane contact angle γ is

$$\cos\gamma = \frac{R^2 + R_s^2 - e^2}{2RR_s}, \tag{4.26}$$

4.5.3 Displacement

The ideal volume displaced per shaft revolution is

$$d = WN\left(\int_0^{\phi}\left(R^2 - R_r^2\right)d\theta - (R - R_r)t\right), \tag{4.27}$$

where W is the depth of the stage, N is the number of vanes, and half the angle between two adjacent vanes ϕ (Fig. 4-8) is

$$\phi = \frac{\pi}{N}. \tag{4.28}$$

4.5.4 Slip Flow

The pressure difference ΔP drives slip through three major pathways: past the sides of the vanes, past the face of the rotor, and through the radial bearing. These contributions are respectively modeled as

$$Q_s = 2\left(C_d\sqrt{\frac{2\Delta P}{\rho}}(2h_s e)\right) + 4\left(\frac{1}{24\mu}\Delta P(1-\beta)h_s^3\right) + 2\left(\frac{1}{6\mu}\frac{\Delta P}{\pi R_b}W_b h_b^3\right), \tag{4.29}$$

where all geometry parameters (e, R_b, W_b, h_b, β and h_s) are all defined in Table 4.4. The slip past the vane sides was treated as an orifice flow with a discharge coefficient of $C_d = 0.6$, while the other contributions are due to Poiseuille flow through the side h_s and bearing h_b clearances.

4.5.5 Friction Torque

The total friction torque for each stage is

$$\begin{aligned} T_{fr} = & \frac{N}{2}\left(\frac{2\mu\omega t R_r^3}{3h_s}\right)\left(\frac{e}{R_r}\left(5\frac{e}{R_r}^2 + 9\frac{e}{R_r} + 6\right)\right) \\ & + 2\left(\frac{\pi\mu\omega R_r^4(1-\beta)^4}{2h_s}\right) + \mu_b \Delta P (2R_s W) R_b + T_{fr,vr} \\ & + T_{fr,vs} + (1-\eta_0)\, T_0. \end{aligned} \tag{4.30}$$

The first two terms relate to viscous drag on the vane sides and rotor faces, respectively. These were derived by integrating the viscous shear stresses acting on those surfaces due to Couette flow within the axial clearance between the rotor and the housing. The third term is the friction torque at the radial bearing due to the net pressure forces acting on the rotor from the high pressure side. The approximate Stribeck number calculated for those bearings at BWRO pressures is

$$St = \frac{\mu\omega}{P_b} = \frac{\mu\omega R_r W_b}{\Delta P R_s W_s} = \frac{2\mu\omega\beta^2}{\Delta P} \approx 5 \times 10^{-8}, \tag{4.31}$$

where P_b is the average pressure acting on the bearing. Since this number does not exceed the value of 1.7 x 10^{-6} typically recommended for full-film lubrication [60], we assume mixed-lubrication conditions and use a mid-range wet friction coefficient of $\mu_b = 0.05$ from data provided by Morgan Advanced Materials for their carbon graphite bearings [61]. The forth and fifth terms in Equation 4.30 are due to sliding friction where the vane contacts the rotor and stator, respectively. These are derived by resolving the vane dynamics as described in the following subsection. Finally, the last term captures other minor losses such as friction at the mechanical seals and shaft misalignment as discussed in Section 4.4.5.

4.5.6 Vane Dynamics

Referring to Figure 4-8, the force and moment balances used to solve for the unknown rotor-vane and stator-vane contact forces F_1, F_2, and F_N for each stage are

$$\begin{bmatrix} 1 & -1 & -\sin\gamma - \mu_s \cos\gamma \\ -\operatorname{sgn}(u)\mu_r & -\operatorname{sgn}(u)\mu_r & \mu_s \sin\gamma - \cos\gamma \\ -l - \frac{1}{2}\operatorname{sgn}(u)\mu_r t & L + \frac{1}{2}\operatorname{sgn}(u)\mu_r t & 0 \end{bmatrix} \begin{bmatrix} F_1 \\ F_2 \\ F_N \end{bmatrix} = \begin{bmatrix} 2m\omega u + P_0 l W \\ m\frac{du}{dt} - m\omega^2 R_{cg} - tb(P_v - \frac{1}{2}P_1 - \frac{1}{2}P_2) \\ -m\omega u L - \frac{1}{2}P_0 W l^2 - \frac{1}{8}W t^2 (P_1 - P_2) \end{bmatrix}, \tag{4.32}$$

where μ_r and μ_t are the rotor-vane and stator-vane friction coefficients, respectively. Pressures acting on the vane take either the high pressure P_h or low pressure P_l values depending on the vane's angular position θ (Table 4.5). In this study, we assume that the low pressure side is at atmospheric pressure and that the high pressure is feed pressure P_f for both pump and ERD stages.

The vane extension velocity u is related to the angular rotation speed ω through

$$u = \frac{dl}{dt} = \omega \frac{dl}{d\theta}. \tag{4.33}$$

Multiplication by the sign of u in Equation 4.32 accounts for the change in direction of the rotor-vane friction force during vane retraction. Using the resolved forces, the average friction torques caused by all N vanes sliding against the rotor and stator are calculated from numerically integrating the total power loss through one rotation:

$$T_{fr,vr} = \frac{N}{2\pi} \int_0^{\Gamma} u\mu_r \left(\operatorname{sgn}(F_1)F_1 + \operatorname{sgn}(F_2)F_2\right) dt \text{ and} \tag{4.34}$$

$$T_{fr,vs} = \frac{N}{2\pi} \int_0^{\Gamma} u_t \mu_t F_N dt. \tag{4.35}$$

Γ is one rotation period and the vane tip velocity tangential to the stator u_t is

$$u_t = \omega R_r cos(\gamma). \tag{4.36}$$

4.5.7 Vane Model Validation

To verify that modeled volumetric and mechanical efficiencies are practical, comparison was drawn against the manufacturer-specified performance of three vane pumps intended for water applications (Fig. 4-9).

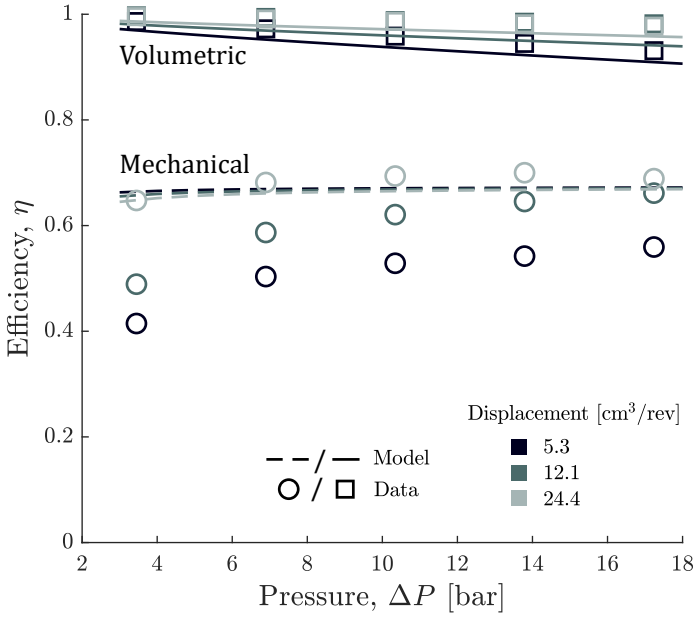

Figure 4-9: **Validation of predicted slip and friction characteristics of the unbalanced vane mechanism.** Mechanical and volumetric efficiencies at 1725 RPM for three Procon sliding vane pumps (Series 2 140 GPH, Series 4 330 GPH, and Series 6 660 GPH) are compared against modeled efficiencies for simulated geometries of equal displacements. The simulated geometries have rotor radii of 15.8, 20.8, and 26.3 mm.

Volumetric efficiencies agreed closely while mechanical efficiencies were over-predicted for the smaller pumps. The discrepancy observed in the latter is acceptable when considering that the geometry and vane loading characteristics assumed in this study may differ from those of the actual pumps. Furthermore, pressure-independent friction such as that resulting from seals was not simulated in this study. Inclusion of these terms would decrease the mechanical efficiency at low pressures. Nevertheless,

this comparison shows that the simulated efficiencies are practical at the size-scales investigated in this study.

4.6 Examining Fixed-Recovery System Behavior

Models defined in the Sec. 4.3 are first used to simulate and explain the coupled behaviour of pump, ERD, and RO train. This general behavior applies to all fixed-recovery systems irrespective of the positive displacement mechanism type that is implemented. Then, the specific differences in performance between gears and sliding vanes are examined as a function of application (BWRO vs. SWRO) and system size in the following section.

4.6.1 Visualizing the Coupled Behavior

The fixed recovery architecture couples the behavior of the pump, ERD, and RO train in the manner visualized in Fig. 4-10A. This representation is agnostic to the type of positive displacement mechanism constituting each stage; it describes fixed-recovery architectures in general. Each component is represented by a surface, and the intersection of the three surfaces indicates the operating point of the system. These surfaces would intersect at the *ideal* operating point if the pump and ERD stages were ideal devices with zero slip. In this case, these devices would be represented by vertical planes at their ideal flow rates. However, slip causes less feed to be pumped to the RO train (Fig. 4-10B), while simultaneously allowing more brine to escape through the ERD (Fig. 4-10C). This non-ideal behaviour is represented by pump and ERD surfaces that diverge from the verticals. As a consequence of this non-ideal behavior, the *actual* operating point occurs at a lower feed pressure, production rate, and recovery ratio than the expected ideal operating point. It follows that volumetric efficiency, which relates slip to ideal flow, directly affects the operating point of the system. For the device to produce the intended permeate production rate and recovery ratio, a high volumetric efficiency is required. The precise relationship is quantified in the following sections.

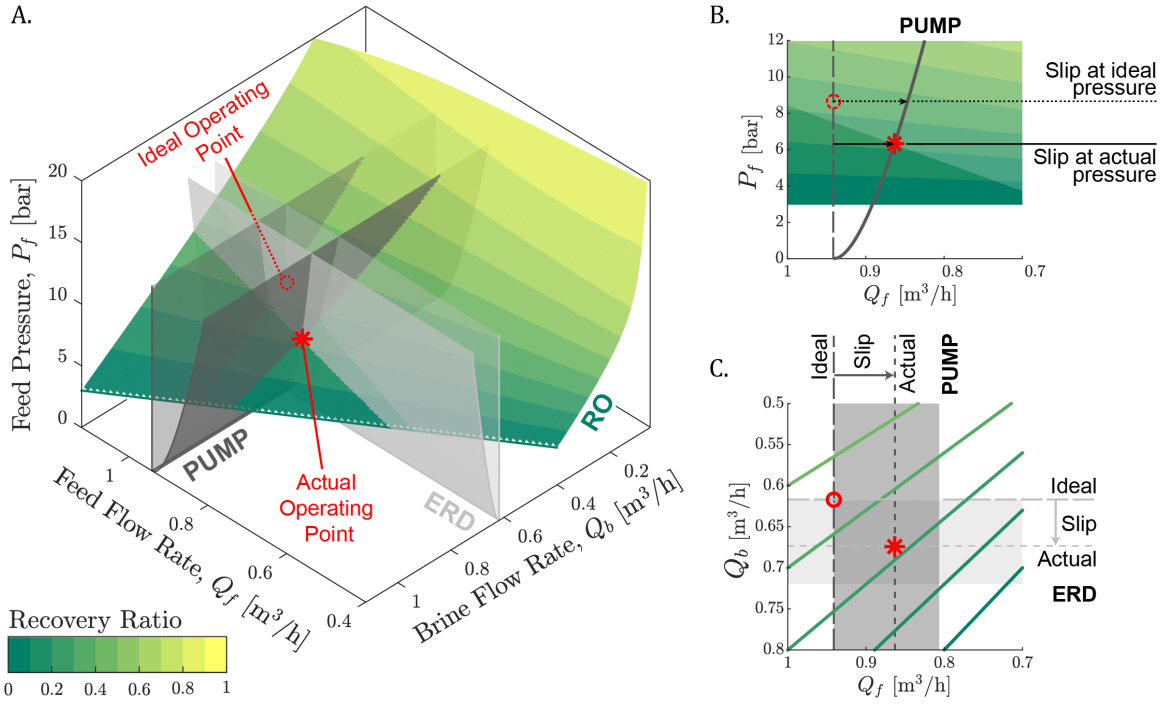

Figure 4-10: **Slip flows in the pump and ERD stages shift the actual operating point to a lower recovery ratio and production rate than the ideal operating point**. (A) The actual operating point occurs at the intersection of the pump ('PUMP'), energy recovery device ('ERD'), and reverse osmosis ('RO') system surfaces. (B) A side view of the pump surface shows slip increasing with feed pressure. This slip decreases the actual feed flow rate relative to the ideal flow rate. (C) This top view shows that while slip decreases feed flow through the pump, it increases brine flow through the ERD. The combination causes the actual recovery to be lower than the ideal recovery. Pump and ERD surfaces were generated for a 2 mm gear mechanism, rotating at 1800 rpm, and designed for 34% recovery. The RO surface was generated using the equations and BWRO parameters provided in Tables 4.1 and 4.2, respectively.

Mechanical efficiency does not impact the operating point in the same direct manner. For certain actuators, such as wind turbines or brushed DC motors, poor mechanical efficiency could raise the required torque and consequently decrease shaft speed. This change in speed would then translate the operating point to lower feed and brine flow rates. This second-order effect is not significant for AC motors, especially if speed is directly controlled using variable frequency drives (VFDs). It is therefore neglected in this feasibility study.

It is also worth noting that RO membrane permeabilities are not constant properties. They will decrease over time due to compaction, scaling, and clogging. These changes would cause the RO surface in Figure 4-10 to be steeper. For the recovery and production rate to be robust to these permeability changes, a high volumetric efficiency is again required.

4.6.2 Recovery Ratio Sensitivity to Volumetric Efficiency

By examining the coupled behavior of the subsystems, it was shown that the pump and ERD volumetric efficiencies affect the extent to which the actual recovery will deviate from the ideal. To understand the extent of this deviation, we plotted the predicted relationship (Eqn. 4.11) at three ideal recovery ratios (Fig. 4-11): 30%, 55%, and 80%. The horizontal lines represent those ideal recoveries while the curves represent the actual recoveries as they vary with volumetric efficiency. The prediction at an ideal recovery of 55% is compared with measurements from Lu et al [8]. Their fixed-recovery vane ERD prototype was configured to provide the same recovery, but the actual recovery decreased with increasing feed pressure. It is seen that Eqn. 4.11 accurately explains the reported deviation of the actual recovery from the ideal recovery with decreasing volumetric efficiency.

By setting r^{act} to zero in Eqn. 4.11, we find that no water is produced below a minimum total volumetric efficiency that is given by

$$\eta_v > 1 - r^{id}. \tag{4.37}$$

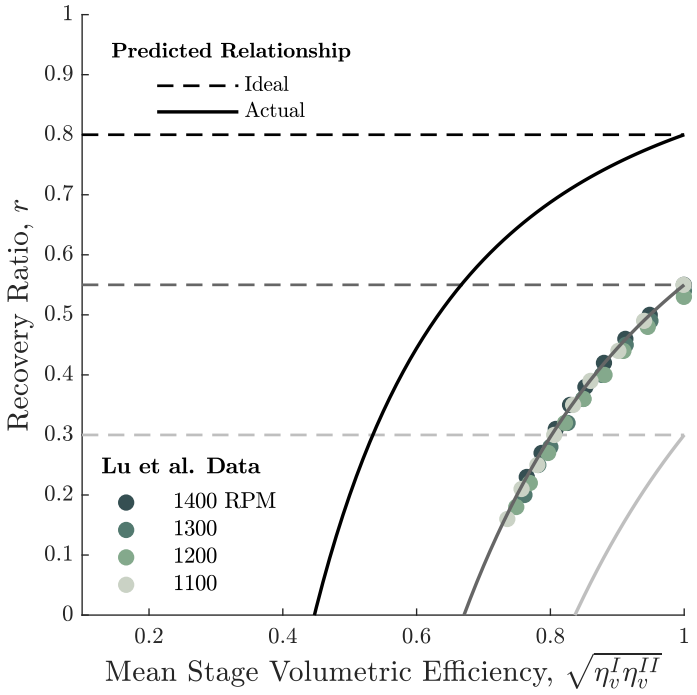

Figure 4-11: **The ideal recovery is determined by displacement ratio, but the actual recovery depends on the volumetric efficiency of both stages.** The dashed lines represent the ideal recovery, while solid lines of the same color represent the actual recovery as a function of volumetric efficiency (Eqn. 4.11). The expected relationship matches vane ERD prototype measurements from Lu et al. [8] at all tested speeds.

This result is non-intuitive because it states that higher volumetric efficiencies are required when targeting lower fixed recovery ratios. For example, a system designed for a 25% recovery must be at least 75% efficient to produce any permeate; however, when targeting 75% recovery, the minimum efficiency is only 25%. This finding explains why piston-based ERDs such as the Clark Pump and Pearson Pump dominate low-capacity and low-recovery applications (Fig. 4-1). Pistons can provide the high volumetric efficiencies that are necessary at the low 7-35% recoveries that those fixed-recovery systems are designed for.

The ability to adjust the displacement of one or both stages would provide control over the ideal recovery. This biasing feature would enable the device to target low recoveries with reduced volumetric efficiencies. For example, a 30% recovery could be enabled at 80% volumetric efficiency (per stage) by adjusting the displacements to artificially target 55% ideal recovery (Fig. 4-11). This solution is not explored

further in this feasibility study, but could be explored as a method to ease volumetric efficiency requirements in low-recovery applications.

This sensitivity analysis reemphasizes the significance of volumetric efficiency. Recall that while both volumetric and mechanical efficiency impact SEC equally (Eqn. 4.7), only the former impacts the operating point. Maximizing volumetric efficiency is therefore critical for minimizing productivity losses in fixed-recovery architectures.

4.7 Comparing Gears and Vanes

Having examined the general behavior of fixed-recovery architectures, this section compares specific implementations with gears versus vanes. The focus is also shifted from an individual configuration of a fixed capacity to a range of configurations with increasing capacities, as represented by larger gear modules and vane rotor radii (Fig. 4-2).

4.7.1 Gear Mechanism BWRO Performance

Considering the BWRO case first, it is clear that productivity losses vary with system size, where the smallest systems have the highest productivity losses (Fig. 4-12A). The smallest simulated geometries (modules of <1.25 mm) do not satisfy the minimum volumetric efficiency requirements for this architecture as dictated by Equation 4.37; therefore, they produce no permeate. However, as the systems increase in size, productivity improves: for 1-5 m^3/h systems, the actual recovery is predicted to be within 85-94% of the ideal recovery. This behavior is related to the pump and ERD volumetric efficiencies, which are plotted for a fixed 10 bar feed pressure through the same range of system sizes (Fig. 4-12B). It is seen that volumetric efficiency improves with increasing system size. The underlying reason is that the ideal flow rate scales as

$$Q_{id} \sim m^3, \tag{4.38}$$

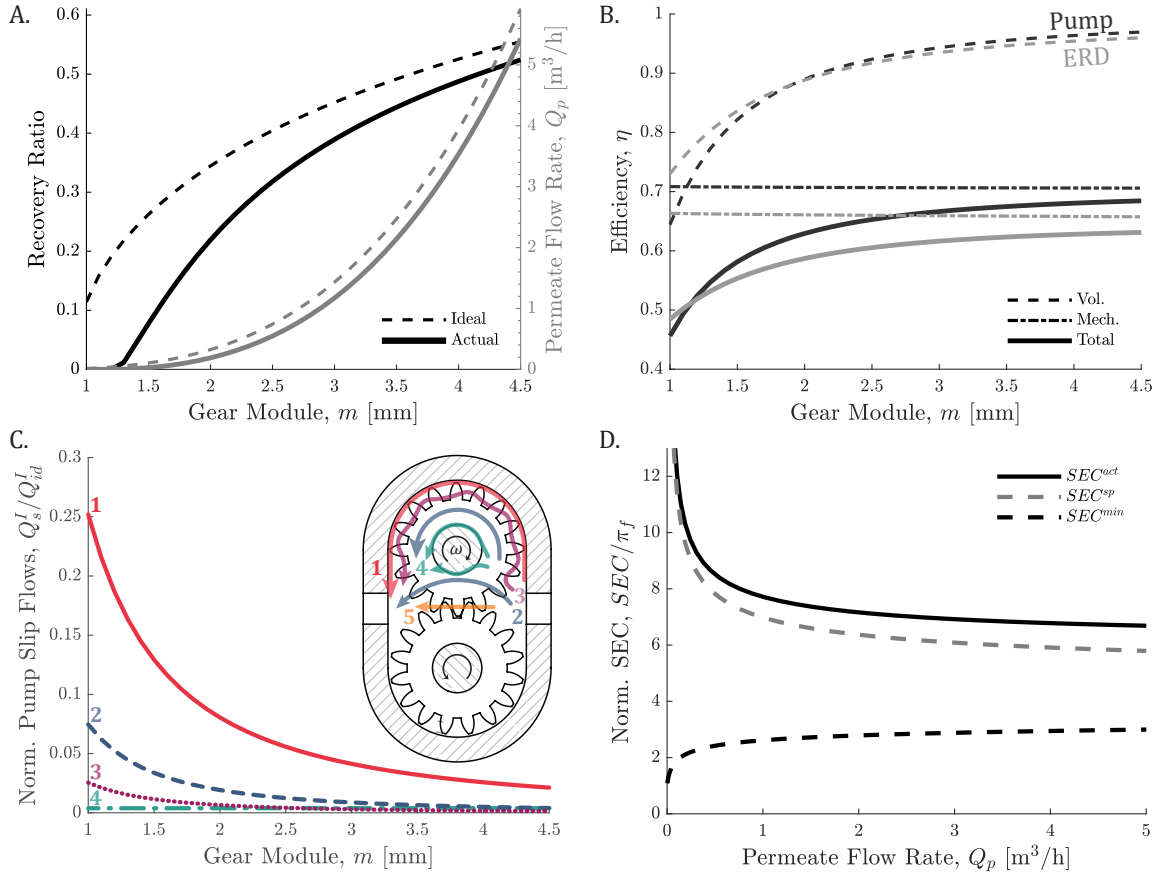

Figure 4-12: **Gear mechanism performance under BWRO conditions.** (A) Actual recovery and permeate production rate are plotted alongside the ideal performance for simulated systems of increasing sizes, as represented by the gear module m. (B) Volumetric, mechanical, and total efficiencies are simulated for systems with increasing gear modules at 10 bar feed pressure and 1800 rpm shaft speed. (C) Pump stage volumetric losses through different slip pathways are plotted under the same conditions, normalized by the ideal flow rate. Colored arrows highlight slip pathways past the gear tips (1), across the gear face (2), across the sides of the gear teeth (3), through the bearing clearance (4), and through the backlash between meshed teeth (5). Note that (5) is neglected in this study for being small with respect to (1)-(4) [45]. (D) At the actual operating conditions presented in subfigure A, the specific energy consumption of the simulated fixed-recovery system SEC^{act} is compared to the minimum achievable energy consumption SEC^{sp} with an ideal pump only, and with both an ideal pump and ERD, SEC^{min}.

from Eqn. 4.17 since the width W is also proportional to the module m (Table 4.3). However the dominant contribution to the slip flow, which occurs past the tips of the gear teeth (Fig. 4-12C), scales at most as

$$Q_{s,t} \sim m^2, \tag{4.39}$$

after accounting for how the clearance scales (Eqn. 4.20) in the slip flow model (Eqn. 4.19). Therefore, the ratio of slip flow to the ideal flow decays as $1/m$, implying that volumetric losses become less significant relative to the displaced flow as the system grows in size. The consequence of this behavior is the observed decrease in productivity losses.

In contrast, mechanical efficiency is insensitive to system size (Fig. 4-12B). The relationship between clearances and system size did not affect the mechanical efficiency because the shearing of water within clearances is a negligible source of friction torque. Instead, bearing friction arising from pressure forces acting on the gears is the dominant loss. Our model additionally prescribed other losses (shaft misalignment, seal friction etc.) to be 10% of ideal torque (Sec. 4.4.5). Together, these two losses fully explain the 70% and 66% mechanical efficiencies predicted for the pump and ERD stages, respectively.

The SEC was evaluated for the simulated systems at the reduced actual production rates and recovery ratios, and compared against benchmarks outlined in Sec. 4.3.3 (Fig. 4-12D). It was found that after accounting for slip and frictional power losses, the addition of the gear ERD stage does not decrease the SEC below the energy consumption of a stand-alone ideal pump. Before addressing the energetic performance however, this evaluation suggests that for gears to be a viable fixed-recovery ERD solution, productivity losses must be first decreased by minimizing slip. Figure 4-12C shows that most of this slip occurs between the gears tips and casing. This contribution could be decreased using two strategies:

1. Finer gear teeth: From Eqns. 4.17 and 4.19, the ratio of tip slip to ideal flow

scales as

$$\frac{Q_{s,t}}{(d)(\omega/(2\pi))} \sim \frac{1/\sqrt{N}}{(m^2 N)(\omega/(2\pi))} \tag{4.40}$$

Therefore, volumetric efficiency can be improved at a constant displacement d by increasing the number of teeth N while decreasing the module m. In practice, increasing the number of teeth increases the resistance to the circumferential flow around the gear.

2. Pressure-compensated housing: Fluid pressure can be used to press a floating casing against the gear teeth to minimize clearances. Using this strategy, Schiffer et al. developed a pump with 1 mm module gears that was capable of volumetric efficiencies as high as 75% at 40-50 bar pressure [44].

Modeling of these strategies could be the focus of future work. In this work, we instead examine the performance of sliding vanes since they are inherently designed to provide higher volumetric efficiencies.

4.7.2 Vane Mechanism BWRO Performance

By providing a sliding seal against the stator (Fig. 4-2), vanes decrease slip and thus provide higher volumetric efficiency relative to gears. The extent to which this higher volumetric efficiency improves performance is examined for the BWRO case in Figure 4-13A. Actual permeate production rate and recovery ratio are now respectively within 89-95% and 91-96% of the ideal values for 1-5 m^3/h systems, relative to 77-92% and 85-94% found previously for gears. Therefore, the higher volumetric efficiency enabled by sliding vanes results in reduced productivity losses.

Comparing Figs. 4-12B and 4-13B, it is seen that the choice between gears and vanes is a trade-off between mechanical and volumetric efficiency. Since volumetric efficiency is more critical to the fixed-recovery architecture examined in this study (Sec. 4.6), vanes are the more suitable choice. However, this improvement in volumetric efficiency is achieved at the expense of decreased mechanical efficiency (Fig. 4-13B). Pump stage mechanical efficiencies of 65-67% were observed for the sliding

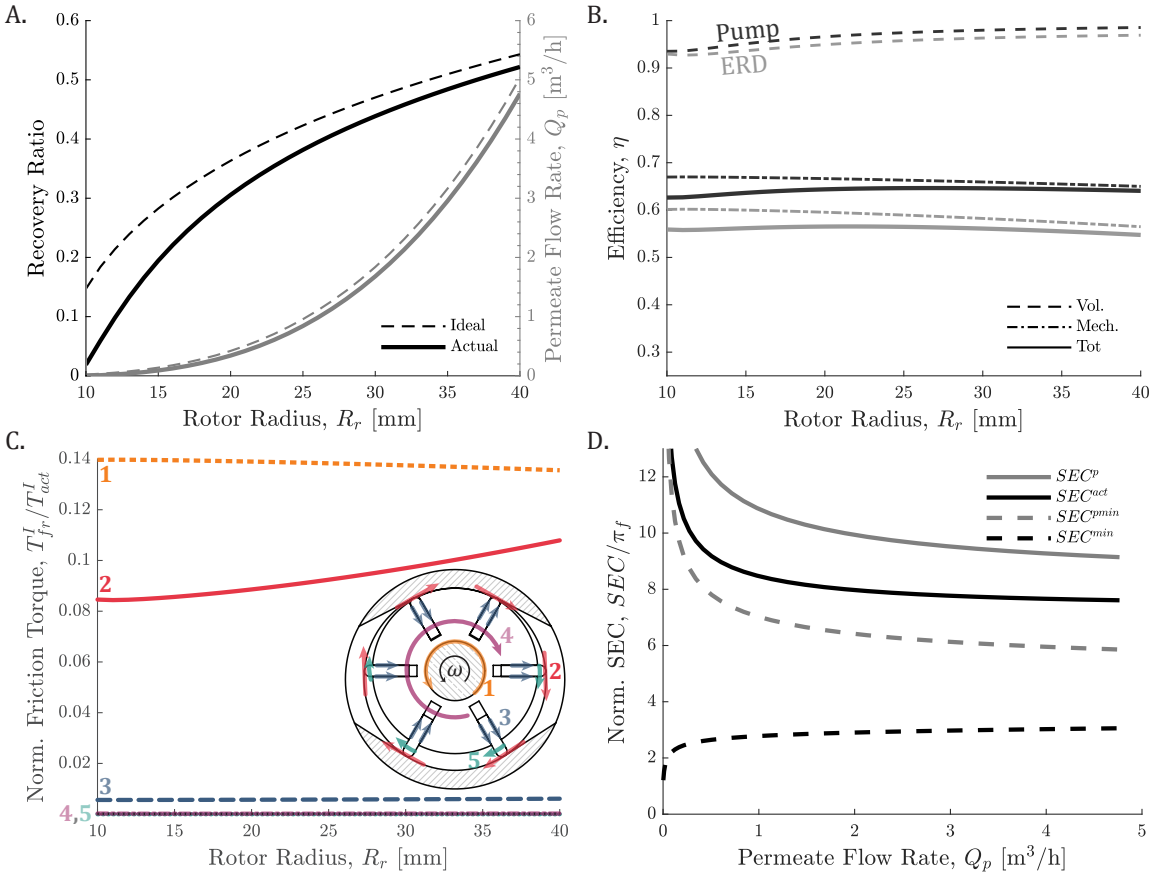

Figure 4-13: **Sliding vane performance under BWRO conditions.** (A) Actual recovery and permeate production rate are plotted with the ideal performance for simulated systems of increasing sizes, as represented by the rotor radius R_r. (B) Volumetric, mechanical, and total efficiency are plotted for those same systems. (C) The various pump mechanical losses are plotted as a fraction of the total pump input torque. Colored arrows highlight friction sources due to bearing friction (1), vane-stator sliding friction (2), vane-rotor sliding friction (3), viscous drag on the rotor (4), and viscous drag on the vanes (5). (D) Efficiencies were used to calculate normalized specific energy consumption SEC^{act} for the simulated device, which is then compared to the minimum energy consumption with and without energy recovery : SEC^{min} and SEC^{pmin}, respectively. Comparison is also made with the energy consumption of a 65% efficient pump without energy recovery SEC^{p}.

vanes versus the 70% observed previously for gears. The most significant mechanical losses are due to bearing friction caused by the pressure loads on the rotor. The next largest source is the vanes sliding against the stator (Fig. 4-13C). Other losses from vane-rotor friction and viscous drag are small in comparison. The observed increase in vane-stator friction is caused by growing centrifugal forces on the vanes since their masses and distances from the center of rotation are both modeled as increasing with system size (Table 4.3). Larger centrifugal forces in-turn produce greater vane-stator contact forces that raise friction. The net result is a decreasing mechanical efficiency. When paired with the increasing volumetric efficiency, the resulting total efficiency is approximately constant at 65% and 55% for the pump and ERD stages, respectively, across simulated rotor radii.

The impact of the inefficiencies was evaluated by comparing SEC with ideal systems, with and without energy recovery, at the actual production and recovery ratios (Fig. 4-13D). The simulated fixed-recovery sliding vane device does not outperform a standalone ideal pump. After accounting for power losses due to slip and friction, the SEC is 20-30% greater than an ideal pump would require. However, if the pump is only 65% efficient as was estimated for the vane pump (Fig. 4-13B), then adding the vane ERD stage is expected to decrease SEC by 16-22% for 1-5 m^3/h systems. Note that the minimum SEC for an ideal pump and ERD combination is approximately 2.5-3x lower than for the simulated design. Therefore, substantial improvements in energy efficiency could be achieved by addressing the dominant losses that were previously identified. Potential solutions to decrease these losses are highlighted in Sec. 4.7.4.

4.7.3 Gear and Vane Peformance for SWRO

Even with optimistic predictions of volumetric efficiency (Sec. 4.4.6), conventional gear mechanisms are not feasible solutions for energy recovery in SWRO applications. Poor volumetric efficiency at the elevated pressures causes high productivity losses (Fig. 4-14A).

Although better-performing than the gear mechanism, the vane mechanism also

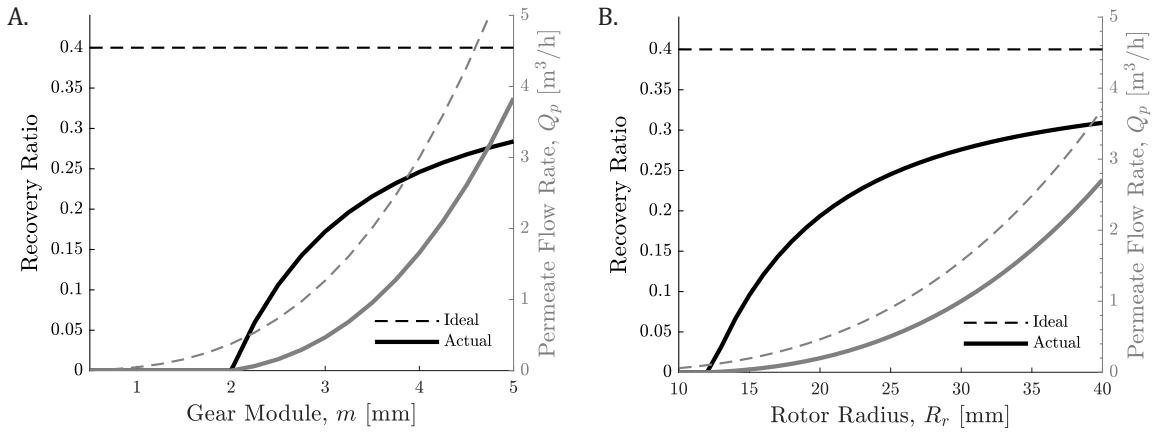

Figure 4-14: **Gear and vane mechanism performance under SWRO conditions.** (A) Large recovery ratio and production rate losses are observed for the gear mechanism. (B) High productivity losses are also observed for the vane mechanism. Small systems with <2 mm gear module and <12 mm rotor radius do not produce permeate because they fail to generate pressures that exceed the 30 bar feed osmotic pressure.

performed poorly in the SWRO application (Fig. 4-14B). Actual production and recovery ratio were significantly lower than the ideal performance due to high volumetric losses at the elevated pressures. These simulation results qualitatively agree with the measured performance of the 2 m^3/h prototype tested by Lu et al [8]. Hence, while previous studies that modeled 1200 m^3/h vane ERDs found them to be over 85% efficient at SWRO pressures [9, 10], this study shows that the same high efficiencies are infeasible when the mechanisms are physically scaled down.

Unlike for BWRO, when evaluating performance for the SWRO application, the systems were all simulated to provide a 40% ideal recovery ratio independent of permeate capacity (Sec. 4.3.2). Neither gears nor vanes were capable of providing suitable production performance despite this high ideal recovery. Based on the sensitivity of actual recovery to volumetric efficiency (Sec. 4.6.2), it is expected that the performance will be further degraded at lower ideal recoveries. It follows that the constant recovery assumption does not impact the outcomes of this study.

4.7.4 Recommended Design Improvements and Future Work

To improve the energetic performance of the sliding vane system, mechanical efficiency must be raised by either minimizing the friction torque or maximizing the displacement without changing rotor radius. Based on the results of this analysis, we suggest three directions where these improvements could be achieved:

1. **Balancing pressure forces on the rotor.** The current study assumes an unbalanced configuration since it is the most common in small water vane pumps. However, this configuration produces unbalanced pressure forces on the rotor that generate high bearing friction (Fig. 4-13C). Adopting a balanced configuration comprising of two diametrically opposed inlets, that are located 90^o about the stator from two diametrically opposed outlets, will therefore mitigate the largest source of friction torque. Adding a second pair of inlets and outlets would provide the added benefit of raising displacement.

2. **Optimizing vane geometry for maximum displacement.** Increasing vane extension will raise displacement, but also increase the bending moments imparted on the vane [62] and increase its likelihood of jamming within the rotor [10]. Optimizing the vane geometry under these constraints may provide efficiency improvements.

3. **Optimizing material selection** Vane-stator friction was the second highest source of mechanical losses. These losses could be potentially decreased by selecting material combinations that have lower friction coefficients.

Finally, while this study emphasizes the production and energetic performance, long-term reliability will also determine viability. For this reason, component wear must also be considered in future design efforts.

4.8 Conclusions

External gear and sliding vane pumps are ubiquitous and inexpensive positive displacement devices. Using simulation, we assessed the feasibility of re-purposing these

mechanisms within a fixed-recovery architecture to enable energy recovery in <5 m^3/h BWRO and SWRO applications.

By modeling the coupled behavior of the pump, ERD, and RO subsystems in this architecture, we showed that high volumetric efficiency is necessary to minimize productivity losses particularly in low-recovery processes. Since sliding vanes provide a higher volumetric efficiency than gears, they were found to be the more suitable mechanism for the investigated architecture. Nonetheless, the volumetric efficiencies of both choices was too low to enable efficient energy recovery at SWRO pressures.

Though sliding vane mechanisms were found be a technically viable solution for energy recovery in BWRO, the energy savings predicted for the simulated geometry were only 16-22% relative to a standalone 65% efficient pump. These savings could be increased by addressing the dominant mechanical losses in the system: bearing friction and vane-stator friction. Among the design improvements that were suggested, adopting a balanced configuration would decrease the impact of both these losses.

By explaining the behavior of fixed-recovery architectures, predicting the performance for two baseline designs, and suggesting improvements to those designs, this work lays the initial steps towards realizing an affordable energy recovery solution for small-scale RO treatment.

Bibliography

[1] Mageed Jean Guirguis. *Energy Recovery Devices In Seawater Reverse Osmosis Desalination Plants With Emphasis On Efficiency And Economical Analysis Of Isobaric Versus Centrifugal Devices.* Master of Science, University of South Florida, 2011.

[2] Dimitros Michas. *Design of an Energy Recovery Concept for a Small-scale Renewable-driven Reverse Osmosis Desalination System.* Master of Science in Sustainable Energy Technology, Delft University of Technology, 2013.

[3] Global Water Intelligence. DesalData Cost Estimator, 2020.

[4] Amy M. Bilton and Steven Dubowsky. The modular design of photovoltaic reverse osmosis systems: Making technology accessible to nonexperts. *Desalination and Water Treatment*, 51(4-6):702–712, 2013.

[5] Dirk Herold and Apostolos Neskakis. A small PV-driven reverse osmosis desalination plant on the island of Gran Canaria. *Desalination*, 137(1-3):285–292, 2001.

[6] A. Valbjørn. ERD for small SWRO plants. *Desalination*, 248(1-3):636–641, 2009.

[7] Jie Song, Tian Li, Lucía Wright-Contreras, and Adrian Wing Keung Law. A review of the current status of small-scale seawater reverse osmosis desalination. *Water International*, 42(5):618–631, 2017.

[8] Yong Lu, Yuanyang Zhao, Gaoxuan Bu, and Pengcheng Shu. The integration of water vane pump and hydraulic vane motor for a small desalination system. *Desalination*, 276(1-3):60–65, 2011.

[9] Osama M. Al-Hawaj. Theoretical analysis of a sliding vane energy recovery device. *Desalination and Water Treatment*, 36(1-3):354–362, 2011.

[10] Fanghua Ye, Jianqiang Deng, Zheng Cao, and Kai Liu. Study of energy recovery efficiency in a sliding vane pressure exchanger for a SWRO system. *Desalination and Water Treatment*, 119:150–159, 2018.

[11] Murray Thomson, Marcos S. Miranda, and David Infield. A small-scale seawater reverse-osmosis system with excellent energy efficiency over a wide operating range. *Desalination*, 153(1-3):229–236, 2003.

[12] Bermudez Contreras. *An energy recovery device for small-scale seawater reverse osmosis desalination*. Doctoral, Loughborough University, 2009.

[13] Geoffrey M. Geise, Ho Bum Park, Alyson C. Sagle, Benny D. Freeman, and James E. McGrath. Water permeability and water/salt selectivity tradeoff in polymers for desalination. *Journal of Membrane Science*, 369(1-2):130–138, 2011.

[14] Jay R. Werber, Akshay Deshmukh, and Menachem Elimelech. The Critical Need for Increased Selectivity, Not Increased Water Permeability, for Desalination Membranes. *Environmental Science and Technology Letters*, 3(4):112–120, 2016.

[15] DUPONT. *Water Solutions, FILMTEC™ Reverse Osmosis Membranes Technical Manual*, 7 edition, February 2021. 45-D01504.

[16] Paulo Cesar Marques De Carvalho, Douglas Bressan Riffel, Cristiano Freire, and Francisco Fabio Damasceno Montenegro. The Brazilian experience with a photovoltaic powered reverse osmosis plant. *Progress in Photovoltaics: Research and Applications*, 12(5):373–385, 2004.

[17] Stewart Dallas, N Sumiyoshi, J Kirk, K Mathew, and N Wilmot. Efficiency analysis of the Solarflow – An innovative solar-powered desalination unit for treating brackish water. *Renewable Energy*, 34(2):397–400, 2009.

[18] Fawzi Banat, Hazim Qiblawey, and Qais Al Nasser. Design and Operation of Small-Scale Photovoltaic-Driven Reverse Osmosis (PV-RO) Desalination Plant for Water Supply in Rural Areas. *Computational Water, Energy, and Environmental Engineering*, 01(03):31–36, 2012.

[19] Douglas B Riffel and Paulo C M Carvalho. Small-scale photovoltaic-powered reverse osmosis plant without batteries: Design and simulation. *Desalination*, 247(1):378–389, 2009.

[20] Stefan André Schmidt, Ephraim Gukelberger, Mario Hermann, Florian Fiedler, Benjamin Großmann, Jan Hoinkis, Ashok Ghosh, Debashis Chatterjee, and Jochen Bundschuh. Pilot study on arsenic removal from groundwater using a small-scale reverse osmosis system—Towards sustainable drinking water production. *Journal of Hazardous Materials*, 318:671–678, 2016.

[21] Katie Guerra and Julie Korak. Evaluation of Solar-Powered Systems for Desalination of Brackish Groundwater (ST-2015-1340-1). Technical Report September, Research and Development Office, US Bureau of Reclamation, Denver, Colorado, 2015.

[22] Sing-Foong Cheah. Photovoltaic Reverse Osmosis Desalination System. Technical report, U.S. Department of the Interior, Bureau of Reclamation, Denver, Colorado, 2004.

[23] Huda Elasaad, Amy Bilton, Leah Kelley, Omar Duayhe, and Steven Dubowsky. Field evaluation of a community scale solar powered water purification technology: A case study of a remote Mexican community application. *Desalination*, 375:71–80, 2015.

[24] António Joyce, David Loureiro, Carlos Rodrigues, and Susana Castro. Small reverse osmosis units using PV systems for water purification in rural places. *Desalination*, 137(1):39–44, 2001.

[25] Manoj Chandra Garg and Himanshu Joshi. A new approach for optimization of small-scale RO membrane using artificial groundwater. *Environmental Technology*, 35(23):2988–2999, 2014.

[26] B S Richards, D P S CapÃo, and A I SchÄfer. Renewable Energy Powered Membrane Technology. 2. The Effect of Energy Fluctuations on Performance of a Photovoltaic Hybrid Membrane System. *Environmental Science & Technology*, 42(12):4563–4569, jun 2008.

[27] Alejandro Ruiz-García and Ignacio de la Nuez-Pestana. A computational tool for designing BWRO systems with spiral wound modules. *Desalination*, 426:69–77, 2018.

[28] M A Alghoul, P Poovanaesvaran, M H Mohammed, A M Fadhil, A F Muftah, M M Alkilani, and K Sopian. Design and experimental performance of brackish

water reverse osmosis desalination unit powered by 2 kW photovoltaic system. *Renewable Energy*, 93:101–114, 2016.

[29] Hazim Qiblawey, Fawzi Banat, and Qais Al-Nasser. Performance of reverse osmosis pilot plant powered by Photovoltaic in Jordan. *Renewable Energy*, 36(12):3452–3460, 2011.

[30] A De Munari, D P S Capão, B S Richards, and A I Schäfer. Application of solar-powered desalination in a remote town in South Australia. *Desalination*, 248(1):72–82, 2009.

[31] Naum Fraidenraich, Olga de Castro Vilela, Milton dos Santos Viana, and Jeffrey M. Gordon. Improved analytic modeling and experimental validation for brackish-water reverse-osmosis desalination. *Desalination*, 380:60–65, 2016.

[32] Maria Diná Afonso, Jamal O Jaber, and Mousa S Mohsen. Brackish groundwater treatment by reverse osmosis in Jordan. *Desalination*, 164(2):157–171, 2004.

[33] Nafiz Kahraman, Yunus A. Cengel, Byard Wood, and Yunus Cerci. Exergy analysis of a combined RO, NF, and EDR desalination plant. *Desalination*, 171:217–232, 2004.

[34] Yunus Cerci. Exergy analysis of a reverse osmosis desalination plant in California. *Desalination*, 142(3):257–266, 2002.

[35] A. Gasmi, J. Belgaieb, and N. Hajji. Technico-economic study of an industrial reverse osmosis desalination unit. *Desalination*, 261(1-2):175–180, 2010.

[36] Manoj Chandra Garg and Himanshu Joshi. Optimization and economic analysis of small scale nanofiltration and reverse osmosis brackish water system powered by photovoltaics. *Desalination*, 353:57–74, 2014.

[37] W. Gocht, A. Sommerfield, R. Rautenbach, Th. Melin, L. Eilers, Apostolos Neskakis, Dirk Herold, V. Horstmann, M. Kabariti, and A. Muhaidat. Decentralized Desalination of Brackish Water by a Directly Coupled Reverse-Osmosis-Photovoltaic-System - A Pilot Plant Study in Jordan. *Renewable Energy*, 14(1-4):287–292, 1998.

[38] I Nyoman Widiasa, Vita Paramita, and Heny Kusumayanti. BWRO Desalination for Potable Water Supply. *Journal of Coastal Development*, 12(2):81–88, 2009.

[39] Habib Cherif and Jamel Belhadj. Large-scale time evaluation for energy estimation of stand-alone hybrid photovoltaic–wind system feeding a reverse osmosis desalination unit. *Energy*, 36(10):6058–6067, 2011.

[40] K Bourouni, T Ben M'Barek, and A Al Taee. Design and optimization of desalination reverse osmosis plants driven by renewable energies using genetic algorithms. *Renewable Energy*, 36(3):936–950, 2011.

[41] Gardenio Diogo Pimentel da Silva and Mostafa H Sharqawy. Techno-economic analysis of low impact solar brackish water desalination system in the Brazilian Semiarid region. *Journal of Cleaner Production*, 248:119255, 2020.

[42] Marwan M Mahmoud. Solar electric powered reverse osmosis water desalination system for the rural village, Al Maleh: design and simulation. *International Journal of Sustainable Energy*, 23(1-2):51–62, 2003.

[43] Gengyuan Gao, Zhongwei Yin, Dan Jiang, Xiuli Zhang, and Yanzhen Wang. Analysis on design parameters of water-lubricated journal bearings under hydrodynamic lubrication. *Proceedings of the Institution of Mechanical Engineers, Part J: Journal of Engineering Tribology*, 230(8):1019–1029, 2016.

[44] Jürgen Schiffer, Helmut Benigni, and Helmut Jaberg. Development of a novel miniature high-pressure fuel pump with a low specific speed. *Proceedings of the Institution of Mechanical Engineers, Part D: Journal of Automobile Engineering*, 227(7):997–1006, 2013.

[45] Yonghan Yoon, Byung Ho Park, Jaesool Shim, Yong Oun Han, Byeong Joo Hong, and Song Hyun Yun. Numerical simulation of three-dimensional external gear pump using immersed solid method. *Applied Thermal Engineering*, 118:539–550, 2017.

[46] Erdem Koç. Analytical and Experimental Investigation into the Sealing and Lubrication Mechanisms of the Gear Ends in Pumps. *Wear*, 135(1):79–94, 1989.

[47] K. Deng, A. S. Dewa, D. C. Ritter, C. Bonham, and H. Guckel. Characterization of gear pumps fabricated by LIGA. *Microsystem Technologies*, 4(4):163–167, 1998.

[48] Emiliano Mucchi, Giorgio Dalpiaz, and Alessandro Rivola. Dynamic behavior of gear pumps: Effect of variations in operational and design parameters. *Meccanica*, 46(6):1191–1212, 2011.

[49] D. Del Campo, R. Castilla, G. A. Raush, P. J. Gamez Montero, and E. Codina. Numerical analysis of external gear pumps including cavitation. *Journal of Fluids Engineering, Transactions of the ASME*, 134(8):1–12, 2012.

[50] Emiliano Mucchi, Gianluca D'Elia, and Giorgio Dalpiaz. Simulation of the running in process in external gear pumps and experimental verification. *Meccanica*, 47(3):621–637, 2012.

[51] Jonathan Harrison, Rodrigo Aihara, and Fabian Eisele. Modeling Gerotor Oil Pumps in 1D to Predict Performance with Known Operating Clearances. *SAE International Journal of Engines*, 9(3), 2016.

[52] Ruilong Du, Yinglong Chen, and Hua Zhou. Numerical analysis of the lubricating gap between the gear shaft and the journal bearing in water hydraulic internal

gear pumps. *Proceedings of the Institution of Mechanical Engineers, Part C: Journal of Mechanical Engineering Science*, 232(12):2297–2314, 2018.

[53] Ruilong Du, Yinglong Chen, and Hua Zhou. Investigation into the lubricating gap between the ring gear and the case in internal gear pumps. *Industrial Lubrication and Tribology*, 70(3):454–462, 2018.

[54] Fnu Rituraj, Andrea Vacca, and Mario Antonio Morselli. Modeling of manufacturing errors in external gear machines and experimental validation. *Mechanism and Machine Theory*, 140:457–478, 2019.

[55] A Subiantoro and K. T. Ooi. Analytical study of the endface friction of the revolving vane mechanism. *International Journal of Refrigeration*, 34:1276–1285, 2011.

[56] Yoshiharu Inaguma and Naohito Yoshida. Small High-Efficiency Vane Pump Based on Vane Pump Theory. *SAE International Journal of Passenger Cars - Mechanical Systems*, 8(2):614–623, 2015.

[57] F. Fornarelli, A. Lippolis, P. Oresta, and A. Posa. Investigation of a pressure compensated vane pump. *Energy Procedia*, 148:194–201, 2018.

[58] Paul W. Michael, Hassan Khalid, and Thomas Wanke. An investigation of external gear pump efficiency and stribeck values. *SAE Technical Papers*, 8(May 2018), 2012.

[59] Osama M. Al-Hawaj. Combined Pump and Energy Recovery Turbine, 2014.

[60] Richard G. Budynas and J. Keith Nisbett. *Shigley's Mechanical Engineering Design*. McGraw-Hill, 10th edition, 2016.

[61] Morgan Advanced Materials. Morgan Carbon Bearings Application Data.

[62] Y. Inaguma and A. Hibi. Vane pump theory for mechanical efficiency. *Proceedings of the Institution of Mechanical Engineers, Part C: Journal of Mechanical Engineering Science*, 219(11):1269–1278, 2005.

Chapter 5

Experimental Evaluation of a Fixed-Recovery Coupled Vane Pump-ERD Prototype

5.1 Introduction

The purpose of this work is to quantify the energy savings enabled by an experimental low-cost energy recovery device (ERD) for small-scale (0.5-2 m^3/h) brackish water reverse osmosis systems (BWRO). Brackish groundwater desalination using reverse osmosis (RO) is an increasingly popular means of producing drinking water in communities where freshwater resources are scarce or piped water supplies are unreliable. These systems have been extensively deployed in India [1–3], the Middle-Eastern [4, 5], and Brazil [6], and are recently gaining popularity in African countries [7–9].

These community-scale desalination systems produce approximately 1-20 m^3/day of drinking water using a small number of RO membrane elements [9,10]. Unlike large BWRO facilities where extensive pretreatment and trains of several membrane elements are used to achieve recoveries of 70-90% [10–12], these smaller units typically recover only 50% of the input feed as drinking water [1, 13]. Dissipation of brine pressure, particularly when such large fractions of the input feed are expelled as brine,

results in high specific energy consumption (SEC). At 50% recovery, for example, approximately half the hydraulic power from the pump is dissipated at the brine throttle. Furthermore, these losses are compounded by the poor efficiency of small pumps and motors. In off-grid applications where photovoltaic (PV) systems are used to power desalination, this high SEC translates to large power system capital costs [3]. A 2018 study found that commercially available 1-10 m^3/h BWRO systems powered by the grid cost \$4,000-8,000, while their PV-powered counterparts cost \$20,000-80,000 [13]. Safe Water Network, an operator of these community-scale water desalination systems, also reports that the capital cost of their standard 1 m^3/h systems rises from \$7,000 -\$10,000 when grid-powered to ∼\$24,000 when PV-powered [3]. Decreasing this capital cost premium by making the process more energy-efficient, via recovering energy from the brine stream, will increase affordability to target users in developing countries [3, 14, 15].

Energy-recovery devices are designed specifically to recapture brine pressure and lower the energy consumption of RO processes. However, existing products are designed to withstand the extreme pressures (50-60 bar) and feed corrosivity encountered in seawater reverse osmosis (SWRO) rather than the much lower pressures and corrosivity of BWRO. The initial costs of existing small ERDs (∼\$10,000 per m^3/h of production capacity [16]) are therefore not justified by their energy savings when applied to BWRO [17, 18]. Hence, there remains a need for low-cost ERDs that are more suitable for small-scale BWRO applications [14, 15].

By investigating concepts for low-cost ERDs, we previously identified that a fixed-recovery architecture that implements sliding vanes (Fig. 5-1) is technically feasible for BWRO [19]. This device couples two positive displacement stages – the sliding vane mechanisms – on a shaft that is driven by an electric motor. Each stage ideally displaces a fixed volume of fluid per rotation of the shaft. The pump stage pressurizes incoming feed volumes while the ERD extracts pressure from smaller outgoing brine volumes. The ratio of the stages' displacements dictates the system recovery ratio, which is the volume ratio of permeate production to feed intake.

In this study, we built and tested a 0.55 m^3/h prototype of the proposed fixed-

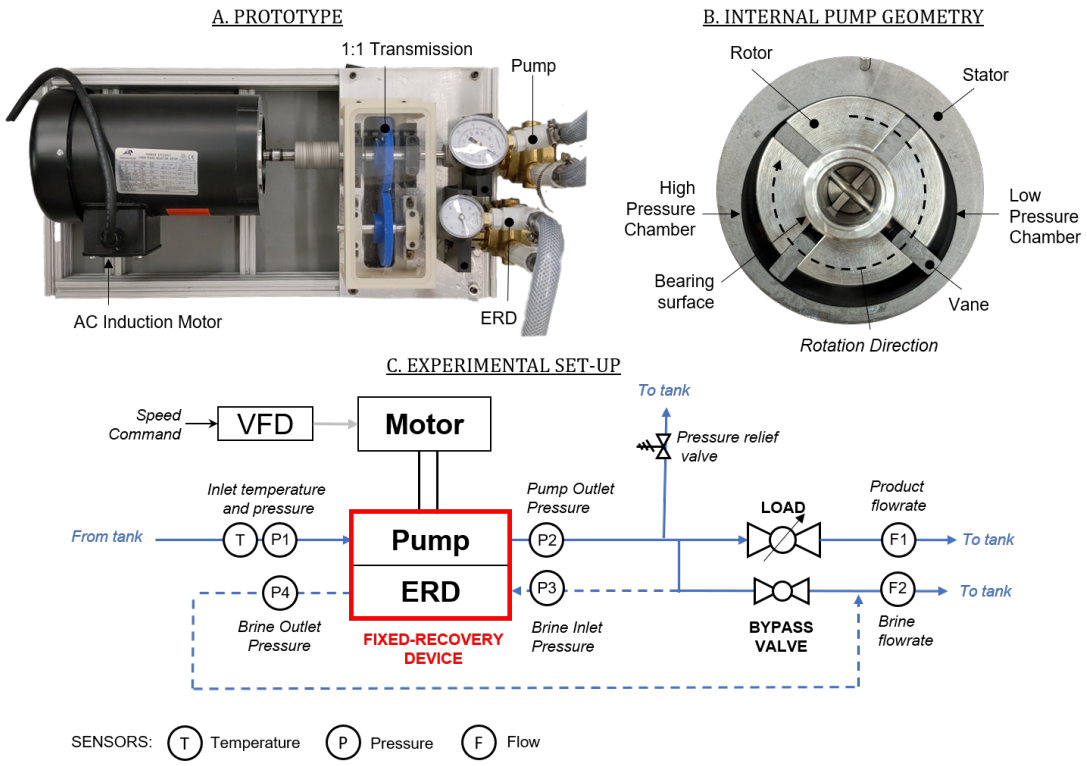

Figure 5-1: **Description of the experimental prototype and test set-up.** (A) The prototype couples two vane pumps through a 1:1 transmission where one was used as a pump while the other was used in reverse as a hydraulic motor, or ERD. (B) These devices consist of four carbon-graphite pressure-actuated vanes that are seated within a stainless steel rotor and slide against a carbon-graphite stator. When operated as a pump, the rotor rotates clockwise to transport fluid from the low pressure chamber on the right to the high pressure chamber on the left. (C) The prototype was fitted into a test set-up where a VFD, pressure sensors, and flow sensors were used to measure the efficiency of converting electrical power to hydraulic power. When the pump is operated independently, the dashed hydraulic lines are disconnected. When both pump and ERD are operated together, those lines transport the brine.

recovery system using purchased water vane pumps and evaluated its efficiency. Using the measured performance, we then estimated the capital cost savings that such a device could provide when applied to PV-BWRO.

5.2 Methods

This section details the experimental prototype followed by the test set-up and procedure used to evaluate it. Additionally, the metrics used to assess the prototype's performance are explicitly defined and expressed in terms of measured quantities.

5.2.1 Experimental System

The experimental prototype couples two purchased vane pumps of different displacements through a custom-built 1:1 gear transmission (Fig 5-1A). A Procon Series 4 1250 L/h vane pump (rated at 1725 RPM and 6.9 bar) was used for the pump stage while a Procon Series 4 750 L/h vane pump was spun in reverse as the ERD stage. The internal geometry of these devices is shown in Fig. 5-1B. Features most relevant to this investigation are:

- The rotor is supported by water-lubricated carbon-graphite bearings. Figure 5-11B highlights the shaft surface that is seated within those bearings.
- The vanes and stator are carbon-graphite components; the rotor-shaft assembly is stainless steel.
- The vanes are pressure-actuated. Pins maintain a minimum separation between diametrically opposed vanes. However, high-pressure fluid that is routed through the shaft to the back of the vanes forces them radially outward against the stator.
- The rotor is unbalanced. Since there is only one inlet and one outlet, there is a net radial pressure force acting on the rotor that is directed toward the right in the image shown.

The geometries of both pump and ERD were measured (Table 5.1) and used to calculate the expected slip flows and friction torques. These results are discussed in Section 5.3. Both devices use the same bearing plates. All measurements that are reported to three decimal places were measured using a vernier micrometers while those reported to two decimal places were measured using digital calipers. The nominal values are the average of five measurements while the errors are the standard deviation.

Table 5.1: Measured internal geometries of the pump and ERD stages.

Property	**Pump Stage**	**ERD Stage**
Rotor Diameter [mm]	44.152 ± 0.001	41.000 ± 0.001
Rotor Depth [mm]	19.044 ± 0.001	19.050 ± 0.001
Vane Slot Width [mm]	3.98 ± 0.01	4.02 ± 0.01
Maximum Stator Diameter [mm]	48.991 ± 0.020	44.997 ± 0.009
Stator Depth [mm]	19.085 ± 0.005	19.074 ± 0.001
Vane Length [mm]	19.045 ± 0.002	19.044 ± 0.001
Vane Thickess [mm]	3.958 ± 0.001	3.961 ± 0.002
Vane Height [mm]	13.953 ± 0.002	12.416 ± 0.028
Number of Vanes	4	
Shaft Diameter at Bearings [mm]	15.847 ± 0.002	15.845 ± 0.006
Bearing Bore Diameter [mm]	15.898 ± 0.011	
Bearing Width [mm]	12.792 ± 0.001	

A schematic of the test apparatus that was used to evaluate the prototype is provided in Fig. 5-1C. Though the device is intended to supply an RO membrane train, the needle valve labeled *LOAD* was instead used to adjust the load since we aim only to characterize the prototype's efficiency in this study. The prototype was driven by a 1.1 kW AC induction motor (IronHorse MTRP-1P5-3BD18) whose speed was commanded using a variable frequency drive (VFD) (WEG CFW300). For heavier loads, the motor speed deviated from the VFD command speed by up to 15 RPM. Therefore, the shaft speed was separately measured using a laser tachometer (Neiko 20713A). The VFD also recorded the electrical power *input* to the motor. To calculate the motor's mechanical power *output*, we separately measured and applied its efficiency. These efficiency curves are provided in Sec. 5.2.2.

The system was operated under two configurations: with only the pump, and with both pump and ERD. When the pump was operated independently, flow meter F1

(King Instruments 7510217A08) was used to measure its flow rate. When both pump and ERD were operated together, flow meter F2 (King Instruments 7511215B08) indicated the ERD flow rate while the flow rates from F1 and F2 together summer to the pump's flow rate. The corresponding pressures at the inputs and outputs of the pump and ERD were measured using pressure gauges. Together, the flow and pressure data that were manually recorded from these sensors were used to calculate the hydraulic power output from the pump and the hydraulic power input to the ERD.

The working fluid used for all experiments was tap water recirculated from a 400 L tank. The water in the tank was separately recirculated through a 10 micron cartridge filter to avoid large particulates from damaging the pump and ERD. The temperature of the incoming water, which was measured using a Type K thermocouple (Proster 4333090752), was within 23-25^{o}C through all experiments; therefore, the impact of temperature on viscosity was neglected when processing results.

5.2.2 Measured Motor Efficiency

The AC motor (IronHorse MTRP-1P5-3BD18) efficiency curves used in processing the experimental results are plotted in Figure 5-2. These curves were measured using the experimental set-up presented earlier (Fig. 5-1) but with a continuous rotation torque sensor (Omega TQ513-100) connecting the pump and motor rather than the transmission. The VFD was used to measure the electrical power input to the motor while the torque sensor and tachometer (Neiko 20713A) were used to measure the mechanical power output. The load on the pump was adjusted using the *LOAD* needle valve while its speed was controlled using the VFD. The manufacturer-reported efficiency at 1800 RPM, represented as the dashed line, agreed with the measurements.

5.2.3 Experimental Procedure

To establish a baseline for comparison, electrical power consumption and flow rates were first measured using only the pump through output pressures of 1.4-12.4 bar

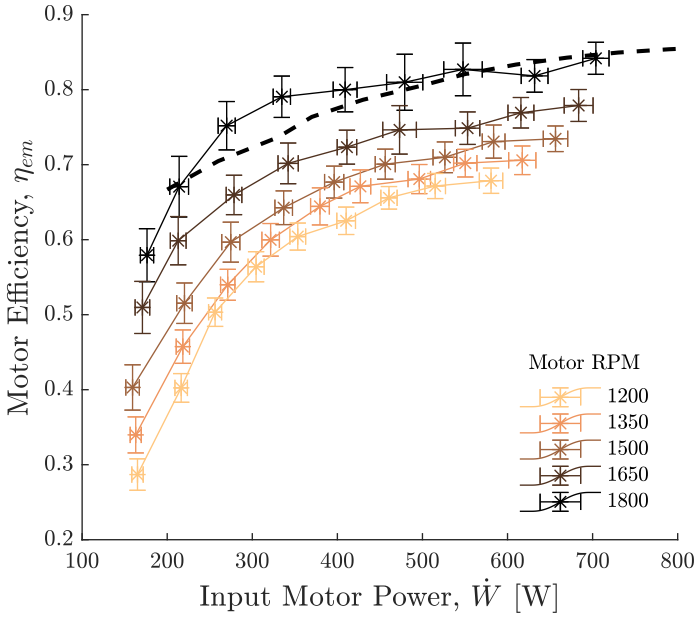

Figure 5-2: **Motor efficiency versus speed and input power.** The data points represent the measured efficiency at varying speeds while the dashed line is the manufacturer-reported efficiency at 1800 RPM. Each data point represents the average of three measurements. The error bars represent the propagated repeatability errors and sensor inaccuracies in quadrature.

in 1.4 bar increments, and through commanded motor speeds of 1200-1800 rpm in 150 rpm increments. Then, to assess the power savings enabled by energy recovery, electrical power and flow rates were measured again with both pump and ERD. Three pairs of tests were conducted, alternating between using the pump alone and then using both pump and ERD together. The alternating order helped to ensure that component wear did not favor either case significantly.

5.2.4 Calculation of Displacement, Slip, and Friction Torque

The measurements were used to evaluate the slip and friction torque within the pump and ERD stages. Slip is the leakage from the high-pressure chamber to the low-pressure chamber of each device. It decreases the flow rate from the pump and increases the flow rate through the ERD, relative to their ideal geometric displacements. Therefore, to assess slip, we first characterized the geometric displacements d of both stages using a standard procedure [20]. In this procedure, the slope of the

actual flow rate Q_{act} versus rotational speed $d\omega$ is evaluated at, and plotted against, different pressure differences ΔP. Then, the displacement is defined as the intercept of the resulting $dQ_{act}/d\omega$ versus ΔP line. Then, the slip Q_s through the pump and ERD are calculated from

$$Q_s^I = Q_{id}^I - Q_{act}^I \text{ and} \tag{5.1}$$

$$Q_s^{II} = Q_{act}^{II} - Q_{id}^{II}, \tag{5.2}$$

where the superscripts I and II signify the pump and ERD stages, respectively. In these expressions, the ideal flow rate Q_{id} is

$$Q_{id} = \frac{d\omega}{2\pi}. \tag{5.3}$$

Since the $LOAD$ valve is used in place of an RO membrane, the flow rate through flow meter F1 is the product flow rate (Fig. 5-1). For an ideal pump and ERD combination, the ideal product flow rate $Q_{p,id}$ is

$$Q_{p,id} = Q_{id}^I - Q_{id}^{II} = \frac{\omega(d^I - d^{II})}{2\pi} \tag{5.4}$$

Friction torque increases the mechanical power required by the pump and decreases the mechanical power produced by the ERD. To estimate the friction torque, we first derive the ideal torque T_{id} from the energy balance

$$T_{id} = \frac{\Delta P d}{2\pi}. \tag{5.5}$$

Then, using the measured electrical power consumption $\dot{W}_p$ of the pump itself, the pump's friction torque is

$$T_f^I = \frac{\eta_{em}\dot{W}_p}{\omega} - T_{id}^I, \tag{5.6}$$

where η_{em} is the motor efficiency. Then, the electrical power consumption $\dot{W}_{pe}$ is measured under the same conditions but with both pump and ERD. Using this mea-

surement, the ERD friction torque is

$$T_f^{II} = T_{id}^{II} - \frac{\eta_{em}(\dot{W}_p - \dot{W}_{pe})}{\omega}. \tag{5.7}$$

5.2.5 Calculation of Efficiencies

We refer to three efficiencies in this study: volumetric, mechanical, and total. The volumetric efficiency η_v is a measure of the actual flow rate relative to the ideal flow rate. Since slip decreases the pump flow rate, its volumetric efficiency is defined as

$$\eta_v^I = \frac{Q_{act}^I}{Q_{id}^I}. \tag{5.8}$$

The inverse applies for the ERD; therefore,

$$\eta_v^{II} = \frac{Q_{id}^{II}}{Q_{act}^{II}}. \tag{5.9}$$

The mechanical efficiency η_m is a measure of the actual torque relative to the ideal torque. Friction raises the pump input torque so its mechanical efficiency is

$$\eta_m^I = \frac{T_{id}^I}{T_{act}^I}, \tag{5.10}$$

but it decreases the ERD torque output so

$$\eta_m^{II} = \frac{T_{act}^{II}}{T_{id}^{II}}. \tag{5.11}$$

Lastly, the total efficiency for either stage is the product of the volumetric and mechanical efficiencies, giving

$$\eta_t = \eta_m \eta_v. \tag{5.12}$$

5.2.6 Theoretical Maximum Power Savings

Assuming the pump is not replaced, the maximum relative power savings ϵ that can be provided by and ideal ERD is

$$\epsilon = \frac{\Delta P Q_{id}^{II}}{\Delta P Q_{act}^{I}} = \frac{Q_{id}^{II}}{Q_{act}^{I}}. \tag{5.13}$$

The pump's actual flow rate is used because the ERD can not recapture power from any flow that slips through the pump. Substituting Eqns. 5.3 and 5.8 simplifies the above expression to

$$\epsilon = \frac{d^{II}}{d^{I}\eta_v^{I}}. \tag{5.14}$$

5.3 Results and Discussion

We first report the measured volumetric performance and power reduction achieved by the prototype. Then, we characterize the ERD friction to provide suggestions on how power consumption can be further decreased. Finally, we use the measured efficiencies to estimate capital cost savings for the target community-scale PV-BWRO application.

5.3.1 Volumetric Performance

Measured flow rates for the pump and ERD stages are plotted as a function of shaft speed and pressure (Fig. 5-3A and B). As pressure increases, the pump flow rate decreases while the ERD flow rate increases due to slip. To quantify the slip flow rates, the geometric displacements are required. These were evaluated to be 12.7 $\pm$ 0.1 mL/rev and 7.6 $\pm$ 0.1 mL/rev for the pump and ERD, respectively, using the procedure specified in Sec. 5.2.4.

Slip is not expected to vary with shaft speed since it is defined as the pressure-driven leakage through each stage. By plotting the calculated slip (Eqns. 5.1 amd 5.2) from measured flow rates, it is seen that this expectation is met (Figs. 5-3C and D). Error-bars are large because slip flow rates are less than 0.07 m^3/h, while the

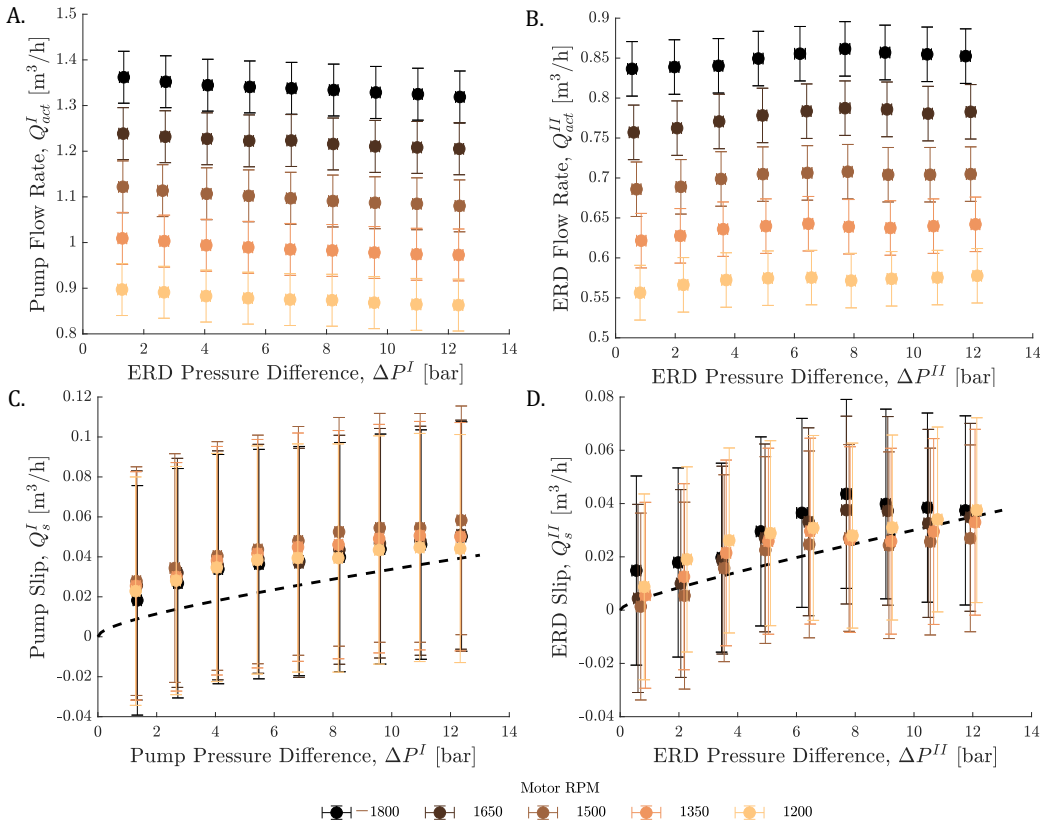

Figure 5-3: **Flow rates of the individual pump and ERD stages through different motor speeds.** Measured pump (A) and ERD (B) flow rates are plotted against the pressure differences across those stages. Slip flow rates at both pump (C) and ERD (D) were calculated from the same flow rate measurements and compared with predictions from a previously proposed model [19]. These predictions, as represented by the dashed lines, agreed with the experiment. Error bars represent propagated repeatability errors and sensor inaccuracies in quadrature.

flow meters F1 and F2 (Fig. 5-1) are only accurate to within ± 0.05 m^3/h (2% of full-scale) and ± 0.03 m^3/h (3% of full-scale), respectively. The dashed lines on the same plots indicate the predicted slip through each stage from the model presented in previous work [19]. This model predicts the slip past the axial rotor faces, vane sides, and through the hydrodynamic bearing of the measured geometry (Table 5.1). Though error-bars are large, The agreement between model and experiment for both pump and ERD suggests that the magnitude of slip is realistically predicted. A more thorough validation would require measuring flow rates more precisely.

Since slip does not increase with shaft speed while the displaced flow rate does, the volumetric efficiencies of both pump and ERD improve with shaft speed (Fig.

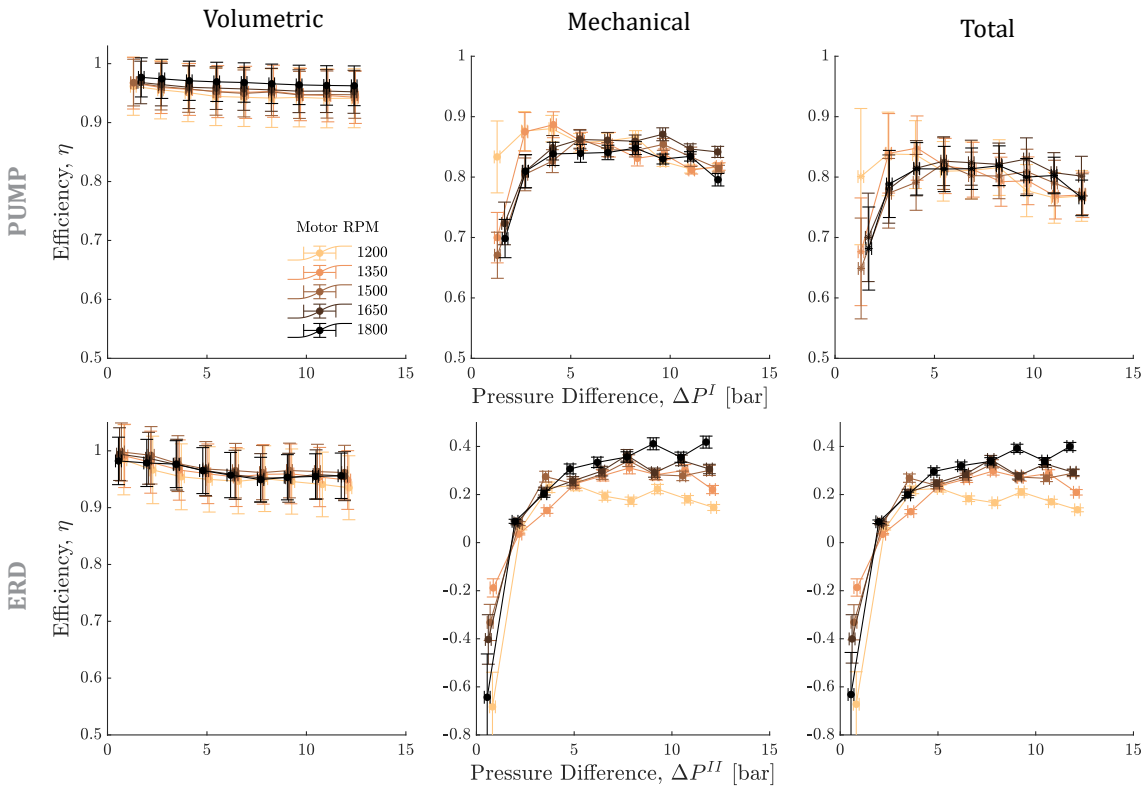

Figure 5-4: **Measured pump and ERD efficiencies through varying pressure differences and motor command speeds.** Pump efficiencies are plotted along the top row while ERD efficiencies are plotted along the bottom row. Volumetric, mechanical, and total efficiencies are plotted from left to right. Colors in all plots relate to the motor command speed as per the legend provided in the top left figure. Error bars represent propagated repeatability errors and sensor inaccuracies in quadrature.

5-4). It follows that to maximize volumetric efficiency, the system should be sized for, and operated at, the maximum acceptable speed. Slip also impacts the system's permeate production rate (Fig. 5-5). The ideal production rate only depends on the displacements and motor speed (Eqn. 5.4). However, slip causes less feed to be conveyed by the pump and more brine to escape through the ERD, thereby decreasing production rate. Since slip does not vary with shaft speed, the absolute decrease in production rate is equal at the maximum and minimum tested speeds of 1800 and 1200 RPM. However, the displaced flow rate varies linearly with shaft speed; hence, the relative decrease in production rate is more pronounced at the lower speed. For example, at the maximum test pressure, the production loss is only 15% at 1800 RPM but 22% at 1200 RPM. Again, it is seen that operating the system at the maximum

acceptable speed is beneficial.

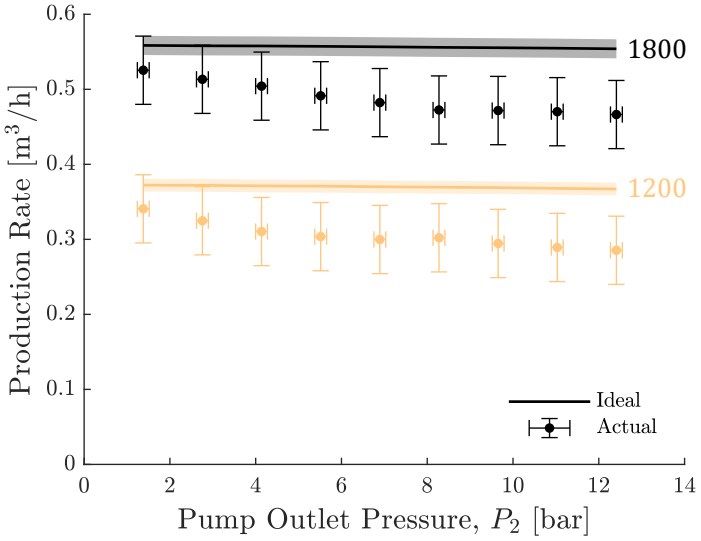

Figure 5-5: **Ideal and actual production rates are compared as a function of pump outlet pressure at the maximum and minimum tested motor speeds.** The ideal production rate is only a function of rotation speed while the actual production rate decreases due to slip at the pump and ERD. The shaded regions represent the propagated uncertainty in ideal production rate due to uncertainty in the calculated pump and ERD displacements. Error bars on measured values represent propagated repeatability errors and sensor inaccuracies in quadrature.

Overall, the system demonstrated high volumetric performance since both pump and ERD stages respectively provided efficiencies exceeding 96 ± 3% and 96 ± 4% at the manufacturer's maximum recommended speed of 1800 RPM, and for pressures up to 12.4 bar (Fig. 5-4). This prototype outperformed the only previous fixed-recovery vane prototype evaluated by Lu et al. [21] whose reported volumetric efficiency was below 96% at pressures above 6 bar.

5.3.2 Energetic Performance

Next, the electrical power consumption was compared with and without the ERD (Fig. 5-6A). No power savings were observed at the lowest pressures because the total ERD efficiency is negative under those conditions (Fig. 5-4). This result indicates for pressure differences of less than 2 bar, the input hydraulic driving power does not exceed the ERD's frictional losses, causing it to behave as a net power dissipator

than a net generator (Fig. 5-6B). Then as this hydraulic driving force increases with rising pressure, the ERD efficiency improves and a net power savings is observed. Power savings also increase with speed because the ERD's total efficiency increases with speed. Despite this improvement, the maximum measured reduction in electrical power consumption over all test conditions was only 17 ± 3% versus the maximum 62 ± 2% that is theoretically achievable with an ideal ERD of the same displacement (Eqn. 5.14).

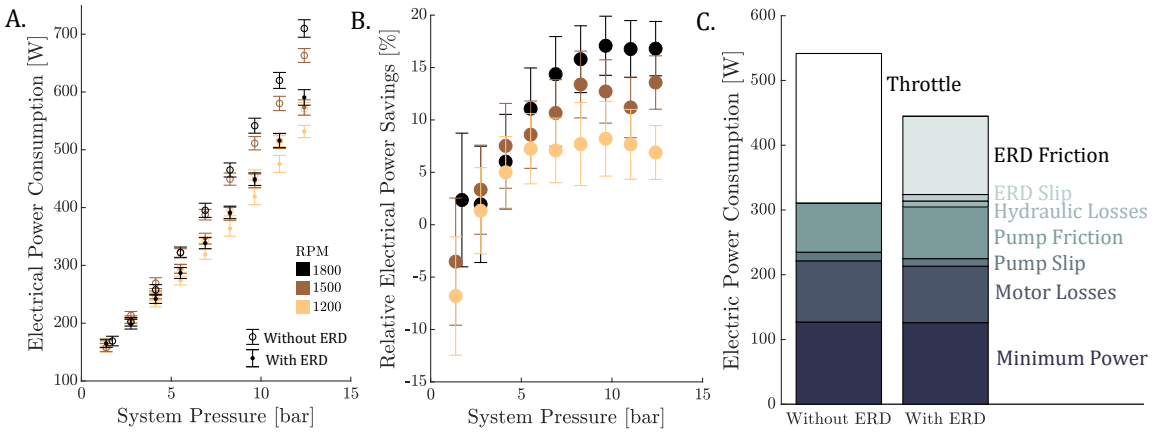

Figure 5-6: **Measured electrical power savings enabled by the ERD.** (A) Electrical power consumption measurements with (o) and without (*) the ERD are plotted as a function of the pump outlet pressure and motor command speed. Data collected at speeds of 1650 and 1350 RPM are omitted for clarity. (B) The electrical power savings provided by the ERD, relative to operating the pump without the ERD, are plotted under the same conditions. A maximum reduction of 17 ± 3% was obtained at the maximum speed and pressure. (C) A comparison of the power breakdown with and without the ERD is presented for a representative operating point (1800 RPM and 9.7 bar) to quantify the various losses.

To better understand the decreased savings, we examined a power breakdown with and without the ERD at a representative operating point: 1800 RPM and 9.7 bar (Fig. 5-6C). The total height of the stacked bars represents the measured electrical power consumption. The lowest bar is the minimum power required to deliver the measured product flow rate at the stated pressure while the bars stacked above represent different losses throughout the system. This representation clearly shows that power losses due to slip at both the pump and ERD are small relative to the total power consumption. This result is consistent with the high volumetric

efficiencies measured for both stages (Fig. 5-4). Instead, the largest losses are due to mechanical friction in the pump and ERD. Hence, decreasing ERD friction is the most effective way to increase power savings. In the following section we assess the sources contributing to this friction to identify strategies for mitigating the corresponding losses.

5.3.3 Sources of ERD Friction

The calculated ERD friction torque (Eqn. 5.7) is plotted against pressure difference through all tested speeds (Fig. 5-7A). The observed linear trend suggests that the friction is generated at five sources: the transmission, the ERD shaft seal, the sliding of the rotor against the axial bearing faces, the sliding of vanes against the rotor and stator, and the radial bearing friction (Fig. 5-7B). Modeling and experimentation were applied together to allocate the total measured frictional power losses to these sources (Fig. 5-7C).

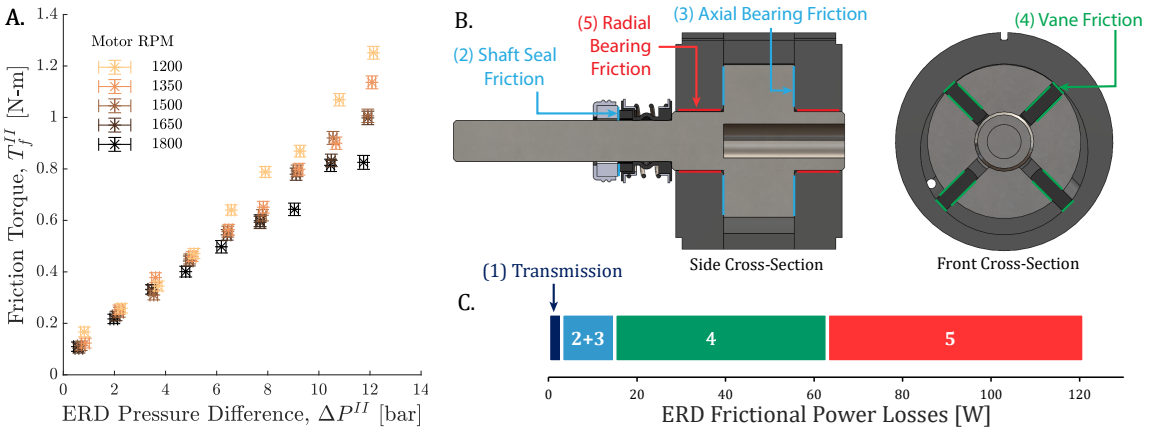

Figure 5-7: **Analyzing the sources of ERD friction.** (A) ERD friction was observed to increase linearly with pressure difference. (B) Sources of this friction are highlighted in front and side cross-sectional views of the ERD. (C) The frictional power losses at these sources were quantified using a combination of experiments and modeling. Colors in the stacked bar chart refer to the sources highlighted in the front and side views.

Losses at the gear transmission were evaluated by comparing the motor power output while running the smaller of the two vane pumps (Procon 750 L/h) directly by the motor and then through the transmission. The difference in power was in-

terpreted as transmission losses. When running the pump through the transmission, the motor's rotation direction was reversed to account for the gears spinning in opposite directions. We assume that this change did not affect the motor efficiency. The measured differences in power consumption are plotted in Fig. 5-8. However, at 1800 RPM and 9.7 bar, these losses on average only account for approximately 3 W of the total 121 ± 5 W lost to friction. Therefore, transmission losses were found negligible.

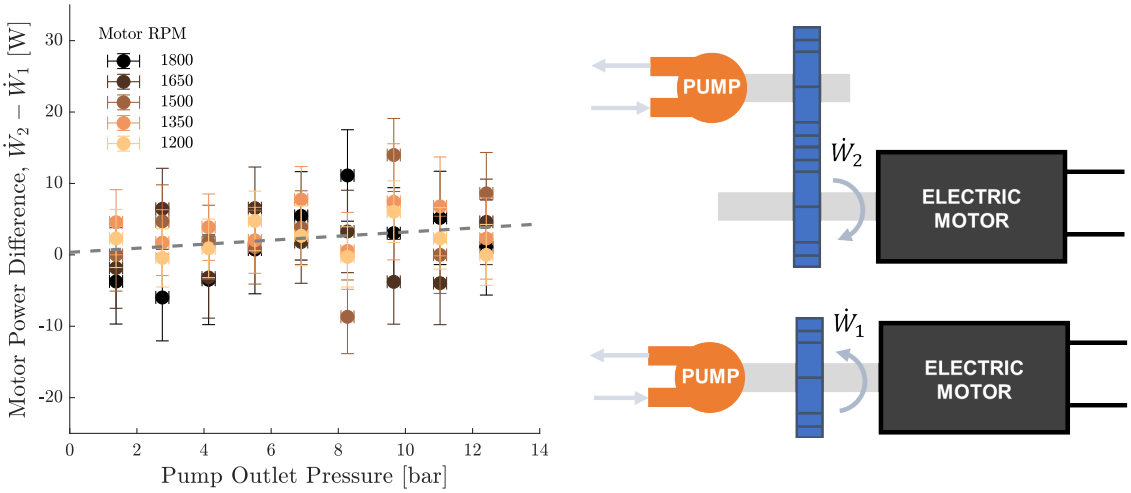

Figure 5-8: **Experimental measurement of the frictional power losses at the transmission.** A vane pump (Procon Series 4 750 L/h) was operated directly and through the transmission (*right*). The difference in motor power output is plotted for varying pump outlet pressures and motor speeds (*left*). The data points represent the average of three measurements and the error bars indicate propagated repeatability and sensor errors in quadrature. The dashed line is a linear fit of the data collected over all speeds.

To isolate losses at the shaft seal and the axial bearing faces, we removed the vanes from the ERD (Fig. 5-9). This modification eliminates two sources of friction. Most obviously, it eliminates sliding friction at the vane-stator and vane-rotor interfaces. Removing the vanes also causes the pressure forces on the rotor to be balanced and therefore additionally minimizes friction at the radial bearing. The modified ERD was then coupled to the pump via the transmission and pressurized water was introduced into its inlet but the outlet was blocked. It therefore behaved as a brake and the observed increase in motor power output was attributed to total friction at the transmission, shaft seal, and axial bearings. Detailed results from this evaluation are

provided in Fig/ 5-10. After subtracting transmission losses, it was similarly found that the seal and axial bearings together contributed minimal friction: ∼12 W at 1800 RPM and 9.7 bar.

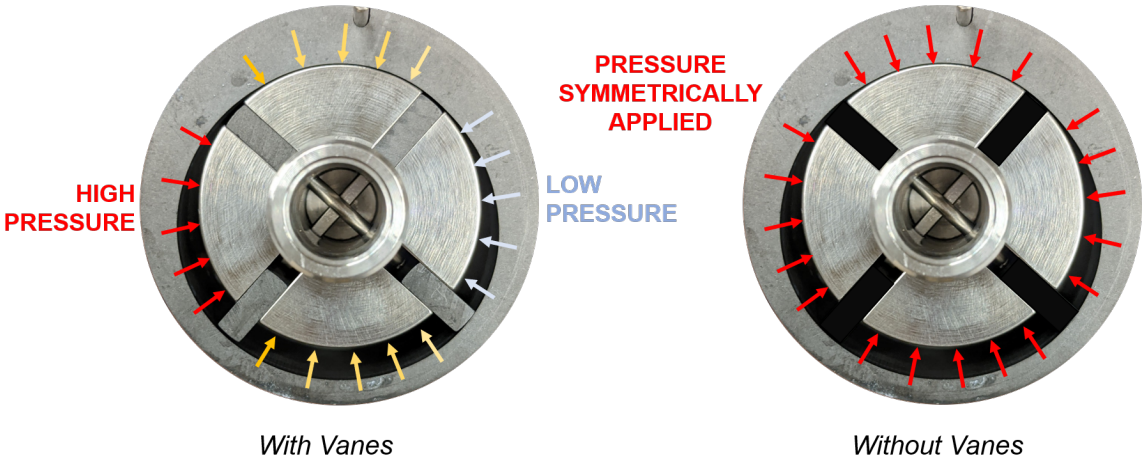

Figure 5-9: **Pressure forces on the rotor are balanced when the vanes are removed.** When the vanes are present, the pressure differences on the rotor cause a net force directed toward the right. When the vanes are removed, the pressure acts symmetrically so there is no net force on the rotor

Vane friction and radial bearing friction could not be experimentally isolated since the pressure-actuated vanes must be present to cause unbalanced pressure loads on the rotor. Consequently, the model described in Sec. 4.5 was used to bound the power dissipated due to the frictional sliding of the vane against the rotor and stator. In this model, a force and moment balance considering both pressure and inertial forces is applied to solve for the frictional forces at the vane tip and sides. These frictional forces are then integrated through one rotation of the rotor to calculate the mean friction torque and power. Using a conservative estimate of 0.15 for friction coefficient at the vane-stator and vane-rotor interfaces [22], we calculated losses due to vane friction to be 48 W. This value accounts for approximately 40% of the total ERD frictional losses at 1800 RPM and 9.7 bar pressure.

The leftover 48% of the measured losses likely occurs at the radial bearing. Conventionally, the friction at hydrodynamic bearings is minimized by maintaining a fluid layer between the stationary and rotating surfaces. However, due to the high radial pressure loads exerted at the bearing and the low viscosity of water, we sur-

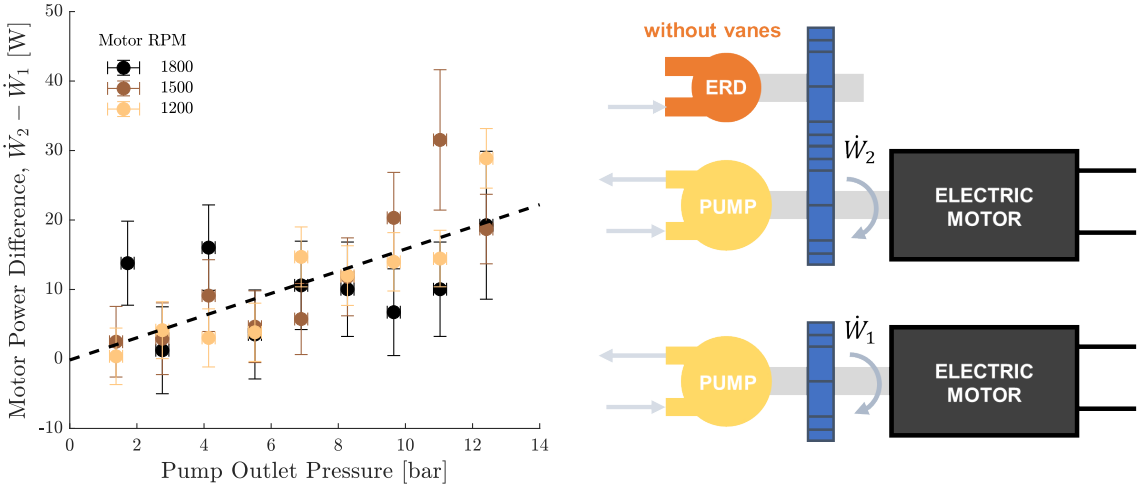

Figure 5-10: **Experimental measurement of the total frictional power losses at the shaft seal, axial bearing, and transmission.** The vanes were removed from the ERD to isolate these frictional sources. Then, with the modified ERD acting as a brake (*right*), the difference in motor power output was measured for varying pump outlet pressures and motor speeds (*left*). The data points represent the average of three measurements and the error bars indicate propagated repeatability and sensor errors in quadrature. The dashed line is a linear fit of the data collected over all speeds.

mise that full-film lubrication conditions are not attained in the tested vane pumps. This hypothesis is supported by observations of the bearing surfaces on the loaded and unloaded sides after use (Fig. 5-11). Relative to the unloaded side, which more closely resembles the original surface, the loaded side showed significant signs of wear by the shaft. This wear indicates that the bearing and shaft are not fully separated by a lubricating layer, resulting in increased friction.

This assessment of friction suggests that the power consumption can be most effectively decreased by implementing a balanced rotor configuration. The simplest balanced configuration has a pair of diametrically opposed inlets and a pair of diametrically opposed outlets. The pressure loads in this configuration cancel out to provide minimal loads on the radial bearing. This modification would minimize frictional losses at the ERD's radial bearings and consequently increase power savings to an estimated 31%, a substantial improvement over the 17% obtained with the present design.

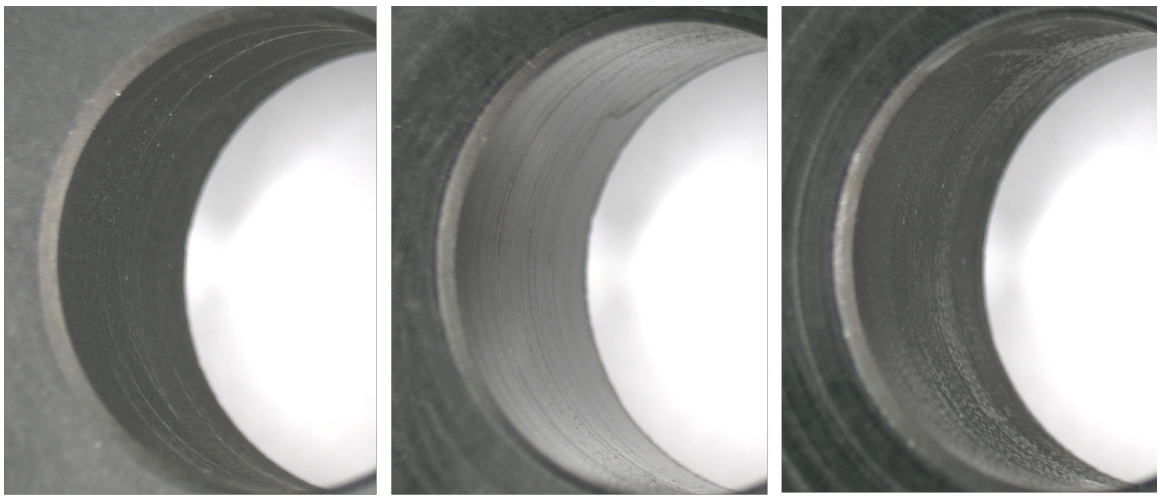

Figure 5-11: **Close-up images of the radial bearing surface before and after pump tests.** The bearing surface before use is seen on the left. After use, the surface on the loaded side of the bearing appears more worn (center) than on the unloaded side (right). All images were captured under similar lighting conditions.

5.3.4 Economic Implications

To contextualize the efficiency results, we estimated the PV capital cost savings that would be enabled by the fixed-recovery system for the target application discussed in the introduction: community-scale BWRO systems. The assumptions made in this analysis are as follows.

- The baseline system represents a 1 m^3/h system,the most common capacity for the target application [3, 23].
- As is typical, the baseline system operates at a recovery of$r = 50\%$ and uses a brine stream throttle to pressurize the feed [13, 24].
- Multi-stage centrifugal pumps are typically used in these BWRO systems. Therefore, a baseline pump efficiency of $\eta_{bp} = 50\%$ is assumed, as this is consistent with the peak efficiencies provided by premium multi-stage centrifugal pumps at the capacities of interest [25].
- A PV system that could power this baseline system costs $8,000. This estimate is on the lower end of the ranges reported by the Safe Water Network [3] and

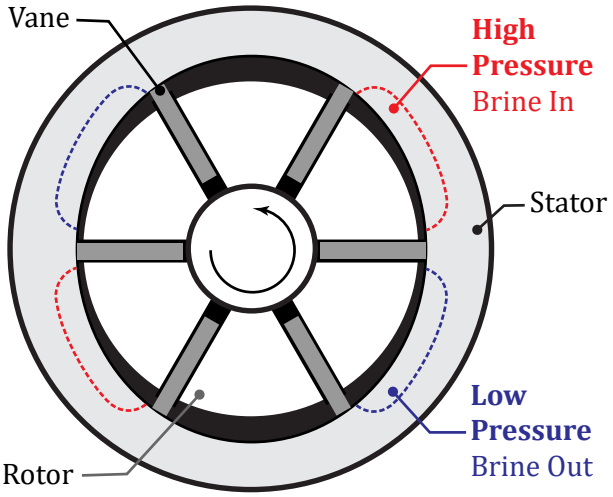

Figure 5-12: **Vane ERD with balanced configuration.** This configuration has two diametrically opposed inlets and two diametrically opposed outlets. Therefore, the pressure forces cancel to provide zero net force on the rotor.

Boden and Subban [13].

- 70% of the PV system capital cost scales with the power requirement, while the remaining 30% represents fixed costs [23].

- The fixed-recovery system that would replace the multi-stage centrifugal pump also provides a 50% recovery.

- The efficiencies of the vane pump and ERD stages are $\eta_p = 80\%$ and $\eta_{ERD} = 40\%$, respectively, based on the measurements made in this study (Fig. 5-4).

- From the assessment of frictional losses (Fig. 5-7C), an improved ERD with minimized bearing friction would provide a higher efficiency of 60% .

Then the power consumed by the pump in the baseline system is

$$\dot{W}_b = \frac{P_f Q_f}{\eta_{bp}}, \tag{5.15}$$

where P_f is the feed pressure and Q_f is the feed flow rate. For a different pump

coupled with an ERD, the estimated power consumption is

$$\dot{W}_n = \frac{P_f Q_f}{\eta_p}(1 - \eta_p \eta_{ERD}(1 - r)), \tag{5.16}$$

Then, taking the ratio of these two power requirements and applying Assumptions 4 and 5, the capital cost of the PV system can be approximated by

$$CC = \$8,000 \left(0.70 \frac{\eta_{bp}}{\eta_p}(1 - \eta_p \eta_{ERD}(1 - r)) + 0.30\right). \tag{5.17}$$

The resulting cost-comparison indicates that simply replacing the multi-stage centrifugal pump with the more efficient vane pump tested in this study would provide a cost savings of $2,100 (Fig. 5-13). Adding the ERD would only provide a further $550 savings. Though each of the pumps used in this work can be purchased for approximately $300, the added complexity of introducing an ERD may not be justifiable in this case. However, if the friction in the ERD were to be addressed by balancing the rotor and increasing efficiency 60%, the resulting savings would be more substantial: $2950 relative to the baseline.

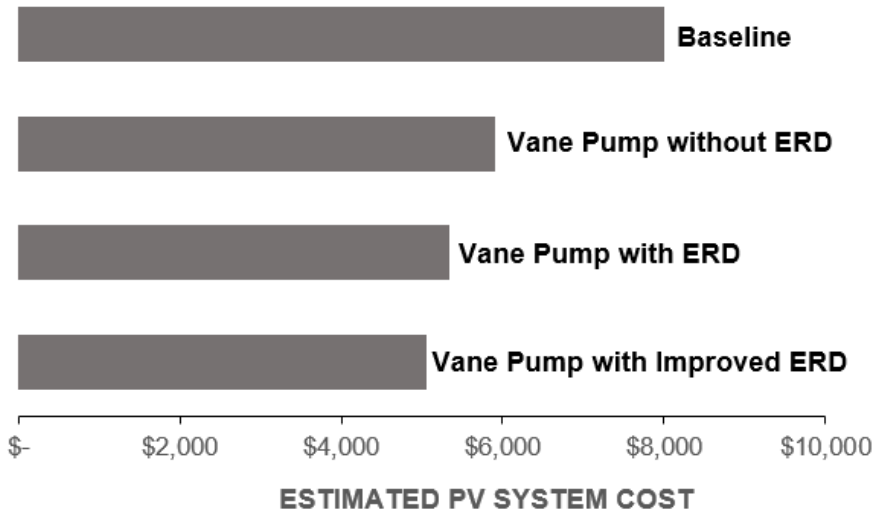

Figure 5-13: **Estimating PV system capital cost savings enabled by the fixed-recovery vane ERD.** The bar lengths indicate the capital cost of the PV system required to power each system configuration. The baseline represents the throttled 1 m^3/h, 50% recovery systems that are commonly used today.

5.3.5 Limitations of this Assessment

While the purpose of this study was to assess the efficiency of a fixed-recovery system comprised of commonly-available vane pumps, there are other factors that will also determine the viability of this solution, including:

- Component wear: Wear will affect the frequency of required maintenance.
- Ability to handle salt solutions: The vane pumps selected for this study are advertised as a being suitable for RO applications. However, more testing is required to quantify the efficiency degradation that might arise from salt precipitating within the device.

In future work, we plan to adapt the experimental set-up developed for this study to assess these factors.

5.4 Conclusions

Community-scale, photovoltaic-powered, brackish water desalination using reverse osmosis (PV-BWRO) could be made more affordable using energy recovery; however, existing solutions are cost-prohibitive. In this work, we experimentally evaluated whether purchased water vane pumps could be used as low-cost energy recovery devices (ERDs) by implementing two vane pumps of different displacements within a fixed-recovery architecture, and measuring energy savings and efficiencies as a function of shaft speed and pressure.

While both pump and ERD stages exhibited high volumetric efficiencies exceeding 96 $\pm$ 3% and 96 $\pm$ 4%, respectively, the maximum reduction in power consumption from adding the ERD was only 17% $\pm$ 3% due to mechanical friction. Using experiments and modeling, it was identified that 48% of those frictional losses occurred at the water-lubricated radial bearings, and were caused by unbalanced pressure loads on the rotor. Thus, to improve the ERD's efficiency and increase power savings, a balanced configuration consisting of two inlets and outlets is recommended.

Finally, using measured efficiencies, we estimated the vane pump alone could provide PV capital cost savings of $2100 while adding the ERD would only yield an additional $550 in savings. However, adopting the recommended balanced configuration for the ERD is expected to raise the total savings to $2950. Therefore, from testing an experimental prototype, we have highlighted a feasible path toward realizing a low-cost energy recovery solution for PV-BWRO.

Bibliography

[1] Natasha C. Wright and Amos G. Winter. Justification for community-scale photovoltaic-powered electrodialysis desalination systems for inland rural villages in India. *Desalination*, 352:82–91, 2014.

[2] APMAS. Case Study: Provision of safe drinking water, Mission Gagillapur. Technical report, Mahila Abhivruddhi Society, Andhra Pradesh (APMAS).

[3] Safe Water Network. India Sector Review - Small Water Enterprises to Mitigate the Drinking Water Challenge. (October), 2018.

[4] Manal Taha and Rashed Al-Sa'ed. Application potential of small-scale solar desalination for brackish water in the Jordan Valley, Palestine. *International Journal of Environmental Studies*, 75(1):214–225, 2018.

[5] Mahmoud Shatat, Karen Arakelyan, Omar Shatat, Tim Forster, Ashraf Mushtaha, and Saffa Riffat. Low Volume Water Desalination in the Gaza Strip – Al Salam Small Scale RO Water Desalination Plant Case Study. *Future Cities and Environment*, 4(1):1–8, 2018.

[6] Renato Saraiva Ferreira, Henrique Pinheiro Veiga, Regina Gleice Batista Dos Santos, Alexandre Saia, Samuel Coelho Rodrigues, Anderson Felipe, Anderson Felipe De Medeiros Bezerra, Luiz Carlos Hermes, Alexandre Moura, and Luis Henrique Cunha. Empowering Brazilian Northeast Rural Communities To Desalinated Drinking Water Access : Programa Água Doce. *The International Desalination Association World Congress*, pages 1–13, 2017.

[7] Namibia Water Corporation Ltd. Project proposal to the Adaptation Fund: Pilot rural desalination plants using renewable power and membrane technology. Technical report, Adaptation Fund, 2017.

[8] Nirat Bhatnagar, Sam Lampert, Vibhor Goyal, Romit Mehta, Raahil Rai, and Ashwin Chandrasekhar. The Untapped Potential of Decentralized Solutions to Provide Safe, Sustainable Drinking Water at Large Scale The State of the Safe Water Enterprises Market. Technical Report January, Dalberg, 2017.

[9] Jean Marie Takouleu. AFRICA: Desalination, now a key component of water supply strategies | Afrik 21, may 2020.

[10] M.A. Alghoul, P. Poovanaesvaran, K. Sopian, and M.Y. Sulaiman. Review of brackish water reverse osmosis (BWRO) system designs. *Renewable and Sustainable Energy Reviews*, 13(9):2661 – 2667, 2009.

[11] W. Arras, N. Ghaffour, and A. Hamou. Performance evaluation of BWRO desalination plant - a case study. *Desalination*, 235(1):170 – 178, 2009.

[12] M.A. Al-Obaidi, A.A. Alsarayreh, A.M. Al-Hroub, S. Alsadaie, and I.M. Mujtaba. Performance analysis of a medium-sized industrial reverse osmosis brackish water desalination plant. *Desalination*, 443:272 – 284, 2018.

[13] Kathryn S Boden and Chinmayee V Subban. A Road Map for Small Scale Desalination. (May), 2018.

[14] Michael Papapetrou, Marcel Wieghaus, and Charlotte Biercamp. Roadmap for the development of desalination powered by renewable energy. Technical report.

[15] Manoj Chandra Garg and Himanshu Joshi. A Review on PV-RO Process: Solution to Drinking Water Scarcity due to High Salinity in Non-Electrified Rural Areas. *Separation Science and Technology (Philadelphia)*, 50(8):1270–1283, 2015.

[16] Amy Bilton. *A modular design architecture for application to community-scale photovoltaic-powered reverse osmosis systems*. Doctoral thesis, Massachusetts Institute of Technology, 2013.

[17] Huda Elasaad, Amy Bilton, Leah Kelley, Omar Duayhe, and Steven Dubowsky. Field evaluation of a community scale solar powered water purification technology: A case study of a remote Mexican community application. *Desalination*, 375:71–80, 2015.

[18] Jie Song, Tian Li, Lucía Wright-Contreras, and Adrian Wing Keung Law. A review of the current status of small-scale seawater reverse osmosis desalination. *Water International*, 42(5):618–631, 2017.

[19] Sahil R. Shah and Amos G. Winter V. Gear and Sliding Vane Mechanisms for Energy Recovery in Small-Scale Reverse Osmosis Applications: A Technical Feasibility Study. *In Preparation*, 2021.

[20] Gijsbert Toet, Jack Johnson, John Montague, Ken Torres, and José Garcia-Bravo. The determination of the theoretical stroke volume of hydrostatic positive displacement pumps and motors from volumetric measurements. *Energies*, 12(3), 2019.

[21] Yong Lu, Yuanyang Zhao, Gaoxuan Bu, and Pengcheng Shu. The integration of water vane pump and hydraulic vane motor for a small desalination system. *Desalination*, 276(1-3):60–65, 2011.

[22] Vaclav Vodicka, Vaclav Novotny, and Jakub Mascuch. Wear behaviour of vanes for a rotary vane expander with various graphite materials under dry sliding conditions. *Acta Polytechnica*, 58(5):315–322, 2018.

[23] Project Asbah. Personal Communication.

[24] Natasha C Wright. *Justification for community-scale photovoltaic-powered electrodialysis desalination systems for inland rural villages in India*. Master's thesis, Massachusetts Institute of Technology, 2014.

[25] Grundfos. CR, CRI, CRN Vertical, Multistage Centrifugal Pump Data Booklet. Technical report, 2021.

THIS PAGE INTENTIONALLY LEFT BLANK

Chapter 6

Evaluating the Production and Energetic Performance of Point-of-Use Reverse Osmosis Devices

6.1 Introduction

The objective of this work is to experimentally characterize the performance of a POU RO system and conduct an exergy analysis to identify key inefficiencies. In doing so, we hope to catalyze new developments in POU RO desalination that address their low recovery and high energy consumption (Fig. 1-6).

Prior studies evaluating POU RO desalination have not investigated the energy losses within such a system. Elfil et al. performed a techno-economic analysis on the use of POU RO devices in Tunisia, which encompassed an evaluation of the scaling propensity and recovery ratio for different feed water compositions and temperatures. They concluded that the treatment cost was 11-30 times greater than can be achieved with large scale plants when water, energy consumption, and membrane replacement were considered. However, they did not quantify the inefficiencies underlying this large difference [1]. To address the low recovery ratio, Thampy et al. proposed hybridization with an electrodialysis process for POU desalination, and demonstrated

that recovery could be raised to 50-60% for 2000-4000 mg/L feeds [2]. The energy consumption of the proposed process was 8-10 kWh/m^3, which equates to approximately thrice the 2.9 kWh/m^3 consumption of the Minjur seawater desalination plant (Fig. 1-6). By analyzing the RO process for POU systems in detail, we aim to identify other strategies for improving recovery with potentially lower energetic penalties.

6.2 General Description of POU RO Systems

Figure 6-1 shows an example of the filtration steps within a POU RO system. The core RO process highlighted in gray is the same across different products, but pre- and post-treatment steps may vary. This process contains a booster pump, RO element, and flow restrictor in the configuration shown. The highlighted subsystem is the focus of this study, as it is the largest energy consumer in the POU system. In this work, we tested the RO subsystem from a Dr. Aquaguard Magna purifier (Eureka-Forbes) [3] which consumes 24 W of the 35 W total electrical power consumption. The remainder is consumed by the ultraviolet (UV) lamp.

Incoming water is sufficiently pressurized for the pre- filtration, but the booster pump provides the pressure for RO desalination and post-filtration. Diaphragm pumps are typically used in this application because they are inexpensive. The pump used in this study was manufactured by CSE Company Ltd. (Model CS-0580Q-AQ); the observed efficiency matches POU RO pumps from other manufacturers. For example, from the data provided by Aquatec (Model 8800) and EFlow (Model ZS-ARO-N75G) for pumps providing similar pressure and flow-rate performance, the peak efficiencies are 47% and 34%, respectively. These values are comparable to the peak efficiency of 45 $\pm$ 2% observed for the pump evaluated in this work. Thus, our findings regarding the impact of pump efficiency are relevant to other POU RO devices.

Spiral-wound POU RO elements are also commodity items manufactured in standard sizes. The element evaluated in this work was manufactured by Infinite Water Solutions Ltd. (HTFC-75 NANO). It has a nominal permeate production capacity

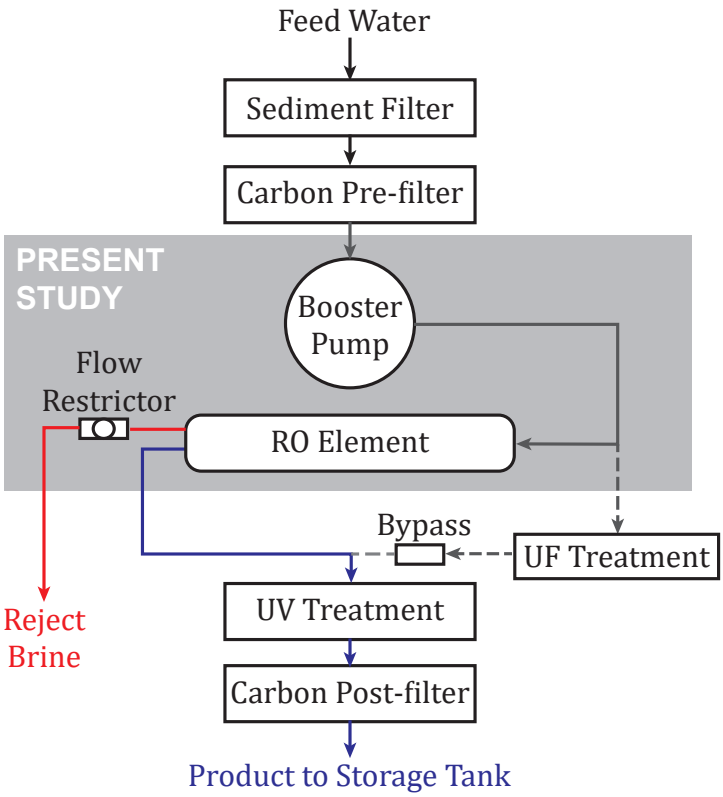

Figure 6-1: The general configuration of POU desalination systems includes a reverse osmosis stage surrounded by other treatment. The RO module of present interest is fixed (highlighted in gray), while the type of pre- and post- filtration may vary across different POU RO products.

of 12 L/h (75 gal/d) and matches the pressure versus flow performance of equivalent Pentair (TLC-75 [4]) and DOW (FilmTec^{TM} BW60-1812-75 [5]) products. This agreement provides further assurance that while only one POU product was evaluated here, the results can be generalized to other devices.

In some POU RO systems, a bypass valve is used to reintroduce salinity to the product stream. The extent to which this valve is opened depends on user preferences. In this work, we assume that there is no mixing of the feed and product to provide an upper bound on the system's second law efficiency.

Finally, it is worth noting that testing was performed on an RO element that was previously unused. Furthermore, the POU system implements a continuous flow configuration (Fig. 6-1) but is intermittently operated under normal use. Membrane permeability coefficients are known to decrease with sustained use [6], and particu-

larly with intermittent operation [7, 8], causing energy consumption to consequently increase and production rate to decrease. It follows that the results presented here represent the upper bound of energetic and production performance for POU RO systems.

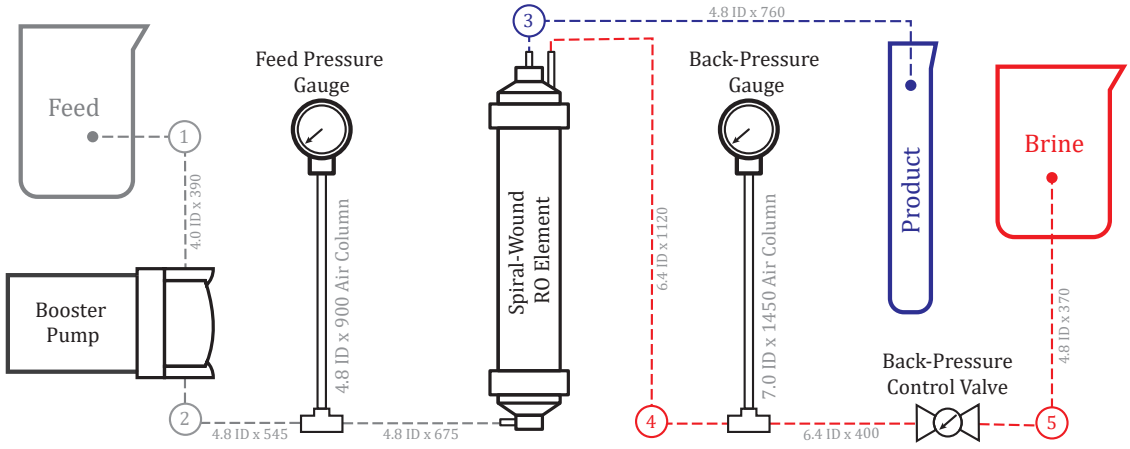

Figure 6-2: This is a schematic of the experimental setup. It incorporated a spiral-wound RO element and booster pump from a POU RO purifier. Flow-rates and concentrations of brine and product were measured for varying feed concentrations and pressures. Streams are numbered 1-5, and referenced in the exergy analysis (Sec. 6.4). The air columns attenuated pressure fluctuations. Tubing lengths and internal diameters [mm] are provided for pressure drop calculations.

6.3 Experimental Methods and Data

We first experimentally evaluated the RO subsystem from a POU purifier. Power consumption, rate of desalinated water production, and recovery ratio were measured to quantify performance (Sec. 6.3.1). To understand the conversion from electric to hydraulic energy, the motor was detached from the hydraulic end of the pump and evaluated independently on a dynamometer (Sec. 6.3.2). In this section, we detail both experiments and provide the raw results.

6.3.1 RO System Evaluation

A diaphragm booster pump and an encapsulated spiral-wound RO element were obtained from a Dr. Aquaguard Magna purifier (Eureka-Forbes) [3], and fitted to a test

setup (Fig. 6-2). The production rate, energy consumption, and recovery ratio of this system was measured at three feed concentrations (approximately 650, 1000, and 1800 mg/L of sodium chloride), and feed pressures ranging between 70 to 630 kPa, for a combined total of 26 tests (Table 6.1). Feed solutions, at all three concentrations, were prepared by adding lab-grade sodium chloride (Sigma-Aldrich) to distilled water whose initial conductivity was $\sim$2 us/cm.

The feed-pressure was adjusted using a control valve fitted to the reject line in approximately 70 kPa increments up to the maximum pump pressure of 630 kPa. This pressure was measured using a dial gauge (Ashcroft 1005). An additional pressure gauge (Dwyer Instruments) was fitted downstream of the RO element, so that viscous losses across the element could be quantified. Pressure fluctuations from the diaphragm pump were attenuated by the air occupying the sensing tubes connected to these gauges.

After setting the feed-pressure for each test, the system was allowed to achieve steady operation over a minimum of 60 s, which is approximately six times the feed residence time within the RO element. At the end of this period, the pump's DC current draw was recorded from the adjustable power supply (Dr. Meter PS-305DM). Then, brine and product were collected over an additional 45-60 s duration in a 2 L beaker and a 250 mL measuring flask, respectively. The collected masses of brine and product, measured using a weigh scale (Ohaus, Scout Pro), were subsequently used to estimate flow rates. Conductivities of the feed, brine, and product were measured at the end of each test using a handheld conductivity meter (Myron L Company, Ultrameter II). The same device was also used to measure feed temperature, which remained between 22-25°C through all tests.

Upon completing the tests, the RO element was unwound so that membrane and spacer dimensions could be measured. These data are provided to facilitate future modelling and design efforts (Table 6.2).

Table 6.1: Results from experimental evaluation of a commercial point-of-use RO desalination system

Test	**Feed Cond.**	**Temp.**	**Current**[a]	**Pressure** [psi]		**Time**	**Mass**[b] [g]		**Conductivity** [μs/cm]	
#	[μs/cm]	[°C]	[A]	Feed	Back	[s]	Prod	Brine	Prod	Brine
	±1%	±0.1°C	±0.01A	±1 psi		±1 s	±2 g	±2 g	±1%	±1%
1	1329	22.0	0.30	10	6.0 ± .1	40	90	1308	170	1333
2	1327	22.4	0.40	20	15.8 ± .2	50	115	1473	116	1356
3	1316	22.2	0.52	30	28.0 ± .5	60	163	1603	83	1383
4	1332	22.7	0.61	40	38.8 ± .1	55	187	1343	69	1430
5	1327	23.6	0.69	50	47.1 ± .3	50	203	1157	52	1474
6	1318	23.3	0.77	60	58.3 ± .3	45	218	943	47	1531
7	1315	24.0	0.85	71	68.0 ± .3	45	245	851	45	1590
8	1310	24.3	0.93	81	78.7 ± .3	45	268	736	44	1690
9	1219	24.2	1.01	91	91.4 ± .2	45	284	364	59	2340
10	1991	22.8	0.29	10	4.6 ± .3	30	87	1054	-[c]	1996
11	1997	23.3	0.40	20	16.7 ± .1	45	106	1334	127	2017
12	2035	23.5	0.51	30	28.4 ± .3	45	134	1213	150	2117
13	2028	23.7	0.60	40	38.0 ± .1	45	158	1133	113	2167
14	2031	23.9	0.68	50	48.5 ± .3	45	184	1028	94	2236
15	2021	24.0	0.77	60	58.5 ± .3	45	208	930	85	2317
16	2010	24.2	0.85	71	68.4 ± .2	45	232	832	91	2412
17	2001	24.3	0.93	81	80.8 ± .1	45	257	686	83	2590
18	1991	24.7	0.99	91	89.9 ± .2	45	269	410	101	3180
19	3514	25.0	0.39	20	16.5 ± .3	45	94	1353	983	3515
20	3493	24.9	0.50	30	28.3 ± .1	45	112	1259	893	3565
21	3507	24.9	0.59	40	37.9 ± .2	45	134	1180	416	3647
22	3502	24.9	0.70	50	49.0 ± .3	45	162	1058	262	3763
23	3497	24.9	0.79	60	59.0 ± .5	50	193	1035	216	3875
24	3487	25.0	0.87	71	69.5 ± .2	45	208	880	197	4018
25	3474	25.0	0.94	81	80.0 ± .6	45	228	750	187	4209
26	3408	24.9	1.00	91	90.4 ± .3	45	239	439	224	5019

a - Pump voltage was held constant at 24.1 ± 0.1 V.

b - Mass measurements include product and brine container masses of 86 ± 1 g and 161 ± 1 g, respectively.

c - The product volume collected in Test 10 was insufficient for conductivity measurements.

Table 6.2: RO element - membrane and spacer dimensions

Parameter	Value
Membrane width within glue strips, W	1.30 m
Membrane length within glue strips, L	0.19 m
Total membrane area[a], $2LW$	0.494 m^2
Feed spacer filament diameter, $d_{f,r}$	0.216 mm
Feed spacer filament spacing	1.75 mm
Feed spacer filament angle[b]	90°
Permeate spacer height	0.254 mm

a - Transport occurs across both walls of the permeate channel
b - Filament angle is defined as in Koutsou et al. [9].

6.3.2 Pump Motor Characterization

The torque-speed relationship of the brushed DC motor used in the booster pump was measured using a dynamometer [10], at its 24 V rating (Fig. 6-3). The speed of the absorber was controlled through 60 steps, from 0 to the motor's 95 rad/s maximum. The motor speed was allowed to settle after each speed command before torque, speed, and current were sampled at 150 Hz for 4 s and averaged.

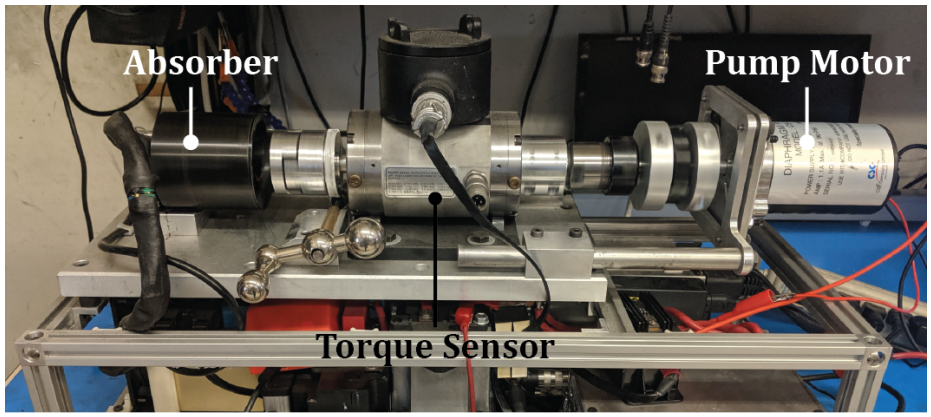

Figure 6-3: The torque-speed characteristics, and efficiency of the pump's motor were measured on a dynamometer. The absorber controls the speed of the motor, while the torque sensor measures torque output from the motor at that speed.

Dynamometer measurements were used to estimate the torque constant k_T [N-m/A], speed constant k_V [V-s/rad] and winding resistance R_m [Ohms] (Table 6.3). The slope and intercepts of the measured torque-current and speed-torque curves

were used to solve these constants (Fig. 6-4). The relevant linear relationships are

$$k_T = \frac{d\tau}{dI}, \tag{6.1}$$

$$k_V = \frac{V}{\omega_{max}}, \text{ and} \tag{6.2}$$

$$\frac{R_m}{k_V k_T} = -\frac{d\omega}{d\tau}, \tag{6.3}$$

where the motor torque is τ [N-m], I is the current [A], and ω_{max} is the no-load speed [rad/s] at voltage V [V]. MATLAB was used to perform the linear regression, and plot the prediction intervals that are shown [11].

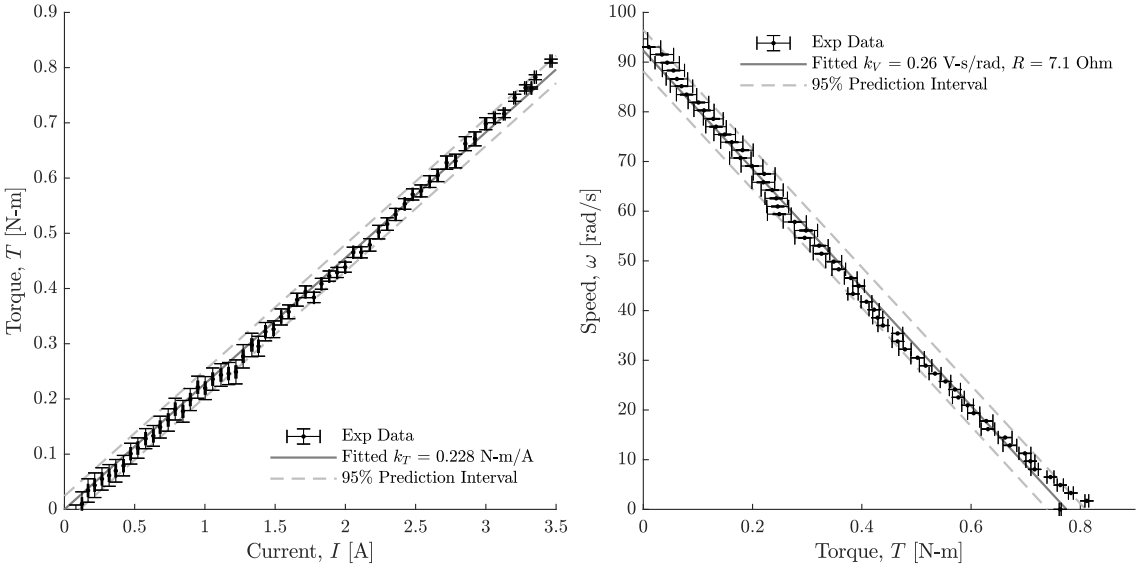

Figure 6-4: k_T equals the slope of measured torque vs. current (*left*). k_V and R_m were estimated from the y-intercept and slope of the measured speed vs. torque (right). The fitted models (Eqns. 6.1-6.3) match all experimental data within error. Each experimental data point represents the mean of 600 measurements. The error-bars on experimental data span the 95% confidence interval of the mean.

Table 6.3: Empirically-fitted motor constants

Parameter	**95% C.I.**
Velocity Constant, k_V [V-s/rad]	0.260 ± 0.003
Torque Constant, k_T [N-m/A]	0.228 ± 0.001
Winding Resistance, R_m [Ohm]	7.1 ± 0.2

6.4 Exergy Analysis

An exergy analysis was conducted to quantify the inefficiencies in the system. An overview of the methodology and key equations are presented here to guide the reader's understanding of the work. However, a more complete description of the exergy concept and its application to analyzing desalination systems can be found in Mistry et al. [12]. The total work of separation $\dot{W}_{sep}$ [W] is represented by the sum

$$\dot{W}_{sep} = \dot{W}_{least} + \sum_i \dot{\Xi}_{d,i}, \tag{6.4}$$

where $\dot{W}_{least}$ [W] is the least work of separation at a finite recovery ratio, and each $\dot{\Xi}_{d,i}$ [W] term represents the exergy destroyed by each component i due to irreversible operation. Normalizing by the volumetric rate of desalinated water production Q_p [m^3/s] allows the specific energy consumption SEC [J/m^3] to be represented as the sum of contributions from the least work and the losses,

$$SEC = \frac{\dot{W}_{sep}}{Q_p} = \frac{1}{Q_p}\left(\dot{W}_{least} + \sum_i \dot{\Xi}_{d,i}\right). \tag{6.5}$$

For the present system, the work of separation is the electrical energy supplied to the motor. Therefore

$$\dot{W}_{sep} = IV, \tag{6.6}$$

where V [V] is the voltage supplied to the motor, and I [A] is the measured current. Then, the second law efficiency of the system η_{II} is

$$\eta_{II} = \frac{\dot{W}_{least}}{IV}. \tag{6.7}$$

Each exergy destruction term is calculated from

$$\dot{\Xi}_{d,i} = \sum_{in-out} \dot{\Xi}_{w,i} + \sum_{in-out} \dot{\Xi}_{s,i}, \tag{6.8}$$

indicating that exergy flows can relate to both work $\dot{\Xi}_w$ or process streams $\dot{\Xi}_s$ [W]. For process streams, the specific exergy per unit mass ξ [J/kg] is defined as

$$\xi = \underbrace{(h - h^*)}_{\text{enthalpy}} - \underbrace{T_0(s - s^*)}_{\text{entropy}} + \sum_i^n \underbrace{w_i(\mu_i^* - \mu_{i,0})/M_i}_{\text{chemical potential}}, \tag{6.9}$$

where h, s, w_i, μ_i, and M_i are the specific enthalpy [J/kg], specific entropy [J/kg-K], the mass fraction of species i of n, its chemical potential [J/mol], and its molar mass [kg/mol], respectively. Properties with the superscript * are evaluated at the temperature T_0 [K] and pressure P_0 [Pa] of the environment, but at the same composition as the stream of interest (restricted dead state). However, properties with the subscript 0 are evaluated at the temperature, pressure, and composition of the environment (global dead state).

Table 6.4: Equations for quantifying each component's exergy destruction and exergy efficiency

Component, i	**Exergy Destruction,** $\dot{\Xi}_{d,i}$	**Exergy Efficiency**, ϵ_i
Full System	$IV - \dot{W}_{least}$, see Eqn. 6.10 for $\dot{W}_{least}$	$\dot{W}_{least}/(IV)$
Pump, Motor	$IV - \frac{k_T}{k_V}(IV - I^2R_m)$	$\frac{k_T}{k_V}(1 - IR_m/V)$
Pump, Hydraulics	$\frac{k_T}{k_V}(IV - I^2R_m) - P_fQ_f$	$P_fQ_f / \left(\frac{k_T}{k_V}(IV - I^2R_m)\right)$
RO Element	$P_fQ_f - P_bQ_b - \dot{W}_{least}$	$\dot{W}_{least} / (P_fQ_f - P_bQ_b)$
Flow Restrictor	P_bQ_b	-

Applying these expressions, we derived the exergy destruction and exergy efficiency for each component. The equations are summarized in Table 6.4, while details are provided in the following subsections. The primary assumptions include:

1. All streams are at the temperature of the feed solution. This is a common assumption for the analysis of RO systems since it is a pressure-driven process. It follows that the enthalpy differences in Equation 6.9 may only arise due to changes in pressure.

2. The disposal of concentrated brine is not treated as lost exergy. Instead, the least work is defined as the minimum work to separate the feed stream into concentrated and diluted streams, at a finite recovery ratio. This definition

allows direct comparison with exergy efficiencies of brackish water RO plants reported in literature. When the disposal of concentrated brine is treated as lost exergy, the maximum second law efficiency drops from 1.80 ± 0.05% (Sec. 6.5.1) to 1.61 ± 0.05% while other conclusions are unaffected. For a detailed discussion on the difference between the two approaches, Qureshi et al. [13] and Mistry et al. [12] are recommended.

3. The solution is treated as incompressible. Therefore, entropy has no pressure dependence.

4. The feed temperature, composition, and atmospheric pressure specify the global dead state for each test.

5. The literature provides different definitions for the exergy efficiency of the RO element. We apply the definition provided by Blanco-Marigorta et al., whereby the RO element is evaluated on its ability to exchange physical exergy for chemical exergy [14].

6.4.1 Least Work of Separation

The least work of separation is the difference in chemical potential energy of the product and brine streams, relative to the feed. From the derivation provided in Appendix C,

$$\begin{aligned} \dot{W}_{least} = 2\dot{m}_{H_2O,p}RT \left[-b_p\phi_p + b_f\phi_f + b_p \ln\left(\frac{\gamma_p b_p}{\gamma_f b_f}\right)\right] \\ +2\dot{m}_{H_2O,b}RT \left[-b_b\phi_b + b_f\phi_f + b_b \ln\left(\frac{\gamma_b b_b}{\gamma_f b_f}\right)\right]. \end{aligned} \tag{6.10}$$

The mass flow rate of water in each stream $\dot{m}_{H_2O}$ [kg/s] and the associated molality of sodium chloride b [mol/kg] were calculated from the raw results using the procedure outlined in Appendix D. R is the gas constant [J/mol-K], T is temperature [K], and the product, brine, and feed streams are differentiated by subscripts p, b, and f,

respectively. The osmotic coefficients ϕ and mean molal activity coefficients γ were taken from Partanen's work [15].

Note that at the limit of infinitesimal recovery ($b_b = b_f$) and pure water production ($b_p = 0$), Equation 6.10 simplifies to

$$\dot{W}_{least} = \frac{\dot{m}_{H_2O,p}}{\rho_{H_2O}} \left(2RTb_f\phi_f\rho_{H_2O}\right) = Q_p\pi_f, \tag{6.11}$$

where π_f [Pa] is the osmotic pressure of the feed.

6.4.2 Pump Motor

As specified earlier, the exergy input to the motor is the electrical power (IV). Exergy output from the brushed DC motor $\dot{\Xi}_{out,m}$ [W] is mechanical power, given by the product of torque τ [N-m] and rotational speed ω [rad/s]. Since these quantities could not be directly measured during operation of the pump, the exergy output was estimated from

$$\begin{aligned} \dot{\Xi}_{out,m} &= \tau\omega = k_T I \left(\frac{V}{k_V} - \frac{R_m}{k_T k_V}\tau\right) \\ &= \frac{k_T}{k_V}\left(IV - I^2R_m\right), \end{aligned} \tag{6.12}$$

using fitted motor constants from dynamometer testing (Table 6.3).

6.4.3 Pump Hydraulics

The two exergy inputs are related to the mechanical power from the motor and the feed stream (Stream 1 in Fig. 6-2). Since this stream defines the dead state properties, $\dot{\Xi}_1 = 0$. Neglecting the dependence of entropy on pressure (Assumption 3), the exergy flow associated with output Stream 2 is

$$\dot{\Xi}_2 = P_f Q_f, \tag{6.13}$$

due to the elevated feed pressure P_f [Pa]. The average feed volumetric flow rate Q_f [m^3/s] for each test can be estimated from the measured product and brine mass flow rates $\dot{m}$ using

$$Q_f = \frac{1}{\rho}\left(\dot{m}_p + \dot{m}_b\right), \tag{6.14}$$

where ρ [kg/m^3] is taken to be the density of the solution at the dead state. Appendix D outlines how the solution density, molality, and molarity were correlated to the conductivity measurements.

6.4.4 RO Element

The exergy input of the feed stream Ξ_2 is given in Equation 6.13, while the brine and product streams form the exergy outputs. Applying Equation 6.9 to the product (Stream 3), we find that the exergy is only related to the chemical potential difference since the temperature and pressure are equal to those of the dead state. Then, applying the same substitutions as in Appendix C,

$$\dot{\Xi}_3 = 2\dot{m}_{H_2O,p}RT\left[-b_p\phi_p + b_f\phi_f + b_p\ln\left(\frac{\gamma_p b_p}{\gamma_f b_f}\right)\right]. \tag{6.15}$$

The brine leaving the RO element (Stream 4) is pressurized to P_b [Pa]. Accounting for both the enthalpy and chemical potential difference,

$$\dot{\Xi}_4 = P_b Q_b + 2\dot{m}_{H_2O,b}RT\left[-b_b\phi_b + b_f\phi_f + b_b\ln\left(\frac{\gamma_b b_b}{\gamma_f b_f}\right)\right], \tag{6.16}$$

where Q_b is the brine volumetric flow-rate.

Note that summing the exergy outputs from the RO element and substituting Equation 6.10 gives the result

$$\dot{\Xi}_3 + \dot{\Xi}_4 = \dot{W}_{least} + P_b Q_b. \tag{6.17}$$

The least work of separation appears in this expression because the separation process occurs within the RO element.

6.4.5 Flow Restrictor

The restrictor depressurizes the brine stream. Therefore the exergy of Stream 5 is simply reduced from that of Stream 4 (Eqn. 6.16) to

$$\dot{\Xi}_5 = 2\dot{m}_{H_2O,b}RT\left[-b_b\phi_b + b_f\phi_f + b_b\ln\left(\frac{\gamma_b b_b}{\gamma_f b_f}\right)\right]. \tag{6.18}$$

6.5 Results and Discussion

The exergy analysis outlined above was conducted using the measured data to estimate second law efficiency, highlight significant losses, and suggest areas for improvement.

6.5.1 Specific Energy Consumption

Specific energy consumption (SEC) is plotted against feed pressure and feed concentration (Fig. 6-5). Tests where the applied pressure only marginally exceeded the osmotic pressure were excluded given that the permeate production rate was far below the RO element's nominal 12 L/h specification. Likewise, tests conducted at 625 kPa were excluded because brine flow was almost fully choked, and the pump was close to stalling. Between these limits, a minimum measured specific energy consumption of 1.54 ± 0.04 kWh/m^3 was obtained at the lowest feed concentration of 650 mg/L, and the highest feed pressure of 560 kPa.

SEC increased with feed concentration as expected, because permeate flux decreases when a constant pressure is applied against increasing feed osmotic pressures. At the same 560 kPa pressure, the SEC was 1.63 ± 0.05 kWh/m^3 and 1.99 ± 0.06 kWh/m^3 for the intermediate and high feed concentrations, respectively. Figure 6-5 also shows SEC decreasing with increasing feed pressure. This behavior is examined more closely in the following subsection.

The stacked bars (Fig. 6-5) present a breakdown of SEC into the least work of separation and accumulated losses due to exergy destruction at the individual components, per Equation 6.5. This breakdown indicates that the booster pump (motor

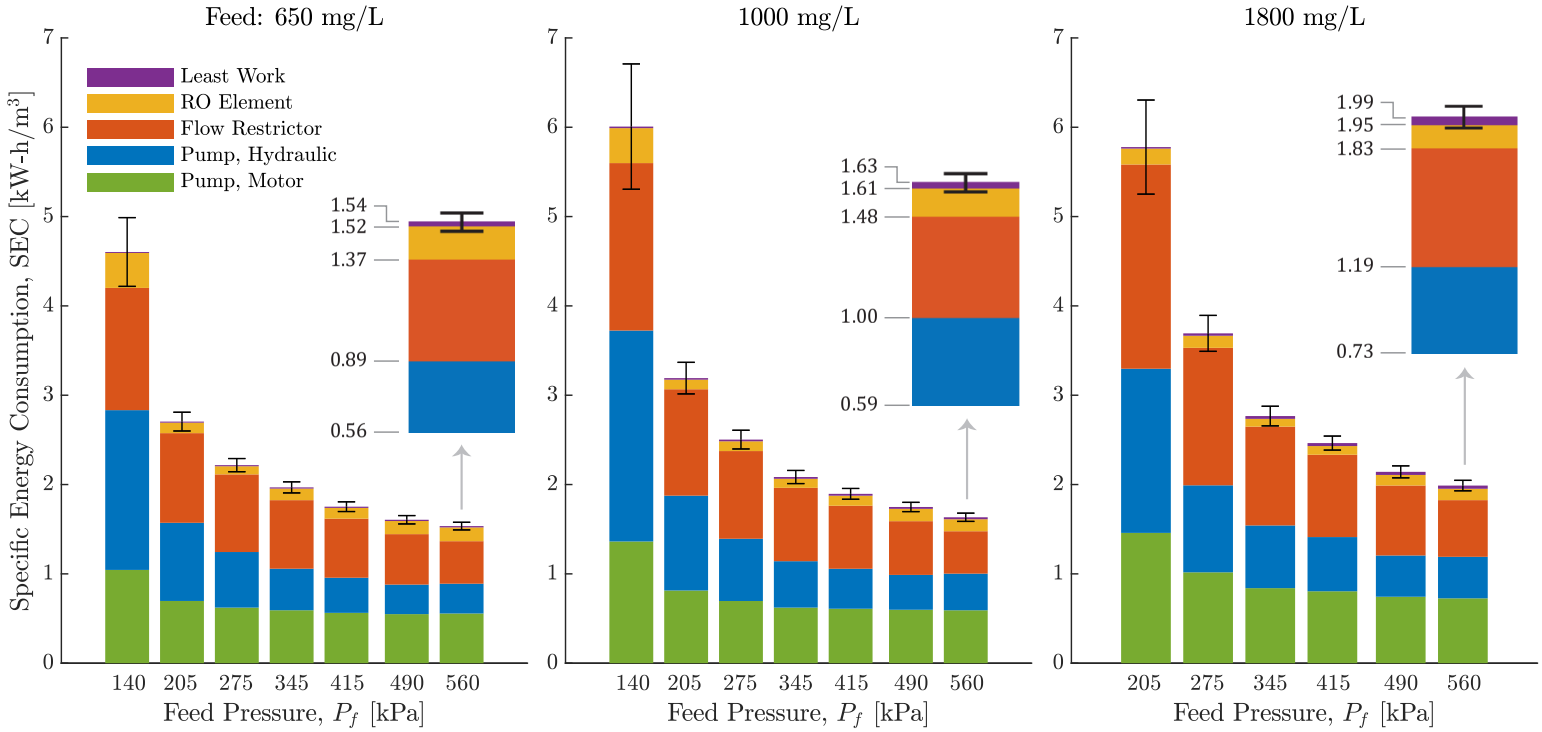

Figure 6-5: The measured specific energy consumption (SEC) is plotted for varying feed pressures at the three different feed concentrations. It is represented as the sum of the least work of separation and the accumulated exergy destruction at components, all normalized by the volumetric production rate. The total bar height at each feed pressure is the SEC, while the ratio of the purple bar height to total height is the system's second law efficiency (quantified in Fig. 6-7). For clarity, pressures were rounded to the nearest 5 kPa after conversion from psi. Error bars represent propagated measurement uncertainty.

and hydraulics, together), followed by the discharge of pressurized brine, contribute the greatest losses in the system. These losses respectively account for 36%, 25%, and 29% of the measured SEC at 1000 mg/L and highest feed pressure. Note that the motor is the most upstream component in the system that was analyzed; hence, it provides the power for all downstream processes. Downstream inefficiencies therefore have a compounded effect on the exergy destruction at the motor. For example, if the exergy destruction associated with brine depressurization were lowered, then the motor would be required to output less power to maintain the same potable water production rate. If the efficiency of the motor remained constant, one could then expect to also see a decrease in the SEC contribution from the motor. It follows that reducing, or recovering, the brine pressure can significantly decrease the system SEC.

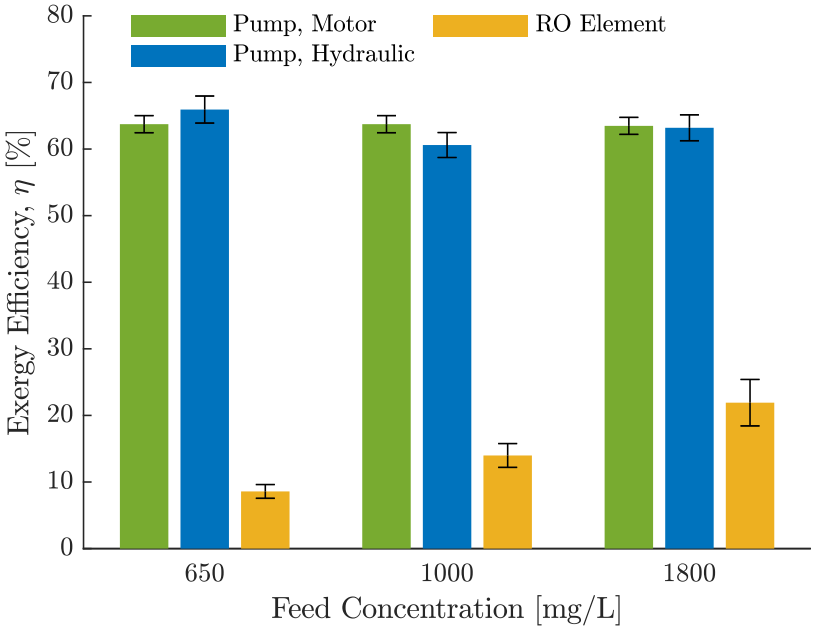

Figure 6-6: Exergy efficiencies of the individual components are plotted against feed concentration, for operation at 550 kPa feed pressure. The efficiency definitions are summarized in Table 6.4. The flow restrictor is a purely dissipative element ($\eta = 0$) and is therefore excluded here. Error bars represent the root mean square of measurement uncertainty and standard deviation.

At 8%, the RO element provides the smallest contribution to the SEC of the system, but a comparison of exergy efficiencies reveals that it is the least efficient component (Fig. 6-6). These two results are consistent because the RO element

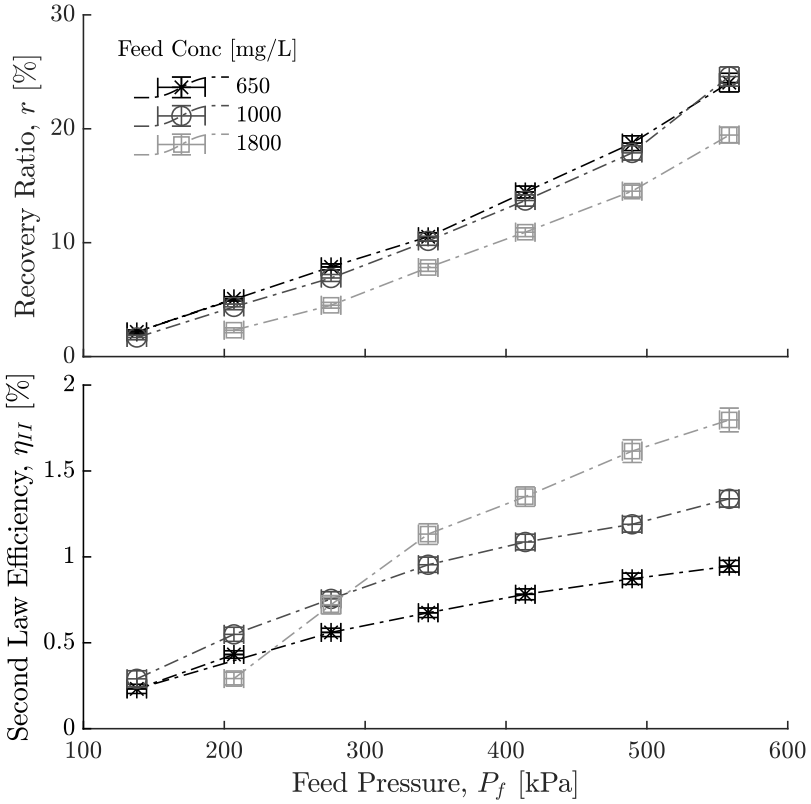

Figure 6-7: Recovery ratio and system efficiency both increased with feed pressure. The maximums were 24.6% ± 0.8% and 1.80% ± 0.05%, respectively. Error bars represented propagated measurement uncertainty.

consumes only a small fraction of the hydraulic power generated by the pump. The remainder is dissipated by the flow restrictor. Therefore, permeation losses, viscous losses, and losses due to concentration polarization at the RO element are small when compared to losses at the other components under the intended system operation. Therefore, improving the efficiency of the RO element alone will not decrease SEC significantly.

6.5.2 Effect of Feed Pressure on Production Rate, Recovery, and Specific Energy Consumption

The maximum measured second law efficiency for the system was 1.80 ± 0.05% at the 1800 mg/L feed and maximum pressure (Fig. 6-7). In the previous subsection, we highlight that one way to improve this efficiency is to recover the exergy destroyed

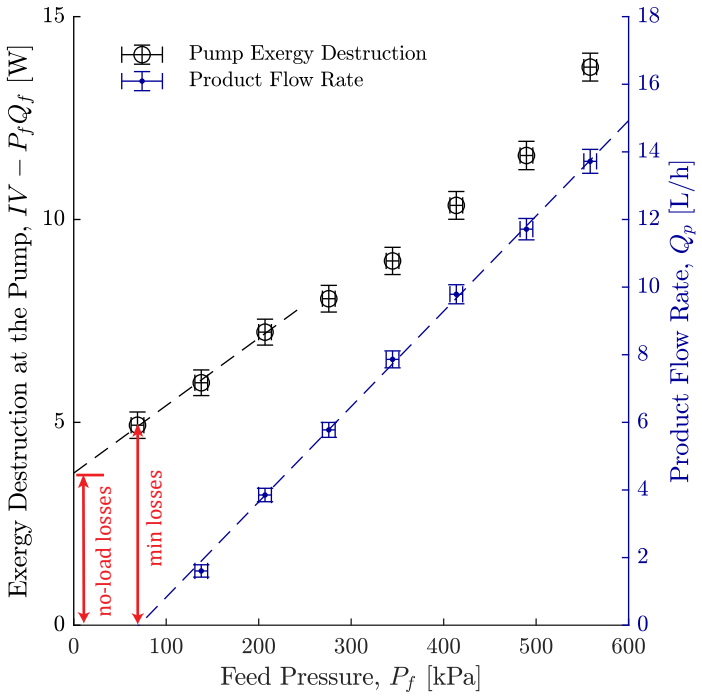

Figure 6-8: Exergy destruction at the pump is plotted with product flow rate against feed pressure. The x-intercept of the flow rate vs. feed pressure plot is the feed osmotic pressure π_f. Above this pressure, the flow rate is linear with the over-pressure ΔP_f. A minimum of 5 W is dissipated by friction at the pump before any desalinated water is produced. Results are plotted for the 1000 mg/L feed, and error bars represent propagated measurement uncertainty.

at the flow restrictor. Here, we show that another potential solution is to increase feed pressure. The observed decrease in SEC with rising feed pressure (Fig. 6-5) is explained by two mechanisms.

1. The SEC decays with feed pressure because a nominal pumping loss is distributed over increasing volumes of produced water. Approximately 5 W are lost to pump friction before any desalinated water is produced from the 1000 mg/L feed (Fig. 6-8). This minimum energy loss is the sum of frictional losses within the pump at no-load conditions and the losses incurred in overcoming the feed osmotic pressure.

2. Increasing feed pressure raises recovery (Fig. 6-7), which in turn decreases exergy destruction at the flow restrictor. To understand this relationship, we begin with the expression for exergy destruction at the flow restrictor (Table

6.4) and neglect viscous pressure drop through the RO feed channel so that $P_b \approx P_f$. Then, the respective contribution to SEC is approximately

$$SEC_f \approx \frac{P_f Q_b}{Q_p} = \pi_f \left(\frac{1}{r} - 1 \right) + \frac{\Delta P_f}{Q_p} Q_b, \tag{6.19}$$

where r is the recovery ratio. Similarly to Mechanism 1 above, the osmotic pressure π_f represents the minimum hydraulic potential before any desalinated water is produced. The first term on the right-hand side of Equation 6.19 pertains to the SEC decay as this energy requirement is divided over increasing product volumes. Meanwhile, ΔP_f represents the over-pressure required to generate permeate flux. The constant slope in Figure 6-8 indicates that the ratio of this term to the product flow rate Q_p is constant. However, brine flow rate Q_b decreases with increasing feed pressure; therefore, the second term also decreases with feed pressure. Note that the exergy destruction at the brine throttle approaches zero as the recovery ratio approaches one.

Raising feed pressure will further decrease SEC contributions at the pump and throttle via both mechanisms, albeit at an evidently diminishing rate (Fig. 6-5). However, an opposite trend is observed with the RO element (Fig. 6-9). By substituting the simplified least work of separation (Eqn. 6.11) within the expression for exergy destruction at the RO element provided in Table 6.4, we get the approximate expression

$$\dot{\Xi}_{d,e} \approx P_f Q_f - P_b Q_b - \pi_f Q_p, \tag{6.20}$$

and the corresponding contribution to the specific energy consumption is

$$SEC_e = \left(\frac{P_f Q_f - P_b Q_b}{Q_p} \right) - \pi_f. \tag{6.21}$$

At low permeate fluxes, when brine flow rates are highest, energy consumption is dominated by viscous pressure drop through the feed channel. At higher permeate fluxes, in the intended operating regime, this viscous pressure drop decreases so that the brine pressure P_b approaches the feed pressure P_f (Table 6.1). Then, Equation

6.21 can be approximated by

$$SEC_e \approx P_f - \pi_f = \Delta P_f. \tag{6.22}$$

The product flow rate grows linearly with this over-pressure (Fig. 6-8). After normalizing the product flow by total membrane area (Table 6.2), the proportionality constant between permeate flux J_w and over-pressure ΔP gives an effective membrane permeability coefficient of $A_m = 5.7 \pm 0.2$ L/m^2-h-bar. This value is lower than the membrane's actual permeability coefficient, because it also accounts for concentration polarization. Substituting this linear relationship into Equation 6.22 gives

$$SEC_e \approx \frac{1}{A_m} J_w. \tag{6.23}$$

The calculated element SEC closely matched this expected linear relationship (Fig. 6-9). The small systematic difference is caused by the pressure drop in the brine stream.

Thus, we have shown that specific exergy destruction at the RO element grows linearly with increasing feed pressure (Fig. 6-9), while at the pump and throttle it decays with feed pressure (Fig. 6-5). For the present system, exergy destruction at the pump and throttle outweigh those at the RO element. Therefore, small increases in feed pressure will produce a net decrease in SEC. There are however two factors that may limit how much feed pressure may be increased:

- Maximum Permeate Flux: Membrane manufacturers recommend an average permeate flux of 23-31 L/m^2-h for brackish water desalination to minimize fouling and prevent mechanical damage [16, 17]. At the highest pressures, the 30 L/m^2-h flux for the present system approaches the upper bound of this design recommendation (Fig. 6-9). As a result, accelerated fouling or membrane damage may be one barrier to raising feed pressure beyond the present range. Additional experimental investigation is recommended to characterize these effects.

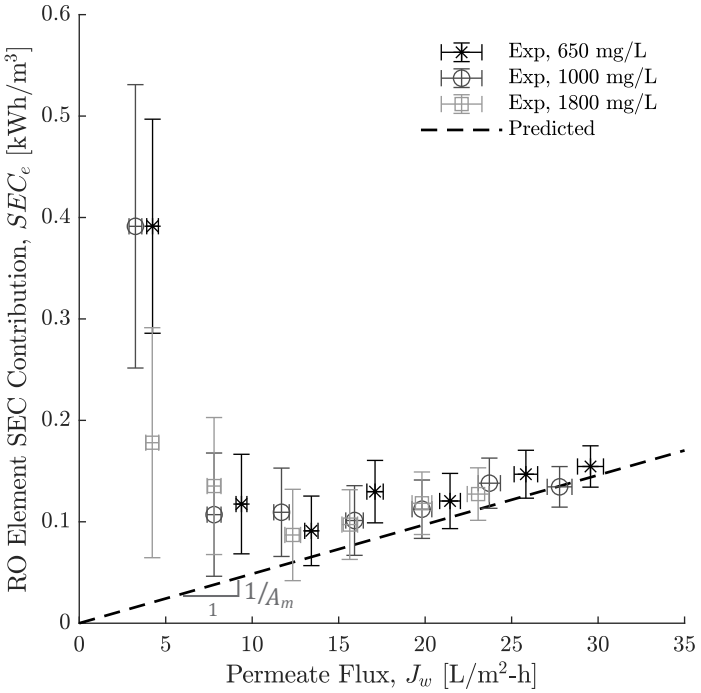

Figure 6-9: The SEC contribution due to exergy destruction at the RO element is plotted against permeate flux J_w. Viscous pressure drop through the brine channel dominates at low flux, while pressure drop due to membrane permeation dominates at high flux. The latter process is expected to produce a linear trend with a slope corresponding to the inverse of the effective membrane water permeability coefficient, A_m = 5.7 ± 0.2 L/m^2-h-bar. Error bars represent propagated measurement uncertainty.

- Maximum Element Pressure: Another barrier to raising feed pressure is the maximum pressure rating: 830 kPa for the present RO element. We did not investigate failure mechanisms that prevent operation at higher pressures. However, other manufacturers provide products that are rated to higher pressures: 1035 kPa for both FilmTec^{TM} [5] (DOW) and NanoH$_2$O^{TM} (LG) products [18]. Therefore, it seems feasible for a system to be designed for higher feed pressures.

Reiterating Mechanisms 1 and 2 above, raising feed pressure decreases SEC by increasing recovery ratio. The same can be achieved by maintaining the same feed pressure and increasing membrane area instead. With this approach, the permeate flux would not exceed recommended design limits. Potential solutions here include an element with larger membrane area or a second RO stage. Alternatively, recovery ratio could be increased by recirculating the brine in a batch or semi-batch process [19–23]

so that the same membrane area is reused several times within a single batch. In all cases, designers would be required to balance the efficiency gains with an increased capital cost. They would also have to fit more equipment within the compact POU purifier bodies.

Examining Figures 6-7 and 6-8 together, it is also seen that recovery ratio, production rate, and second law efficiency improve simultaneously with increasing feed pressure. This synergy could be potentially exploited to improve system performance across-the-board.

6.5.3 Pump Performance

Summing electric and hydraulic losses, we find that the booster pump assembly (motor and hydraulic end together) is the greatest source of losses (Fig. 6-5). These losses could be decreased by raising the pump efficiency η_p, which peaked at 45 ± 2% and remained relatively flat over a wide operating range (Fig. 6-10). However at this peak, the motor efficiency η_m is 70 ± 1%, giving an estimated hydraulic efficiency η_h ($= \eta_p/\eta_m$) of 64 ± 1%. These efficiencies are acceptable given the small size of the pump and it would be therefore difficult to increase them substantially.

6.6 Conclusions

Point-of-use reverse osmosis (POU RO) devices have been useful in enabling households to produce drinking water from saline water supplies. However, they are inefficient when compared to large-scale processes, with respect to both recovery ratio and specific energy consumption (SEC). In this work, an RO element and corresponding pump from one such POU device was experimentally evaluated at varying feed pressures of 70 - 630 kPa and three sodium chloride concentrations: 650, 1000, and 1800 mg/L. A subsequent exergy analysis using the experimental results indicated a maximum second law efficiency of 1.80 ± 0.05% for the system, and a minimum SEC of 1.54 ± 0.04 kWh/m^3.

Four directions for decreasing SEC were identified. First, the depressurization

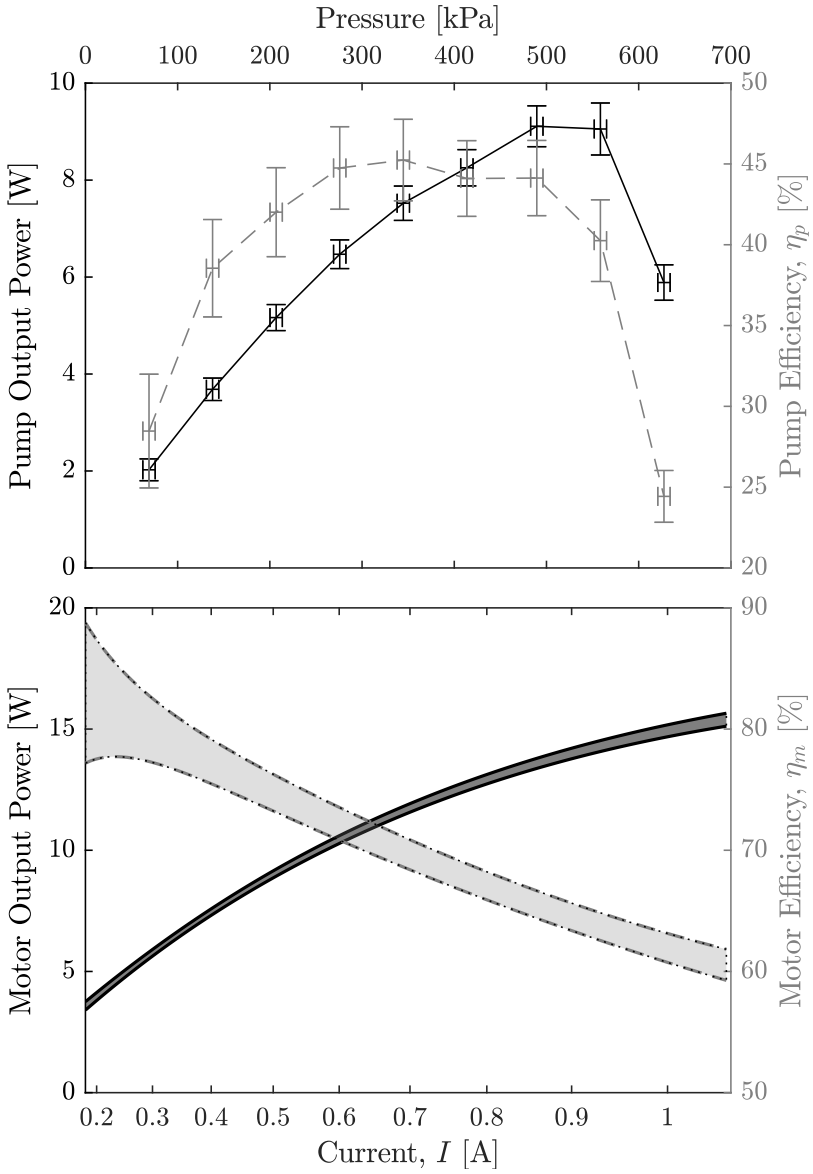

Figure 6-10: The measured pump (motor and hydraulic) power and efficiency are plotted against feed pressure (*top*). The 95% prediction interval for motor power and efficiency are represented by the shaded region for the same operating range, by correlating pump pressure to current draw (*bottom*). The combined pump efficiency peaked at 45 ± 2%, while the motor alone is most efficient at low output powers where small currents decrease ohmic losses. Error bars in the top graph represent measurement uncertainty.

of brine at the flow restrictor accounts for 29% of the specific energy consumption. Recovering this energy will also decrease losses at the upstream pump. The second suggestion involves raising feed-pressure to increase recovery ratio. This approach would decrease exergy destruction due to brine throttling, and distribute pump frictional losses over greater volumes of produced water. However, since the 30 L/m^2-h permeate flux at the highest pump pressures already approaches the maximum recommended values for brackish water desalination, operation at even higher pressures may increase fouling propensity. To overcome this concern, a third approach is to maintain the same feed pressures but increase membrane area. Finally, the recovery could also be increased by recirculating the brine through the RO element in a batch or semi-batch process.

The spiral-wound RO element had an exergy efficiency of 8.6 - 21.9% at maximum pressure, when SEC was lowest for each feed. Losses were primarily caused by over-pressure due to concentration polarization and permeation through the membrane. These losses account for only 8% of the system's SEC at the 1000 mg/L feed. Improving the element's efficiency alone is therefore unlikely to decrease the overall system SEC significantly. However, element upgrades that enable higher pressure operation, or increase water recovery, could promote significant energy savings at other components.

This work can guide new developments to decrease the impact of POU RO devices on scarce energy and groundwater resources in countries such as India, where they are increasingly used.

Bibliography

[1] H. Elfil, A. Hamed, and A. Hannachi. Technical evaluation of a small-scale reverse osmosis desalination unit for domestic water. *Desalination*, 203(1-3):319–326, 2007.

[2] Sreekumaran Thampy, Girish R. Desale, Vinod K. Shahi, Babubhai S. Makwana, and Pushpito K. Ghosh. Development of hybrid electrodialysis-reverse osmosis

domestic desalination unit for high recovery of product water. *Desalination*, 282(1418):104–108, 2011.

[3] Eureka Forbes Ltd. Dr. Aquaguard Magna RO Purifier. `https://www.eurekaforbes.com/water-purifiers/dr-aquaguard-magna-nxt-hd-ro-uv`. Accessed: 2019-01-05.

[4] Pentair Filtration & Process. TLC^{TM} Thin Layer Composite Residential Membranes. `https://www.pentair.com/content/dam/extranet/brochures-and-catalogs/water-purification/tlc/4001415-rev-d-mr14.pdf`. Accessed: 2019-09-21.

[5] Applied Membranes Inc. DOW FilmTec^{TM} BW60-1812-75 Membrane Specifications. `https://www.appliedmembranes.com/media/wysiwyg/pdf/membranes/bw60-1812-75_membrane_specifications.pdf`. Accessed: 2019-09-20.

[6] Emily W. Tow, David M. Warsinger, Ali M. Trueworthy, Jaichander Swaminathan, Gregory P. Thiel, Syed M. Zubair, Allan S. Myerson, and John H. Lienhard. Comparison of fouling propensity between reverse osmosis, forward osmosis, and membrane distillation. *Journal of Membrane Science*, 556:352 – 364, 2018.

[7] M. Freire-Gormaly and A.M. Bilton. Impact of intermittent operation on reverse osmosis membrane fouling for brackish groundwater desalination systems. *Journal of Membrane Science*, 583:220 – 230, 2019.

[8] Ch. Tzotzi, T. Pahiadaki, S.G. Yiantsios, A.J. Karabelas, and N. Andritsos. A study of caco3 scale formation and inhibition in ro and nf membrane processes. *Journal of Membrane Science*, 296(1):171 – 184, 2007.

[9] C. P. Koutsou, S. G. Yiantsios, and A. J. Karabelas. A numerical and experimental study of mass transfer in spacer-filled channels: Effects of spacer geometrical characteristics and Schmidt number. *Journal of Membrane Science*, 326(1):234–251, 2009.

[10] Ben Katz. Build Its in progress: Motor dyno. `http://build-its-inprogress.blogspot.com/2016/10/motor-dyno-updates-first-tests.html`. Accessed: 2018-09-05.

[11] MATLAB. *version 9.6.0 (R2019a)*. The MathWorks Inc., Natick, Massachusetts, 2010.

[12] Karan H Mistry, Ronan K McGovern, Gregory P Thiel, Edward K Summers, Syed M Zubair, and John H Lienhard. Entropy Generation Analysis of Desalination Technologies. *Entropy*, 13(12):1829–1864, sep 2011.

[13] Bilal Ahmed Qureshi and Syed M. Zubair. Exergetic analysis of a brackish water reverse osmosis desalination unit with various energy recovery systems. *Energy*, 93:256–265, 2015.

[14] A. M. Blanco-Marigorta, A. Lozano-Medina, and J. D. Marcos. A critical review of definitions for exergetic efficiency in reverse osmosis desalination plants. *Energy*, 137:752–760, 2017.

[15] Jaakko I. Partanen. Mean Activity Coefficients and Osmotic Coefficients in Dilute Aqueous Sodium or Potassium Chloride Solutions at Temperatures from (0 to 70) °C. *Journal of Chemical and Engineering Data*, 61(1):286–306, 2016.

[16] Hydranautics. Hydranautics Design Limits. `http://membranes.com/docs/trc/Dsgn_Lmt.pdf`. Accessed: 2019-09-25.

[17] LANXESS Lewabrane. Guidelines for the Design of Reverse Osmosis Membrane Systems. `http://membranes.com/docs/trc/Dsgn_Lmt.pdf`. Accessed: 2019-09-25.

[18] LG Chem. Nano H_2O^{TM} Membranes, Residential Reverse Osmosis (RO) Element. `https://watertechgroup.com/images/Datasheets/ro-nano-uf/lg-membrane/lg-residential/Water-Tech---LG-Chem-Residential-RO-Membranes.pdf`. Accessed: 2019-09-21.

[19] Tianyu Qiu and Philip A. Davies. Comparison of configurations for high-recovery inland desalination systems. *Water*, 4(3):690–706, 2012.

[20] David M. Warsinger, Emily W. Tow, Kishor G. Nayar, Laith A. Maswadeh, and John H. Lienhard. Energy efficiency of batch and semi-batch (CCRO) reverse osmosis desalination. *Water Research*, 106:272–282, 2016.

[21] Jay R. Werber, Akshay Deshmukh, and Menachem Elimelech. Can batch or semi-batch processes save energy in reverse-osmosis desalination? *Desalination*, 402:109 – 122, 2017.

[22] Quamtum J. Wei, Carson I. Tucker, Priscilla J. Wu, Ali M. Trueworthy, Emily W. Tow, and John H. Lienhard. Batch Reverse Osmosis: Experimental Results, Model Validation, and Design Implications. In *Membrane Technology Conference & Exposition*, New Orleans, LA, 2019. American Membrane Technology Association.

[23] Quantum J. Wei, Carson I. Tucker, Priscilla J. Wu, Ali M. Trueworthy, Emily W. Tow, and John H. Lienhard. Impact of salt retention on true batch reverse osmosis energy consumption: Experiments and model validation. *Desalination*, 479(October 2019):114177, 2020.

Chapter 7

Engineering a Semi-Batch Reverse Osmosis System for Point-of-Use Applications

Grace Connors and Quantum Wei contributed to the work presented in this chapter. In addition, the work was heavily informed by research conducted by the Lienhard Research Group.

7.1 Introduction

In the previous chapter, it was identified that point-of-use reverse osmosis (POU RO) desalination could be made more energy- and water-efficient by adopting a batch or semi-batch configuration, where the brine is recirculated to increase recovery. This chapter justifies the selection of a semi-batch configuration over batch, describes the design of a prototype system, and outlines the additional improvements that could be made.

7.1.1 Batch vs. Semi-Batch RO Systems

Brine can be recirculated through the RO element to increase recovery in three different manners (Fig. 7-1). In continuous RO processes, a fraction of the brine from the output of the RO element can be recycled and mixed with feed at the input (7-1A). While this recycling increases recovery, it also raises the concentration of the water that is being desalinated. The greater the fraction of brine that is recycled, the higher this feed concentration. Raising the feed concentration could in turn decrease the production rate and increase the likelihood of salt precipitation within the RO element; therefore, the other methods of recirculating brine were favored for the POU application.

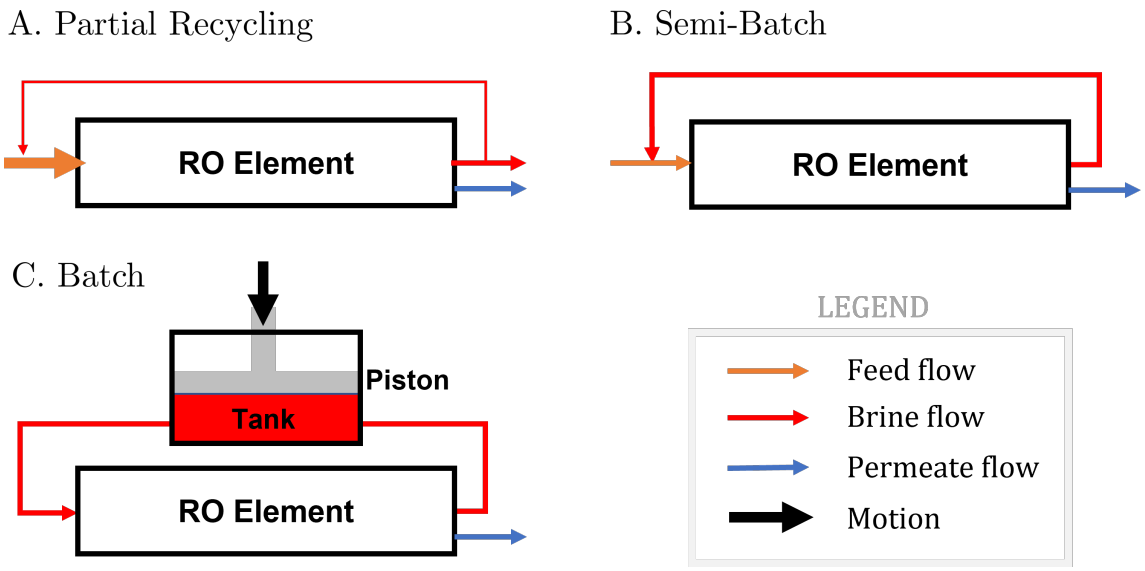

Figure 7-1: **There are different methods for recirculating brine.** (A) A small fraction of the brine can be mixed with the feed inflow in a continuous RO desalination process. Alternatively, RO desalination can be performed in batches. In a semi-batch process (B), all the brine is recirculated and mixed with incoming feed until the brine concentration reaches a specified maximum. Then it is flushed out and the process is reset. Alternatively, in a true batch process (C), there is no mixing of the brine with incoming feed. Instead, brine is recirculated through a variable volume tank to account for permeate volume losses. Once the brine concentration reaches a specified maximum, it is flushed out and replaced with new feed.

In semi-batch and true batch processes, water is treated in *batches*. In a semi-batch RO process, all the brine leaving the RO element is recirculated and mixed

with incoming feed (Fig. 7-1B). This process continues until the brine concentration reaches a specified maximum. Then it is flushed out of the system and replaced with new feed. In a true batch process, there is no mixing of brine with feed. Instead, a variable volume capacity is added to accommodate losses in the total brine volume as permeate is produced (Fig. 7-1C). Once the brine is sufficiently concentrated, it is flushed and replaced with new feed. There are different solutions for how a varying brine volume can be accommodated, including a bladder [1, 2], a double-acting piston [3, 4], and a tank or reservoir [5]. While both semi-batch and true batch RO processes can be used to increase recovery, the following factors influenced the selection of the former over the latter:

Footprint

In a batch process, the feed that is initially held in the reservoir gradually permeates across the RO membrane over the batch cycle. The concentrated brine that remains in the system at the end of this cycle is then flushed out. Therefore, the minimum reservoir volume V_r increases with the target recovery ratio r of the process according to

$$V_r = V_s \frac{r}{(1-r)}, \tag{7.1}$$

where V_s is the hold-up volume of the RO element and piping system [6]. For the 60% recovery ratio mandated by the NGT, the reservoir volume is 1.5 times the system volume. This additional volume would make it more challenging to fit a batch RO process within compact POU water purifiers. In contrast, semi-batch RO processes have smaller footprints because they do not require this separate reservoir.

Feed-Brine Mixing

By preventing the mixing of brine with feed, true batch RO can consume less energy than semi-batch RO. For brackish water desalination, these savings only become significant for recoveries exceeding 60-70% [6, 7]. Since the mandated recovery sits at this threshold, a batch process does not provide a significant energetic benefit over a

semi-batch process for this application.

Incomplete Flushing and Salt Retention

Incomplete flushing of brine at the end of one batch cycle will result in salt retention that elevates the concentration at the start of the subsequent cycle. Lee et al. found that for their experimental semi-batch RO system, a minimum of three to four times the system volume was needed for flushing (without that volume being recycled) [8, 9]. Wei et al. took a different approach by flushing their batch RO system with only one times the system volume [2]. They minimized the feed volume lost to flushing and accepted the resulting feed salinity elevation. In both approaches, minimizing system volume will decrease the feed volume lost to flushing. Since semi-batch RO systems tend to have smaller system volumes, they provide an advantage over true batch RO systems on this metric.

Flux Penalty

To equate the overall production rates of continuous and batch RO processes, some studies specify that the permeate flux must be greater during the production phase of batch processes to compensate for zero permeate production during their flush phase [2, 5, 9]. POU purifiers operate intermittently to replace the water that the user withdraws from the storage tank. Therefore, there is no need to operate at an elevated flux for this application. Hence, there is also no obvious advantage from a semi-batch process over a true batch process, or vice-versa.

7.2 Design and Operation of Semi-Batch Systems

A semi-batch RO system (Fig. 7-2) consitutes:

1. One or more RO elements housed within pressure vessels.
2. A high-pressure pump (HPP). This pump introduces feed into the system and generates the necessary pressure for desalination.

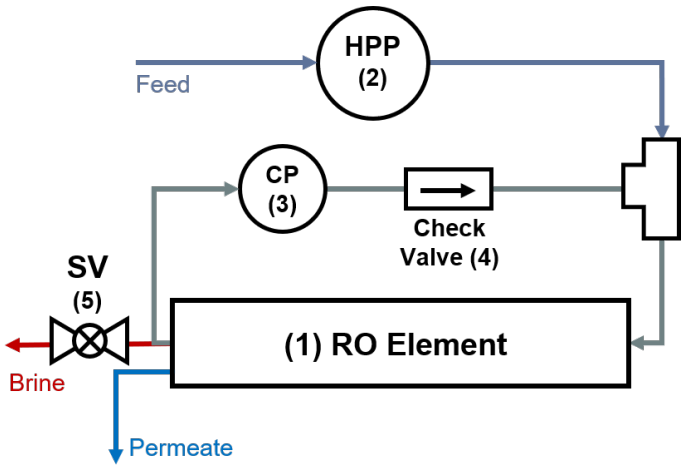

Figure 7-2: **Schematic of a semi-batch RO system.** The system consists of the RO element, a high-pressure pump (HPP), a circulation pump (CP), a one-way check valve, and a solenoid valve (SV).

3. A circulation pump (CP) that recirculates brine in a closed loop through the RO element at a flow rate that exceeds the manufacturer's specified minimum. Recirculating the brine is necessary to prevent excessive concentration polarization. Given its function, the circulation pump only needs to provide sufficient pressure to overcome flow losses through the feed channel and piping.

4. A one-way check valve to control the flow direction within the circulation loop

5. A solenoid valve (SV) to control the release of brine.

The system operates cyclically though two phases: production and flushing (Fig. 7-3). During the **production phase**, the solenoid valve is shut. The high-pressure pump introduces feed into the system while the circulation pump recirculates the brine through the RO element. The inflow from the high-pressure pump causes the system pressure to rise above the osmotic pressure of the brine, which in turn causes water to permeate through the RO membrane, and the brine to become concentrated. Once the system is pressurized, the rate of feed inflow equals the permeate outflow. Permeate production is maintained until the brine becomes sufficiently concentrated. Then, the **flush phase** is initiated by opening the solenoid valve. Opening this valve depressurizes the system and ceases permeate production. The circulation and feed

pumps are then used to eject the concentrated brine and replace it with new feed.

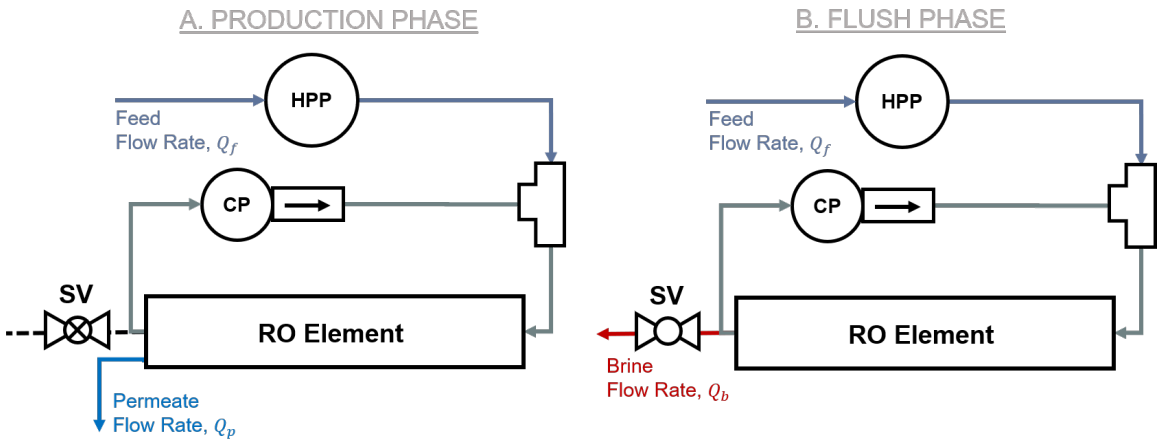

Figure 7-3: **A semi-batch RO process cycles through two phases.** In the production phase, the solenoid valve is shut and the brine is recirculated through the RO element, growing more concentrated with each pass. In the flush phase, the solenoid valve is opened and this concentrated brine is ejected

There are three key advantages to the semi-batch configuration over the continuous configuration that is currently used in POU products:

1. Since POU RO systems are used intermittently, reducing exposure to concentrated brine during down-time will likely extend membrane life. The semi-batch system is flushed with new feed after each production phase. Since no portion of the RO element sits exposed to concentrated brine over an extended duration, the risk of scaling is minimized. It may be possible to completely eliminate scale formation if exposure to supersaturated conditions is minimized and any formed crystals are dissolved during the flush phase [10, 11]; however, this may be difficult to accomplish in practice [8]. In comparison, the tail end of the RO element in a continuous process will always be exposed to the maximum brine concentration.

2. RO elements are designed to operate with a minimum brine flow-rate and within a maximum permeate flux. These two specifications together bound the maximum recovery that is feasible with one RO element in a continuous process. A semi-batch process offers independent control over the permeate flux and the

brine flow rate so that higher recoveries are feasible while operating within the aforementioned specifications.

3. In Chapter 6, it was shown the brine stream throttle in a conventional continuous POU RO system dissipates 29% of the input electrical power due to the low recovery ratio of the process. This dissipation is avoided by recirculating the brine in a semi-batch process, which may lead to potential power savings.

7.3 Prototype Description

A prototype semi-batch RO system was assembled using mass-produced off-the-shelf components (Fig. 7-4). The prototype uses a standard encapsulated 12 L/h (75 GPD) RO element, which is a common size for POU RO purifiers. It uses diaphragm pumps for both the high-pressure and circulation pumps. By design, diaphragm pumps are equipped with check-valves on their outlet ports, thereby eliminating the need for a stand-alone check valve (Fig. 7-2). Finally, the controller for the prototype uses pulse-width modulation (PWM) to control the voltage applied to the high-pressure pump. Controlling pump voltage actively through the production phase may be necessary, as will be explained in Section 7.4.3.

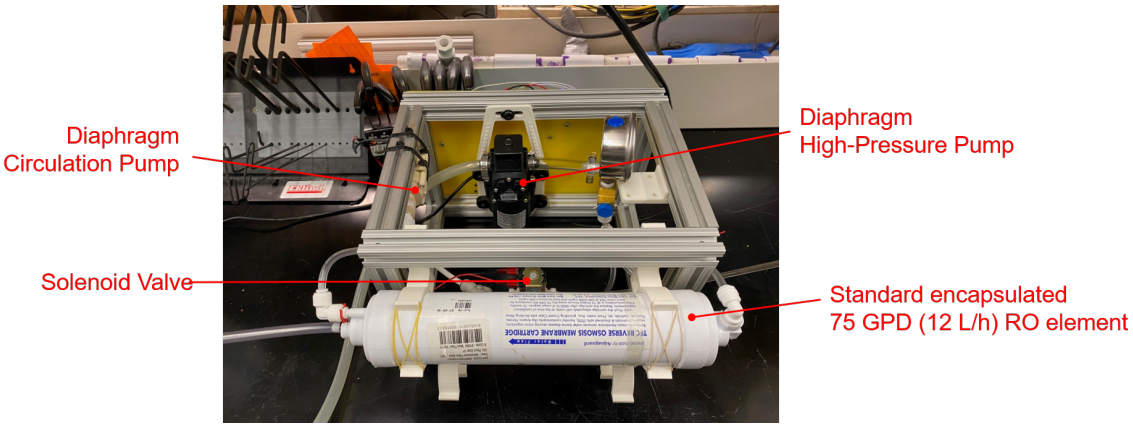

Figure 7-4: **Photograph of prototype semi-batch system.** The prototype was assembled using a standard 12 L/h (75 GPH) element and off-the-shelf pumps.

7.3.1 Preliminary Testing

The prototype was used to desalinate concentrated tap-water. Tap water was mixed with the brine from one test to form the feed for the consecutive test. Measured production rates, recovery, and average permeate concentrations are tabulated below (Table 7.1). The total permeate volume produced for each test was 1 - 1.25 L.

Table 7.1: Results from initial testing of the semi-batch POU RO prototype

Feed Conductivity (μS/cm)	Production Rate (L/h)	Recovery (%)	Permeate Conductivity (μS/cm)
1350	15.3	67	56
1474	14.2	75	80
1800	13.6	75	110
2171	12.3	75	116
2400	12.0	75	132
2730	11.1	75	158
3600	11.0	71	209

As seen, the prototype is capable of recovery ratios that exceed the 60% threshold that the National Green Tribunal (NGT) aims to enforce as a mandatory minimum. This recovery ratio r is defined as

$$r = \frac{V_p}{V_p + V_f}, \tag{7.2}$$

where V_p is the produced permeate volume and V_f is the feed volume used to flush the brine out of the system at the end of the batch cycle. The flush volume was set to approximately twice the system hold-up volume V_s to ensure adequate flushing, however some sources suggest that this may be insufficient [8, 9]. Therefore, optimization of this flush volume is still required.

The system is also capable of production rates that are similar to those of existing products (9-15 L/h). This average production rate $\overline{Q}_p$ was calculated from

$$\overline{Q}_p = \frac{V_p}{\tau_p}, \tag{7.3}$$

where τ_p is the production phase period. Flush durations were excluded in this

calculation because the system is not expected to process batches continuously. It will only process a batch when drinking water is withdrawn from the purifier's storage tank. However, since the flush phase takes only 10-15 s, accounting for the flush duration would decrease the tabulated production rates by less than 5%. While these production rates are acceptable, they can be further increased as is discussed in Section 7.4.3.

The NGT also aims to mandate a minimum product concentration of 150 mg/L, which corresponds to a conductivity of roughly 250 μS/cm. The permeate concentration from the prototype is lower than this minimum. As is typical for existing RO products, blending of the permeate with small feed quantities could be used to raise the product concentration to permissible levels.

Power consumption was not measured during these tests. Therefore, it is yet to be determined whether this semi-batch prototype saves energy relative to conventional continuous systems.

7.4 Proposed Improvements to the System

Before the system can be integrated into a product, additional features may be needed to ensure that the performance is robust to changes in temperature, feed concentration, and membrane permeability. Concepts for how these features could be implemented are described below.

7.4.1 Monitoring Batch Progress

The time to achieve a certain recovery ratio will vary with feed concentration and membrane permeability. To accommodate membrane aging, as well as seasonal and geographical variations in feed water composition, a method of monitoring the batch progress is required.

Sensing of the recirculated brine conductivity or permeate flow rate through the production phase process would enable accurate control over the process recovery ratio. Unfortunately, measuring conductivity and flow rates accurately, with minimal

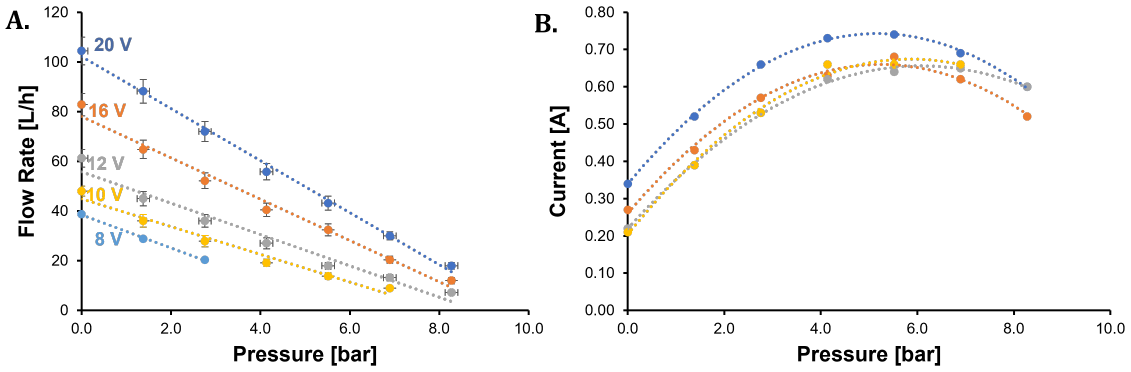

Figure 7-5: **High-pressure pump curves**. (A) Flow-rate is plotted against pressure for varying pump voltages. (B) Current is plotted against pressure for varying pump voltages.

sensor recalibration, is prohibitively expensive. An alternative low-cost solution is measuring the pump outlet pressure and inferring the feed flow rate from the linear pump curve (Fig. 7-5A). The feed flow rate is equal to the permeate flow rate during the production phase; therefore, this approach could be used to monitor batch progress. This approach is attractive because when compared to conductivity and flow rate sensors, pressure transducers are inexpensive.

Another approach could be to measure the voltage and current drawn by the pump, and to use those two parameters to deduce the flow rate and pressure. However, for the small diaphragm pumps used for this prototype, the current is insensitive to pressure in the typical operating pressure range of 5- 7 bar (Fig. 7-5B). Therefore, it would be difficult to infer the pressure reliably from current measurements.

7.4.2 Virtual Feed Concentration and Membrane Permeability Sensor

We can leverage our understanding of the semi-batch process to estimate the feed concentration and membrane permeability using a time series of pressure data and the high-pressure pump curve (Fig. 7-5). To illustrate the basic concept, the following simplifications are made:

1. The per-pass recovery is low so that the brine concentration can be treated as

spatially uniform within the circulation loop. The brine concentration is then treated as only changing temporally.

2. Concentration polarization can be neglected, or can be approximately modeled with a decreased membrane permeability coefficient.

3. The permeate is pure water.

4. The osmotic pressure is proportional to concentration.

5. Pressure drop through the feed-channel is negligible

Then, at any time during the production phase of each batch cycle, the instantaneous permeate flow rate Q_p is

$$Q_p = A_{mem} S (P_f - \pi_b), \tag{7.4}$$

where A_{mem} is the membrane water permeability coefficient, P_f is pressure applied by the high-pressure pump (Fig. 7-5), S is the total membrane area of the RO element, and π_b is the instantaneous brine osmotic pressure, assuming that the concentration through the element is uniform (Assumption 1).

Additionally, a mass balance during the production phase gives that

$$V_s(C_b - C_f) = C_f \int_{t=0}^{t} Q_f dt, \tag{7.5}$$

where V_s is the system hold-up volume, C_b is the instantaneous average brine concentration, C_f is the feed concentration, Q_f is the feed flow rate, and t is the elapsted time. The left side of the equation represents the salt accumulation within the system and the right side is the inflow of salt into the system. The outflow of salt in the permeate stream is negligible (Assumption 3). Note that during the production phase, the feed flow rate equals the permeate flow rate, so

$$Q_f = Q_p, \tag{7.6}$$

and if the osmotic pressure is proportional to concentration (Assumption 4), then Eqn. 7.5 can be written as

$$V_s(\pi_b - \pi_f) = \pi_f V_p. \tag{7.7}$$

where V_p is the accumulated permeate volume at time t:

$$V_p = \int_{t=0}^{t} Q_p dt. \tag{7.8}$$

Rearranging the above gives

$$\frac{\pi_b}{\pi_f} = 1 + \frac{V_p}{V_s}. \tag{7.9}$$

Combining Equations 7.4 and 7.9 gives the expression

$$Q_p = A_{mem} S \left(P_f - \pi_f \left(1 + \frac{V_p}{V_s} \right) \right). \tag{7.10}$$

If the pressure P_f is measured, then the instantaneous permeate flow rate Q_p can be inferred from the pump curve (Fig. 7-5A). Integration of Q_p over time gives the accumulated permeate volume V_p. Therefore, P_f, Q_p, and V_p, are quantities that are *measured* in time. The system volume V_s and the membrane area S are *known* quantities by design. Thus, the only two unknowns are the membrane permeability A_{mem} and the feed osmotic pressure π_f. It follows that these two quantities can be estimated using the time series data of the measured quantities.

One way to perform such an estimate is to apply gradient descent. To do this, Eqn. 7.10 is rewritten as

$$[A] = x[B] - xy[C], \tag{7.11}$$

where $x = A_{mem}$ and $y = \pi_f$ are unknown scalars. A, B, and C are vectors that are calculated from known quantities and the time series data of measured quantities, where

$$A = \frac{Q_p}{S}, \tag{7.12}$$

$$B = P_f, \text{ and} \tag{7.13}$$

$$C = \left(1 + \frac{V_p}{V_s}\right). \tag{7.14}$$

Using this formulation, we aim to optimize the values of x and y, that will minimize the mean squared error (MSE) of the residual function E, where

$$[E] = [A] - x[B] + xy[C], \text{ and} \tag{7.15}$$

$$MSE = \frac{1}{m}\sum_{i=1}^{m} E_i(x,y)^2. \tag{7.16}$$

$E_i(x,y)$ is the i^{th} of m elements of the vector $[E]$ evaluated for a given combination of x and y values. Applying gradient descent, x and y can be optimized iteratively through

$$\begin{bmatrix} x \\ y \end{bmatrix}^{new} = \begin{bmatrix} x \\ y \end{bmatrix}^{old} - \alpha \begin{bmatrix} \frac{\partial MSE}{\partial x} \\ \frac{\partial MSE}{\partial y} \end{bmatrix}^{old} = \begin{bmatrix} x \\ y \end{bmatrix}^{old} - \alpha \begin{bmatrix} \frac{2}{m}\sum E_i(x,y)(-B_i + yC_i) \\ \frac{2}{m}\sum E_i(x,y)(xC_i) \end{bmatrix}^{old}, \tag{7.17}$$

where α is the learning rate that will have to be tuned through experimentation. The above optimization could be performed on-board the POU RO purifier in real-time as each batch is processed. This virtual sensor could be used to track variations in feed water processed by the purifier, and monitor membrane life, without the need for additional physical sensors.

7.4.3 Maximizing Production Rate

For the preliminary tests, the high-pressure pump was operated at a fixed voltage, commanded using PWM. However this type of operation does not maximize the production rate of the system (trajectory 1 in Fig. 7-6). At a fixed voltage, the permeate flow-rate will decrease as the batch progresses.

An improved method of controlling the process would be to initially increase the voltage to operate at the maximum allowable flux of the membrane element, then to decrease voltage to operate at its maximum allowable pressure (trajectory 2 in Fig. 7-6).

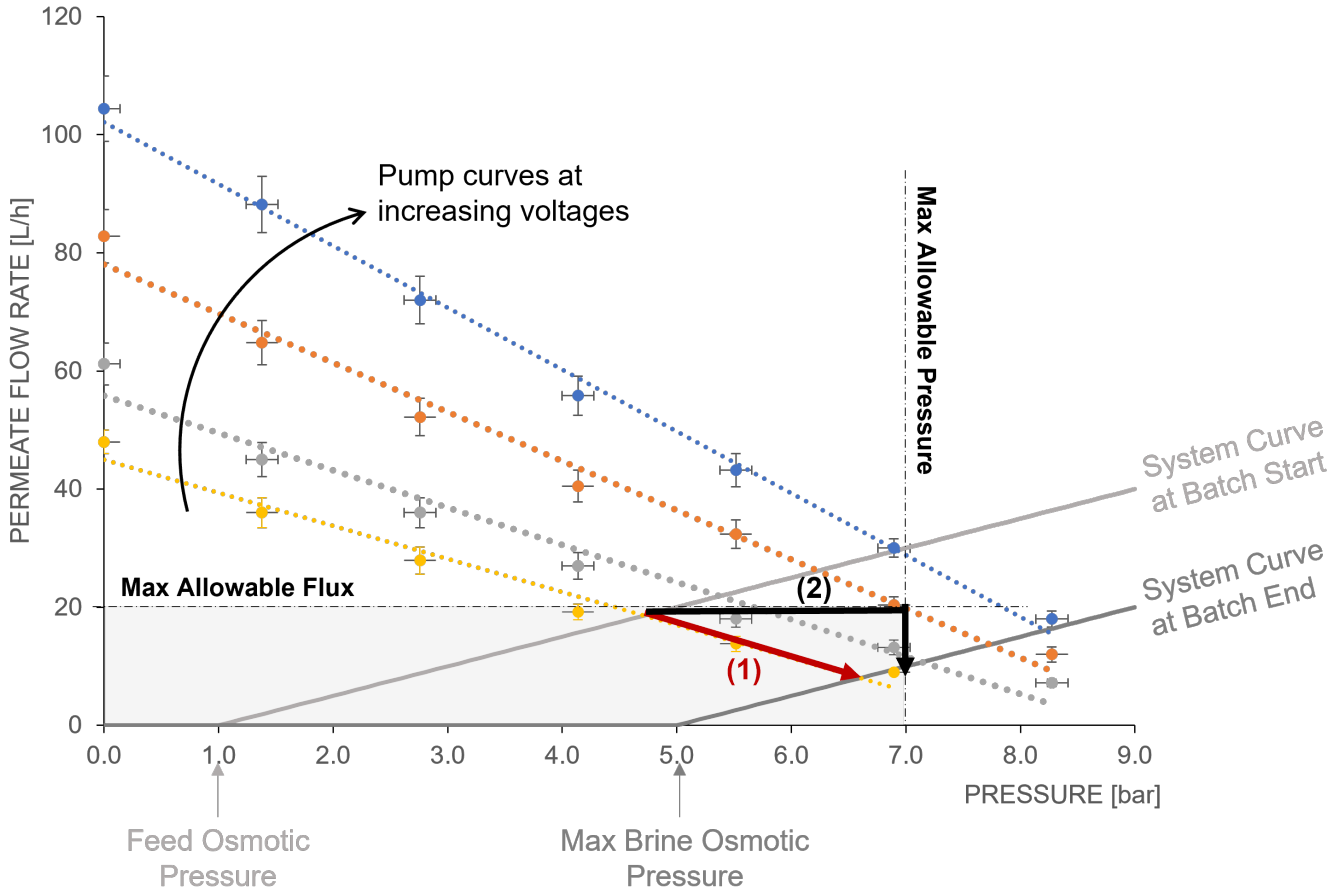

Figure 7-6: **Maximizing the production rate of the semi-batch system.** Colored lines represent the measured flow rate vs. pressure behavior of the high-pressure pump at varying applied voltages (Fig. 7-5A). The grey lines are the system curves at the start and end of the production phase. The slope of the system curves is related to the membrane permeability and the x-intercept is the instantaneous brine osmotic pressure. As the brine becomes more concentrated, the system curve shifts toward the right. The instantaneous operating point during the production phase lies at the intersection of the pump and system curves. If the pump is operated at a constant voltage, then to avoid exceeding the maximum allowable flux, the operating trajectory follows (1). However, the most productive strategy (2) is to initially increase the voltage, to operate at the maximum allowable flux, then to decrease the voltage, to operate at the maximum allowable pressure.

7.5 Conclusions

This section describes the design of a semi-batch RO system intended for point-of-use treatment. Initial testing indicates that this system is capable of meeting the recovery ratio, production rate, and permeate concentration targets required for the application. Long-duration testing on hard water is now required to test whether this performance can be sustained over the expected life of the membrane. In addition, we have outlined several features that could be added to enhance the system's performance at minimum additional cost.

Bibliography

[1] David M. Warsinger, John H. Lienhard, Emily W. Tow, Ronan K. McGovern, and Gregory P. Thiel. Batch Pressure-Driven Membrane Separation with Closed-Flow Loop and Reservoir, 2017.

[2] Quantum J. Wei, Carson I. Tucker, Priscilla J. Wu, Ali M. Trueworthy, Emily W. Tow, and John H. Lienhard. Impact of salt retention on true batch reverse osmosis energy consumption: Experiments and model validation. *Desalination*, 479(October 2019):114177, 2020.

[3] Sandra Cordoba, Abhimanyu Das, Jorge Leon, Jose M Garcia, and David M Warsinger. Double-acting batch reverse osmosis configuration for best-in-class efficiency and low downtime. *Desalination*, 506:114959, 2021.

[4] Kiho Park, Liam Burlace, Nirajan Dhakal, Anurag Mudgal, Neil A. Stewart, and Philip A. Davies. Design, modelling and optimisation of a batch reverse osmosis (RO) desalination system using a free piston for brackish water treatment. *Desalination*, 494(August):114625, 2020.

[5] Jaichander Swaminathan, Emily W. Tow, Richard L. Stover, and John H. Lienhard. Practical aspects of batch ro design for energy-efficient seawater desalination. *Desalination*, 470:114097, 2019.

[6] David M. Warsinger, Emily W. Tow, Kishor G. Nayar, Laith A. Maswadeh, and John H. Lienhard. Energy efficiency of batch and semi-batch (CCRO) reverse osmosis desalination. *Water Research*, 106:272–282, 2016.

[7] Jay R. Werber, Akshay Deshmukh, and Menachem Elimelech. Can batch or semi-batch processes save energy in reverse-osmosis desalination? *Desalination*, 402:109 – 122, 2017.

[8] Tae Lee, Jin Yong Choi, and Yoram Cohen. Gypsum scaling propensity in semi-batch RO (SBRO) and steady-state RO with partial recycle (SSRO-PR). *Journal of Membrane Science*, 588(May):117106, 2019.

[9] Tae Lee, Anditya Rahardianto, and Yoram Cohen. Multi-cycle operation of semi-batch reverse osmosis (SBRO) desalination. *Journal of Membrane Science*, 2019.

[10] David M. Warsinger, Emily W. Tow, Laith A. Maswadeh, Grace B. Connors, Jaichander Swaminathan, and John H. Lienhard. Inorganic fouling mitigation by salinity cycling in batch reverse osmosis. *Water Research*, 137:384–394, 2018.

[11] Avi Efraty and Joseph Septon. Closed circuit desalination series no-5: High recovery, reduced fouling and low energy nitrate decontamination by a cost-effective BWRO-CCD method. *Desalination and Water Treatment*, 49(1-3):384–389, 2012.

Chapter 8

Conclusions

In this thesis, modeling, prototyping, and experimentation were applied to investigate methods to improve the cost, energy efficiency, and water recovery of ED and RO for community-scale and point-of-use desalination of brackish groundwater. After recognizing that membranes are underutilized in a conventional batch ED process, a controller was designed and experimentally implemented to increase yield so that the ED stack cost could be decreased (Chapter 2). With community-scale RO systems, it was identified that recovering hydraulic power from the brine stream could lower the capital cost barrier for off-grid deployment. Modeling was used to demonstrate the feasibility of a fixed-recovery coupled vane pump-ERD concept (Chapters 3-4), which was then prototyped and shown to save energy (Chapter 5). Finally, by evaluating a POU RO purifier, it was identified that a semi-batch RO system could increase recovery while simultaneously saving energy (Chapter 6). A prototype was engineered but awaits further testing (Chapter 7). In addition to the findings summarized within each chapter, key overarching conclusions of this thesis follow:

1. Controlling the applied current to track with the limiting current through the batch ED process (as was demonstrated in Chapter 1) enables minimum membrane usage. To significantly decrease the cost of ED systems further, the underlying unit cost of ion-exchange membranes must decrease.

2. As the diluate salinity decreases in an ED process, it becomes increasingly more

expensive to remove each additional ounce of salt, both in terms of energy consumption and membrane usage. The former is caused by decreasing diluate conductivity while the latter is a function of decreasing limiting current density. For this reason, using ED to desalinate to concentrations of less than approximately 200-300 mg/L is possible, but it is akin to “fighting the physics" of the process.

3. Basic modeling of salt flux, water flux, and energy consumption is notably more challenging for ED than for RO. Investment in simplified modeling tools and software will make it more approachable for engineers to design ED process, and perhaps contribute to the technology being adopted more widely.

4. Using measured efficiencies, it was estimated that adopting the fixed-recovery vane prototype would decrease the energy consumption of typical community-scale BWRO systems (that use multi-stage centrifugal pumps) by approximately 47%. Pairing this estimate with the pilot study measurements (Table 1.2), it is calculated that the fixed-recovery RO system would consume less energy than GEAR Lab's ED pilot: 2.0 kWh/m^3 vs. 3.7 kWh/m^3 for the same 100 mg/L TDS output, respectively. Therefore, if it can be made to operate reliably, then the proposed system would be a significantly more cost-effective method to decreasing energy consumption than switching to ED. On the other hand, it would not increase recovery.

5. Solutions tend to fail in the field when they cannot be maintained. There is an established network of suppliers and expertise for maintaining both community-scale and point-of-use RO systems. Leveraging these same networks could help ensure that new solutions in these markets, such as ED, ERDs, or semi-batch systems, will succeed.

8.1 Future Directions

In this thesis, three solutions to make decentralized desalination more affordable were proposed and demonstrated. However, much work remains before these solutions can be deployed at scale. Specific tasks and directions that would advance this work are outlined as follows:

1. The strategy of tracking the limiting current with a safety margin (Chapter 1) can be implemented with current feedback. In this approach, only the limiting current density would have to be calculated in real-time, based on diluate conductivity measurements. A separate model to calculate the applied voltage would not be required, thereby simplifying the controller.

2. If the ED stack can be modeled accurately, then by simply measuring the current through the stack at a given voltage, it would be possible to ascertain the conductivity of the water flowing through the stack. Therefore, the ED stack could be used as both actuator and sensor in low-cost applications.

3. In next steps, the fixed-recovery prototype should be coupled to an RO train and used to desalinate a saline feed. Monitoring of wear during such a test would help determine whether the existing solution is viable, or whether alternative vane and stator materials must be considered.

4. A preliminary evaluation of the semi-batch POU RO system was used to test whether the recovery, production rate, and permeate concentration targets could be achieved. Having demonstrated feasibility, longer-duration testing is now recommended on water compositions that are more representative of groundwater in India.

5. If the semi-batch RO system proves successful at achieving high recovery ratios and low energy consumption over an extended duration, without increasing the frequency at which membranes must be replaced, then it should also be investigated as a potential solution for community-scale desalination.

THIS PAGE INTENTIONALLY LEFT BLANK

Appendix A

Estimating water and energy usage of POU RO systems in Delhi

In Table A.1, we estimate the aggregate daily feed intake, product output, and energy consumption for all point-of-use (POU) Reverse Osmosis (RO) systems in the city of Delhi, grouped by high (HIG), middle (MIG), low (LIG) income group households. Device usage statistics were collected by Ghosh et al. [1] for each income group, while total households in the same categories were taken from Chaturvedi et al. [2]. The assumed recovery ratio and energy consumption was taken from manufacturer specifications [3].

Table A.1: Estimating the scale of water production and energy consumption of POU RO devices in Delhi

	HIG	**MIG**	**LIG**	**Total**
Number of Households in Delhi	156 518	486 945	2 967 884	3 611 347
Percentage with Device [%]	77	44	27	
Mean Household Size	4.12	4.06	4.25	
Average Feed Consumption [L/person-day]	9.4			
Specific Energy Consumption [kWh/m^3]	3			
Recovery Ratio [%]	25			
Feed Intake [x 10^6 L/day]	4.7	8.2	32.0	44.9
Product Output [x 10^6 L/day]	1.2	2.0	8.0	11.2
Energy Consumption [MWh/day]	3.5	6.1	24.0	33.7

Bibliography

[1] Ruchira Ghosh, Arun Kansal, and Sakshi Aghi. Implications of end-user behaviour in response to deficiencies in water supply for electricity consumption – A case study of Delhi. *Journal of Hydrology*, 536(March 2015):400–408, 2016.

[2] Mayuri Chaturvedi, Tilottama Ghosh, and Laveesh Bhandari. Assessing Income Distribution at the District Level for India Using Nighttime Satellite Imagery. *Proceedings of the Asia-Pacific Advanced Network*, 32(0):192, 2011.

[3] Eureka Forbes Ltd. Dr. Aquaguard Magna RO Purifier. `https://www.eurekaforbes.com/water-purifiers/dr-aquaguard-magna-nxt-hd-ro-uv`. Accessed: 2019-01-05.

Appendix B

Tapered Flow Paths for Continuous Electrodialysis

B.1 Introduction

In Chapter 2, I showed that to minimize membrane usage, the applied current density should track the limiting current density throughout the process. In batch electrodialysis (ED), where the diluate is desalinated to the target concentration via recirculation, this tracking was achieved by applying a time-varying voltage to the stack. However, in continuous ED processes, the diluate is desalinated to the required concentration within a single pass through the stack. In this case, the matching of the applied and limiting current densities can be achieved by tuning the flow path geometry.

When we analyze the applied current density for rectangular flow paths, we find that the applied current density only approaches the limiting current density toward the outlet of the stack (Fig. B-1). As a consequence, the applied current is lower than the limiting current at the stack inlet, leaving an *untapped capacity*. This capacity can be interpreted as either underutilized membrane area or wasted pumping power, since the limiting current density increases with flow velocity.

A tapered flow path like the one illustrated in Figure B-1 causes a decrease in the limiting current density at the inlet of the stack, resulting in an overall better match

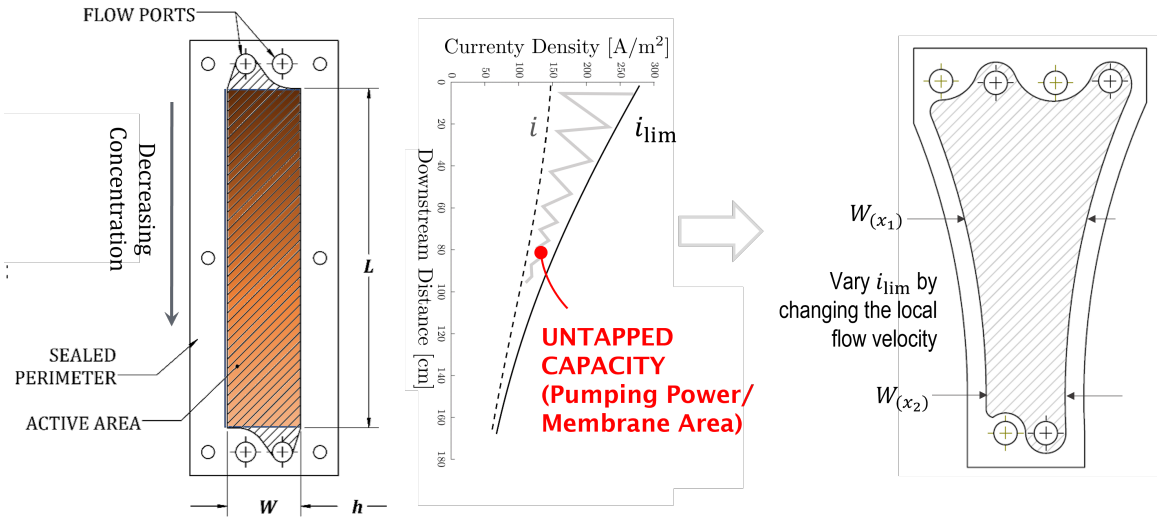

Figure B-1: **Rectangular flow paths cause a mismatch between the applied and limiting current densities.** As diluate travels down the rectangular flow path on the left, its concentration decreases. The resulting applied and limiting current densities are plotted as a function of the downstream distance in the middle plot. It is seen that the applied current is much lower than the limiting current toward the inlet of the flow path, thereby resulting in *untapped capacity*. Instead, the tapered flow path on the right has a width that decreases as a function of diluate concentration so that the applied current tracks more closely with the limiting current.

between the applied and limiting current density curves. As a result, it may utilize less membrane area or consume less pumping power. In this analysis, I calculated the tapered flow path shapes that enabled this matching, and evaluated their performance against a conventional rectangular flow path.

B.2 Calculation of the Ideal Flow-Path Geometry

To calculate the geometry, the flow path was discretized along its length (Fig. B-2) and the following steps were applied iteratively, beginning at the inlet ($x = 0$).

1. The local applied current density i was calculated using an equivalent circuit model. This approach is thoroughly described in previous work [1].

2. The required limiting current density i_{lim}, for a specified current density ratio $r_i = i/i_{lim}$, was calculated. This ratio represents the safety factor against

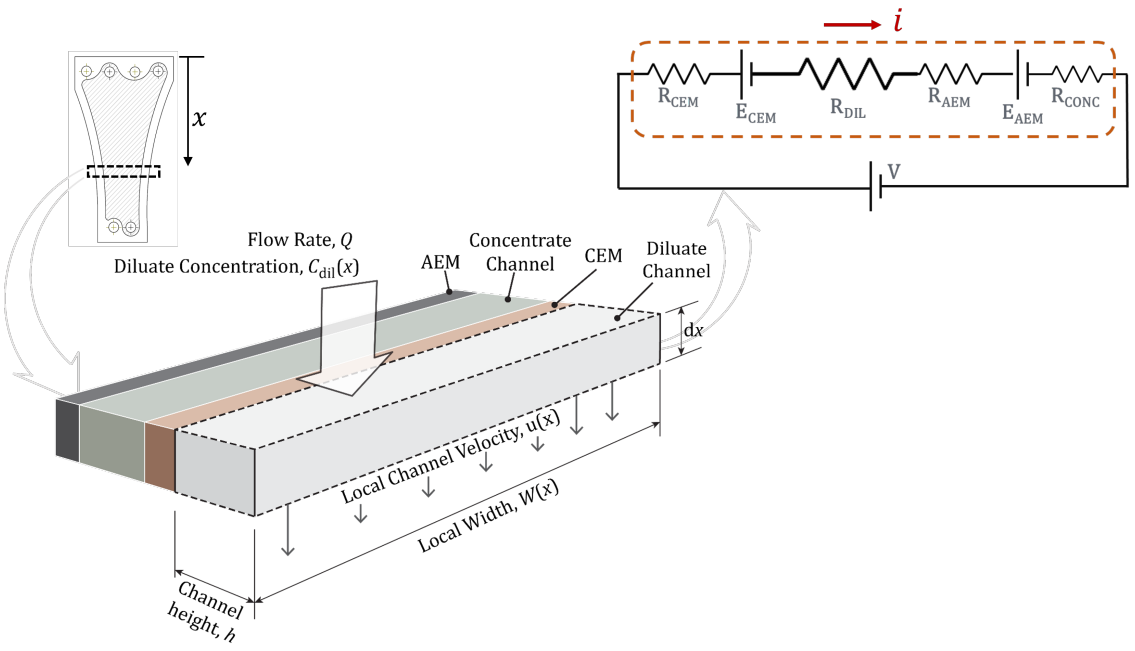

Figure B-2: **Calculating the tapered flow path geometry.** The flow path was first discretized along its length. The applied current density was calculated for each discrete element using an equivalent circuit model. Then, the width at those elements was tuned so that the resulting local flow velocity provided a fixed ratio of applied-to-limiting current.

limiting current.

3. The width $W(x)$ was adjusted to give the local flow velocity $u(x)$ corresponding to the limiting current density i_{lim} calculated in the previous step. The equations relating the flow velocity to limiting current density are described in Chapter 2.3.1.

4. Finally, a mass balance was applied to determine the salt removal at that discrete element.

This process was repeated sequentially for all the elements along the flow path length, giving the diluate concentration at the outlet of the stack, and the width and current density distribution along the flow path. These results were then post-processed to calculate three metrics for comparing flow path geometries: membrane area, the electrical power for desalination, and the hydraulic power for pumping diluate through

the flow channel. The membrane area A is

$$A = \int_{x=0}^{L} W(x)dx, \tag{B.1}$$

where L is the length of the flow path. The desalination power P_d consumption is

$$P_d = V \int_{x=0}^{L} \eta i(x) W(x)dx, \tag{B.2}$$

where η is the open-area fraction of the flow spacer and V is the applied voltage. Finally. the pumping power P_p is estimated from

$$P_p = \Delta P Q, \tag{B.3}$$

where ΔP is the pressure drop and Q is the diluate flow rate. In this analysis, we integrate the frictional pressure drop using

$$\Delta P = \int_{x=0}^{L} \frac{f\rho u(x)^2}{4h} dx[2], \tag{B.4}$$

where h is the channel height and the friction factor f is correlated to the Reynolds number Re as per

$$\begin{aligned} f &= \frac{1400}{Re} \text{ for } Re < 61, \text{ and} \\ f &= \frac{104.5}{Re.^{0.37}} \text{ for } Re \geq 61. \end{aligned} \tag{B.5}$$

The Reynolds number used in these correlations is defined as

$$Re = \frac{uh}{\nu}, \tag{B.6}$$

where ν is the kinematic viscosity of water.

B.3 Comparison with Rectangular Flow Path

A case-study was conducted to compared the performance of the tapered flow path to a rectangular flow path. The rectangular flow path geometry used in this comparison is from the Suez (formerly GE) MkIV-2 ED stack [3]. Though this flow path is actually arranged in a U-shape, we treated it as being straight in this analysis. The dimensions, sample operating parameters, and calculated performance metrics for this geometry are provided in Table B.1.

Table B.1: **Geometry, sample operating parameters, and calculated performance of the Suez MkIV-2 rectangular flow path.**

Geometry	
Width	20 cm
Length	1.60 m
Membrane Area	0.32 m^2
Spacer Open-Area Fraction	0.70
Channel Height	71 μm
Operating Parameters	
Feed Concentration	2000 mg/L
Flow Rate per Diluate Channel	35 L/h
Recovery Ratio	80%
Voltage per Cell-Pair	0.62 V
Calculated Performance	
Flow Velocity u	7 cm/s
Product Concentration	722 mg/L
Desalination Power per Cell-Pair P_d	13 W
Pressure Drop ΔP	52 kPa
Pumping Power per Diluate Channel P_p	5 W
Maximum Current Density Ratio r_i	0.7

A tapered flow path geometry was derived for the same operating parameters, salt removal, and maximum velocity as the rectangular flow-path (Fig. B-3). It was found that the pumping power could be decreased by 48% relative to a rectangular flow path without significantly increasing the membrane area and desalination power consumption. This power savings comes from decreasing the flow velocity toward the inlet of the flow channel, where the limiting current density greatly exceeds the applied current density. Note that the pressure required to accelerate the flow through the

taper ($1/2\rho u^2 \sim 2$ Pa) is negligible relative to the frictional pressure drop; therefore, it was excluded in this analysis.

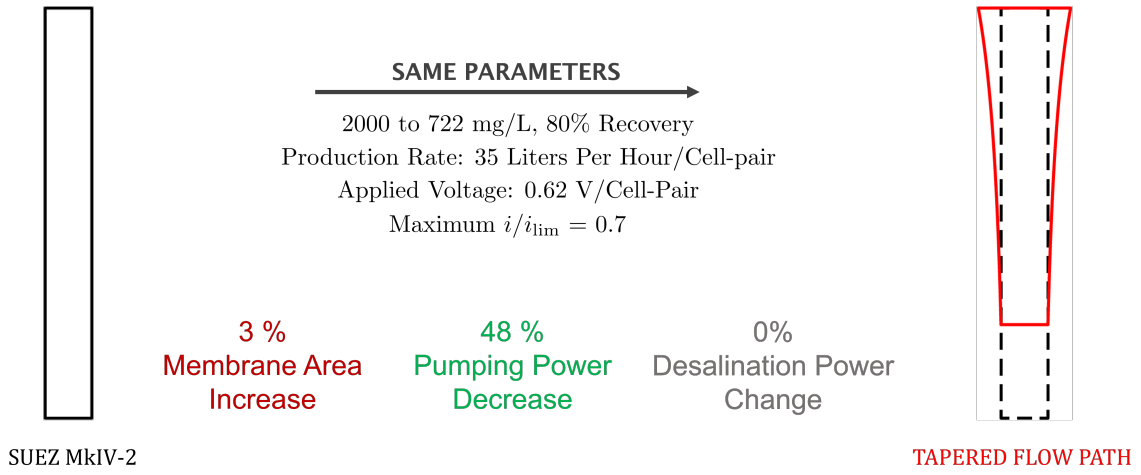

Figure B-3: **For similar membrane area and desalination power consumption, the tapered geometry can decrease pumping power.** The rectangular flow path is shown on the left, and the calculated tapered flow path is shown on the right.

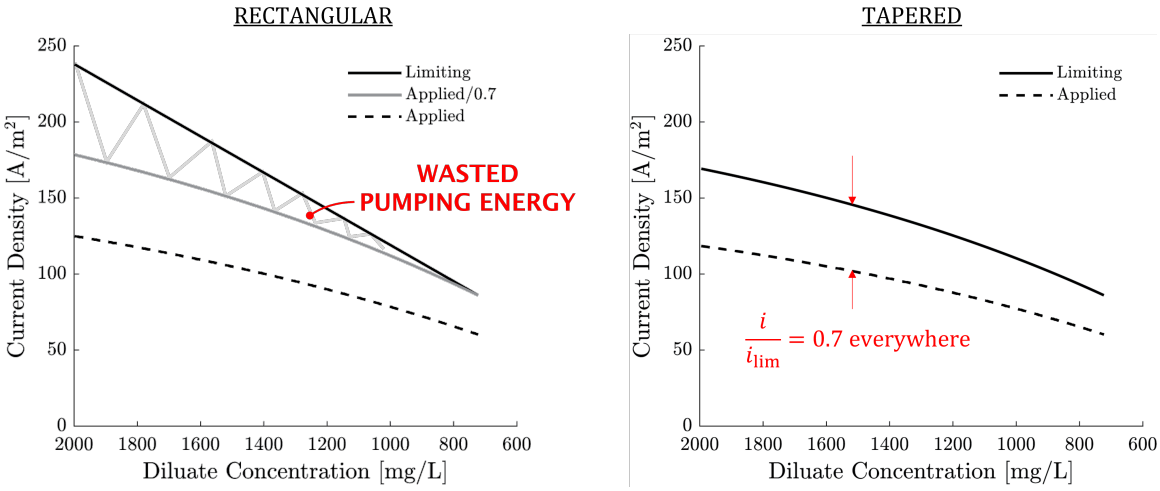

Figure B-4: **The tapered flow path has a constant ratio of applied to limiting current density.** In doing so, the tapered flow path decreases the wasted pumping energy, relative to the rectangular flow path.

The calculated applied current density and limiting current trajectories are plotted for the same two flow path geometries (Fig. B-4). For the rectangular flow path, the current density ratio r_i is less than 0.7 in upstream portions of the flow path. The

tapered flow path saves pumping power by lowering the flow velocity, and therefore also limiting current density, in this portion so that $r_i = 0.7$ everywhere.

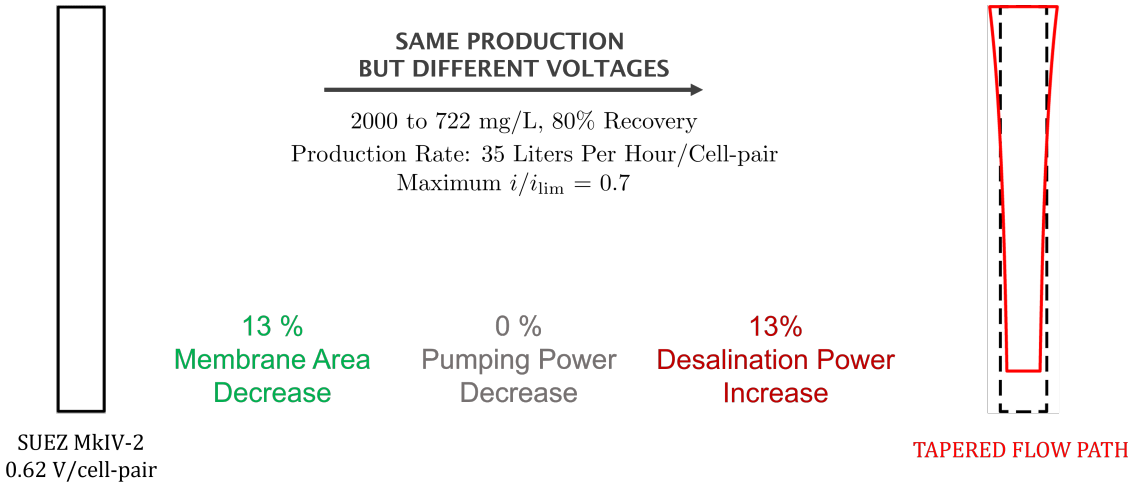

Figure B-5: **For the same pumping power, the tapered geometry can decrease membrane usage.** The rectangular flow path is shown on the left, and the calculated tapered flow path is shown on the right.

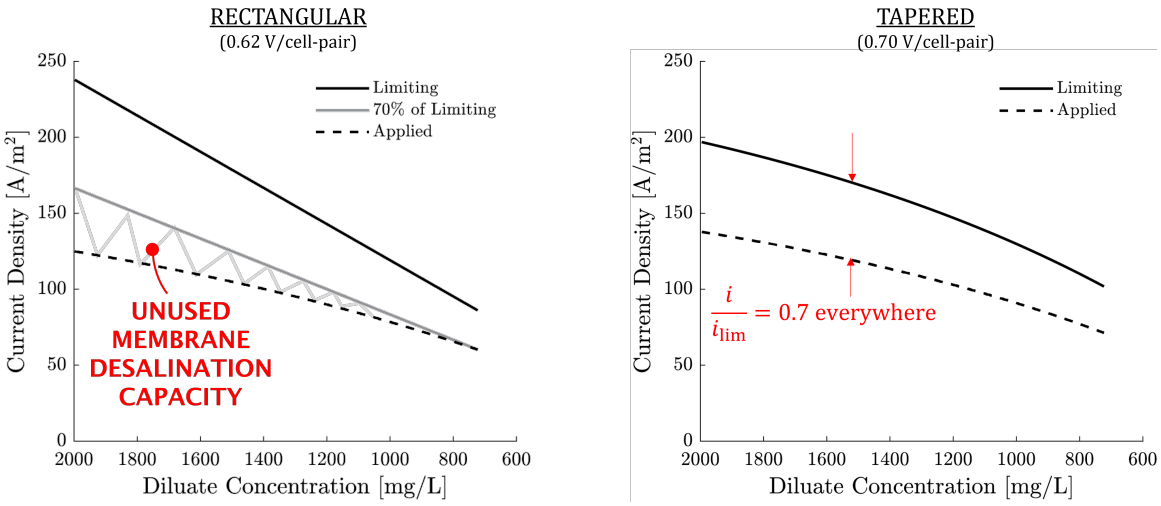

Figure B-6: **The tapered flow path provides a constant ratio of applied to limiting current density at a higher voltage.** In doing so, the tapered flow path enables a higher current density, which in turn decreases membrane usage.

Another approach to obtain a fixed current density ratio is to increase the applied current density by raising voltage. A different tapered flow path results from this approach (Fig. B-5). In this case, the pumping power is unchanged but membrane area decreases due to the higher overall applied current density (Fig. B-6). The

desalination power increases due to the higher applied voltage. Since the equipment cost of brackish water ED desalination typically outweighs its energy costs [4–6], it would be more cost-effective to tune the tapered flow path geometry to minimize membrane usage, as shown in this case (Fig. B-5), than low power consumption (Fig. B-3), as in the former case.

B.4 Remarks on Practicality

The case-study above shows that the *untapped capacity* in rectangular flow paths can be recaptured by adopting tapered geometries that provide either an increase in the applied current density to decrease membrane usage, or a decrease in the limiting current density to decrease pumping power. While these savings were shown to be theoretically feasible, there are several practical factors that are likely to hinder the adoption of such geometries:

- ED membranes are typically manufactured as continuous rolls. The individual membranes for an ED stack are then stamped out of this roll. The 13% decrease in membrane usage shown in Figure B-5 only applies to bounded area of the flow path geometry. However, this area savings may not translate to a manufacturing cost savings since unlike rectangular geometries, the tapered geometries do not pack tightly side-by-side. The resulting manufacturing material wastage may outweigh the savings on flow path area.

- More work is needed to assess the sensitivity of a tapered flow path's performance to changes in the operating parameters. A tapered flow path geometry optimized under one set of conditions may perform poorly under a different set of conditions.

- In calculating the tapered flow path geometries, it is assumed that the membrane area is constant and known (Fig. B-2). In practice, this resistance changes as a function of diluate and concentrate concentrations. It is also likely to increase with membrane degradation and scale formation. These phenomena

would affect the applied current density, thereby possibly shifting the current density ratio away from the value for which the tapered geometry was designed.

For the reasons stated above, tapered flow paths were not investigated in further detail in this thesis.

Bibliography

[1] N.C. Wright, S.R. Shah, S.E. Amrose, and A.G. Winter V. A robust model of brackish water electrodialysis desalination with experimental comparison at different size scales. *Desalination*, 443, 2018.

[2] Francesco Nicolo Ponzio, Alessandro Tamburini, Andrea Cipollina, Giorgio Micale, and Michele Ciofalo. Experimental and computational investigation of heat transfer in channels filled by woven spacers. *International Journal of Heat and Mass Transfer*, 104:163–177, 2017.

[3] Author Antonia Von Gottberg and Product Manager. New High-Performance Spacers in Electro- Dialysis Reversal (EDR) Systems. 2010.

[4] Ronan K. McGovern, Syed M. Zubair, and John H. Lienhard V. The cost effectiveness of electrodialysis for diverse salinity applications. *Desalination*, 348:57–65, 2014.

[5] Karim M. Chehayeb, Daniel M. Farhat, Kishor G. Nayar, and John H. Lienhard V. Optimal design and operation of electrodialysis for brackish-water desalination and for high-salinity brine concentration. *Desalination*, 420(June):167–182, 2017.

[6] Sahil R. Shah, Natasha C. Wright, Patrick A. Nepsky, and Amos G. Winter. Cost-optimal design of a batch electrodialysis system for domestic desalination of brackish groundwater. *Desalination*, 443:198–211, oct 2018.

THIS PAGE INTENTIONALLY LEFT BLANK

Appendix C

Least work of separation derivation

The least work corresponds to the power required to separate the feed stream into a diluted product stream, and a concentrated brine stream at the same temperature and pressure as the feed. It is derived on a mole basis from the first and second laws of thermodynamics in [1] to be

$$\begin{aligned}\dot{W}_{least} = &\left[\dot{n}_{H_2O} RT \ln\left(a_{H_2O}\right) + \dot{n}_{NaCl} RT \ln\left(a_{NaCl}\right)\right]_p \\ &+ \left[\dot{n}_{H_2O} RT \ln\left(a_{H_2O}\right) + \dot{n}_{NaCl} RT \ln\left(a_{NaCl}\right)\right]_b \\ &- \left[\dot{n}_{H_2O} RT \ln\left(a_{H_2O}\right) + \dot{n}_{NaCl} RT \ln\left(a_{NaCl}\right)\right]_f .\end{aligned} \tag{C.1}$$

The molar flow rates of water and salt are $\dot{n}_{H_2O}$ and $\dot{n}_{NaCl}$ [mol/s], respectively. R is the gas constant [J/mol-K], T is the temperature [K], and the product, brine, and feed streams are differentiated by subscripts p, b, and f, respectively. The water and salt mole balances

$$\dot{n}_{H_2O,f} = \dot{n}_{H_2O,p} + \dot{n}_{H_2O,b}, \text{ and} \tag{C.2}$$

$$\dot{n}_{NaCl,f} = \dot{n}_{NaCl,p} + \dot{n}_{NaCl,b} \tag{C.3}$$

are substituted into the above equation to give

$$\begin{aligned}\dot{W}_{least} = &\left[\dot{n}_{H_2O,p} RT \ln\left(\frac{a_{H_2O,p}}{a_{H_2O,f}}\right) + \dot{n}_{NaCl,p} RT \ln\left(\frac{a_{NaCl,p}}{a_{NaCl,f}}\right)\right] \\ &+ \left[\dot{n}_{H_2O,b} RT \ln\left(\frac{a_{H_2O,b}}{a_{H_2O,f}}\right) + \dot{n}_{NaCl,b} RT \ln\left(\frac{a_{NaCl,b}}{a_{NaCl,f}}\right)\right]\end{aligned} \tag{C.4}$$

The activities are expressed in terms of the osmotic coefficients ϕ and mean molal activity coefficients γ using

$$\ln(a_{H_2O}) = -\nu\phi b_{NaCl} M_{H_2O} \text{ and} \tag{C.5}$$

$$\ln(a_{NaCl}) = \nu \ln(\gamma b_{NaCl}), \tag{C.6}$$

where $\nu = 2$ because one mole of sodium chloride dissolves to form two moles of ions. These thermodynamic properties were taken from [2] at atmospheric pressure, and the temperature of the feed solution. Note that

$$\frac{\dot{n}_{NaCl}}{\dot{n}_{H_2O}} = b_{NaCl} M_{H_2O}, \tag{C.7}$$

where b_{NaCl} is the molality of NaCl and M_{H_2O} [kg/mol] is the molar mass of water. Substituting Equations C.5-C.7 into C.4 gives the final expression

$$\begin{aligned} \dot{W}_{least} =& 2\dot{m}_{H_2O,p} RT \left[-b_{NaCl,p}\phi_p + b_{NaCl,f}\phi_f + b_{NaCl,p} \ln\left(\frac{\gamma_p b_{NaCl,p}}{\gamma_f b_{NaCl,f}}\right)\right] \\ &+ 2\dot{m}_{H_2O,b} RT \left[-b_{NaCl,b}\phi_p + b_{NaCl,f}\phi_f + b_{NaCl,b} \ln\left(\frac{\gamma_f b_{NaCl,b}}{\gamma_f b_{NaCl,f}}\right)\right], \end{aligned} \tag{C.8}$$

where the mass flow rate of water $\dot{m}_{H_2O}$ [kg/s] in each stream is

$$\dot{m}_{H_2O} = \dot{n}_{H_2O} M_{H_2O}. \tag{C.9}$$

Bibliography

[1] Karan H. Mistry and John H. Lienhard V. Effect of Nonideal Solution Behavior on Desalination of a Sodium Chloride (NaCl) Solution and Comparison to Seawater. Volume 6: Energy, Parts A and B:1509–1523, 11 2012.

[2] Jaakko I. Partanen. Mean Activity Coefficients and Osmotic Coefficients in Dilute Aqueous Sodium or Potassium Chloride Solutions at Temperatures from (0 to 70) °C. *Journal of Chemical and Engineering Data*, 61(1):286–306, 2016.

Appendix D

Molality, molarity, and density relations

Solution molarities c [mol/L] were calculated using the Onsager-Falkenhagen relation,

$$\Lambda = \Lambda_0 - (K_1\Lambda_0 + K_2)\frac{\sqrt{c}}{1 + K_0 a\sqrt{c}}, \tag{D.1}$$

where the specific conductance Λ [S-cm^2/mol] is related to the conductivity measurements σ [uS/cm] through

$$\sigma = (1000 \text{ uS/S})\Lambda c. \tag{D.2}$$

The coefficients $K_0 - K_3$ and a are tabulated for 20°C and 25°C, and linear interpolation was applied to calculate Λ at intermediate temperatures.

Table D.1: Onsager/Falkenhagen constants for NaCl solutions [1]

Temp [°C]	Λ_0	a	K_0	K_1	K_2
20	113.76	4	0.3276	0.2269	53.48
25	126.45	4	0.3286	0.2289	60.32

Conversion from molarity to molality b [mol/kg] was performed using

$$b = \frac{c}{\rho/1000 - cM_{NaCl}}, \tag{D.3}$$

where the density of the solution ρ [kg/m^3] was itself correlated to molality through

$$\rho = \rho_{H_2O} \frac{1 + bM_{NaCl}}{1 + A_0 b \rho_{H_2O} + B_0 b^{3/2} \rho_{H_2O} + C_0 b^2 \rho_{H_2O}}. \tag{D.4}$$

Here, M_{NaCl} [kg/mol] is the molar mass of sodium chloride, $\rho_{H_2O} = 997.047$ kg/m^3 is density of pure water at 25°C, and the empirical coefficients are $A_0 = 16.62$ x 10^{-6}, $B_0 = 1.773$ x 10^{-6}, and $C_0 = 0.098$ x 10^{-6} [2].

The average total (water and salt) mass flow rate $\dot{m}$ [kg/s] for each stream is taken as the ratio of the measured mass over time. The associated volumetric flow rate is

$$Q = \frac{\dot{m}}{\rho}. \tag{D.5}$$

The mass flow rate of only water $\dot{m}_{H_2O}$ [kg/s] in the stream is subsequently

$$\dot{m}_{H_2O} = \rho_{H_2O} Q. \tag{D.6}$$

Bibliography

[1] G. Kortum. *Treatise on Electrochemistry*. Elsevier Publishing Company, 1965.

[2] Robert W. Potter and David L. Brown. The Volumetric Properties of Aqueous Sodium Chloride Solution from 0 to 500 degC at Pressures up to 2000 Bars Based on Regression of Available Data in the Literature. Technical report, United States Department of the Interior, 1977.